

KfK 5288
EUR 15466 EN
Dezember 1993

**Nuclear Fusion Project
Annual Report of the
Association KfK/EURATOM**

October 1992 - September 1993

Projekt Kernfusion

Kernforschungszentrum Karlsruhe

KfK 5288
EUR 15466 EN
Dezember 1993

Nuclear Fusion Project
Annual Report of the
Association KfK/EURATOM
October 1992 - September 1993

compiled by

G. Kast

Kernforschungszentrum Karlsruhe

Als Manuskript gedruckt
Für diesen Bericht behalten wir uns alle Rechte vor

Kernforschungszentrum Karlsruhe GmbH
Postfach 3640, 76021 Karlsruhe

ISSN 0303-4003

Preface

The Nuclear Research Centre Karlsruhe (KfK) contributes to the European Fusion Programme in developing the key technologies needed to build the International Thermonuclear Experimental Reactor (ITER) and to design commercial fusion reactors.

The historical basis of the present fusion activity are various nuclear technology projects and accelerator development. Whereas the nuclear projects gave the background for the present fusion related materials programme, blanket - fuel cycle - and safety activities, the earlier accelerator work gave origin to the present disciplines of superconductivity and rf-heating.

Technologies developed for the Next European Torus (NET) are made available to ITER. During the ten years of existence of the KfK fusion project major test facilities have been built which constitute a considerable potential to test components and systems relevant for ITER in a technical scale. In particular the ITER model coil test facility TOSKA, the in-vessel-handling demonstration facility EDITH, the tritium laboratory TLK and the test arrangement for first wall components FIWATKA shall be named.

One of the important technological missions of ITER will be the qualification of first wall and fuel cycle components, in particular the breeding blankets. Within a European Community wide cooperation KfK elaborates breeding blanket designs for a Demonstration Reactor (DEMO) and conducts the basic r+d to qualify these concepts for implementation as test sections in ITER. Associated to the blanket activities is a programme to develop and qualify structural materials with sufficient lifetimes and reasonable activation properties. The work conducted in this frame necessitates extensive reactor and accelerator irradiations and subsequent hot cell examinations. Reactor irradiations are performed out of site, whereas two cyclotrons combined as Dual Beam Facility provide a unique tool for simulation of irradiation effects and for activation measurements.

The safety related part of the fusion project contributes to the component studies (blankets, superconducting magnets) and investigates the risk of severe accidents of fusion installations in nuclear operation.

The present yearly report of the KfK fusion project compiles the work under contract with the Commission of the European Community. References given on the responsible staff and on available reports may serve to provide the interested reader with more information on our programme.

J.E. Vetter

Report of the Next Step Technology Programme

<u>Structural Materials, Plasma Facing Components, Plasma Engineering</u>		1
PSM 3	Low Cycle Fatigue of 316L and Welds	3
PSM 8	High Emissivity Coatings on 316L	4
PPM 1	Development and Characterization of Graphites and CFCs	5
PPM 3	Off-Normal High Heat Loads	8
PPM 4	Ceramics for Heating and Current Drive Systems	9
PPM 6	Erosion, H-Retention, Gas Interaction	13
PDT 1	First Wall Mock-up and Tests	14
PDT 2	Divertor Mock-up and Tests	16
<u>Superconducting Magnets</u>		18
MCOI	Model Coil	19
MCON	Full-Size 40 kA Conductor	20
MTOS	TOSKA Upgrade for Model Coil Testing	22
MBAC	High Field Operation of NbTi at 1.8 K	31
<u>Vacuum and Fuel Cycle</u>		32
TPV 1	Mechanical Vacuum Components	34
TPV 2	Optimization of Cryogenic Vacuum Pumping of Plasma Exhaust	37
TEP 2	Permeation und Catalytic Cracking: Alternative Options	44
<u>Nuclear Engineering / Basic Blanket</u>		
NDB 2	Neutronics Data Base - Benchmark Experiments	51
<u>Remote Handling / Maintenance</u>		53
RHB 1	RH Common Subsystems	54
RHT 1	Articulated Boom Transporter	56
RST 2	Cutting and Welding Tools	63

<u>Safety and Environment</u>	64
SEA 3 Analysis of Reference Accident Sequences	65
SEP 1 Radioactive Inventories and Source Terms	69
SEP 2 Environmental Impact of Tritium and Activation Products	70
<u>Long Term Program for Materials Development</u>	72
LAM 2.1 Low-Activation Fusion Materials Development	73
LAM 3.2 Development of Low Activation Martensitic Steel	75
MANET 1.1 Characterization and Optimization of MANET-II-Steel	77
MANET 2.3 Diffusion Welding	78
MANET 3.2 Pre- and Post-Irradiation Fatigue Properties	79
MANET 3.4 Pre- and Post-Irradiation Fracture Toughness	83
MAT 5 Ion-Beam Irradiation Fatigue and Creep Fatigue Tests	85
<u>Test Blanket Development</u>	88
<u>BS - Solid Breeder Test Blanket</u>	89
BS DE-D 1 Solid Breeder Test Blanket Design	89
BS BE-D 1 Beryllium	93
BS BR-D 1/D 2 Preparation and Characterization of Ceramic Breeder Materials	97
BS BR-D 3 Irradiation Testing and Post Irradiation Examination	98
BS BR-D 4 Tritium Release	101
BS BR-D 5 Irradiation Testing and Post-Irradiation Examination	102
BS BR-D 8 Thermochemistry of the Reaction of Lithium Orthosilicate with Hydrogen	104
BS NN-D 1 Helium Blanket Test Loop	106
BS NN-D 2 Irradiation Experiments and Non Nuclear Tests	108
BS NN-D 3 Irradiation Experiments and Non Nuclear Testing	114
<u>BL - Liquid Metal Test Blankets</u>	116
BL DE-D 1 Liquid Metal Test Blanket Design	116
BL PC-D 2 Active and Inactive Impurities and Clean-up of Molten Pb-17Li	119
BL EI-D 1 Electrical Insulation and Coatings	121
BL MH-D 1 Liquid Metal MHD	125
BL SA-D 1 Reliability Assessment	131
BL SA-D 2 Safety Analysis of Self-cooled LM Breeder Blankets	133

Development of ECRH Power Sources	136
TRIT-1 - Tritium Supply and Management	143
Study Contracts for ITER / NET	144
Extended Jacket Material Characterization of the Model Coil	145
Crack Growth in the NET First Wall	147
Impact of ITER Liquid Metal Blanket Design Options on Safety Level and Licensing in Germany	148
Appendix I: Allocation of Tasks	150
Appendix II: Table of NET Contracts	153
Appendix III: KfK Departments Contributing to the Fusion Project	154
Appendix IV: Fusion Project Management Staff	155

Structural Materials, Plasma Facing Components, Plasma Engineering

Introduction and Overview:

Due to the complexity of First Wall and plasma-near structures the range of topics in these task areas is somewhat inhomogeneous, a fact that is also reflected by diversity of tasks with KfK-participation. On the other hand our contributions in certain subtasks are rather small so that a concentration of work seems to be reasonable. In this sense some of the activities reported here will run out in the near future unless a strong interest is expressed by ITER.

Within PSM3 (subtask 9) KfK has made an essential contribution to the understanding of failure mechanisms in 316L structures under complex cyclic loading conditions. This work has not been funded from the 1992–94 programme.

Final work has also been done on the interaction of high emissivity coatings and thermal fatigue of 316L within PSM8 (subtask 3) of the 1989–91 programme. In most cases the coatings survived severe thermal cycling in excellent condition.

Under task PPM1 (subtask 3) KfK has determined room temperature mechanical properties and isothermal fatigue behaviour of high conductivity CFC. The work suffered from the poor availability of composite material on the market. The equipment for high temperature testing has been set up.

Not funded but considered as a valuable contribution to subtask 7 is the work on thermophysical properties of CFC s, the first results of which are also reported here.

Within the frame of the plasma stream target interaction modelling (PPM3, subtask 2) priority was given to the calculation of radiative energy transfer in the target plasma expanding across the toroidal magnetic field. A vapor shield, reducing further power deposition in the solid surface to ca. 4%, is fully established in less than 4 μsec . The resulting erosion is therefore limited to about 0.5 μm . The influence of vapor expansion across magnetic field lines is described by the field diffusion equation. Calculations show that vapor expansion is slowed down by a backstreaming motion of the magnetic field lines that are initially dragged away by the expanding plasma. This supports the vapor shield effect.

Complementary experimental work is ongoing but not yet contained in the task definition, and therefore not reported here.

Comprehensive work has been done on ceramics for ECRH windows (PPM4, subtask 3). A major part of the activities has been devoted to an extension and consolidation of thermophysical and dielectric data in the cryogenic temperature region. In addition, in order to assess the neutron dose effects on mechanical properties at low temperature,

the changes in bending strength and fracture toughness have been evaluated.

An understanding of mechanisms leading to mechanical degradation was attained, but on the other hand it can be stated that the dielectric properties are much more prone to irradiation effects.

Significant progress was made in the evaluation of very low dielectric loss data by elimination of a systematic scatter due to a temperature-dependent disbalancing at the mirrors of the Fabry-Pérot resonator device. With the settlement of the measurement base it was possible to identify sapphire grades whose dielectric losses at about 70 K range not far from intrinsic loss model predictions. The influence of irradiation showing up to about 10^{-3} dpa could also be quantified. Some measurements have been started on the radiation-induced electrical degradation (RIED) effect, but the relevance of the phenomena as such is still controversial.

In completion of subtask 2 of PPM4 thermophysical properties of various insulator materials under consideration for ECRH-windows have been determined down to 70 K. The theory of thermal resistivity comprising the three terms "3-phonon umklapp-process", phonon scattering at point defects and boundary scattering has been established and the constants defining the relative contributions of these partial processes have been determined.

A coordinated ECN/KfK program has been initiated under PPM6 (subtask 2) on the effect of radiation for tritium trapping in beryllium and carbon-based materials. A high-temperature equipment was installed at KfK for loading (irradiated) specimens with tritium in a stagnant atmosphere and afterwards annealing in a He + 0.1% purging gas stream. Difficulties were experienced by a chemical reaction of Al_2O_3 containers with C-based materials. For Be samples the interference of loaded with intrinsic tritium (from neutron reactions) has to be sorted out.

In the frame of PDT1 (subtask 4) first wall mock-ups are tested under thermocyclic loads close to those during pulsed tokamak operation. The plasma heat flux is simulated by low inertia surface heaters. The NET specimen was tested without protection tiles at rather low heat loads and afterwards with radiatively cooled graphite tiles at realistically high power levels. After an only low number of cycles the tile attachment failed due to a rather elementary design error. The next test will be on the same specimen with a modified tile attachment accounting for the hitherto underestimated bowing forces. FEM analyses always accompany the tests in order to determine full information on the temperature/stress/strain fields in the mock-up.

In completion of PDT2, subtask 1, bonded divertor samples have been cycled in the modified plasma spray facility. A broad range of substrates, protection and braze materials has been covered and a comprehensive final report has been delivered.

In summary a number of options have proved to be viable with a TZM/3D-CFC/Cu-Ti braze combination being the most favorable option tolerating more than 13000 cycles of 15 MW/m² and 1 ... 3 sec duration in perfect condition.

H.D. Röhrig

PSM 3 Low Cycle Fatigue of 316L and Welds

Subtask 9: Tubular Uniaxial and Multiaxial Isothermal and Thermal Fatigue on 316L

First thermal cycling tests are finished now [1]. Crack initiation and crack propagation was measured by a videoptical measuring system. The crack initiation in all tests was in longitudinal direction parallel to the specimen axis, depending on the loading, after 50 %-80 % of lifetime. The cracks grow from the inner and from the outer surface. At 3/4 of the wall thickness from the inside a sharp separating line is visible. This line separates the both crack propagation directions.

In addition Finite-Element calculations have been done. Depending on the temperature distribution on inner and outer surface the stresses and strains were estimated using the Chaboche Model.

The complete report will be presented in September/October 93.

Literature:

- [1] Kirsten Becker: "Untersuchungen zur Rißentstehung und Rißausbreitung an thermozyklisch belasteten Rohren aus dem austenitischen Stahl 1.4909", Diplomarbeit, Universität Karlsruhe (TH), IZSM, August 1993

Staff:

K. Becker

W. Hartlieb

B. Schinke

B. Windelband

A. Zeller

PSM 8 High Emissivity Coatings on 316L

Subtask 3: Thermal Fatigue Effect on Emissivity of High Emissivity Coatings

The mechanical integrity of several candidate coatings for the first wall or their vulnerability to failure was examined in thermomechanical cycle tests under temperature and stress conditions relevant to normal first wall operating conditions. Circular stainless steel samples of 5 cm diameter and 0.8 cm thickness, coated at one side, have been used as test specimens. Seven types of coatings, basically the three materials $Al_2O_3+TiO_2$, TiC, and Cr_2O_3 , applied to the substrate by different processes and manufacturers were investigated (see Table 1).

The samples were exposed to a plasma flame for a predetermined pulse length as to achieve adequate temperature (typically 400 °C at the coated surface) and thermal stress amplitudes during one cycle. After the heat pulse the samples dissipated their heat to the water cooled sample holder during the dwell time, reaching approximately 150 °C before the next cycle started.

A first set of six samples has been tested up to 104 cycles and a second set has been tested up to 2000 cycles. Microscopical surface inspections revealed at 9 out of 12 samples no cycle damage besides the color changes within the flame spot. At two of the samples (IS4 and IS5) a network of hair cracks was found, and sample EC1 showed a beginning flake-off of the coating (Table 1).

The experiments are finished. The final report is in progress.

Staff:

K. Kleefeldt
K. Schramm

KD1	$Al_2O_3-40TiO_2+NiCrAlY$	10,000	c/a
KD2	$Al_2O_3-40TiO_2+NiCrAlY$	2,000	b,d/a
KD4	$Al_2O_3-13TiO_2+NiCrAlY$	10,000	b/a
KD5	$Al_2O_3-13TiO_2+NiCrAlY$	2,000	b/a
KD7	$Al_2O_3-13TiO_2$	10,000	b/a
KD8	$Al_2O_3-13TiO_2$	2,000	b/d
IS1	Cr_2O_3	2,000	b,d/a
IS2	Cr_2O_3	10,000	c/a
IS4	Cr_2O_3, Cr	10,000	c,e/a,e
IS5	Cr_2O_3, Cr	2,000	b,e/a,e
EC1	TiC (without interlayer)	10,000	f/a
EC2	TiC+ 5wt% $Al_2O_3-3TiO_2$	2,000	a/a

Remarks refer to conditions at flame spot/edge (S/E):

- a) No visible change compared to virgin state.
- b) Slight color changes but no visible damage.
- c) Pronounced color changes but no visible damage.
- d) Minor faults, not attributed to thermal cycling.
- e) Network of surface cracks.
- f) Beginning flake-off of coating.

Tab. 1: Summary of Tests

PPM 1 Development and Characterization of Graphites and CFCs

Subtask 3: High Conductivity CFC Materials

Mechanical properties, fracture strength and elastic moduli, of the industrial 3D carbon/carbon composite SEPCARB N 112 have been determined in all directions. The fiber structure of the material is manufactured by needling of fabric layers of carbon fibers. Two plates of the material with heights (needling direction) of 35 mm were available. The specimens were cut from plate No. 1 according to the plan shown in Fig. 1. From the plate No. 2 up to now only specimens from region I were taken. The fracture strength was measured in three-point bending tests at room temperature. The standard dimensions of the prismatic bars for these tests were 3.5 x 4.5 x 45 mm³. Some tests were carried out with longer specimens (III). The standard dimensions were reduced to 2.7 x 3.5 x 35 mm³ when the sample length was identical with the plate height. The load was applied at a rate of 2 N/s. The elastic properties, Young's modulus and shear modulus, have been determined by measuring the oscillation periods of bending and torsional vibrations with a Grindo Sonic device.

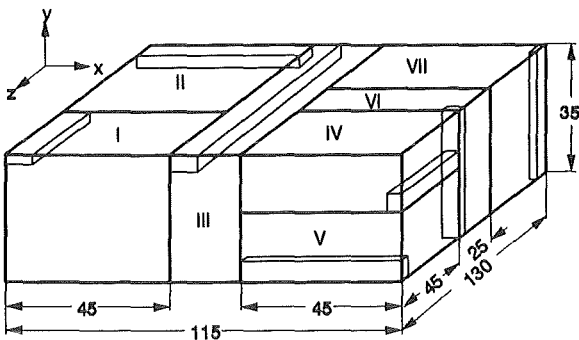


Fig. 1: Plan for specimen cutting.

The test results, mean ultimate bending strength with Weibull modulus (m), Young's modulus, and shear modulus, are presented in Table 1. There is a significant difference in the mechanical data of the two plates. The specimens cut from plate 2 (I/2) exhibit both a higher bending strength and a higher Young's modulus. Generally, the scattering of the strength values in the x-z-plane is low. It is higher when sample length or width are in needling (y-) direction. The lowest values of strength and Young's modulus are measured when the length is in needling direction. The bending tests with the longer specimens yield only slightly higher fracture strengths indicating an insignificant influence of the shear stress on the ultimate bending strength of the standard samples. Cyclic tests were performed in a cantilever bending arrangement with load application by loud speakers. In tests with a constant loadspeaker current the resulting bending moment decreases with increasing test duration, i.e. the specimen compliance increases monotonically. This can be understood as an increase of inner damage as for instance dissolution of fibre/matrix interfaces, generation of cracks in

Reg.	UBS MPa	E GPa	G GPa
I	83.7 ± 5.6 m = 16.0	27.2 ± 1.8	6.7 ± 0.2
II	83.1 ± 6.6 m = 13.4	24.9 ± 3.3	7.5 ± 0.5
III	88.5 ± 5.5 m = 15.6	26.6 ± 3.4	-
IV	86.2 ± 9.6 m = 9.1	27.3 ± 1.3	5.4
V	81.0 ± 11.1 m = 7.6	24.6 ± 2.2	5.0
VI	69.4 ± 9.6 m = 6.9	14.1 ± 4.7	5.1
VII	60.9 ± 6.7 m = 8.6	16.9 ± 0.2	6.3
I/2	99.2 ± 7.5 m = 14.1	32.1 ± 3.5	-

Table 1: Ultimate bending strength (UBS), Young's modulus (E) and shear modulus (G) of SEPCARB N 112.

the matrix and fracture of single carbon fibres. Fig. 2 shows typical curves for tests carried out with different loads.

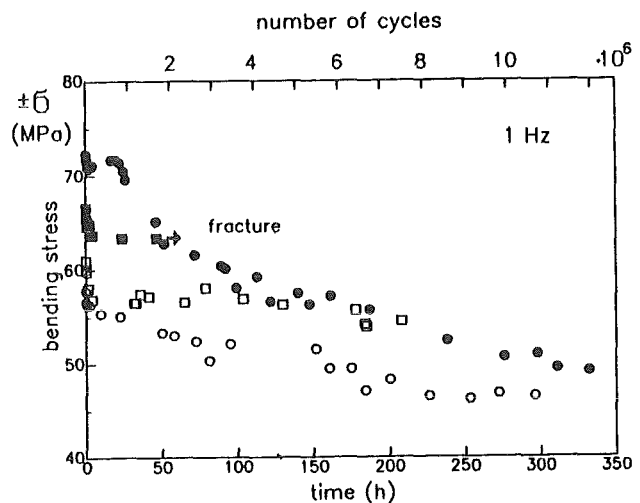


Fig. 2: Decrease of bending stress during cyclic tests with loads kept constant throughout each curve

Staff:

- M. Blumhofer
- H. Zimmermann
- T. Fett
- G. Thun

Contribution to

Subtask 7: Thermophysical Properties (not funded)

The investigation of the industrial 3D carbon/carbon composite SEPCARB N112 started in measuring the specific heat capacity with a Netzsch DSC 404 up to 1300 °C. Fig. 3 shows the mean value with standard deviation. No difference could be found between samples of different plates of the material. Metallographic sections of the material were prepared (fig. 4a - c) to start the microstructural analysis. The mean volume content of fibres has been determined in the x-direction by image analysis.

Staff:

B. Schulz
P. Severloh
Ch. Zeisluft

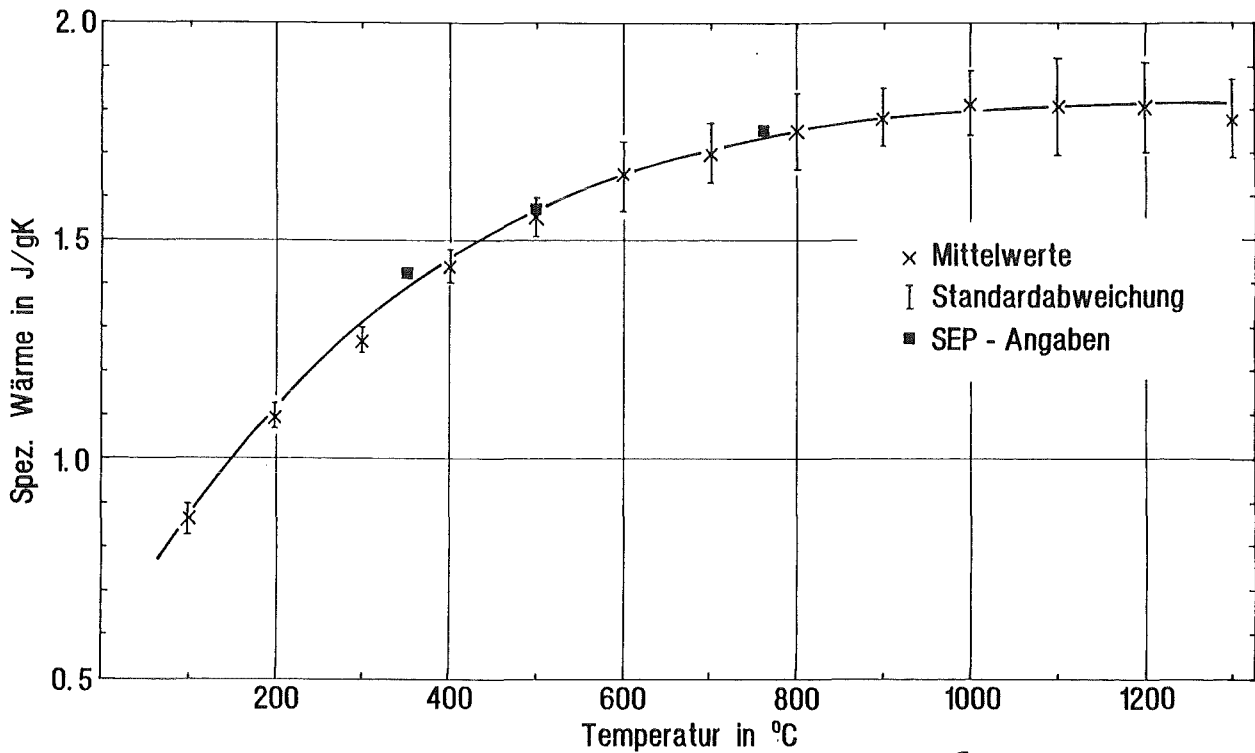
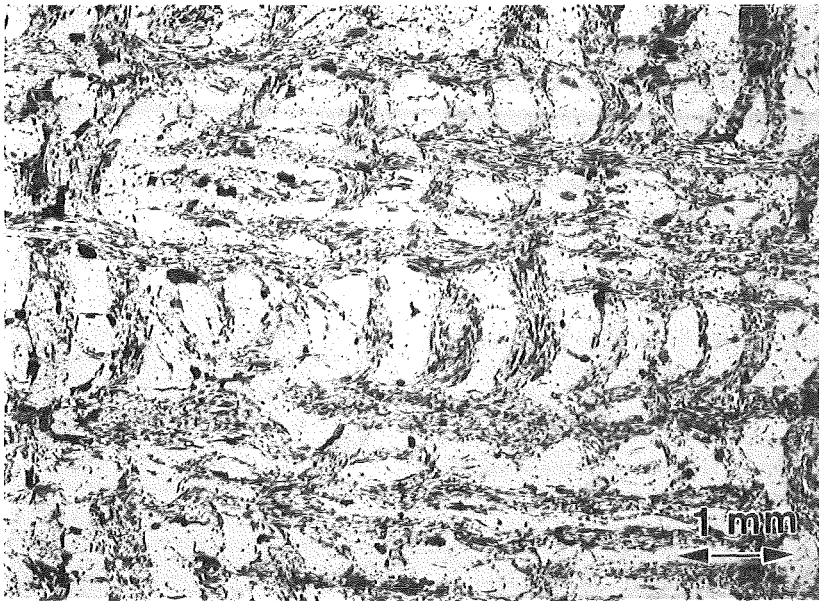


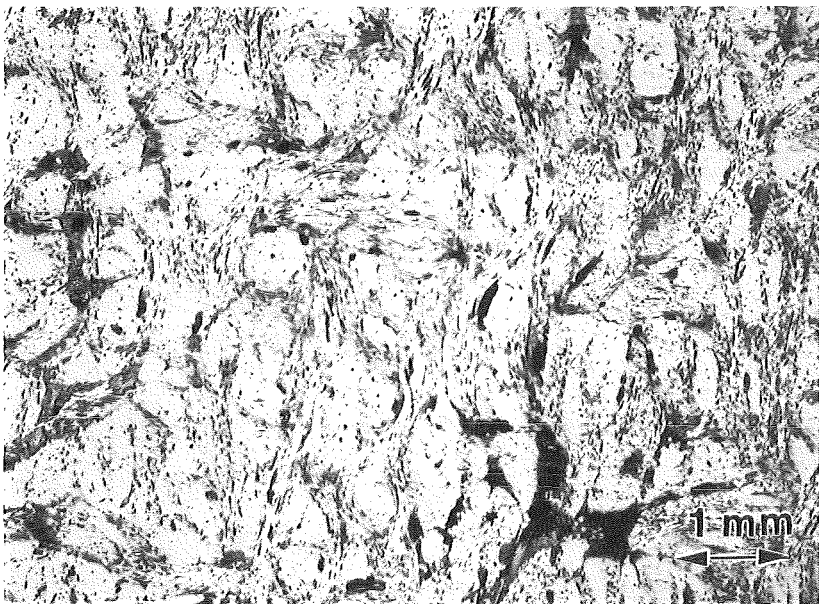
Fig. 3: Specific heat of SEPCARB N112 vs. temperature.



a.)



b.)



c.)

Fig. 4: Microsections of SEPCARB N112
as) x-x-direction; b) y-y-direction; c) z-z-direction.

PPM 3 Off-Normal High Heat Loads

Subtask 2: Simulation of Off-Normal Plasma Material Interactions

For a first modeling of off-normal plasma material interactions and first estimations of the vapor shield the radiation hydrodynamic code KATACO was applied. In these first applications the plasma beam was modeled by deuteron ions with an impact energy of 10 keV, the beam thereby impinging perpendicularly onto a carbon target. 10 keV electrons impinging under an impact angle of 5° show a comparable penetration length. A magnetic field was not taken into account. The first KATACO calculations predict a rather effective vapor shield effect which prevents the carbon divertor from excessive evaporation [1]. Moreover it was shown that the dominant energy transport mechanism in the vapor cloud is radiation.

In a second step of interaction modeling work priority was given to the calculation of the radiation energy transport in the vapor cloud by applying the forward reverse transport approximation. Moreover the target plasma expansion across the magnetic field lines was modeled. For describing the optical properties of the target plasma few and many group Planck and Rosseland opacities calculated by applying a collisional radiative equilibrium model were used [2, 3].

The vapor shield is fully established in less than 4 μ s. After vapor shield formation the power arriving at the target is only around 4 % of the beam power. About 1 % of that heat load can be handled by heat conduction into the bulk target. Assuming that the target plasma layer is stable the erosion remains rather small and reaches about 2 μ m for a beam energy density of 10 MJ/m² and a time interval of 100 μ s.

For describing the influence of the vapor expansion across magnetic field lines the magnetic field diffusion equation was solved. The vapor expansion velocity across magnetic field lines is decreased by a factor of 10 in comparison with the free expansion along magnetic field lines. The consequences in terms of radiative heat transport to the target (magnetic shielding layer) have still to be determined.

Literature:

- [1] B. Goel, W. Höbel, H. Würz; Numerical simulation of radiation transport on super computers. Int. Conf. on mathematical methods and super-computing in nuclear applications, April 19 - 23, 1993, Karlsruhe
- [2] I. Landman, I. Konkashbaev, H. Würz, B. Goel, W. Höbel; Radiative energy transport in a cold carbon plasma layer typical for the interaction of an intense plasma stream with solid carbon targets. Proceedings ICPIG XXI Sept. 19 - 24, 1993, Bochum.
- [3] H. Würz et al; Numerical modeling and experimental simulation of vapor shield formation and divertor material erosion for ITER typical plasma disruptions. Proc. 6. ICFRM Sept. 27 - Oct. 1, 1993, Stresa.

Staff:

B. Goel
W. Höbel
H. Würz

PPM 4 Ceramics for Heating and Current Drive Systems

Subtask 2: Pre-Irradiation Properties at Cryogenic Temperatures
(supplement from preceding program period)

In 1992/93 the investigation of the thermophysical properties thermal diffusivity, thermal conductivity [1], thermal expansion [2] and specific heat down to 70 K on AlN Shapal, poly-crystalline α -Al₂O₃, Hemex sapphire and MgAl₂O₄ has been finished. The results are shown in Fig. 1 for thermal expansion and Fig. 2 for thermal diffusivity. Thermal conductivity data were derived and are given in Fig. 3 for Hemex sapphire.

The discussion of thermal conductivity data, derived from thermal diffusivity, follows the theoretical work of Klemens for pure phonon conducting dielectrics. From this possible scattering mechanisms of phonons are derived.

- a) 3-phonon umklapp-process, which gives the intrinsic, i.e. the lowest possible thermal resistivity of a material:

$$\frac{1}{\lambda_i} = \left(A C_V \exp \left(\frac{\theta}{\alpha' T} \right) \right)^{-1}$$

with A to be calculated according to Slack and α' as the ratio of the Debye frequency to the phonon frequency at the zone boundary of the first Brillouin zone. For sapphire as well as for MgAl₂O₄ the phonon spektra are known.

- b) The thermal resistivity caused by point defects defined by the mass difference and the strain field in the vicinity of point defects and dislocations:

$$\frac{1}{\lambda_d} = CT + D T^{-2}$$

While C can be derived from measured thermal resistivity data at room temperature minus the intrinsic thermal resistivity λ_i , the equation for the influence of the strain field (D) include empirical constants (p.e. Abeles). Thus we decided to take D from a mathematical fit of all measured low (T < 300 K) temperature data of thermal conductivity.

- c) The thermal resistivity due to boundary scattering

$$\frac{1}{\lambda_B} = \frac{3}{c_v \rho \bar{v} \bar{d}}$$

\bar{d} - mean grain size (= sample size for single crystal), \bar{v} - mean velocity of:

All thermal conductivity data follow a function of the type

$$\lambda_{tot.} = \left(\frac{1}{A \exp \frac{\theta}{\alpha' T}} + CT + DT^{-2} + \frac{3}{c_v \rho \bar{v} \bar{d}} \right)^{-1}$$

The values for the constants in this equation are summarized in table:

	Sapphire	Al23	MgAl ₂ O ₄ s.c.
A in g/cms	0.08	0.08	0.055
α'	1.5	1.5	1.75
C in cm/W	0.00314	0.00314	0.00044
D _d in cmK ³ /W	86	2990	3000
E in cmK ⁴ /W	-2	-2	-2
θ in K	950	950	850
λ_i in W/cmK	0.50	0.50	0.23
λ_{RT} in W/cmK	0.34	0.34	0.22

Additionally the thermal expansion of Vacon 709, an alloy, used for construction of the liquid nitrogen cooled microwave windows has been measured (Fig. 4).

Literature:

[1] St. Burghartz, B. Schulz: 6th ICFRM, Stresa, Italy, 27.9. - 1.10.1993
 [2] St. Burghartz, G. Haase, B. Schulz: 13th European Thermophysical Properties Conference, 30.8. - 3.9.93, Lissabon

Staff:

St. Burghartz
P. Fitzi

G. Haase
B. Schulz

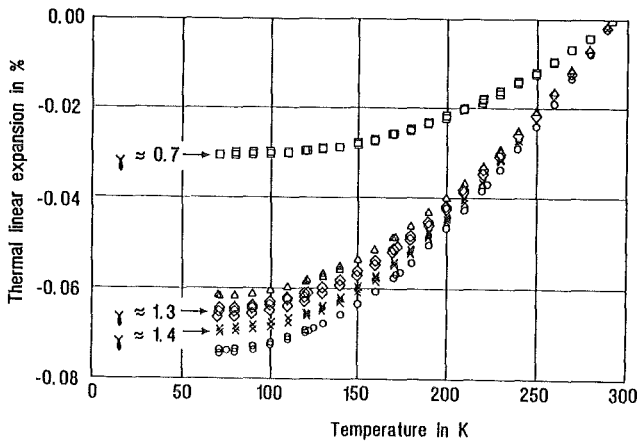


Fig. 1: Thermal linear expansion of sapphire (o || c, Δ || a), α -Al₂O₃ (◇), AlN Shapal (□), MgAl₂O₄ (x) γ - Grüneisen constant.

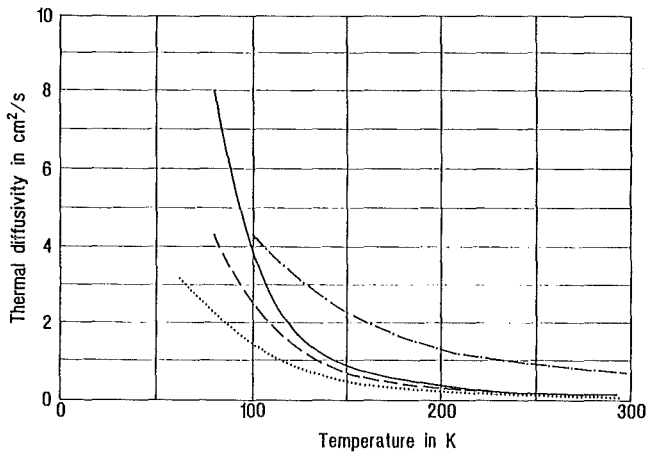


Fig. 2: Mathematically fitted dependency of measured thermal diffusivities vs temperature AlN - - -; sapphire (|| a) —; α -Al₂O₃ - · - ·; MgAl₂O₄ s.c. ...

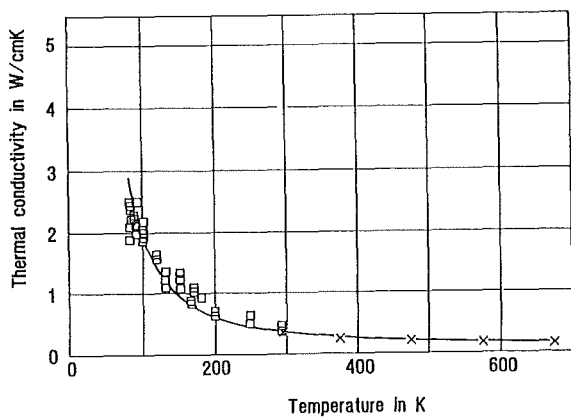


Fig. 3: Measured thermal conductivity of sapphire and calculated eqn. 7 (—).

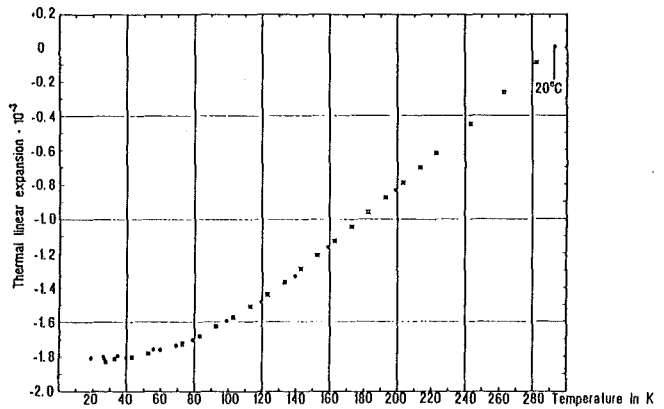


Fig. 4: Thermal expansion of Vacon 70.

Subtask 3: Performance of ECRH Windows under NET/ITER Conditions

The central part of the work has been devoted to extend and consolidate the relevant data base for a cryogenically-cooled window operationable in Electron Cyclotron Resonance Heating (ECRH) systems. Consequently, special emphasis has been laid on measurements of the dielectric and thermophysical properties of sapphire (monocrystalline Al₂O₃) at cryogenic temperatures. But as a consequence of the results achieved in the preceding subtasks on the irradiation effects in ceramic insulators, an additional HFR (Petten) irradiation experiment was evaluated to clarify the strength change of ceramic insulator materials at comparatively low neutron fluence (about $2 \times 10^{25} \text{ n/m}^2$, $E > 0.1 \text{ MeV}$) and low irradiation temperature (about 100 °C).

The bending strength data measured, mostly on 26 irradiated samples each, are given in Table 1. The Al₂O₃ types are sapphire (s.c.) and polycrystalline grades, both fine-grained (about 1 μm grain size: 10 % ZrO₂, VITOX, BIO) and coarser grained (AL23, 8 μm). All these materials show a similar reduction in strength (15 - 25 %) which leaves the pre-irradiation ranking unchanged. Along with former results obtained at $> 5 \times 10^{25} \text{ n/m}^2$ and 400 - 500 °C, the new data suggest the following conclusions: 1) The extrapolated fluence threshold for a considerable strength decrease is expected in the range of 3 to 5 $\times 10^{24} \text{ n/m}^2$ ($E > 0.1 \text{ MeV}$). 2) The irradiation effect on the fracture strength is weakly dependent on the irradiation temperature in the range concerned. Both conclusions together indicate that the strength reduction is probably due to large defect aggregates (efficient damage dose $> 0.5 \text{ dpa}$), and that these aggregates form spontaneously, independent of considerable thermal diffusion.

On the other hand, the MgAl₂O₄ result corroborates literature data indicating a strength increase of this material under neutron irradiation. Finally, the sintered AlN grade applied showed an extremely large strength reduction which, however, is in rough agreement with Japanese results

Material	unirradiated MPa	irradiated MPa
Al ₂ O ₃ -SC	372 ± 48	273 ± 39
Al ₂ O ₃ -10 ZrO ₂	503 ± 46	427 ± 59
Al ₂ O ₃ -VITOX	418 ± 35	352 ± 46
Al ₂ O ₃ -BIO	322 ± 35	255 ± 36
Al ₂ O ₃ -AL23	208 ± 24	150 ± 30
MgAl ₂ O ₄	148 ± 53	168 ± 49
AlN-SHAPAL	301 ± 21	112 ± 12

Table 1: Change of the mean ultimate bending strength (with standard deviation) of various ceramic materials measured after irradiation to 2.0 (± 0.2) x 10²⁵ n/m² (E > 0.1 MeV) at 100 - 115 °C.

measured on the same type of AlN material.

Fracture toughness measurements on samples from former irradiation experiments have shown that the reduction under irradiation is much smaller than that of the bending strength. Therefore one has to conclude that the reduction of the fracture strength is co-determined to a great extent by irradiation-induced facilitation of the crack initiation process. This could be explained by the assumption that crack initiation is due to an inhomogeneous distribution of microstresses in the material microstructure, and that the inhomogeneity is enlarged by irradiation defect aggregates.

The hemispherical Fabry-Pérot resonator technique for dielectric loss measurements at 145 GHz was carefully revised with respect to the data evaluation procedures involved. Previously low loss materials, especially sapphire (ordinary ray) and s.c. quartz, had shown systematic scatter in the loss data, when the dielectric loss tangent (tan δ) was evaluated below ~ 150 K. At that time, systematic measurements with various specimen geometries had been initiated which could now be successfully used to redefine one basic factor in the standard data treatment, the so-called loading factor F_L. It was shown that a new temperature dependent quantity, the redistribution parameter M(T), had to be included into the calculation of F_L (cf. Fig. 5). It is required to account for a disbalancing of the losses at the two mirrors of the resonator which becomes relevant at low temperature. Then the contribution of the coupling holes at the spherical mirror adds strongly to the contribution from surface resistivity. The revised tan δ values fall between the two extremes given in the last progress report, and the scatter is virtually statistical.

With the settlement of measurement base, the temperature range between 25 K and 300 K was systematically covered for three different sapphire grades: HEMEX (Crystal Systems), a grade produced by the Bridgman technique under vacuum; Ti: Sapphire (Crystal Systems)k, a grade similar to HEMEX except for an addition of 0.02 w% TiO₂; CZ-Sapphire (Union Carbide), a grade produced by the Czochralski technique in

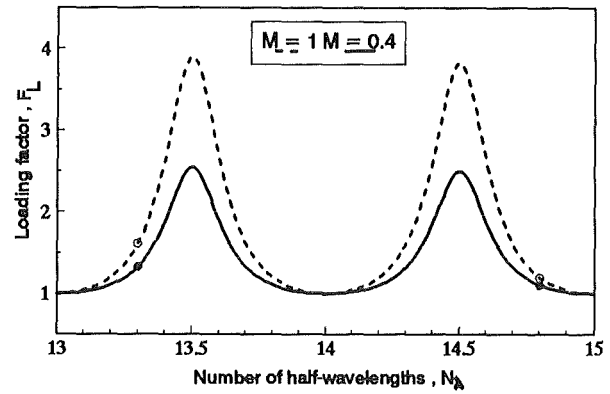


Fig. 5: The reformulation of the data evaluation procedure in open resonator dielectric loss measurements: The redefinition of the loading factor F_L exemplified for values of the redistribution factor M based on standard assumptions (M = 1) and typical observations (M = 0.4).

air. In parallel, a theoretical model was adapted to describe the intrinsic loss levels expected in sapphire in terms of the two-phonon model. At temperature above ~ 100 K, all grades show the same loss levels which correspond rather well also to the curve predicted by the model (cf. Fig. 6a). At lower temperatures, however, strong differences appear between the various grades. Most important is the observation of a levelling-off to a constant loss value in the HEMEX grade. In contrast, the two other grades show a steep loss dependence with an exponent close to 4 at 70 K (cf. Fig. 6b). Basic differences are also seen in optical spectroscopy where an absorption line at 220 nm gives evidence of point defects (oxygen vacancies) in the HEMEX grade.

The effect of neutron-irradiation on dielectric loss at cryogenic temperatures has been measured so far at 70 - 300 K. An irradiation task at GKSS (Geesthacht) was finished where HEMEX grade sapphire was irradiated at T_{irr} ≈ 320 K to three different low to moderate fluence levels (10²⁰ n/m², 10²¹ n/m², 10²² n/m²; E > 0.1 MeV). They were compared to results obtained on specimens from previous irradiations: GKSS.23 (3.5·10²³ n/m², T_{irr} = 320 - 370 K) and HFR.24 (2·10²⁴ n/m², T_{irr} ≈ 500 K). It was found that up to 10²¹ n/m² - corresponding to 10⁻⁴ dpa - the loss curves of the unirradiated HEMEX grade are reproduced and only slight changes appear at 10²² n/m² (cf. Fig. 7). At the higher fluence levels, losses are strongly increased and show complex changes, including modifications in the temperature dependence of tan δ and possibly also a limited post-irradiation recovery.

A CZ-sapphire specimen which was subjected to the RIED effect under electron irradiation at CIEMAT (displacement damage: 6·10⁻⁵ dpa) gave evidence of no increased mm-wave loss at temperatures above 120 K and a levelling-off to constant tan δ values below. Compared to HEMEX neutron irradiated to 10⁻⁴ dpa, the constant tan δ level is higher and is probably caused by changes in the defect type and concentration induced by the electrical field under irradiation (cf. Fig. 6a).

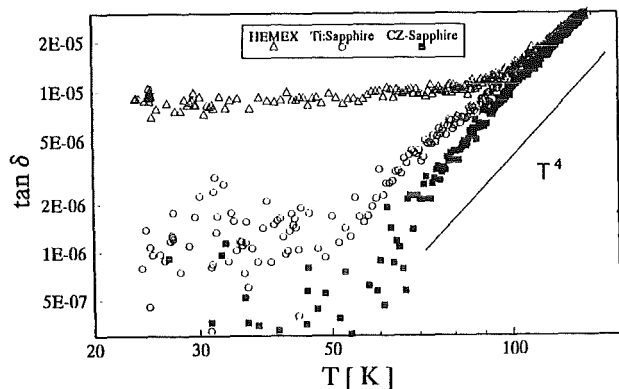
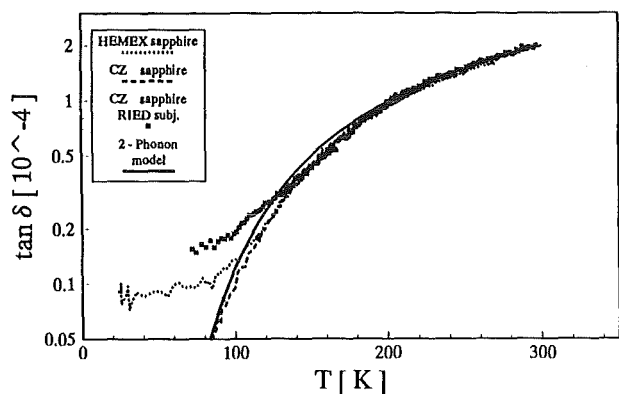


Fig. 6: Dielectric loss at 145 GHz measured in various unirradiated sapphire grades
 a) Presentation of the fully inspected temperature range and description with 2-phonon-model (included are results for CZ-Sapphire subjected to RIED effect)
 b) Presentation of the temperature below 150 K.

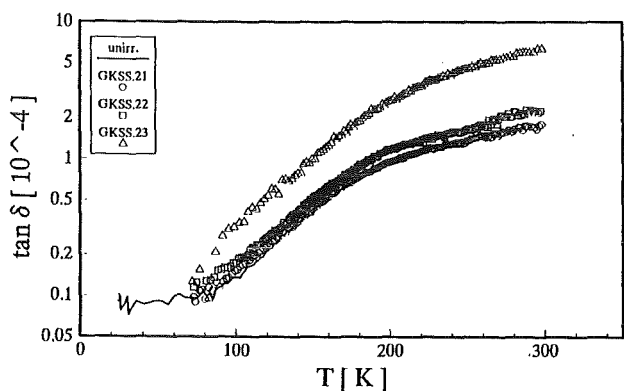


Fig. 7: Dielectric loss at 145 GHz measured in HEMEX sapphire before and after fast neutron irradiations at low to moderate fluence levels.

Fusion Reactor Materials, Stresa, 27/9 - 1/10/1993, Paper F003

- [3] J. Mollá, R. Heidinger, A. Ibarra; Alumina ceramics for heating systems, 6th. Int. Conf. on Fusion Reactor Materials, Stresa, 27/9 - 1/10/1993
- [4] V.V. Parshin, R. Heidinger, G. Link; Experimental studies with open resonators on frequency-dependent dielectric loss at mm-wavelengths, 18th Int. Conf. on Infrared and Millimeter Waves, Colchester, 6 - 10/9/93
- [5] R. Heidinger, G. Link; Dielectric loss measurements between 25 - 300 K with a hemispherical Fabry-Pérot resonator, 18th Int. Conf. on Infrared and Millimeter Waves, Colchester, 6 - 10/9/93
- [6] G. Link, R. Heidinger; Modelling of intrinsic mm-wave absorption in low loss dielectrics with complex crystal structure, 18th Int. Conf. on Infrared and Millimeter Waves, Colchester, 6 - 10/9/93
- [7] R. Heidinger, S. Nazaré; Tailoring microstructure for microwave dielectric properties - theory and experiment, 3rd IUMRS Int. Conf. on Advanced Materials, Tokyo, 30/8 - 4/9/93
- [8] J. Mollá, R. Heidinger, A. Ibarra, G. Link, Dielectric properties of alumina/zirconia composites at millimeter wave lengths, J. Appl. Phys. 73 (11) (1993) 7667-7671

Staff:

M. Blumhofer
 J. Bürkin
 W. Dienst
R. Heidinger
 G. Link
 S. Nazaré
 H. Zimmermann

Literature:

- [1] W. Dienst, H. Zimmermann; Fracture toughness and strength change of neutron-irradiated ceramic materials, 6th Int. Conf. on Fusion Reactor Materials, Stresa, 27/9 - 1/10/1993, Paper F002
- [2] R. Heidinger; Dielectric measurements on sapphire for electron cyclotron wave systems, 6th. Int. Conf. on

PPM 6 Erosion, H-Retention, Gas Interaction

Subtask 2: H/T Retention Studies in Neutron Irradiated Graphites, CFCs and Doped C Composites

Carbon-based materials as well as beryllium are considered for protection of plasma facing components of fusion reactors. Previous experiments indicate a huge (factor hundred) increase of tritium trapping capacity in carbon-based materials induced by neutron damage. A check of these results and a better understanding of neutron irradiation effects on tritium retention in these materials is urgently required.

A common NET/ECN/KfK program has been initiated. ECN will mainly concentrate on the temperature range below, KfK on that above 1000 °C. Irradiated carbon-based materials (irradiated up to 3.5 dpa) and Be samples (irradiated up to 4×10^{22} 1/cm² fast fluence) are available. An equipment capable of heating the samples to 1300 °C in tight Al₂O₃-containers for loading with tritium (in a stagnant H₂/T₂ atmosphere) and for annealing the loaded tritium by purging with He + 0.1 % H₂ has been installed.

Whereas loading at 1300 °C under stagnant H₂/T₂ was without problems, during annealing at 1300 °C by purging with He + 0.1 % H₂ the graphite evidently reacts heavily with the Al₂O₃-container. Future annealing tests therefore have to be performed in a high-temperature-steel container. Tritium inventories of about 2 and 15 GBq/g were observed for graphite samples loaded at 800 and 1300 °C, respectively [1].

Before studying tritium trapping behavior of the irradiated Be samples, the tritium generated during irradiation by fast neutrons has to be annealed. This was done by purging and heating up to 850 °C. Large amounts of tritium, up to about 10¹¹ Bq/g for the highest fluence samples, were released. It has to be checked if the number of irradiation - induced trapping sites is decreased by annealing.

Literature:

- [1] H. Kwast et al., "The Effect of Neutron Irradiation on the Trapping of Tritium in Carbon-Based Materials", ICFRM-6, Stresa, Sept. / Oct. 1993.

Staff:

T. Eberle
M. Glugla
J. Lebkücher
M. Möschke
K.H. Simon
H. Werle

PDT 1 First Wall Mock-up and Tests

Subtask 4: Thermomechanical Tests on Specimens Protected by Mechanically Attached Carbon Based Tiles

The test facility FIWATKA was designed for thermo-mechanical testing of first wall (FW) mock-ups in order to:

1. observe the integral behaviour of different FW concepts including protection tiles.
2. provide an experimental basis to improve confidence in the prediction of thermal fatigue life by:
 - a) validation of computational methods for
 - thermo-mechanical analysis
 - crack initiation by cyclic plastic-deformations
 - fatigue crack propagation in complicated geometries
 - b) lifetime determination including
 - observation during life
 - study of failure modes for prototype FW sections under representative thermo-mechanical conditions.

The test specimens will be tested under mechanical boundary conditions and thermal loads close to those of a fusion device except for internal heat sources in the specimens irradiation and for disruption forces.

The specimen will be positioned in a vacuum chamber; it will be actively cooled with water and will be heated by thermal radiation in a cyclic manner.

A resistance heater made of a graphite plate at temperatures up to 2200 °C in vacuum will serve as a heat source. It will radiate heat for a few minutes onto the surfaces of two specimens placed on both sides of the heater plate in a distance of two or three centimeters. The heater power will be turned down periodically for one or two minutes with the result that the temperature profile and the corresponding stress and strain profiles in the specimen change also periodically and cause thermal fatigue.

Since the heat flux arriving at the specimens surface is the most important parameter for this kind of tests close attention was directed towards determining its average value and its spatial distribution. The average value is measured calorimetrically with the cooling water of the specimen itself which includes the influence of the individual surface emissivity. The spatial distribution was determined by scanning the specimen plane with a high resolution movable heat flux sensor; after several improvements of the heat

source and the shielding the uniformity became better than $\pm 2\%$ of the av. heat flux.

The NET specimen TS1 which is highly instrumented was used without protection tile in the first steady-state and cyclic tests at heat fluxes of up to 70 W/cm² generating temperature and strain data from the instrumentation as it is; the specimen was tested both mechanically unconstrained and constrained at the side walls. These data may be compared with earlier data taken at JRC Ispra. Most of the strain-gauge data seem reliable, most of the thermocouple data do not.

In the second test series the specimen TS1 was protected by a radiatively cooled graphite tile (B-YFZ). Since this test aimed at examining the attachment technology and heat transfer through the contact points of the attachment studs a tile made of fine grained graphite (FE 219) rather than of CFC (not available at this time) could be used. The attachment studs and TS1 were instrumented with additional thermocouples close to the contact points. The test resulted in failure of the tile after a test sequence consisting of steady state and cyclic tests both at heat fluxes of up to 55 W/cm² with totals of 48 cycles and 10 hours at power. Lessons to be learned from this test were:

- a. Differential bowing in vertical direction between TS1 and tile was much greater than the design gap would allow for; therefore the attachment stud experienced tension and broke off part of the tile in the attachment area.
- b. Cyclic changing of tension forces resulted in corresponding changes of the contact pressure of the contact pressure at the contact points and in turn of heat transfer at these points; this is clearly visible from the strong temperatures changes measured in the area. In fact the stud forces, though not intended, may have produced information on the heat transfer rates typical for the contact points of the particular design and for a rather wide spectrum of contact pressures experienced.

The third series is a repetition of the second one with a radiatively cooled tile but this time with a gap wide enough for differential bowing not resulting in stud forces. In preparation is a test with two conductively cooled CFC tiles with the compliant layer consisting of a specially made exfoliated graphite. Temperature distributions and long term layer flexibility under cyclic load will be the goals.

Analyses by means of the finite element method (FEM) accompanied the tests. Precalculations were performed to find suitable test conditions, e.g. optimal heat cycles for the following series of tests with the compliant layer.

The bowing behaviour of the radiatively cooled graphite tiles was fully analyzed by a 3D model. The deformation behaviour of the TS1 specimen was analyzed by a 2D model under both boundary conditions (free and clamped) used in the tests. A

first evaluation shows a good agreement between experimental data and computation.

Staff:

E. Diegele

E. Eggert

G. Hofmann

B. Schinke

G. Schweinfurther

PDT 2 Divertor Mock-up and Tests

Subtask 1: Pretests of Bonded Divertor Samples

The testing program on the thermomechanical behavior of candidate divertor and high heat flux components materials has been completed. The last testing phase involved bonded samples of different types of protection materials brazed to candidate structural materials as characterized below.

- Protection materials:
 - A05: AEROLOR, 2-D CFC, Le Carbone Lorraine
 - N112: SEPCARB, 3-D CFC, Société Européenne de Propulsion
 - HOPG: Highly oriented pyrolytic graphite, Le Carbone Lorraine
- Substrate materials:
 - TZM: Molybdenum alloy, annealed 1700 °C
 - Al25: GLIDCOP, Al₂O₃-dispersion strengthened copper
- Braze Materials:
 - TiCuSil: Melting range 830-850 °C
 - CuTi: Melting range 1050-1080 °C

The disc-shaped samples, 5 cm in diameter and 0.8 cm thick, (0.4 cm of which is protection material) were exposed to heat pulses of 15 MW/m², 1-3.1 s duration up to 13000 cycles. Test evaluation and post test examination have been described in a draft final report submitted to NET [1]. The results are summarized as follows.

A05/TZM Samples

Six samples of this combination have been tested up to 3000-13000 cycles, in which the nominal melting temperature of the braze had been approached in the case of the two CuTi-brazed samples and had been exceeded for the others. The thermal contact between the A05 and the TZM remained intact throughout the test. The temperature drop through these samples differs by less than $\mp 10\%$. The mean values agree with finite element calculations to within $\approx \mp 10\%$.

The A05 surface has a porous structure. Pores and voids are typically up to 200 μm large and distributed all over the surface. Several of the largest pores have been traced throughout the tests, but only minor changes were observed. The braze filler had welled up to the surface at the assembly joints, where the protection layer had been assembled from several pieces, and was gradually removed as the temperature levels exceeded the melting point. However, the assembly gaps remained extremely narrow. Overall, the samples did not suffer any cycle damage.

N112/TZM Samples

Six samples of this combination have been tested up to 3000-13000 cycles, essentially under the same test conditions as the A05/TZM samples. The thermal response is qualitatively

similar to the one described above. On the average, peak surface temperatures and peak rear side temperatures are 40 and 90 °C lower, respectively, compared to the A05/TZM samples, reflecting the better radial heat conduction and the somewhat lower axial conduction. Hence, the mean peak temperature at the braze turned out to be lower by about 100 °C at equal heating times, i.e., it oscillated between 100 and 680 °C in the initial phase and then increased gradually to the peak values of between $\approx 810 - 1100$ °C as the heating time was raised. The melting temperature of the braze was exceeded at three of the six samples. Again, the total temperature drop at the samples remained stable over all cycles, suggesting that there was no detachment.

The prevailing fiber orientation is parallel to the sample plane. The N112 layer is fabricated from a single piece and, hence, there are no assembly joints and no braze filler coming up to the surface. Therefore, the surface appears to be, macroscopically, very uniform, resembling a hexagonal woven fabric. All samples were in perfect condition showing no evidence of cycle damage.

HOPG/TZM Samples

Four HOPG/TZM samples (two without interlayer and two with A05 interlayer) have been tested up to 104 cycles and the nominal melting temperature of the TiCuSil braze was gradually approached and finally exceeded at two samples. Since the HOPG layer was assembled from 5x5 mm² bars, the braze filler had penetrated into the gaps between the bars during brazing showing up locally at the surface, from where it was gradually removed during cycling. In addition, several delaminations of basal planes, a few mm long, were found before the test already, which widened up to typically 100 μm width during cycling. Also numerous stairway type cracks developed. It is obvious, that the mechanical strength of the HOPG layer is negligible.

Macroscopically, however, the HOPG is unaffected by the test at 3 out of 4 samples, shows no measurable erosion and no indication of detachment. The permanent deflection is negligible, but with a tendency for thickness growth. There is one exception: one sample showed local overheating after ≈ 2500 cycles at one of the HOPG bars. This proved to be a poor bonding, presumably a fabrication fault. Surprisingly, significant propagation and gross detachment of HOPG did not occur and the overall condition in terms of weight loss and permanent deflection was normal.

A05/TZM/Al25 Samples

Two samples have been tested up to 10.000 cycles, i.e., one at peak temperatures of the Al25 (equal to temperature at braze 2) of 620 °C, and the other one reaching 760 °C. Up to 8000 cycles no thermal or mechanical anomalies were observed. Only in the final stage one sample showed an increase in the temperature drop across the thickness of $\approx 30\%$. Post test examination revealed a 32 mm long and up to 0.2 mm wide diametrical fracture, running in the Al25 substrate all the way through and ending at the TZM interlayer. In the

central region ($R < 10$ mm) the originally 0.2 mm thick braze layer was entirely deteriorated by cracks (Figure 1). The picture shows also the special brazing technique adopted: an array of cones was burned into the protection material by laser to enlarge the surface.

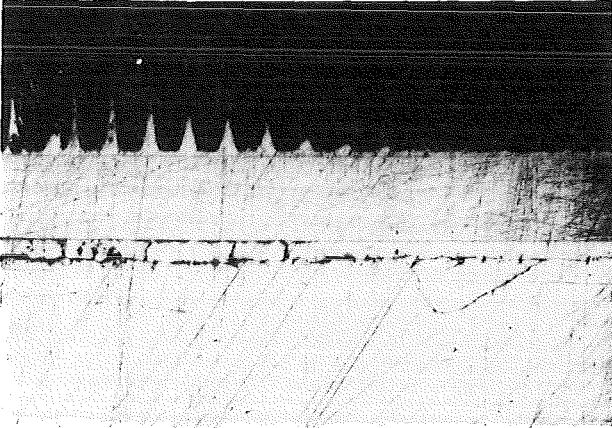


Fig. 1: Cross section through a 3-layer sample (12 x). The materials are from top to bottom: A05 (dark area with braze cones), TZM interlayer, TiCuSil braze (deteriorated), Al25 substrate

Conclusions:

A05/TZM and N112/TZM combinations with CuTi and TiCuSil braze are viable options for high cycle numbers. HOPG/TZM seems to be feasible, but has deficiencies in terms of fabricability, unreliable thermal contact, crevices, fragility. A05/TZM/Al25 yields low tolerable temperature, poor toughness of Al25 and problems with the TZM/Al25 brazing. The most favorable option is N112/TZM with CuTi braze.

Literature:

- [1] K. Kleefeldt, K. Schramm, C. Strobl: Unpublished Report of KfK

Staff:

K. Kleefeldt

K. Schramm

Superconducting Magnets

Introduction:

The confinement of plasma in ITER relies on a superconducting magnet system consisting of 24 D-shaped toroidal field coils, a central solenoid to drive the plasma current and a set of poloidal field coils for plasma stabilization. KfK is together with the EC Home Team and other associated European laboratories involved in the development of these magnet systems. Components of ITER conductors, subsize conductor assemblies are examined for their performances. Materials to be used in coil construction are qualified for their application under cycling load. Cryogenic loops and components are developed to establish stable forced flow conditions to cool the magnets. An important task consists of upgrading the existing large magnet test facility TOSKA to test model coils made out of different industrially manufactured conductors.

The safety of superconducting magnets is analyzed by code development and by experimental studies of effects, potentially initiating a sequence of events leading to an accident.

H. Knuth

MCOI Model Coil

Subtask 1: Monitoring Manufacture of Model Coil Modules

The aim of the subtask is the support of the home team in the fabrication of the ITER model coils.

The subtask is delayed. All work performed for the conceptual design of the model coils is described in task MTOS.

Subtask 3: Development for High Voltage Components for Model Coils

The aim of the subtasks is the transfer of the know how in the development of high voltage components gained in the Polo project is transferred to the ITER model coils.

The conceptual design of the model coils is running. For the magnet workshop in January 1993 a contribution for the electrical quality assurance testing methods were prepared. A review of breakthrough voltage measurements of dielectric materials was sent to the Joint Central Team in Naka.

Staff:

M. Irmisch

A. Ulbricht

MCON Full-Size 40 kA Conductor

Subtask 3: I_c Characterization and FBI Upgrade

The aim of the sub-task is the critical current characterization of Nb_3Sn strands and subcables under the effects of field and external strain in the high field test facility FBI. The task is funded in the 1989-91 program. It is still continued caused by difficulties in the strand fabrication combined with delay in delivery.

1. Improvements of the FBI Facility

- The new 14 T split coil is working perfectly almost one year.
- The LHe transfer line supplying the big cryostat has been installed and is in operation now. An extension of this line for the small apparatus is in preparation.
- A new tensile test rig (1 kN - 250 A) with an increased test length for I_c vs ϵ measurements of strands has been fabricated in our workshop and will be tested soon.
- The data acquisition has been extended by a new system (rhothron) and has to be prepared for the use at FBI.

2. Testing of ITER Subcables

Different types of Nb_3Sn "Cable in Conduit" (CIC) conductors delivered by CEA and ENEA have been tested successfully.

2.1 CEA-Subcables: Drastic Improvement of I_c by Prestraining at RT

The degradation of I_c due to axial prestrain of the Nb_3Sn filaments of fusion conductors containing a high volume fraction of stabilization material has been confirmed many times. This effect is pronounced at CIC conductors where the (steel) conduit has to be heat treated together with the Nb_3Sn cable. Several possibilities exist reducing the prestrain onto the Nb_3Sn filaments which results in an increase of I_c :

- Attaching the stabilizers onto the Nb_3Sn cable after the reaction heat treatment at RT, as shown for the NET subsize conductor developed by KfK/ITP [1].
- The use of stabilizers with low coefficient of expansion (Titanium, Incoloy), comparable with that of Nb_3Sn . Therefore CIC samples with Titanium jacket are in preparation.
- Prestraining of the conductor after the reaction heat treatment at room temperature. This method has been performed the first time at KfK in collaboration with CEA, Cadarache, and is being described below [2].

The CIC conductor (~ 40% void fraction) tested consists of an outer 316 LN conduit (O.D.= 7.7 mm) and an inner Nb_3Sn

cable with 36 MJR processed strands ($\phi = 0.73$ mm). First the sample was tested without applied strain at 12.5 T and 4.2 K corresponding to $I_{c0} = 2.01$ kA in Fig. 1, which presents the I_c vs. ϵ curve. Then the conductor was warmed up to $T = 275$ K, plastically strained up to a residual value of 0.3% and cooled to 4.2 K again. The following I_c measurement without loading leads to $I_{c1} = 3.15$ kA, which corresponds to an increase of 57%. After that I_c vs ϵ has been performed step by step (the numbers indicate the sequence of testing) under loaded (Δ) and unloaded (∇) conditions up to $\epsilon = 0.93\%$ (17) and the following residual strain $\epsilon = 0.45\%$ (18) in the unloaded state.

Taking into account the prestrain of 0.3%, the values of both $\epsilon_m = 0.73\%$ and the ratio $I_{c0}/I_{cm} = 0.50$ are within a few percent the same than those obtained at identical samples without prestraining. The improvement of the ratio $I_{c0}/I_{cm} = 0.50$ to $I_{c1}/I_{cm} = 0.78$ and the corresponding decrease of $\epsilon_m = 0.73\%$ to $\epsilon_m = 0.43\%$ in this case are adjustable up to $I_{c0}/I_{cm} = 1$ and $\epsilon_m = 0$ by performing the demanding prestrain at room temperature. Like in former investigations I_c vs ϵ behaves reversible up to $\epsilon_{irr} \approx 1\%$ (Fig. 1).

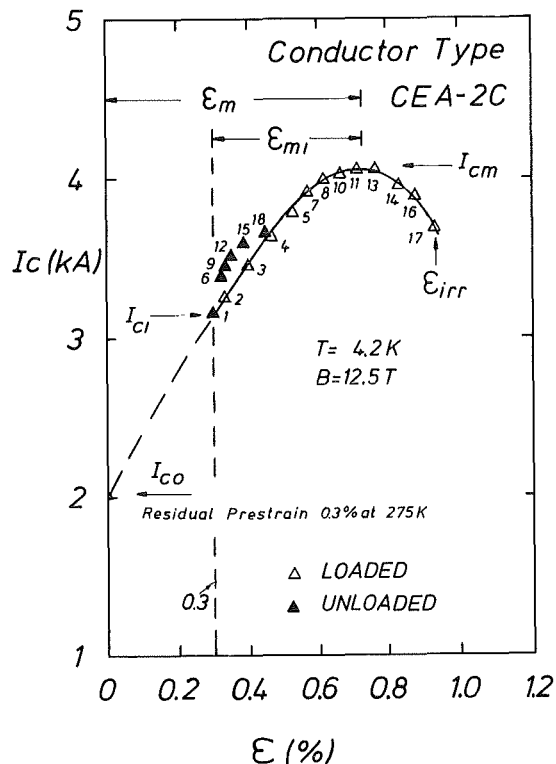


Fig. 1: I_c vs ϵ for a conductor (SS jacket) 0.3% residual prestrain at RT.

2.2 ENEA Conductor

This CIC conductor has been used for the fabrication of a 0.6 m bore wind-and-react solenoid, designed for a maximum field of 12 T at an operating current of 6 kA. The coil is planned to be inserted into the SULTAN facility.

The rectangular conduit (316 LN) of 13.8×13.8 mm² houses 128 MJR processed Nb_3Sn strands and 16 copper wires (both

0.78 mm \varnothing) at a void fraction for helium flow of about 40% (Fig. 2).

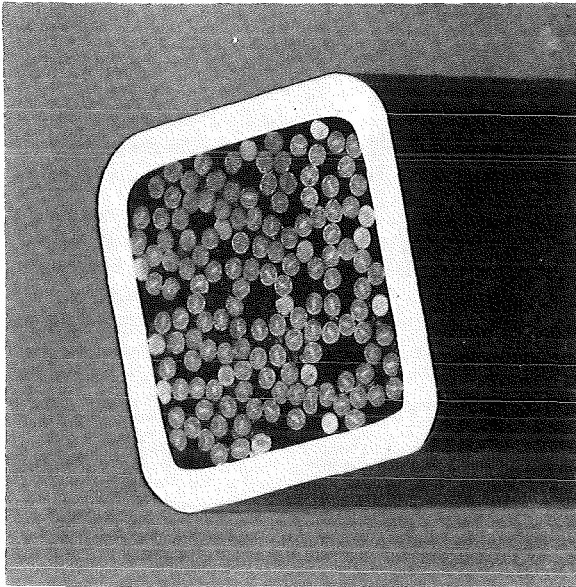


Fig. 2: CIC conductor for the ENEA 12 T/6 kA magnet, manufactured by Europa Metall-LMI.

First results at $T = 4.2$ K:

B (T)	I_{co} (kA)	I_{cm} (kA)	ϵ_m (%)	ϵ_{irr} (%)
12	9.74	-	-	-
14	5.10	10.70	0.75	> 1

These results are in agreement with former investigations made at comparable conductors. Further measurements are in preparation.

Literature:

- [1] W. Specking, A. Nyilas, A. Ulbricht, P. Komarek, R. Flükiger, IEEE Trans. Magn., 27, 1912-1915, 1991.
- [2] A. Torrosian, W. Specking, J.L. Duchateau, to be presented at SOFE, MIT Plasma Fusion Center, Cambridge, USA, Oct. 11-15, 1993.

Staff:

H. Kiesel
W. Specking

MTOS TOSKA Upgrade for Model Coil Testing

Subtask 1: Preparation of the TOSKA Facility for the Test of the ITER Model Coils

The aim of the task is the upgrading of the TOSKA facility for testing ITER model coils. An intermediate step is the testing of the LCT coil at 1.8 K up to 11 T field level in the task MBAC. Useful basic component developments and testing methods which can be transferred later on to ITER model coils are running in the Polo project (previous tasks M4, M8 and MTOR).

A highlight was the approval for the extension of the TOSKA facility as an ITER toroidal field model coil test facility in December 1992 by the ITER Council.

The 2 kW refrigerator successfully passed its commissioning phase and is now operated in the responsibility of KfK/ITP.

A pair of force flow cooled high power current leads of 23 kV, 30 kA were successfully tested.

The Polo model coil passed its acceptance test at the manufacturers site and was delivered to KfK at the beginning of July 1993.

1. The New 2 kW Refrigerator [1.1]

The main work was to take into operation the new refrigerator with a 4.4 K equivalent refrigeration capacity of 2 kW.

After assembling of the components (Aerzener screw compressors, cold box with 3 Sulzer/Linde expansion turbines, valve box with subcooler and calorimeters, liquid helium dewar from Messer Griesheim, the Siemens Teleperm M process control system) the leak checking and plant testing was started by the main contractor Linde AG, München, including a leak test at operation temperature. After the first refrigeration capacity measurements modifications on the compressors were necessary to obtain the specified mass flow rate (Fig. 1). After improvements the test program performed demonstrated that the cooling power specified in each of the 6 operation modes was obtained (Table 1).

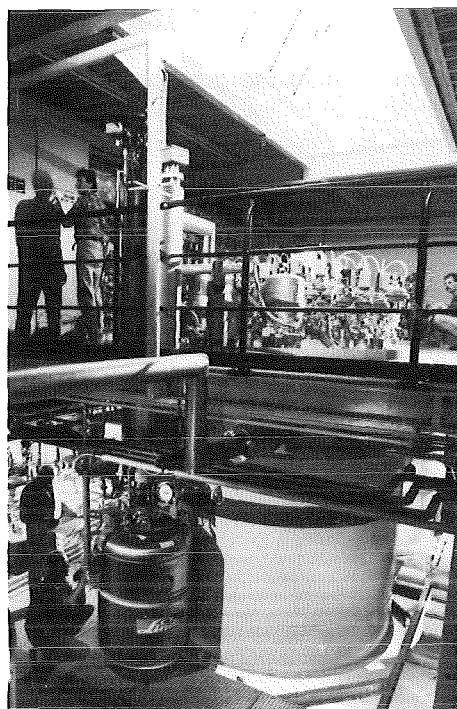


Fig. 1: View at the calorimeter, valvebox and coldbox during the acceptance test of the new 2 kW refrigerator.

Also the required 20 kW cool down capacity for large sc coils was confirmed by a measurement with the outer calorimeter. The automatic steady state operation worked well. For non steady state conditions and transition between two operation modes the control circuits had to be adapted to the real process condition.

After this improvement a test run confirmed the full operability of the refrigerator. Since the end of February 1993 it is operated in the responsibility of KfK/ITP.

2. The TOSKA Facility for Testing an ITER TF Model Coil

The ITER EDA design of the magnet system has strong differences in the design of the central solenoid (CS) and the toroidal field (TF) coils. This fact requires two model coils, one CS model coil and one TF model coil. While in the CS model coil test the design principles of the CS coil inclusive the 13 T field level shall be tested, the TF model coil test shall be an

Operation mode	Precooling with		Refrigeration capacity			Liquefaction rate 4.4 K	Electric power consumption of the Compressors
	LN ₂	LHe	3.3 K	4.4 K	70 K		
1 Basic design	-	5.5 g/s	700 W	400 W	1000 W	9 g/s	855 kW
2 Stand by	50 g/s	-	500 W	230 W	1000 W	12.3 g/s	819 kW
3 Full load	43 g/s	-	700 W	400 W	1000 W	8.8 g/s	847 kW
4 Pure refrigeration	-	-	-	1440 W	-	-	610 kW
5 Pure liquefaction	-	-	-	-	-	9.1 g/s	614 kW
6 Pure liquefaction	68 g/s	-	-	-	-	21 g/s	671 kW

Table 1: Specified operation modes for the acceptance test.

electromechanical test of the new TF configuration layers in grooved stainless steel plates. A magnet expert meeting recommended to the ITER organization (Technical Advisory Committee TAC, Management Advisory Committee MAC, ITER Council IC) the construction of two facilities for testing a CS and TF model coil in parallel in order to keep the tight time schedule within the 6 year duration of the EDA. In December 1992 it was decided by the ITER Council that the TOSKA facility at KfK Karlsruhe in the EC will be extended for testing the TF model coil. At JAERI in NAKA a new facility for the CS model coil will be constructed.

In a series of three expert group meetings of the ITER partners agreement on ITER conductors and model coils as well as the structural assessment of the ITER magnet system was obtained. The ITER credit limitation for Nb₃Sn strand material (19.5 t for CS, 6.5 t for TF) defined by the Joint Central Team (JCT) stimulated the use of existing large magnets to obtain the force simulations necessary for testing. Therefore a configuration was created where the TF model coil is tested adjacent to the EC LCT coil (Fig. 2). A set of parameters for such a configuration is presented in Table 2 showing ampere turns, required conductor length field and forces obtained. It has to be emphasized that the given conductor quantities require an operation current of 80 kA to get the required field and forces. A conceptual design of a TF model coil, the gravitational support and the intercoil structure were performed. The gravitational support uses the same elements which were already successfully used for supporting the LCT coil. The configuration is in the process of optimization for obtaining the goals defined by the JCT. There are two items which have the highest priority:

1. The winding of the TF model coil shall have compression stresses of 90 MPa in one leg of the TF model coil.
2. The later use shall be considered with respect to generating a background field for testing of the 1:1 ITER TF coils.

Item 1 can be obtained by a displacement of the magnetic center of the coil and a suitable structure. For item 2 a racetrack coil seems to be more suitable than a D-shaped coil. The LCT coil was investigated considering its electrical and mechanical properties. Nothing was found which limits the operation of the model coil. The cryogenic power for the operation of 80 kA current feedthrough is sufficient as summarized in Table 3. For the estimation the experimental results of the Polo current lead test were the basis (see section 3).

Besides the electromechanical tests it was also recognized that high voltage pulse testing is necessary. Therefore the experts recommend to use the Polo switching circuit for that purpose.

The configuration will be assembled outside the vacuum

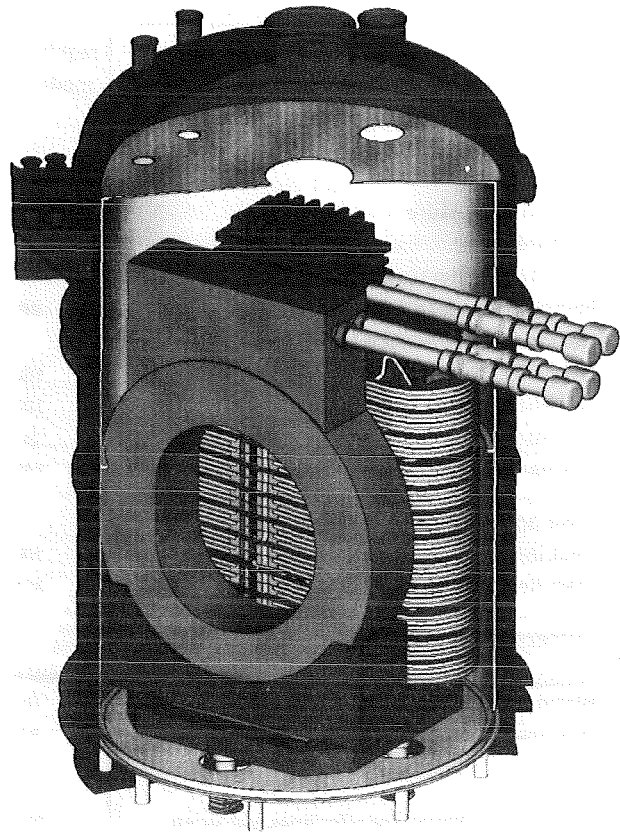


Fig. 2: A TF model coil adjacent to the EC LCT coil. The TF model coil will be operated at 80 kA to obtain relevant forces. The final configuration may not use a D-shaped model coil.

vessel and then lifted as one piece by means of two cranes and a lifting beam into the vacuum vessel.

Status: The 50 kA power supply was taken into operation. The acceptance test was concluded beginning 1993. The power supply is now operated in the responsibility of KfK/ITP. The first experimental application was the test of the 30 kA Polo current lead (see section 3). The connection between the 30 kA and 50 kA power supply in parallel to get 80 kA was ordered with busbars and the control circuit. The components are being in fabrication.

Possible switching circuits for removal of energy from the model coil at 80 kA are being investigated. At the present status and according to the present experimental requirements an arc chute or an AC power switch seemed to be the most reliable solution.

A second crane of 80 t for lifting the complete test configuration is being ordered.

The cold line which connects the new 2 kW refrigerator and the TOSKA facility is under construction at the manufacturers site.

The present developments in the ITER TF model coil testing grow more and more in the existing capabilities of the TOSKA

Winding	required for ITER model / LCT coil	available at the specific 2 kW refrigerator	available at the general laboratory refrigerator
Mass flow rate (ITER model coil 1 channel 800 m)	18 / 70 g/s	500 g/s	50 g/s
Operating pressure	6 bar	< 10 bar	< 20 bar
Pressure drop (m = 18 g/s, di = 10 mm, L = 800 m)	2 / 0.3 bar	6 bar	6 bar
Pumping power ($\eta = 0.6$)	80 W		
Heat load sc-joints at coil ($10 \times 2.5 \times 10^{-9} \Omega$)	160 W		
Radiation and conduction to coil	100 W		
AC-losses	20 W		
Nuclear heat simulation	160 W		
Case and support structure			
Heat input	100 W		
Mass flow rate (in series with winding)	80 g/s		
Current leads (4 pieces)			
Nominal current	80/12 kA		
Warmgas flow rate (2x80 kA, 2x12 kA)	10 g/s		
Heat load joints ($2 \times 2 \times 10^{-9} \Omega$, $2 \times 6 \times 10^{-9} \Omega$)	30 W		
Facility			
Heat load in dewar, transfer lines, valves etc.	200 W		
Total refrigeration capacity at 4.4 K	850 W + 10 g/s	1000 W + 12 g/s	500 W
Available margin	650 W + 2 G/s		

Table 2: The cryogenic load of the ITER TF model coil test adjacent to the LCT coil.

facility to come to a model coil testing within a reasonable cost frame.

Together with HPE (Hauptabteilung Prozeßinstrumentierung und Elektronik) a data acquisition system was elaborated which shall be installed after the test of the Polo coil. It will be used the first time for 1.8 K of the LCT coil and later on extended for the model coil test. The programmable logic controllers (PLC), the computers rtVAX 300, the controllers and a scanning system are linked by a star coupler (Fig. 3). All these components are in the control room in the experimental area of TOSKA and exposed to a magnetic field of 2 mT. A linkage to a remote control room about 50 m away from TOSKA with the host computer (VAX 4090-1) and control terminals are realized by glasfiber. The experiment can be controlled completely via terminals from this area. For the data acquisition the data base management software ORACLE is used as specified for ITER.

3. The Polo Project

The Polo project was started in the previous task M4 to develop the technology for poloidal field coils of tokamaks. It should be demonstrated in task M8 later on MTOR (outer poloidal field coil for TORE SUPRA) that the developed technology is suitable for application. The conductor is the first long length conductor produced with a fusion conductor like stainless steel jacket. Most of the components developed

can be immediately used or they are an intermediate step in the development for the ITER model coils like insulators, feedthroughs, current leads, instrumentation cables etc. because the nominal voltage of the Polo coil and the model coils are nearly the same. The testing technique used for the Polo model coil to generate transient fields changes is intended to be applied also for the ITER model coils. Therefore the project can now be considered as a precursor of the model coils developing most of the components which are independent from the Nb₃Sn technology.

3.1 Fabrication of the Polo Model

The insulation system of the Polo model coil was completed by two vacuum impregnations of the winding. After the first impregnation the winding insulation (turn to turn, pancake to pancake) was successfully tested by a pulse voltage of 24 kV across each winding half. Then the ground insulation was wrapped around the winding and vacuum impregnated. A repetition of the pulse voltage test and further electrical tests (DC 50 kV, AC 16 kV partial discharge measurement) confirmed a sound electrical insulation system. The SS steel fixtures and the SS steel plate for carrying the supporting structure of the terminals were carefully aligned and assembled. Conductors were bent to meet the position of the terminals and leak tested. The total number of conductor bending operations during coil fabrication was about 30 times. Never a leak was observed in the laser beam welded

ITER D-Shaped Model Coil TEST (LCT)							
Model coil		MC-108 turns x 80 kA			MC-132 turns x 80 kA		
Simulation of conductor dimensions	cm x cm	5.7 cm (radial) x 5.62 (axial)			5.7 cm (radial) x 5.62 (axial)		
Minimal bending radius of MC	m	0.7			0.7		
Turns (radial x axial)		9 x 12 = 108			11 x 12 = 132		
Radial winding thickness	m	0.513			0.627		
Axial winding thickness	m	0.675			0.675		
Average turn length	m	10.12			10.48		
Conductor length (without spare conductor)	m	1100			1400		
Winding volume	m ³	3.51			4.1		
Current density in MC	kA/cm ²	2.496			2.496		
LCT-coil	kA	0	10	15	0	10	15
Magnetic fields	T	attainable in midplane and in the (region of smallest bending radius)			attainable in midplane and in the (region of smallest bending radius)		
B _{max} at MC with LCT	T	6.43 (7.45)	7.44 (8.42)	7.97 (8.93)	7.33 (8.5)	8.34 (9.47)	8.87 (9.98)
B _{max} at LCT coil	T	< 2.5	6.45	9.2	< 3.0	6.8	9.5
Forces and stresses		attainable in Model Coil			attainable in Model Coil		
Out-of-plane force	MN	0	-76	-114	0	-96	-144
Average axial pressure	MPa	0	~ 15	~ 22	0	~ 15	~ 22
Average radial pressure	MPa	~ 20	~ 30	~ 36	~ 20	~ 41	~ 41
Stored energy		in single coils and total system			in single coils and total system		
Inductance of MC	H	0.044			0.066		
Stored self-energy of MC	MJ	140	140	140	210	210	210
Stored self-energy of LCT-coil	MJ	0	80	180	0	80	180
Total stored energy (MC + LCT)	MJ	140	292	426	210	382	526

Table 3: Typical field and forces for the configuration TF model coil adjacent to the LCT coil. The values remain in the same order if a racetrack shape will be used for the model coil.

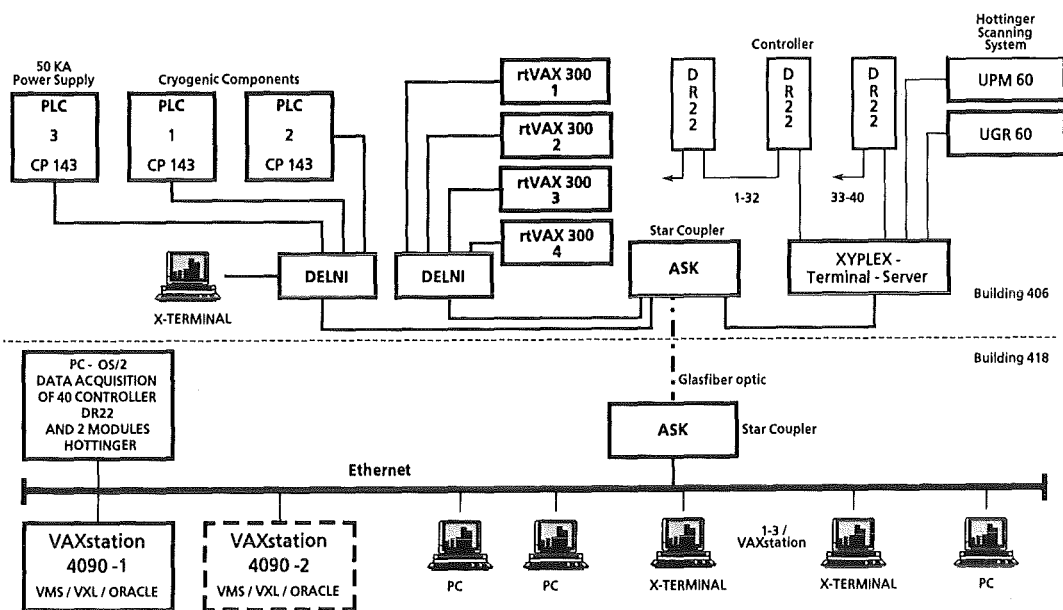


Fig. 3: Diagram of the hardware components of the data acquisition system

jacket. The supporting structure for the terminals was assembled and aligned. The conductor ends were welded in radial insulation breaks to insulate and to support them against the ground potential. The three copper rods with their contact surfaces to the current leads were soldered to the subcables and the hydraulic joints of the primary and secondary cooling channels to their in- and outlets were fabricated. Great care was taken for the correct alignment of the contact surfaces to each other in order to assure easy installation of the current leads in the TOSKA facility. The conductor ends running to the terminals were insulated by hand wrapping by epoxy wetted glass fiber tapes. After a high voltage test the SS support structure was welded around the conductors and filled with epoxy resin wetted sand.

The acceptance test was started with a high voltage test and a leak test. During the DC insulation test an axial insulation break in supply line of one of the terminals failed even though it passed successfully the pretests. The problem was cleared by exchanging the axial insulation break.

A more serious problem occurred during the leak test where two big leaks were found on the top of one of the axial insulations of the joint boxes between pancake 1 and 2 as well as pancake 3 and 4. It was analyzed that the origin of the leaks were the low voltage insulation breaks which were already leaky before the first impregnation (reason: wrong welding procedure) and which were tightened by Stycast. These leaks opened during the second impregnation and found an axial path through the glassfiber filament winding of the high voltage axial insulation break. It has been found out that this was a weak point of this type of insulation breaks.

Taking also into account the electrical breakthrough of the axial insulations break of the terminals the following solution was realized to close the leaks as well as to give electrical and vacuum technical redundancy for a successful performance of the experiment. All outgoing helium supply lines of all three

joint boxes were extended by a second insulation break of another type. The leaks were closed as tight as possible by a special resin. The final barrier is the wet hand wrapping between both insulation breaks. The sockets of the outgoing supply lines were covered by a hat the lower part of which was made by glassfiber reinforced epoxy by filament winding technique to obtain a better matching between the thermal contraction of the socket and the hat. In this way a guard vacuum was created which is separated from the vessel vacuum and can be operated at different pressure levels for avoiding the Paschen minimum in a case of a leak (Fig. 4).

The repairment described needed a lot of electrical and vacuum technical verification tests to assure the concept. In a joint effort of the manufacturer GEC-Alsthom, Belfort and KfK/ITP, Karlsruhe, the repairment was performed within 2,5 months. Fig. 5 shows one of the completed guard vacuum boxes.

The coil was delivered to KfK Karlsruhe, on July 2, 1993 (Fig. 6) after connection of the high voltage instrumentation cables and the repetition of the acceptance tests which now met the specification. The acceptance tests were repeated at KfK Karlsruhe, which indicated some minor new deficiencies which did not exist before. It demonstrates the stony path in the development of a specified reproducible industrial product.

The instrumentation on ground potential outside of the coil were mounted. The work for the installation of the Polo coil in the TOSKA vacuum vessel is running in schedule. The test shall start beginning 1994.

3.2 Special Investigations for the High Voltage Tests of the Polo Coil

The insulation system of the Polo coil was tested by DC, AC and pulse voltages. The understanding of the pulse voltage

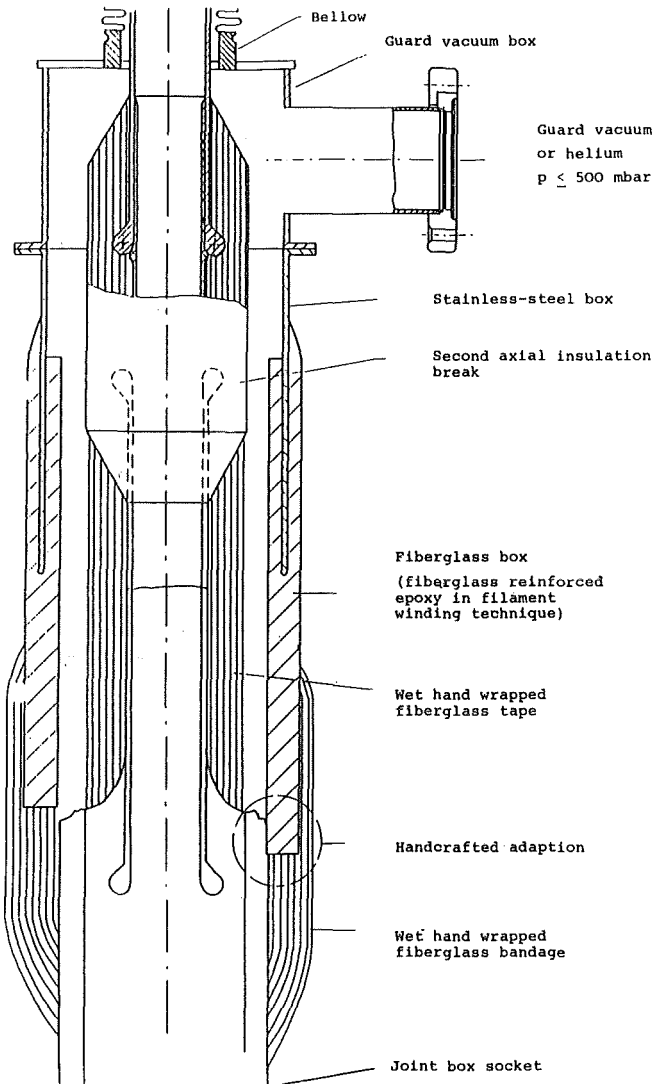


Fig. 4: Sketch for the repairs of the leaks observed during the acceptance test on the top of the axial insulation breaks of the supply pipes to the joint boxes.

tests require an equivalent circuit which can simulate in a computer code the test conditions. The computer code P-SPICE was implemented on a PC and a suitable equivalent circuit for the Polo model coil was elaborated. The measured voltage and current traces were in agreement with those calculated by the computer code. During the pulse voltage test high voltage was observed on the coil surface which was painted with a conductive paint. This voltage led partly to changes of grounded sensors on the coil surface. The effect was simulated by a computer calculation. The reason was the resistivity of the paint which prevented a fast enough charge removal during pulse. A parallel grounding with a copper wire solved the problem.

3.3 The Test of the Polo Current Lead for 30 kA, 23 kV [3.1]

For the test of the Polo model coil a 30 kA, 23 kV current lead was developed and constructed.

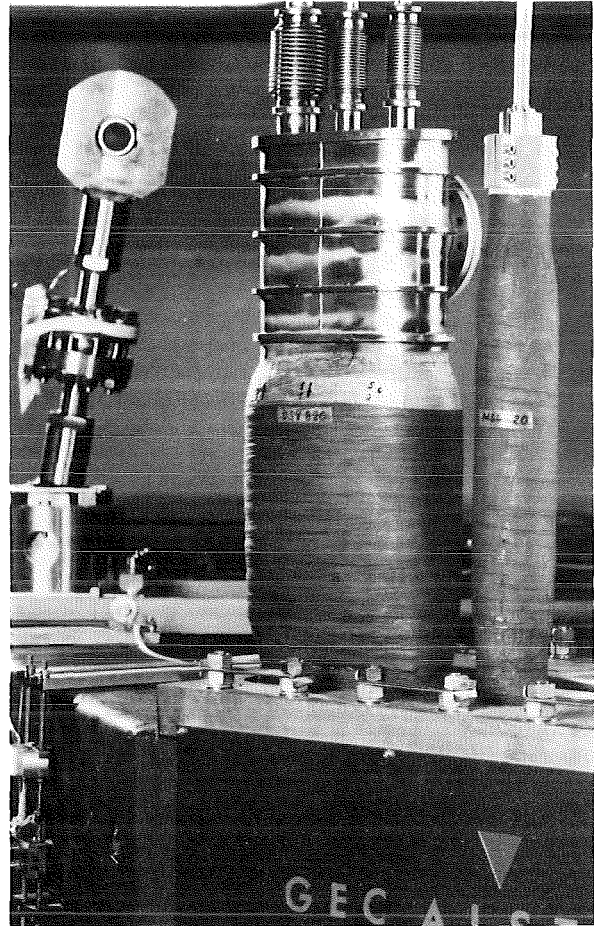


Fig. 5: The fabricated guard vacuum box on one of the joint sockets. On the left hand side a rod equipped with the load cell for the suspension of the coil. On the right hand side a feedthrough with a high voltage instrumentation cable.

The current lead behaviour was tested in the large vacuum vessel of the TOSKA facility. Two current leads were installed and shortened by a superconducting bus bar. The latter one consists of a 3 m long POLO conductor bent in an U-shape. Both ends of the superconducting cable were soldered in copper rods which have exactly the same shape as the terminals of the POLO model coil. Also the cryogenic and electrical interfaces were identical to the coil terminals. Fig. 7 shows the SC shortcircuit bus bar including both terminals. One of the current leads was highly instrumented whereas the other one has its standard instrumentation as it will be used in the coil test lateron. The same cryogenic control and supply system was used as foreseen for the test of the POLO coil. Therefore the current lead test can be considered as an integrated test of the model coil terminals and their current leads under high current and high voltage which could be performed only independently.

The maximum test voltage of the whole system was 28 kV according to the electric strength of the superconducting bus bar. The test configuration was supplied by a 50 kA power supply. So it was possible to test the leads up to 50 kA.

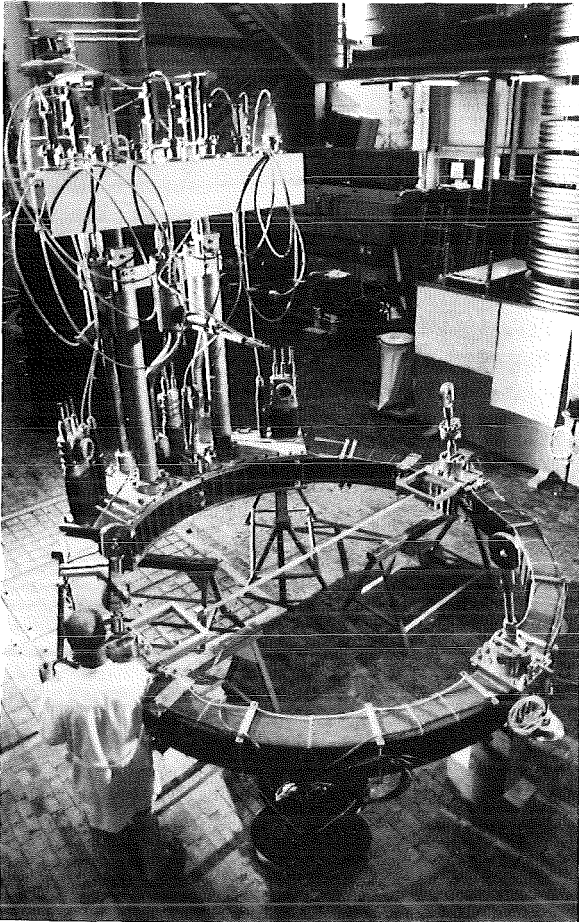


Fig. 6: The Polo model coil during installation in the TOSKA facility. The four suspension rods and the three guard vacuum boxes are clearly seen. The three terminals are partially covered by the fixture of the high voltage instrumentation cables and its vacuum vessel feedthrough which is provisionally fixed at the terminals during the installation work.

Experimental results: Steady state currents between zero and 30 kA and cooling with 0.4 MPa (4 bar) supercritical helium have been performed. By experimental experience, the forced-flow cooled leads have different advantages compared to bath-cooled current leads:

- Easy adjustment of the cryogenic operation parameters, i.e. mass flow and pressure.
- Adaption of the mass flow by changing the operation conditions in advance.
- No oscillations of mass flow and pressure even during pulsed operation.

The electrical resistances of the clamp contacts at the coil end had been measured to be $\leq 6 \text{ n}\Omega$. No changes in performance during one warm-up and cool-down cycle had been observed.

The effectiveness of the Nb_3Sn inserts has been verified. Fig. 8 shows the temperature of the conductor at different

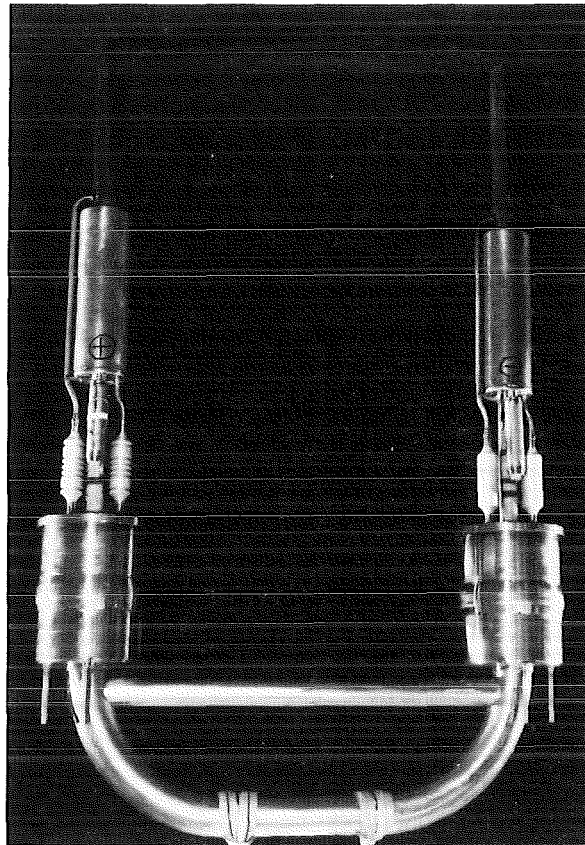


Fig. 7: Superconducting bus bar for short circuiting both current leads in the test configuration

positions of the current lead for zero current (crosses), 15 kA (full rhombi) sep. 30 kA (full circles). For comparison, the calculated temperature profiles have been drawn as full lines. The agreement is good proofing that the leads behave as expected.

Fig. 9 shows the mass flow rate normalized to the current as a function of the operational current. The agreement is good. At 30 kA, the result is slightly above the maximum optimized current as the mass flow rate normalized to the current increases considerably. The effectiveness of the superconductor inserts is clearly seen. A design without superconductor inserts has to be optimized with respect to the maximum operational current. Therefore, in our case, the helium mass flow rate is drastically reduced for currents smaller than the optimum one.

As a second consequence of the use of superconductor inserts the helium mass flow rate at zero current is drastically reduced due to the enlarged length of the current lead. This mass flow rate was measured to be only about 40% compared to that without Nb_3Sn inserts (Fig. 10).

The current lead behaviour in case of loss of mass flow has been simulated by closing the valve for both terminals at 25 kA and measuring the temperatures and voltage drops across the contact area resp. the superconducting short circuit bus bar. The time difference between the loss of mass flow and the thermal runaway of the temperature at the coil terminal is important for a safety discharge of the superconducting coil which is recommended in this case. After almost 4 minutes,

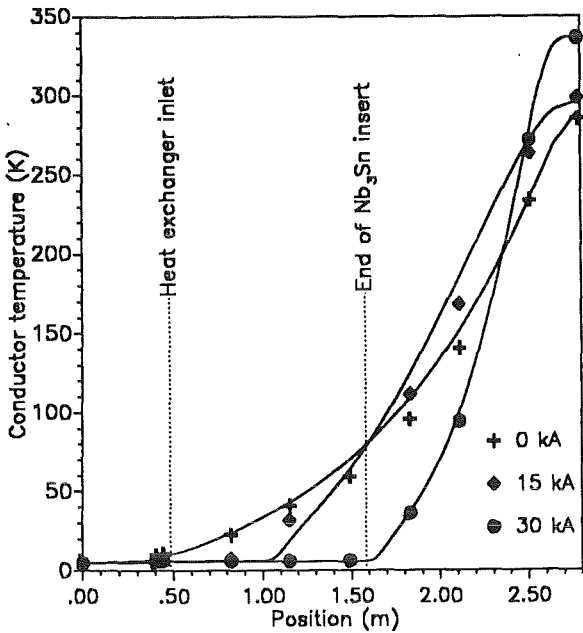


Fig. 8: Measured and calculated temperature profiles for 0, 15, and 30 kA. It is clearly seen that for an operational current of 15 kA the region of the superconductor inserts is partly in the superconducting and partly in the normal conducting state according to the optimized mass flow.

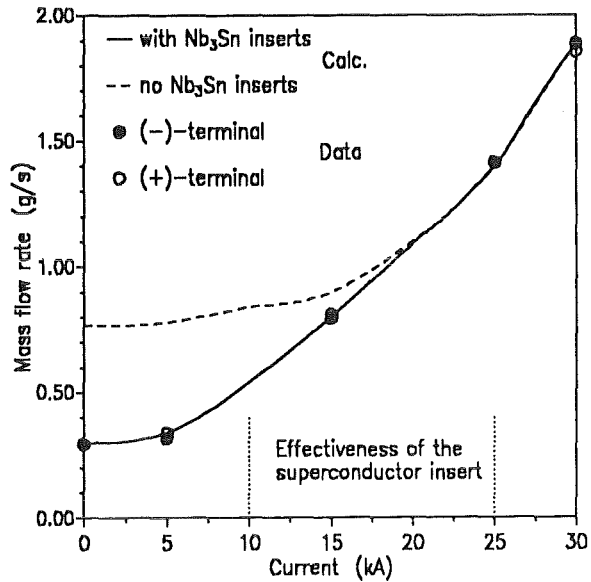


Fig. 10: Measured and calculated mass flow rate vs current

calculations the helium inventory as well as the heat capacity of the copper plates is included, the agreement validates their influence.

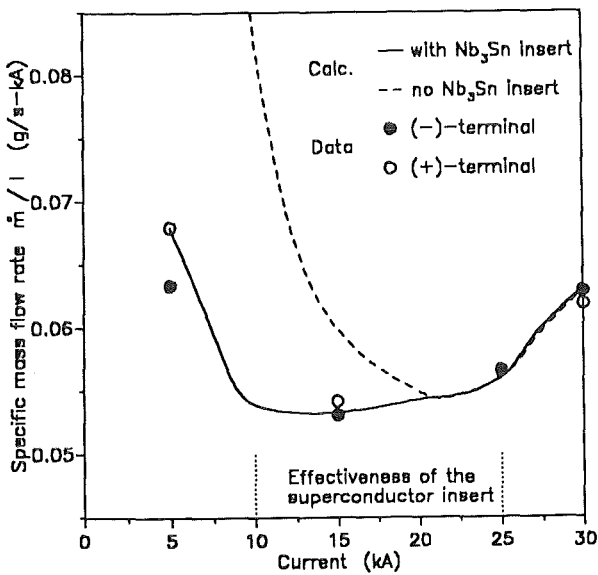


Fig. 9: Measured and calculated mass flow rate normalized to current vs current. The full and open circles are the measured quantities of both terminals (+ and - current lead) whereas the calculation results are given as a full line. For comparison, a calculation is shown without the use of Nb₃Sn inserts (dashed line).

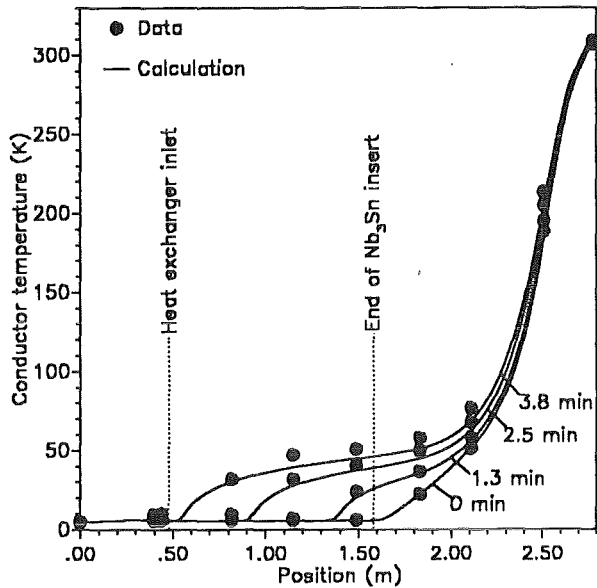


Fig. 11: Measured and calculated temperature profiles in case of loss of mass flow at 25 kA with the time as parameter.

the shortcircuit bus bar became normal conducting, the protection system gave a signal and the power supply was switched off. Fig. 11 shows the measured (full circles) and calculated (full lines) temperature profiles for different times up to the quench of the short circuit bus bar. Because in the

An overcurrent test has been performed at 50 kA. The result was that the heat exchanger works even at this current, i.e. no normal conducting length has been observed. But both lead ends are the limiting factors of the current lead. In addition, the water cooled cables from the power supply are not designed for 50 kA, their temperature did actually limit the measurement time during this experiment.

In general, comparison to calculations of this current lead test shows good agreement which allows extrapolation to

operational currents up to 80 kA needed for ITER model coil tests in the TOSKA test facility at KfK (Task MTOS).

Literature:

[1.1] F. Spath, R. Heil, W. Lehmann, J. Lesser, H. Schimmer, J. Weber, Performance Tests of a 2 kW Refrigerator for SC Magnet Tests Down to 3.3 K, Proc. CEC, Albuquerque, USA, NM, July 5-9, 1993.

[3.1] R. Heller, G. Friesinger, W. Herz, M. Irmisch, G. Nöther, L. Schappals, K. Schweikert, L. Siewerdt, M. Süßer, A. Ulbricht, F. Wüchner, G. Zahn: Test of a Forced-Flow Cooled 30 kA/23 kV Current Lead for the Polo Model Coil, Proc. MT-13, Vancouver, Canada, Sept. 20-24, 1993.

Staff:

H.Barthel
A. Baumgärtner
H. Bayer
F. Becker
P. Duelli
S. Förster
G. Friesinger
A. Götz
P. Gruber
A. Grünhagen
W. Heep
R. Heil
R. Heller
W. Herz
H. Irmisch
H. Kathol (since 1.12.92)
R. Kaufmann
P. Klingenstein
B. König
W. Lehmann
W. Maurer
G. Nöther
A. Nyíás
J. Ohlenroth
U. Padligur
G. Perinić (since 1.4.93)
C. Ruf
K. Rietzschel
L. Schappals
C. Schmidt
K. Schweikert
L. Siewerdt
Ch. Sihler (since 1.4.93)
F. Spath (for 1.)
E. Specht
A. Speier
H.-J. Spiegel
F. Süpfle
F. Süß
M. Süßer
E. Ternig

A. Ulbricht (for 3.)
D. Uhlich
D. Weigert
F. Wüchner
G. Würz
G. Zahn (for 2.)
H.P. Zinecker
V. Zwecker

MBAC High Field Operation of NbTi at 1.8 K

Subtask 1: He II Forced Flow Cooling: 1.8 K Tests of EC LCT Coil plus Development of Circulation Pumps

The 1.8 K cooling technique is indispensable, if technically applicable superconducting materials shall obtain their highest field levels. Therefore the task was started with a program part for the development of components included in such a cooling circuit and is continued with the operation of a large forced flow cooled fusion magnet, the Euratom LCT coil. The last experiment is an intermediate step in the sequence for upgrading the TOSKA facility for the ITER model coil test (Task MTOS).

1. The 1.8 K Test of the Euratom LCT Coil

The assembling of the reinforcement structure of the LCT coil was concluded with the pretensioning of the belts. Each belt was heated up to 50 °C by propan radiators and then the two bolts on each side were tightened up to a certain torque moment. The pretensioning of the belts was performed in a certain sequence in order to obtain a homogeneous distribution across the coil. The measured deformation of the coil under the effect of the pretensioned belts was 70% of that calculated by the finite element model. This result demonstrates a good force transmission of the reinforcement to the coil. It confirms that the fabrication tolerances for the sophisticated structure are kept.

The cold transfer line between the 1.8 K control cryostat and the TOSKA vacuum vessel was taken in operation. The measured He leak rate was $< 10^{-8}$ mbarl/s under operation conditions (1.8 K, 1-10 bar). The thermal losses could be measured only indirectly for both flow directions and were about 4.5 W. In this modified and extended loop the piston and the thermomechanical pump was tested again. New inlet valves were installed in the piston pump. The measured volumetric efficiency for HeII was the same one as for He I measured for another piston pump of the same type. The thermomechanical pump got new superfilters with a larger diameter. With the larger superfilters the mass flow of the thermomechanical pump was increased by about 30%. The insulation of the Polo current lead type was modified and a superconducting bus was constructed to supply current up to 20 kA to the LCT coil.

Staff:

H. Barthel
H. Bayer
F. Becker
G. Friesinger
A. Götz
A. Grünhagen
A. Hofmann
W. Herz
M. Irmisch
W. Lehmann
W. Maurer
K. Rietzschel
C. Ruf
L. Schappals
L. Siewerdt
F. Spath
J. Spiegel
F. Süß
M. Süßer
A. Ulbricht
D. Uhlich
T. Völkel
B. Vogeley
G. Zahn

Vacuum and Fuel Cycle

Introduction and Overview:

KfK holds a major share in both parts of the Fuel Cycle task area, i.e. it contributes essentially to the Vacuum Pumping tasks and to the Tritium Processing tasks. Most of the work is related to stages I and IIA of the 1992–1994 period but some of the results refer to the preceding programme period due to difficulties in the experiments or unexpected effects that caused a redirection of task objectives or additional theoretical work.

This is e.g. evidenced by the TPV 1-task (subtask 1), where dust transport proved to be much more complex than initially expected. With the help of University a model has now been set up that does not only correctly describe the experiments in the test facility, but is also capable of accounting for reactor conditions by means of a newly developed similarity criterion. The practical consequences in the case of an air ingress incident are quite severe: Dust, which seems to be unavoidable in a fusion reactor, will be transported over long distances and may affect the vacuum components.

Fortunately, in the case of graphite dust and elastomer-sealed valves this may not cause too much trouble, as was demonstrated by the experiments of subtask 2, but this may only be true for this scenario.

In view of the changes of ITER-specifications, and in accordance with the European Home Team these investigations have been concluded for the moment.

Within the TPV-2 task the various aspects of cryogenic pumping of plasma exhaust gases, containing typical impurities and a fraction of helium up to about 5%, are addressed.

Apart from the completion of characterization and performance testing for cryopumping panels of the first generation the main interest has moved to thin-layer cryosorption panels for the reason of limiting the vulnerable tritium inventory in cryopumps to a tolerable quantity. Within subtask 1 a nozzle spraying method has successfully been developed and patented, its He sorption capacity has been determined and its durability against thermal cycling verified. In the pumping performance tests, carried out under subtask 2, the specific pumping speed has so far been shown to be fully satisfactory for charcoal-coated panels. What concerns the pump configuration it could be demonstrated that co-pumping of hydrogen isotopes and helium on the same panel is feasible in the molecular flow regime.

Subtask 3 had the objective of endurance testing of the cryocompound pump principle based on an optimized cryosorption panel. In order to allow for an extended period of pumping/regeneration cycles with a minimized He consumption together with a high degree of flexibility in the pump configuration a new design of a test facility had been elaborated and a tendering procedure started. But, in view of a largely increased pressure level during the burn mode in the

new ITER-design, priority has now been given to investigations on the feasibility of cryopumping in the transient or viscous flow regime.

Significant progress has been made in the area of forepump testing (subtask 5). The pumping characteristics of the three available large Normetex pumps and the Metal Bellows pump have been measured for a wide range of operation conditions in single and series connection, and it could be shown that it is possible to use these pumps for backing of the primary pumps of a fusion reactor or even for primary pumping under the aforementioned new ITER-conditions. Some studies have also been performed on an optimum protection of pumps from particles with a minimum loss of conductance, but due to lack of funding this work is not further pursued.

In TEP 2 three major aspects of tritium recovery from plasma exhaust gas are compiled. Some of the work, however, is also of importance for tritium technology and process analytics in other areas of the fuel cycle of a fusion reactor. As a prerequisite for the ongoing and future work the Tritium Laboratory Karlsruhe (TLK) is now taking up operation.

In subtask 1 a tritium loop has been constructed for long-term performance tests on tritium-compatible permeators that constitute the center-piece of most of the processes proposed and elaborated by KfK for fuel recovery from tritiated gas streams. Most of the work in the reporting period was devoted to the commissioning of the loop and its auxiliary equipment for cold operations, and to the installation and testing of the systems belonging to the second containment, i.e. the glove boxes. Measurements and calculations were carried out on the heat load resulting from loop operation that led to the necessity of installing an additional cooling unit. The functioning of safety-relevant sensors on the primary loop is described in this report with some detail.

The objective of subtask 2 is to demonstrate the tritium operation of an integral fuel clean-up system based on the process principle developed at KfK. The technical facility was designed for a throughput scaleable to ITER conditions, constructed at the NNC company and successfully tested at the manufacturers' site. After delivery to KfK in April 1993 the facility has been installed in the TLK and connected to its infrastructure. For the completion of acceptance tests and cold commissioning some paperwork to comply with licensing conditions remains to be done.

In subtask 5 the influence of tritium radioactivity on side reactions interfering with tritiated water reduction by means of the water gas shift reaction is studied in more depth than will be possible in the integral fuel cleanup experiment of subtask 2.

As a first step the rate of catalytic methane formation was determined with protium as a model gas. For use with tritium a

small loop was constructed and equipped with a gas chromatograph, a small volume ionization chamber and, in addition, with a Fourier transform IR-spectrometer for on-line process analytics. In spite of the high tritium concentration the overall quantity is low so that it may be possible to run these tests outside the TLK.

H.D. Röhrig

TPV 1 Mechanical Vacuum Components

Subtask 1: Dust Transport Experiments

1. Introduction

The possible states of accident of a fusion reactor defined by ITER and the simulation of these accident states at the SPARTA (Solid Particle Transport test facility) were explained and the results of the first experimental investigations were discussed [1].

In the course of these experiments at the test facility, extensive raising of the dust was observed when simulating a sudden pressure increase. As dust raising can be caused by pressure shock waves, the latter shall be discussed and a model transfer shall be accomplished.

2. Similarity Consideration

In an external expert opinion the similarity relations presented in the present section were derived [1].

In case of gas ingress into the vacuum reactor, the following flow regimes can occur:

1. Passing of a shock wave at supersonic flow Mach number $M > 1$;
2. Equalising flow under continuous supersonic flow $M > 1$;
3. Equalising flow after exceeding the critical values $M = 1$.

For particle transport, the first two processes are of paramount importance. In the following sections, these two flow regimes shall be studied with regard to the similarity, starting from the assumption that the inflowing gas comes from a point of constant pressure p_0 during the complete process. Furthermore, the changes of state of the gas are assumed to be adiabatic.

Raising of a particle requires an axial movement of the particles. Here, the ratio of the wall shear force to gravity can be applied as the similarity requirement:

$$\alpha = \frac{\pi \cdot d^2 \cdot \tau}{4} \cdot \frac{6}{\pi \cdot d^3 \cdot \rho \cdot g} \quad (1)$$

where

- d : particle diameter
- ρ : density
- τ : wall shear stress
- g : acceleration due to gravity

The balance of forces in a cylindrical pipe gives:

$$\tau_w = \left(\frac{dp}{dl}\right) \cdot \left(\frac{D}{4}\right) \quad (2)$$

with

D: diameter of the flow cross-section

dp/dl: pressure gradient along pipe length

With the variables d, ρ and the surface properties of the wall in the reactor and the model being the same, the similarity requirement

$$D \cdot \left(\frac{dp}{dl}\right) = konst. \quad (3)$$

holds.

The similarity conditions are obtained as a function of the pressure increase with time dp/dt [1]:

$$v^{14} \cdot \rho_0 \cdot V^7 \cdot \left(\frac{dp}{dt}\right)^4 \cdot \left(\frac{\rho_0 \cdot R \cdot T_0}{M}\right)^7 \cdot D^{-15} \cdot \left(\frac{p_0}{p}\right)^{\frac{3}{4k}} = konst. \quad (4)$$

with

v: kinematic viscosity

ρ_0 : density

V: volume

dp/dt: pressure gradient

R: gas constant

T_0 : temperature

M: molar mass

p_0 : external pressure

p: vacuum pressure

When the external pressure p_0 and the Temperature T_0 in the reactor and the model are the same, the similarity conditions can be reduced as follows: obtained for the pressure increase:

$$V \cdot \left(\frac{dp}{dt}\right) \cdot D^{-15} = konst. \quad (5)$$

$$\left(\frac{dp}{dt}\right)_{model} = 20 \cdot \left(\frac{dp}{dt}\right)_{reactor} \quad (6)$$

According to this calculation a pressure increase rate in the model should be 20 times larger than the pressure increase rate in the reactor ($p=250$ mbar/s) in order to realize similar conditions in the model.

		Reactor	Model
Duct diameter	[m]	2	0,1
Volume	[m ³]	2600	0,218

Table 1: Data of reactor and model

3. Performance and Results of the Experimental Investigations

In another external expert opinion the shock dynamics was investigated both theoretically and experimentally [1].

To measure the pressure behaviour with time in the pipe of the model facility, three piezoresistive absolute pressure transducers manufactured by the Kistler company (type 4043A1) with a measuring range of 0–10 bar were installed at distances of 0.5 m (p1), 2.5 m (p2), and 3.87 m (p3), respectively, from the gas inlet vessel. It was ensured that the measuring diaphragm of these transducers was in line with the inner surface of the pipe.

The sensor element is made up of piezoresistive elements designed as strain gauges measuring the strain of a mechanical spring element and changing their resistance accordingly. Resistance variation of the strain gauges is evaluated by means of an appropriate differential amplifier. Piezoresistive sensor designs may be used for high-frequency vibrations and shock measurements.

By means of these pressure transducers (natural frequency >14 kHz), pressure signals smaller than 1 mbar can be measured perfectly. The pressure signals are led to a high-resolution, multi-channel transient recorder and subjected to further processing in a personal computer.

For the sudden pressure rise in the facility, a diaphragm (plastic and aluminium foil and an orifice with an aperture of 6 mm (orifice 1) or 26.4 mm (orifice 2) behind it) is installed at the inlet of the gas inlet vessel. To start the experiment, the diaphragm is pierced by a needle, as a result of which the transient recorder is triggered off.

The complete behaviour of the filling pressure by orifice 1 and 2 was measured. Pressure in the facility was 5×10^{-3} to 7×10^{-2} mbar. The pressure shock waves expected did not occur in any of the experiments. This suggested that the process

was "smeared" by the gas inlet vessel upstream of the pipe, such that only normal filling flow could be observed. This assumption was supported by films in the facility with the dust applied at a filming speed of the high-speed camera of 500 frames/s. Assignment of the frames and pressure behaviours to time shows that the dust is raised only when it is passed by the filling flow.

In the following experiments, the inlet vessel was therefore flanged off and the tube was directly sealed with foil using different orifices ($d=25$ mm (orifice 3), 50 mm (orifice 4), and 100 mm (orifice 5), respectively). Pressure increase amounted to 5 bar/s at $d=25$ mm and >50 bar/s at $d=100$ mm.

Compared to previous experiments, the pressure exhibits a completely different behaviour. The pressure increases, which are accompanied by more or less intense pressure surges, are much steeper than in the experiments with the inlet vessel. At measuring point (p2), relatively strong pressure oscillations occur, which may probably be attributed to reflection effects. This effect can also be noticed in the films, where first the dust is blown away in the direction of flow as in the previous experiments, but then also oscillates as if it were passed by a backstream.

Flow velocity was determined from the time of arrival measured and the path known between the end of the pipe and the respective pressure transducer. In the experiments with orifice 2, flow rates of $v=733$ m/s were measured. In the experiments with orifice 1, the values measured amounted to $w=278$ m/s. The theoretical flow rate is $v=761$ m/s. Flow rate at orifice 1 was in the subsonic range such that no compression shocks were expected. As far as orifice 2 was concerned, a standing pressure shock could be discussed at the most.

The pressure gradient of 385 mbar/s at an aperture of 26.4 mm and an air filling duration of $t=3.63$ s was measured. The pressure gradient calculated is $dp/dt=502$ mbar/s.

By comparison with the experimental value, a discharge coefficient of 0.767 is obtained. The calculated filling time is $t=3.65$ s, which is in good agreement with the time determined experimentally.

Results of a similar quality were reached for orifice 1. Here, the experimental value was $dp/dt=23$ mbar/s compared to the theoretical value of $dp/dt=20$ mbar.

As mentioned above, the conditions prevailing are different in the experiments without inlet vessel. The flow rate measured amounts $v=1162$ m/s. This indicates a compression shock entering the pipe.

The flow rate of the wake flow calculated is $v_2=1381$ m/s. Taking into account the "discharge coefficient", this is in good agreement with the value measured. In these experiments, however, extensive pressure surges can be observed, which probably may be attributed to the increase in the initial pressure p_1 developing during filling.

Determination of the pressure gradient is more difficult, as in the initial phase the increase is superimposed by the pressure surges, and, hence, a steep gradient is pretended to have occurred. Nevertheless, the experimental results can be interpreted in terms of shock dynamics, such that transfer to the reactor conditions can be accomplished as far as flow technology is concerned.

4. Conclusions

The theoretical/experimental investigations with regard to shock dynamics are in good agreement. Propagation of the shock waves is influenced by the geometry conditions. It is therefore important to define at which points of the reactor accidents are to be expected and to generate the model accordingly.

A simple similarity considerations (shear force/gravity) for a rough estimation shows that the pressure increase rate in the model for the similar conditions should be 20 times larger than in the reactor. Measurements during a sudden pressure rise at the model test facility indicate propagating shock waves, causing a very strong raising of the dust. At the pressure rise rate 5000 mbar/s for the simulation of the air inflow in the reactor (250 mbar/s) all the graphite dust (1–500 μm) applied is blown over the test section (1 m). Hence much dust transport is expected for the specified reactor accident types with the pressure rise rate of 250 mbar/s. A dust separation system is required to protect the components of the torus exhaust system of ITER.

Literature:

- [1] Özdemir, I.
Experimental Investigations for Determining the Raising and Transport Path of Solid Particles under Conditions of a Sudden Pressure Rise in the SPARTA Test Facility; Part II: Similarity Consideration and Model Transfer;
Unpublished report prepared

Subtask 2: Dust on Elastomer Seals

1. Introduction

The dusts generated by plasma/wall interaction can be entrained through the exhaust ducts into the valves in front of the pumps where they can impede the functioning of the valve seals.

The dust compatibility of elastomer seals is experimentally studied at the SPARTA model test facility where the flow conditions can be simulated to be similar to those prevailing in the evacuation pipe between torus and manifold of ITER. Dust typical of a tokamak with graphite liners can be metered in [1].

2. Test Valves and Procedure

Three electro-pneumatically operated bellows gate valves ND 100 of the company VAT were installed in the model test facility [1]. The double discs of the valves are sealed on both sides by means of vulcanised elastomer seals. Three materials are examined. The following parameters were varied in these experiments:

- Number of cycles: 100, 200, 500, 1000, 2000 and 5000
- Graphite dust size distribution: Dust 1: $d_{VS}=1 \mu\text{m}$, Dust 2: $d_{VS}=15 \mu\text{m}$
- Elastomer seals: VITON, BUNA-N and EPDM

In a preselected number of cycles dust was permanently metered in. After each test cycle first the rates of outward and inward directed leaks in the valve seat were determined. Then the pressure surge simulating the ITER accident conditions was released. At the end of a test the leak rate was determined a second time. The following additional operations were carried out in a test: dismounting the valves, sample collection from the sealing surface, and evaluation of the samples collected using an image analysing system for determination of the degree of dust coverage and the size of the dust agglomerates.

3. Results of Valve Tests Involving Elastomer Seals

The tightness of the elastomer-sealed valves has been surprisingly good in all cycles and for all degrees of graphite dust coverage. The measured leak rates of the valves are less than 10^{-6} mbar l/s although the degree of dust coverage amounts to up to 80% and the particle mean diameter of the dust agglomerates on the sealing surface is up to 100 μm .

The leak rate extrapolated to the ITER valves amounts to $1,5 \cdot 10^{-5}$ mbar l/s which is smaller by one order of magnitude than the leak rate specified for ITER.

Literature:

- [1] Özdemir, I.
Investigation at the Model Test Facility of Graphite Dust Compatibility of Elastomer Sealed Valves;
Unpublished report, June 1993

Staff:

W. Höhn
I. Özdemir
D. Perinic
R. Rinderspacher

TPV 2 Optimization of Cryogenic Vacuum Pumping of Plasma Exhaust

Subtask 1: Sorbent Preselection, Cryopanel Development

This task is aimed at developing and optimizing cryogenic vacuum pumping of plasma exhaust containing helium. To develop cryosorption panels a variety of eligible material combinations for helium cryosorption have been tested on a reduced scale. The best suited technical solutions will be optimized on the technical scale under simulated ITER operating conditions as a result of these investigations design data and requirements will be obtained with respect to the operation of the cryopumps to be used in the plasma exhaust pumping system of a fusion machine.

To optimize the preparation of thin layer cryosorption panels two industrial coating technologies electrostatic and spray coating were compared in according to their possible adaptation.

For the reproducible production of large sorption panels a new coating apparatus was designed and constructed. With this apparatus it is now possible to produce sorbent/bonding layers on plates up to 500 mm diameter with a thickness in the range of 0.1 to 3.0 mm.

The first thin layer sorbent panel (430 mm diameter) was coated in June 1993.

In parallel to these activities the search for the optimal sorption material and in addition the cryosorption tests with different sorption materials continued.

As a result of a tendering procedure three types of activated charcoal powder with particle sizes in the range between 5 μm and 160 μm (114A and GFF 30 from Chemviron and Type 5963.1 from Roth) were procured. For the tests at the HELENE test facility activated charcoal thin layer specimens were prepared with these three charcoal powders fixed with Thermoguss 2000 as cement on aluminium plates (50 mm diameter).

After the thermal cycling at the TARZAN test facility, sorption tests were executed with the three activated charcoal thin layer specimens at the HELENE test facility. The best results in terms of relative pumping speed (8 l/s) were measured for the charcoal Type GFF 30 from Chemviron. The two other types of charcoal powder (114A from Chemviron and type 5963.1 from Roth) are not useful with respect to the low results for the pumping speed.

According to the investigations to optimize molecular sieves for cryosorption pumps, helium and nitrogen adsorption isotherms for zeolite Y and ZSM 5 were measured and compared. The small porous ZSM 5 with a pore diameter of 5A was found to be the more advantageous material with respect to the helium adsorption capacity.

For the sorption tests in the HELENE test facility the following materials were selected:

LINDE Type 5A; (0.41 nm), Sodalith; (0.36 nm), ZSM 5; (0.5 nm).

Subtask 2: Sorbent Pumping Speed

1. Introduction

In the TITAN test facility, pumping of gases similar to the plasma exhaust generated in the ITER machine during the burn mode is investigated. It is the objective of the investigation to obtain cryosorption panels which have been tested under simulated operation conditions of a tokamak.

One of the test goals is to find suitable sorbents. This report covers panels with sorbent layers between 1 and 2 mm. Another goal is to prove that copumping is possible. Copumping means that the baffle at liquid helium temperature is removed and pumping of hydrogen isotopes and helium is performed simultaneously in the same stage [1].

The pumping speed, which is determined by the constant pressure method, is used as a criterion for the performance of the cryosorption panels.

2. TITAN Test Facility

TITAN consists of a ~ 700 l vacuum vessel and includes a measuring dome designed according to the PNEUROPS standard and a liquid helium bath cryopump installed inside the vessel. A gas dosage device and several pressure gauges are connected with the vessel. The temperature is measured in each stage of the cryopump. The test facility has already been described in [1].

The cryopump in the TITAN vacuum vessel consists of a liquid helium bath and a sorbent panel which is directly mounted to the bottom. One or two optically tight CHEVRON baffles shield the panel against heat radiation from the vessel, which has room temperature.

The sorbent panel is a circular metal plate covered with a sorbent, which is fixed by means of an inorganic bonding agent. At the bottom of the liquid helium bath an electric heater is installed. This heater is used to reactivate the panel which means to release the adsorbed gas after a pumping cycle. In Table 1, all thick-layer panels that have already been tested and the thin-layer panels that will be tested are listed [1].

In total, 6 cryosorption panels of $\varnothing 430$ mm coated with thick (> 1 mm) sorbent/ bonding layers have been tested. One of the panels (no. 3) was bonded by reactive braze, the other by an inorganic cement. Four panels (nos. 12, 14, and 16) were coated with activated charcoals and two panels (nos. 15 and 17) with molecular sieve. Panel no. 17 was prepared using

panel no. 15 and grinding off 1 mm from the surface of the sorbent/bonding coating.

The panel no. 14 has been prepared differently from other cement bonded panels. A mixture paste of cement and sorbent particles was sprayed over the substrate in a thick layer and after hardening a surface layer of about 1 mm was ground off. Small scale specimens prepared in a similar way achieved the best pumping results.

Panels nos. 12, 15, 16, and 17 were prepared by the nozzle spraying method. At first a cement layer was sprayed onto the substrate, and in a second step sorbent particles were sprayed in the same way. This method was developed at KfK for machine coating of large panel surfaces.

Panel no.	Sorbent	Bonding	Preparation	Substrate
3	Activated charcoal DEGUSORB AS 16/45 Cylinders 1.6 mm	Reactive braze DEGUSSA 7200+TI	Sorbent and bonding spread	Copper E-Cu 57
12	Activated charcoal CHEMVIRON SC II particle ~1 mm	Inorganic cement THERMOGUSS 2000	Sorbent and bonding Sprayed	Copper E-Cu 57
14	Activated charcoal DEGUSORB AS 16/45 Cylinders 1.6 mm	Inorganic cement THERMOGUSS 2000	Sorbent and bonding Sprayed	Copper E-Cu 57
15	Molecular sieve Merck 5A, no. 5705 pearls 2 mm	Inorganic cement THERMOGUSS 2000	Sorbent and bonding Sprayed	Copper E-Cu 57
16	Activated charcoal GOODFELLOW C003550 fabric 0.5 mm	Inorganic cement THERMOGUSS 2000	Bonding sprayed, sorbent pressed on	Copper E-Cu 57
17	Panel no. 15	Panel no. 15	~1 mm Sorbent layer ground off the panel no. 15	Copper E-Cu 57
19	Activated charcoal CHEMVIRON GFF 30 powder: $d_{V50} = 15 \mu\text{m}$	Inorganic cement THERMOGUSS 2000	Sorbent and bonding Sprayed 120 μm layer Thickness	Aluminum

Table 1: Review of the cryosorption panels

3. Test Procedure and Test Matrix

A test includes the following procedure which has already been described in [1]:

- Cooling down
- Pumping
- Regeneration
- Heating

In the pumping tests, the pumping properties of the panel-baffle-recipient system are determined. Pumping is characterised by the pumping speed.

During the pumping tests, the parameters of dosage rate [mbarl/s], pressure [mbar] and temperature [K] are measured and recorded (Table 2).

Pumping speed [l/s] is determined by means of the constant pressure method. It is obtained from the dosage rate/pressure ratio.

The gases dosed in the tests are listed below. The sequence of the tests is determined by the saturation pressures of the gases. The test cycle starts with the highest saturation pressure to minimise the effect of the gas which has not been released during regeneration of the test executed before.

Test run:

- Two-stage pumping: - Helium, protium, deuterium and mixture 7 respectively
- Three-stage pumping: - Helium and mixture 7 respectively

Dosage run	Dosage rate [sccm]	Dosage time [min]	Equalisation time [min]
1	1	15	15
2	1	He : 80 H ₂ : 80 others:15	15
3	5	15	15
4	10	15	15
5	15	15	15
6	20	15	15
7	25	M7 : 80 D ₂ : 80 others: 15	approx. 1 h
8	100	10	15
9	200	10	15
10	400	5	15
11	600	5	15
12	800	5	15
13	1000	5	15

Table 2: Test matrix

4. Test Results

The activated charcoal panel 3 and the molecular sieve panel 15 are not tested in conformity with the test scheme shown above. Due to the deviation from the test scheme, the test results of panels 3 and 15 are represented as points, whereas the results of the other panels are shown as curves.

The pumping speed below is indicated as a specific pumping speed related to the size of the panel surface of 1186 cm².

4.1 Helium Pumping Tests

The pumping speed curves in Figs. 1 and 2 are represented. The figures are a review of the tested panels 16, 12, 15, 3, 14 and 17. Up to now, panel 17 has been tested in the two-stage mode only, while panel 3 has been tested in the three-stage mode exclusively.

For each panel, the helium pumping speed increases by changing from the three-stage pumping mode to the two-stage pumping mode. The increase of the pumping speed in case of the two-stage pumping mode is probably caused by the reduction of the flow drag on account of having taken away one baffle.

At higher pressures, the curve of pumping speed generally tends to decrease. In the two-stage pumping mode, the decrease is significantly steeper than in the three-stage

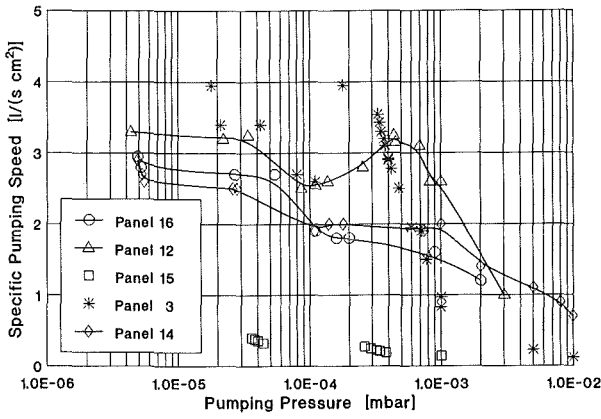


Fig. 1: Helium three-stage pumping

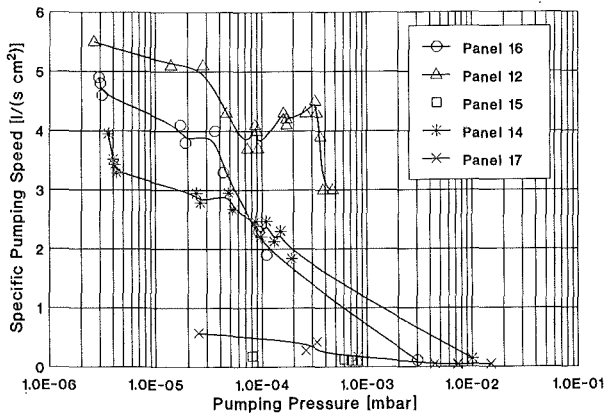


Fig. 2: Helium two-stage pumping

pumping mode. The decrease of the pumping speed probably results from two reasons: Saturation of the sorbent and temperature increase of the sorbent, especially in the two-stage pumping mode. Both reasons are more severe in the high pressure range, as the high pressure is a result of high dosage rates (>0.017 mbar/l/s). In the two-stage pumping mode the temperature increase mainly is a result of the 80 K radiation impinging on the sorbent surface instead of the 5 K radiation and secondly of the 80K temperature of the sorbed gas amount instead of 5 K.

The activated charcoal panel 12 has the largest helium pumping speed and the largest pumping speed increase of 60.6% by changing from three-stage to two-stage pumping. This is remarkable, because panel 12 is an activated charcoal panel like panel 14. However, the sorbent surface of panel 14 is ground with the intention to open the pores. But it seems that grinding destroys or smears the pores such that the pumping speed decreases.

Independent of the pumping mode, the pumping speed is almost constant for pumping pressures less than 3×10^{-5} mbar in case of helium pumping. This range of constant pumping speed is of great interest, because helium partial pressure of the ITER-machine is in this range during the burn mode.

The pumping speed of the molecular sieve panels 15 and 17 is significantly smaller than that of the activated charcoal panels 12, 14, and 16.

4.2 Gas Mixture Pumping Tests

Figs. 3 and 4 represent the pumping speed curves of panels 16, 12, 15, 3, 14 and 17 in case of gas mixture pumping.

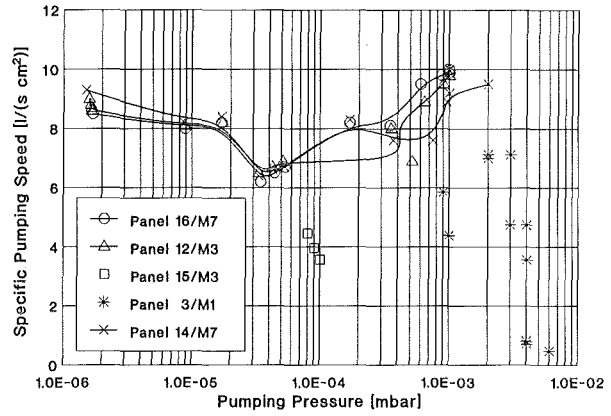


Fig. 3: Gas mixture three-stage pumping

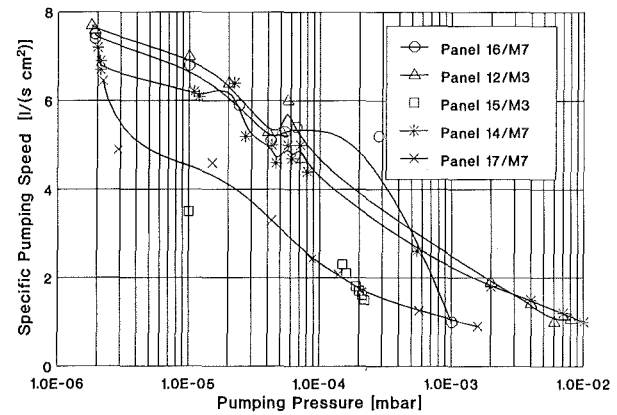


Fig. 4: Gas mixture two-stage pumping

In the case of two-stage pumping, the pumping speed is less than in case of three-stage pumping, which does not depend on the dosage rate. This is in contrast to helium pumping, where two-stage pumping results in higher pumping speeds at pressures less than 4×10^{-4} mbar. In general, the gas mixture pumping speed in the two-stage pumping mode tends to decrease steadily with increasing pressure.

In the three-stage pumping mode, the pumping speed decreases until a pressure of 4×10^{-5} mbar is reached. At pressures higher than this, pumping speed constantly increases with increasing pressure.

5. Conclusions

As an overall result it can be stated that cryosorption is appropriate for plasma exhaust pumping. Pumping is possible with two baffles, called three-stage pumping, as well as with one baffle, which is referred to as two-stage pumping. Three-

stage pumping results in larger pumping speed except for helium pumping of small dosage rates where two-stage pumping leads to higher pumping speeds. The pumping speed of the tested molecular sieve panels reaches an average value of $0.3 \text{ l}/(\text{s cm}^2)$, while the average pumping speed of the activated charcoal panels is about $8 \text{ l}/(\text{s cm}^2)$.

In the copumping mode, the gas mixture pumping speed in general decreases with increasing pressure.

In the three-stage pumping mode, the pumping speed decreases until a pressure of $4 \cdot 10^{-5} \text{ mbar}$ is reached. At pressures higher than this, the pumping speed constantly grows with increasing pressure.

A comparison of the results of the pumping speed as a function of pumping pressure under copumping conditions shows a lower pumping speed in case of gas mixture pumping and a higher pumping speed in case of helium pumping.

Literature:

- [1] Illbruck, H. and Özdemir, I.
Cryopanel Thick-Layer Tests at the TITAN Test Facility;
Unpublished report, June 1993

Subtask 3: Endurance Testing of Cryosorption Panels

For the endurance testing of cryosorption panels under simulated ITER operating conditions ($p < 10^{-4} \text{ mbar}$, gas flow rate - $29 \text{ mbar}/\text{s}$) a test facility should be procured.

This test facility includes the following parts:

- LHe supply with three 450 l LHe tanks;
- LN-supply from a 3000 l tank;
- The supply of the facility with cryogenic liquids (LHe; LN) with a main transfer line (MTL);
- Test gas injection system (GIS);
- Vacuum pump station (VPS);
- Data acquisition system (MES);
- Process instrumentation and control (SPS);
- The main test facility is divided into two modules (- Service module (SM) and Experimental module (VTC))

Based on the results of the conceptual and planning phase the procuring of the test facility started in January 1993.

For the manufacture and assembly of the main cryogenic assemblies of the test facility a call of tender was started. The main cryogenic assemblies are the main transfer line (MTL), the service module (SM) and the vacuum test chamber (VTC).

In addition to this tendering procedure of the main cryogenic assemblies KfK prepares the infrastructure and procures and manufactures all other components of the test facility.

For the supply of the test facility with LHe, KfK provides the needed 450 l LHe tanks and the transfer lines between these 450 l LHe tanks and the main transfer line (MTL).

Because of the hydrogen inventory the safety checkup of the test facility design documents was done with the TÜV (German technical control board).

All pressure transducers and temperature gauges have been ordered. KfK prepares the electrical power supply and the wiring. Also KfK ordered a process control unit (SPS) and a data acquisition system (MES). The gas injection system (GIS) will be manufactured by KfK. Mass flow meters and a vacuum pump for this system are delivered. The vacuum pumping station (VPS) which will be connected to the vacuum test chamber (VTC) has been delivered. A specification for cold valves was prepared and the tendering procedure starts in June. For an analytical system of gas (GEAS) a specification was in preparation.

The delivery of the test facility components was planned for March 1994. Because of modifications in ITER requirements for plasma exhaust (higher exhaust pressure, lower T_2 inventory, location of primary pumps inside of a 80 K cryostat) calling for major changes in the cryopump design the tendering procedure was stopped and a new technical concept is being developed for the pumping system and the testing facility.

Subtask 5: Backing Pumps and Particle Separators

Backing Pumps Tests

After completion of the phase of construction trial operation of the FORTE test facility was started in August 1992. Test operation proper (first test phase) which in conformity with the test matrix related to the gases hydrogen (99.9999 vol.-%), deuterium (99.8), the representative ITER gas mixture M7 (3 He, 1.12 CH₄, 1 H₂, 0.16 CO, 0.16 N₂, 0.16 O₂, 0.08 Ar, 0.08 CO₂, rest D₂), nitrogen (99.996), and helium (99.9999) was started in December 1992 and terminated in June 1993. After consultation with the home team the test series involving argon was dispensed with. Thus, a total of 70 tests were needed in this first test phase.

Besides, after this test series the ratios of compression of all four single pumps were determined in additional tests

conducted in the pressure range $p=0$ to 1200 mbar for the gases H_2 , N_2 , and for the ITER gas mixture.

It has appeared from the tests that among all gases tested hydrogen is pumped most badly by the single pumps of 1300, 600 and 60 m^3/h capacity (NORMETEX). For these pumps the pump characteristic of the delivered gases improves in the order $H_2 < D_2 < M_7 < He < N_2$. On the other hand, the pump behaviour of the 6 m^3/h pump (METAL BELLOWS) is nearly the same with all gases tested. The reason for the difference in behaviour of these two types of pump lies in the different pump concepts: the spiral displacement pump with backstreaming fluid in the duct, on the one hand, and the bellows pump with valve sealant, on the other hand.

Figures 5, 6 and 7 show the pumping speed plotted versus the suction pressure for the groups of pumps connected in series. The maximum pumping speed is achieved for all gases tested, except for H_2 , with suction pressures $p_A > 1$ mbar and $S=200$ to 300 l/s. The pumping speed for H_2 is improved with additional pumps connected. With only two pumps connected in series (1300+600), the pumping speed for H_2 is much poorer than that for other gases and attains a maximum of $S \sim 60$ l/s at suction pressures $p_A > 40$ mbar. The ultimate pressure for H_2 is $p_E \sim 1$ mbar. With three pumps (1300+600+60) connected in series, H_2 is delivered more effectively than the other gases already in the range of suction pressures $p_A > 10^{-1}$ mbar. With this combination of pumps an ultimate pressure of $p_E \sim 3 \times 10^{-3}$ mbar was measured for H_2 . With four pumps (1300+600+60+6) connected in series, the pumping speed for H_2 surpasses that of the other gases within the entire range recorded of suction pressures $p_A > 10^{-4}$ mbar. The ultimate pressure for H_2 in this case is $p_E \sim 2 \times 10^{-5}$ mbar.

In the experiments performed with a backpressure $p_G = 1200$ mbar ultimate pressures have been measured on the suction side of the first pump with a gas flow $V=0$ (Tab. 3).

At $P_G = 600$ mbar backpressure the pumping speed in the range of the suction pressures indicated before for H_2 is already better with the combination of pumps 1300+600 than it is for the other gases. This tendency becomes even more pronounced with the combinations 1300+600+60 and 1300+600+60+6.

It has been demonstrated by these experiments that light gases, especially including H_2 and representative Tokamak plasma exhaust gas mixtures, can be delivered very well with the oil-free spiral and bellows pumps connected in series. Therefore, application of similar pumps in the ITER plasma exhaust system is recommended.

At the end of this test series the plant will be expanded to accommodate higher gas flows. It is envisaged above all to simulate smaller pump units by supply of rather large amounts of gases between the NORMETEX 1300 and 600 compressors. This second test phase is scheduled to start in September 1993.

Combination of pumps	H_2	D_2	N_2	M7	He
1300+600	1.1	1.6×10^{-3}	1.1×10^{-5}	1.1×10^{-3}	1.0×10^{-4}
1300+600+60	3.3×10^{-3}	3.0×10^{-4}	4.0×10^{-6}	1.1×10^{-4}	6.0×10^{-6}
1300+600+60+6	2.0×10^{-5}	1.0×10^{-4}	2.0×10^{-6}	3.0×10^{-4}	7.0×10^{-6}

Tab. 3: Ultimate pressures [mbar] of pump trains

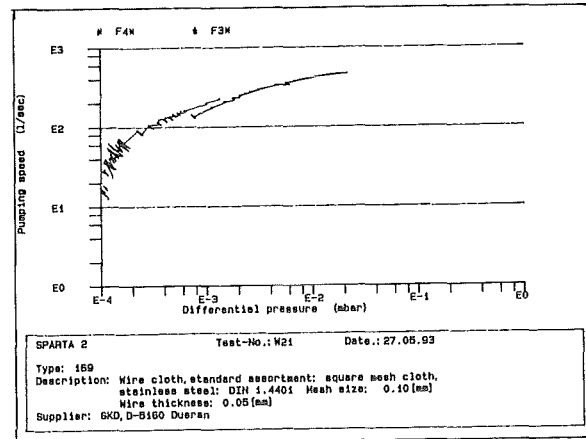


Fig. 8:

Development of Particle Separators

The test facility was built by HBT and set up in a scaffold in January. After successful completion of the vacuum leak test, preliminary tests were started in February 1993. 32 wire meshes and 3 fleece specimens were procured to determine the specimen with the smallest pressure loss. Test operation with the test matrix was taken up in April and completed in July. The tests were performed at an air flow rate $Q = 1 \times 10^{-3}$ mbarl/s to 10 mbarl/s and a pump pressure downstream of the specimen of $p = 1 \times 10^{-4}$ mbar to 1×10^{-1} mbar.

The maximum pumping speed $S=Q/p$ and, hence, the minimum pressure loss were measured with specimen No. 21. The pressure loss behaviour is obvious from Fig. 8.

The tests are reproducible. All tests yield identical pumping speeds dependent on the pump pressure. Specimen No. 21 is made of smooth cloth with square meshes of linen texture, mesh width 0.10 mm, wire thickness 0.05 mm, and DIN 1.440 stainless steel.

In a second step, it had been planned to manufacture a basket-filter type particle separator from the cloth above in a prototype size suitable for the FORTE test facility and to optimize it for use as main filter of the forepump station.

As the funds have been cut, further experimental investigations have been stopped.

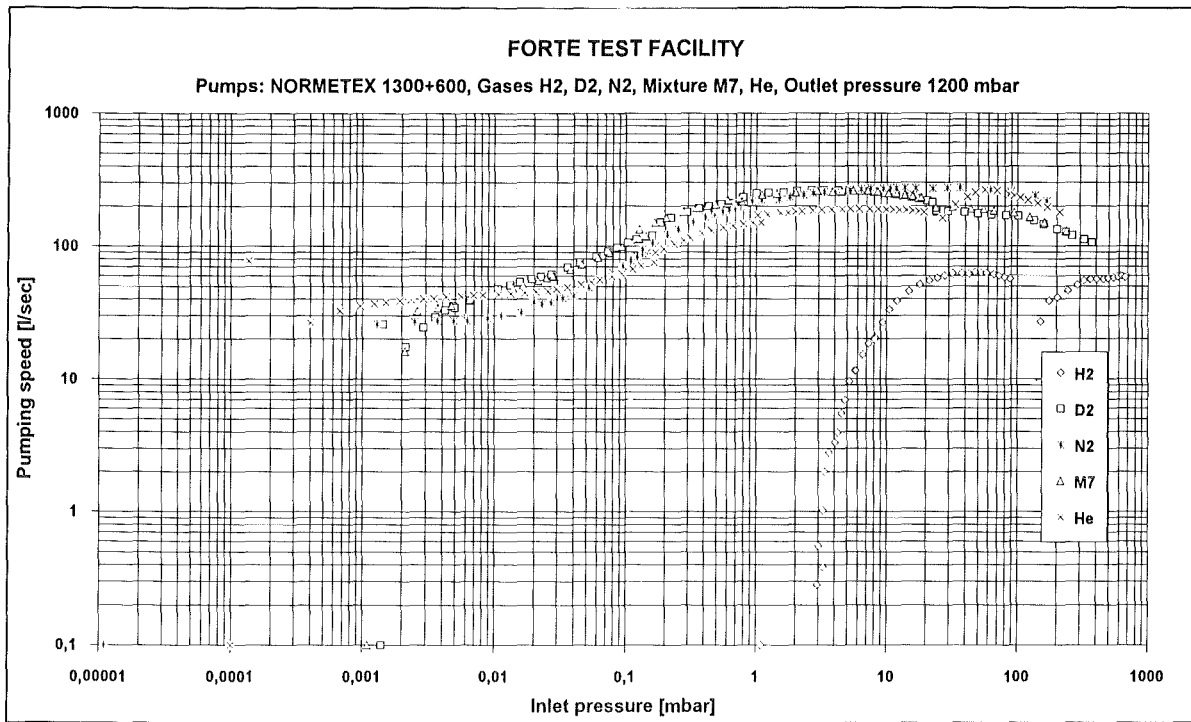


Fig. 5: Pumping speed of the combined NORMMETEX 1300+ 600 pumps for various gases at PG = 1200 mbar backpressure.

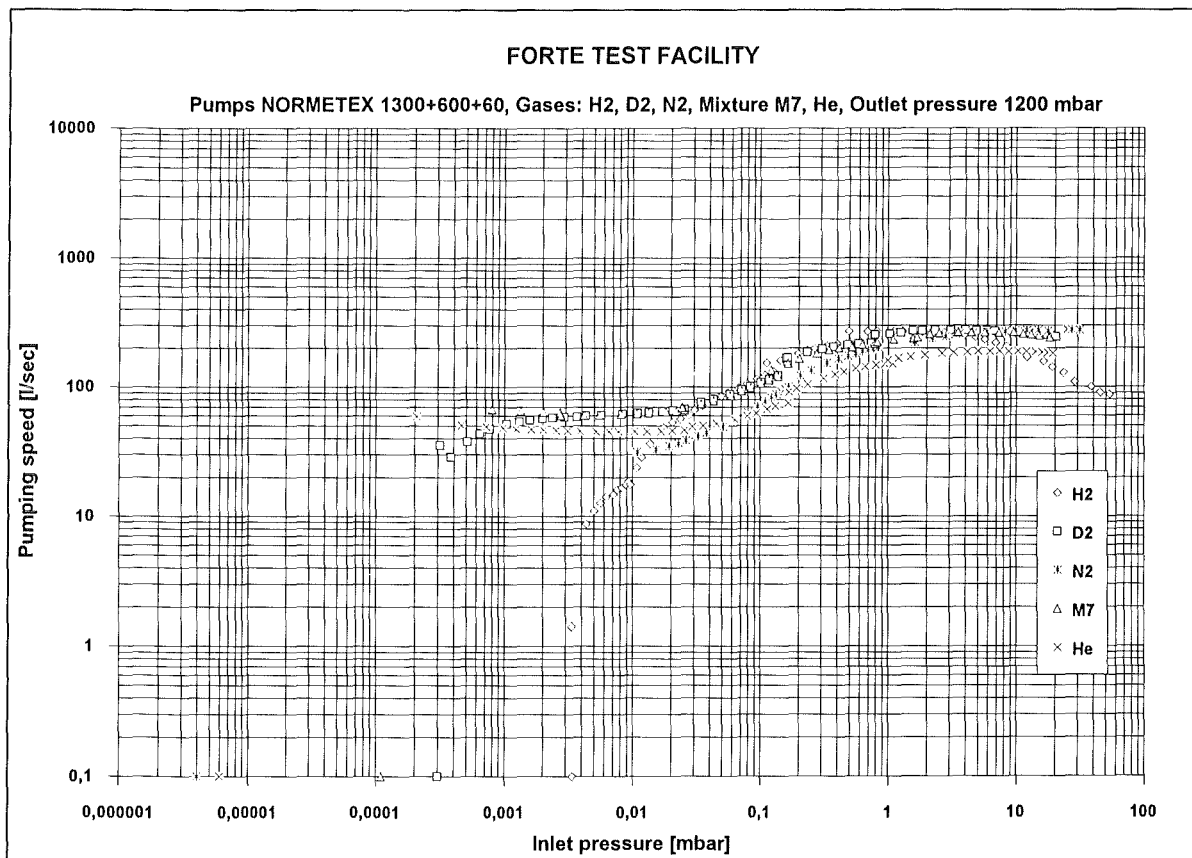


Fig. 6: Pumping speed of the combined NORMMETEX 1300+ 600+ 60 pumps for various gases at PG = 1200 mbar backpressure.

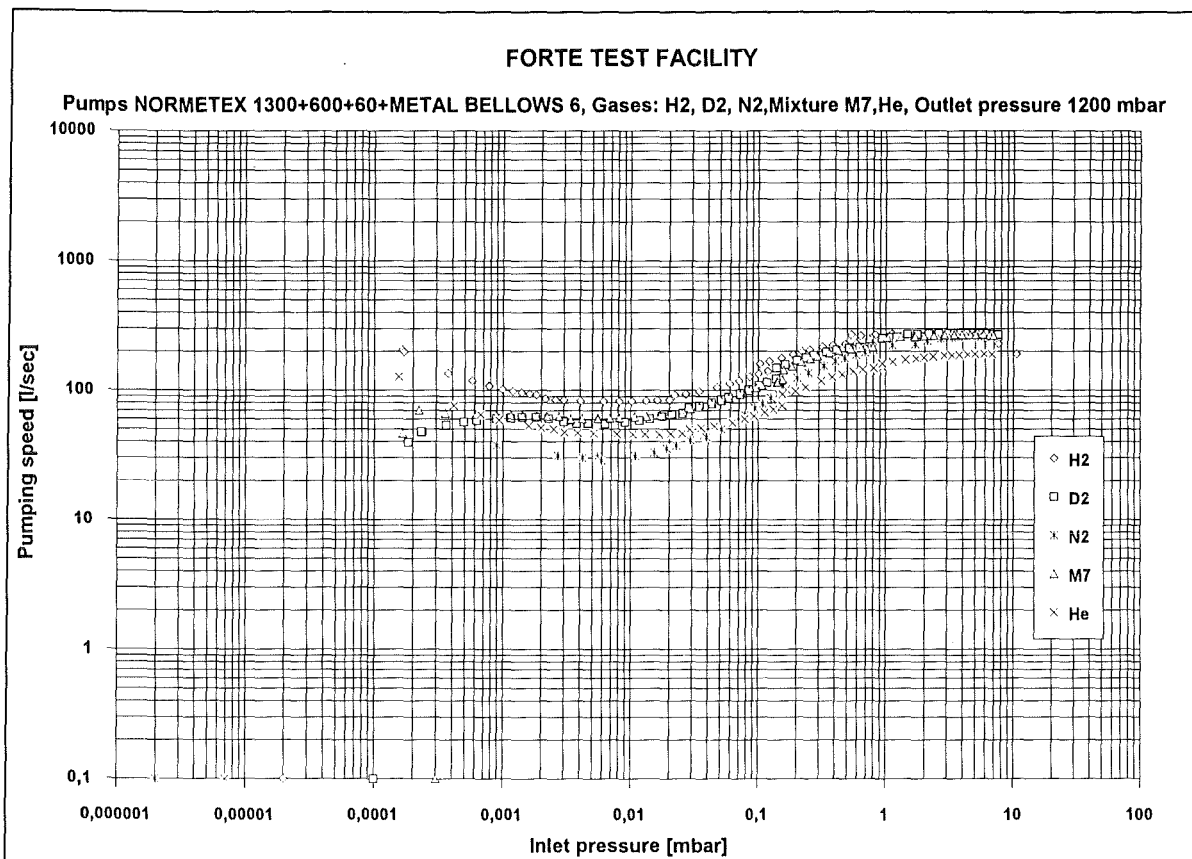


Fig. 7: Pumping speed of the combined NORMETEX 1300 + 600 + 60 + METAL BELLOWS 6 pumps for various gases at $p_G = 1200$ mbar backpressure.

Staff:

- D. Burghardt
- A. Edinger
- H. Haas
- J. Hanauer
- W. Höhn
- S. Horn
- H. Illbruck
- B. Kammerer
- U. Kirchhof
- H. Knauß
- J. Laier
- H. Lukitsch
- A. Mack
- D. Perinic
- W. Reeb
- D. Stern
- J. Weinhold
- D. Zimmerlin

TEP 2 Permeation und Catalytic Cracking: Alternative Options

Subtask 1: Permeator Studies

The PETRA experiment in the Tritium Laboratory Karlsruhe has been designed for a long-term performance test of a tritium compatible permeator, for the development of infra red process analytics, and for the investigation of the continuous operation performance of auxiliary systems such as pumps and other measurement devices common to tritium conducting systems. The primary system of the PETRA experiment has been installed in one of two glove boxes. All basic services to the experiment, e.g. cooling water, power supply, helium, and compressed air supply are ready for operation.

Part of the tritium retention system of the glove box is contained within one of the boxes, i.e. the two catalyst reactors, and a blower. Placed outside of the box are the heat exchanger as well as two molecular sieve beds. The performance of the tritium retention system is controlled by two ionization chambers, one placed before and the other placed behind the tritium retention system.

To assess the max. period of operation of the molecular sieve beds used in the tritium retention system it is necessary to consider that at 21°C and 45% rel. humidity (specified for the TLK atmosphere) the atmospheric water content corresponds to 8.4 g_{H₂O}/m³. The max. effective water loading of the molecular sieve beds will be limited to 0.225 kg_{H₂O}/bed to keep the tritium concentration in the glove box atmosphere at very low levels. Assuming a constant air leak of 0.1 vol. %/h into the 6.6 m³ large PETRA box an annual loading of each molecular sieve bed of 0.486 kg_{H₂O}/a is calculated. If a permeation coefficient of 4.4 E-3 g_{H₂O}/h·m² is assumed for the polycarbonate windows having a total surface area of 7.8 m² one can estimate an annual contribution to the loading of 0.301 kg_{H₂O}/a. The contribution of each start-up to the molecular sieve bed loading arising from 6.6 m³ of air containing 8.4 g_{H₂O}/m³ air is calculated to be 0.055 kg_{H₂O}/start-up. Another source term is a glove rupture. In this event the retention system continues to operate while the excess air intake into the box is extracted via the TLK ring line. Assuming an air exchange of 5 (33 m³/h) by the tritium retention system a contribution of molecular sieve bed loading of 0.277 kg_{H₂O}/h *glove rupture* is estimated. From these results it is concluded that with one start-up followed by continuous operation the life time limit of a molecular sieve bed will be of the order of 92 days. If two start-ups are included, the operation time is reduced 67 days. In case of the glove rupture the molecular sieve bed reaches the tolerable H₂O concentration in less than 1 hour.

A few runs were carried out to determine the need of a cooling system for the PETRA glove boxes. The max. temperature of the glove boxes during normal operation has been limited to 40°C. The temperature that establishes when

heat is released into the glove boxes was estimated from calculation and from experiments:

The heat release into the glove box during continuous normal operation is estimated to be of the order of 2 kW. If it is assumed that heat transport from the box into the environment occurs by natural convection only, a rough estimation of the temperature attained by the glove box atmosphere upon release of 2 kW can be obtained from the relationships:

$$dQ/dt = K \cdot A \cdot \Delta T \quad (1)$$

in which dQ/dt=heat flow, K=heat transport coefficient [w/m² K], A=area [m²], and ΔT=temperature difference. With this equation a box temperature of approx. 42.7°C can be estimated at T_{amb}=21°C. This exceeds the tolerable temperature by 3°C.

The set up employed for the experimental evaluation of the temperature distribution within the boxes on the basis of the heat transport into the laboratory air is depicted in Fig. 1.

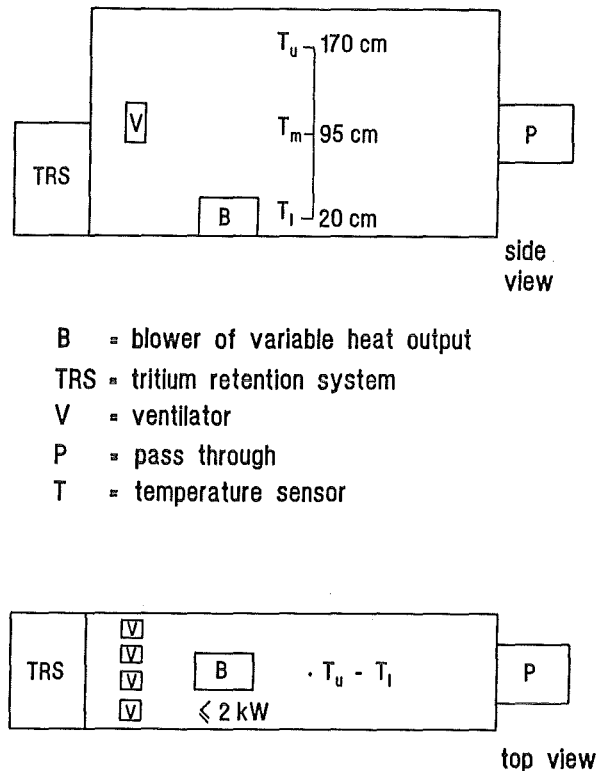


Fig. 1: Experimental arrangement to investigate the temperature profile in the PETRA glove boxes as a function of heat release

Heat was released into the empty glove boxes with a blower of variable heat output. Several thermocouples were placed within the box at various heights. Gas circulation within the glove box was enhanced with four ventilators placed at half height at one end of the glove box. Runs in which the heat output was reduced in steps on 0.5 kW from 2 down to 1 kW indicated that already a release of 1.5 kW causes the max. tolerable temperatures to be significantly exceeded (see

Fig. 2). A summary of all runs is given in Table 1. The results of

heat power [kW]	lower temp. [°C]		middle temp. [°C]		upper temp. [°C]	
	WV	Nv	WV	NV	WV	NV
2.0	44.0		47.0		49.0	
1.5	40.3		43.5		44.9	
1.0	35.5	24.6	37.2	38.0	38.0	43.2
0.8	32.0		33.6		34.2	

WV = with ventilators; NV = no ventilators

Table 1: Temperature distribution within the empty PETRA box without cooling system

the experiments substantiate the conclusions obtained from the calculations, i.e.: if more than 1.5 kW are released into the glove boxes a cooling unit is required during the operation of the PETRA experiment.

In view of the above a cooling unit for the PETRA boxes was specified to 4 kW to allow for future incorporation of additional components. The selected arrangement is given schematically in Fig. 3. The cooling unit is cooled with water from the TLK having an inlet temperature of 20°C and an outlet temperature of 28°C, respectively. A thermocouple regulates the operation of the cooling unit within a given temperature window. The results accomplished are shown in Fig. 4 und Table 2. Clearly, with the cooling unit operated to generate water of 6°C it is possible to maintain the temperature in the glove box atmosphere below the

stipulated temperatures, even when the amount of released heat is as high as 4 kW.

Table 3 contains the results of a long duration experiment carried out with a constant release of 2 kW into the glove boxes. This run demonstrates that the unit operates satisfactorily over an extended period of time.

For the control of the experiment a local process control system (LLS), a hard wired safety system (SS), and a central process control system (PLS) are used. The LLS controls the operation of the primary system of the PETRA experiment. The LLS also provides the SS with a binary "life" signal to indicate its intact state of operation. In case of its malfunction the experiment is shut down.

All heated components of the PETRA facility are provided with two thermocouples. One, which is used to control the temperature (C value), also shuts off the experiment when a given limit value (S value) is exceeded. The other serves to register the temperature (R value). In addition, a virtual temperature, obtained from a comparison between a C value and an R value from a given component, serves to detect a faulty performance of either one of the devices. A departure of the virtual temperature from a preestablished upper (or lower) value (S value) will cause the shut down of the experiment. In addition, should any of the above mentioned S values be exceeded by a certain margin (preestablished Z value) the experiment is shut off by the SS. To make certain that the isolation vacuum of the permeator, which will be permanently in operation, is intact, a thermocouple monitors the outer wall temperature of the vessel and shuts off the experiment should a preestablished value to exceeded.

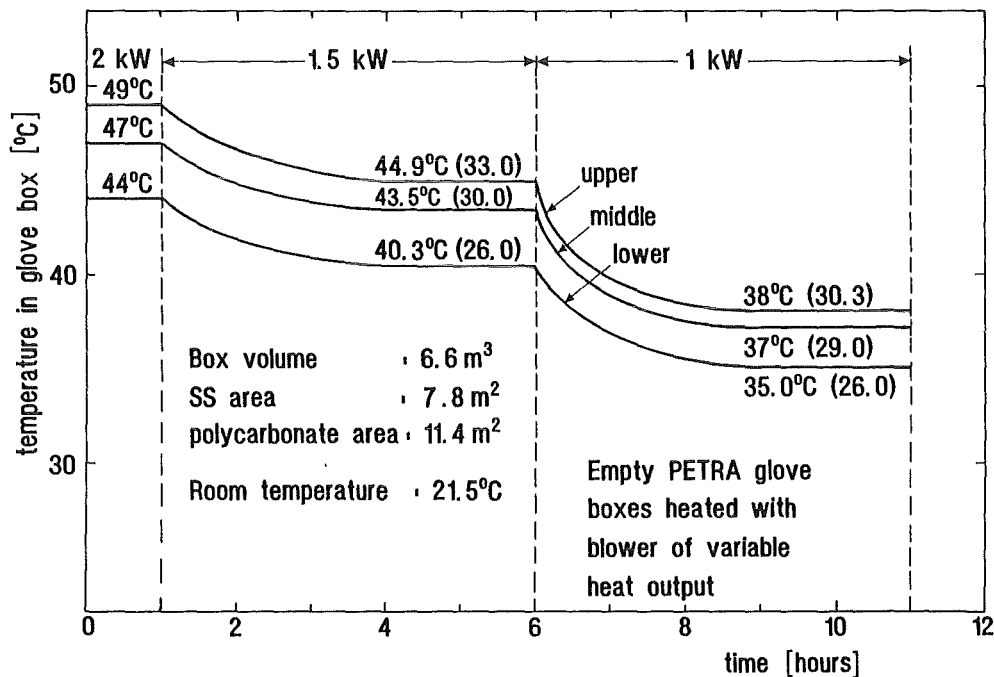


Fig. 2: Temperature distribution within the PETRA glove boxes upon decreasing release of heat

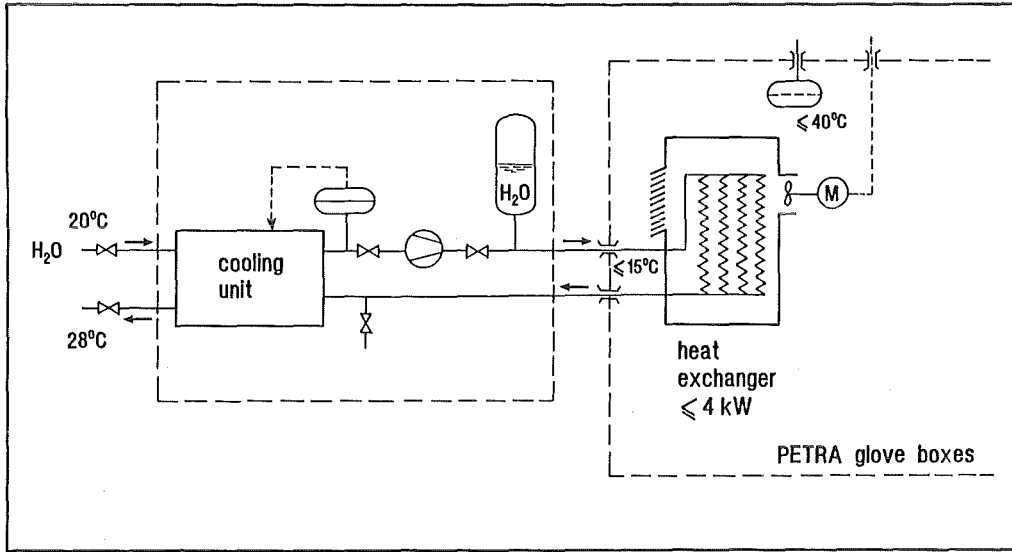


Fig. 3: Cooling concept of the PETRA glove boxes

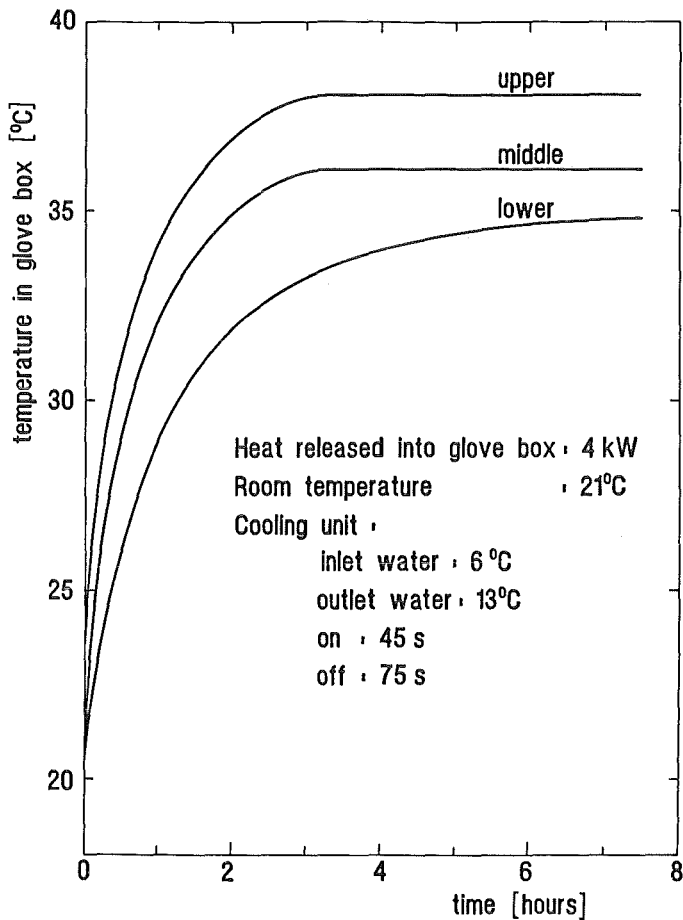


Fig. 4: Temperature profiles in the PETRA glove boxes upon release of 4 kW heat with the cooling unit in operation. The curves give the upper, middle and lower temperature of the box (see also Fig. 1).

A number of pressure sensors control the operation of the PETRA experiment. These sensors measure the total pressure

heat released into box [kW]	duration of expm. [h]	equil. temp. reached after [h]	upper temp. [°C]		
			lower	middle	upper
2	70	4	27	28.6	28.5
4	7.5	3	34.8	36.1	37.7

Table 2: Test of the cooling unit of the PETRA glove boxes (with experimental facility in the box) using a heat blower of variable output (room temperature 21°C)

catalyst temp. [°C]	duration of experim. [h]	steady state temperature [°C]		
		lower	middle	upper
100	62	20.9	22.5	23.5
180/200	97	22.5	29.1	31.3

Table 3: Test of the tritium retention system of the PETRA box (room temperatures 21°C)

in the buffer vessel, the vacuum in the second containment of the metal bellows pumps, the pressure of the bleed gas, the pressure of the pure hydrogen isotope stream, the pressure between the metal bellows pump and the scroll pump used to evacuate the permeator, and the relative pressure inside of the two safety cells that protect each of the infrared cells. Safety relevant sensors of a given component are compared between each other to obtain virtual values, which are used to control the "in operation" condition of both devices.

Singular sensors are used for the surveillance of the vacua in the secondary containments of heated components and to measure the vacuum achieved by the high vacuum system. Pressure sensors are also used at positions in which gases are introduced into the primary system or removed via sampling ports. The bleed stream and the pure hydrogen stream that exit the permeator are each provided with a flow rate measurement device as well as with a small volume ionization chamber. They serve to monitor the continuous performance of the permeator.

The surveillance of the operation of the second containment (glove box) is performed by the central PLS.

Staff:

E. Kirste
R.-D. Penzhorn

Subtask 2: Catalytic Cracking Process

To recover high purity tritium in near quantitative amounts from all primary exhaust gases of ITER while producing a waste gas stream of very low concentration of tritium a catalytic process combined with selective permeation of hydrogen isotopes through palladium silver membranes was developed at the IRCh. Tests performed during the past years included integral laboratory experiments with up to 50% of tritium and technical scale experiments. To demonstrate the tritium operation of an integral fuel clean-up system based on the catalytic cracking / permeation process the technical facility CAPRICE (Catalytic Purification Experiment) was designed to process simulant reactor exhaust gases at the following maximum target throughputs:

tritium / (deuterium, hydrogen)	8.700 mol/h
tritiated methane / (hydrocarbons)	0.270 mol/h
helium / (argon)	1.240 mol/h
water vapour	0.040 mol/h
carbon oxides	0.060 mol/h
nitrogen (also as ammonia)	0.050 mol/h
total	10.4 mol/h

The various exhaust gases from a fusion reactor during different operational conditions are simulated with appropriate gas mixtures produced in a toNs mock-up within Caprice. The target throughput for the processing of liquid tritiated water (1 tritium or less) is 8.7 mol/h employing 13 mol/h of carbon monoxide as a carrier gas. Product streams of the Caprice facility are high purity hydrogen isotopes with

less than 3 ppm total contaminants and a waste gas stream with an activity of less than $2 \cdot 10^{12}$ Bq/m³ (50 Ci/m³).

The CAPRICE project was initiated in March 1991 with a contract award for the detailed engineering, manufacture, assembling and commissioning of the facility to National Nuclear Cooperation (NNC), Great Britain. Following completion of works assembly, of works inspection, of the control and instrumentation system and of software module testing the commissioning tests of the experimental rig at the manufacturers site were commenced in December 1992. The main objectives of these tests were to confirm the operability of the plant, to establish the performance characteristics at ambient and operating temperatures, to check and adjust the flow, pressure and temperature control loops and to check the automatic sequences controlled by the programmable logic controller. These first tests also covered alarms, interlocks and safety shut down features. After successful completion of this phase the plant was delivered to the Tritium Laboratory Karlsruhe (TLK) in April 1993. Installation and connection to the infrastructure of the TLK is now complete. The next steps will be acceptance tests with hydrogen and deuterium and tests of the safety related instrumentation, safety trips and cold tests of the operation of the facility in combination with the infrastructure systems of the TLK.

In Fig. 5 the three-dimensional CAD layout of the main process rig having overall dimensions of 6m x 1 m x 2m is shown. Several two stage double containment Metal Bellows 601 pumps (KPO01, KP002, VA012, VA023 and VA032), two 15 m³/h Normetex spiral pumps (VA022 and VA03 1) and a magnetically suspended turbomolecular pump (VA02 1, Edwards, STP-H600C) are located in the lower part of the system, while a 150 m³/h Normetex pump (VA0 11, not shown) employed to evacuate the primary permeator is installed on a separate rig in a separate secondary containment. The primary and secondary permeators (PP001 and PP002) are horizontally mounted on the back side of the rig in order to allow easy maintenance and replacement, if necessary. Three catalyst vessels (KT001, KT002 and KT003) are used to crack tritiated methane and other hydrocarbons and to catalytically convert water into hydrogen via the water gas shift reaction. The fourth catalyst vessel (KT004) is part of the torus mock-up and is used for the continuous synthesis of tritiated methane by isotopic exchange between deuterated methane and tritium. Three buffer vessels (BD001, BD002 and BD003) are employed for the intermittent storage of process gases. Of these only BD002 is inherent to the process. The other two vessels are necessary to operate the facility in the environment of the laboratory.

The CAPRICE glove boxes are provided with highly efficient heat exchange units capable of removing the heat liberated by pumps and heated components.

A comprehensive safety report has been submitted to the licensing authorities.

Caprice

Layout

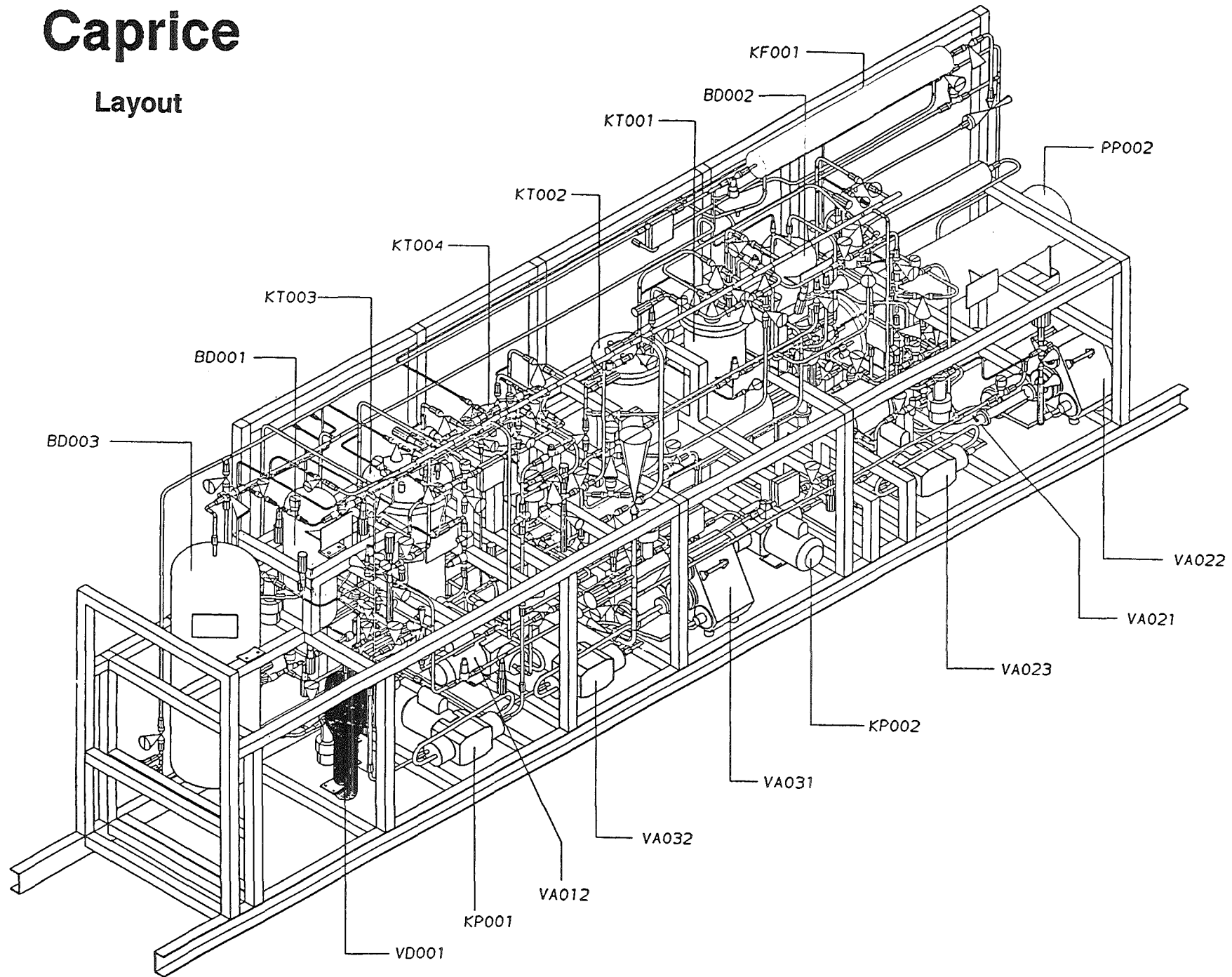


Fig. 5

A facility for the production of deuterated methane from deuterated water and aluminum carbide has been built. About 60 ℓ of deuterated methane have been prepared and compressed into a 1 ℓ gas bottle for the continuous feed of tritiated methane into the primary CAPRICE loop.

A gas chromatograph with three separation columns will be used for gas analysis of the various process streams of the CAPRICE facility. After completion of all calibration runs with typical gas mixtures such as expected, the GC has been installed in the CAPRICE rig.

Staff:

M. Glugla

K. Günther

T.L. Le

W. Leifeld

R.-D. Penzhorn

K.-H. Simon

Subtask 5: The Water Gas Shift Reaction for the Conversion of Tritiated Water into Hydrogen

The water gas shift reaction has been proposed for the catalytic conversion into hydrogen of liquid tritiated water produced from the oxidation of impurities present in the exhaust gas of a fusion reactor. In combination with a palladium/silver permeator the chemically liberated hydrogen isotopes can be recovered in a highly pure form.

In previous laboratory scale runs it was shown that with two water gas shift catalyst bed - permeator units in series it is possible to decrease the water partial pressure in a carbon monoxide carrier stream from initially 200 mbar down to levels below the detection limit of the employed moisture sensor, i.e. 10 ppm. With a technical laboratory facility it was demonstrated that up to 2 ℓ of liquid water can be converted into hydrogen when carbon monoxide containing about 400 mbar of water vapor is passed through a bed filled with 1000 g of zinc stabilized copper chromite catalyst.

To extend the application of the water gas shift reaction to the processing of water having a high specific content of tritium it is necessary to examine the mechanism and determine the kinetics of the reaction of hydrogen and of tritiated hydrogen with carbon oxides at 200°C in the presence of zinc stabilized copper chromite. In studies of the radiation induced reaction of hydrogen isotopes with carbon monoxide and carbon dioxide, other investigators have shown that a variety of products are formed and an acceleration of the reactions by certain adsorbers and catalysts occurs. To evaluate the possible contribution of catalytically formed hydrocarbons during the period between the occurrence of the water gas shift reaction in the catalyst bed and the zone in which the removal of hydrogen isotopes

takes place in the permeator an experimental investigation is now under way at KfK

The reaction between hydrogen and carbon dioxide catalyzed by zinc stabilized copper chromite was found to be rather slow. When a 1:1 mixture of 400 mbar each of CO₂ and H₂ diluted in 200 mbar helium up to 1 bar was passed over the catalyst at 200°C at a flow rate of 10 l/min the only product observed by Fourier transform infrared spectroscopy or by gas chromatography was methane. After 167 hours of recirculation only approx. 0.05 mbar methane were formed. In view of this, it was decided to concentrate the investigations without tritium on the comparatively fast catalytic reaction between hydrogen and carbon monoxide.

Preliminary runs to determine the rate of the reaction of molecular hydrogen with carbon monoxide in the presence of zinc stabilized copper chromite at 200°C indicated that the reaction of carbon monoxide with hydrogen is much slower than with water. From thermodynamics the equilibrium constant at 200 °C for the reaction



was calculated to be $K_{\text{eq}} = 1.425 \text{ E} + 11$. To obtain measurable product partial pressures reaction times of several hundred hours were necessary. During this time the gaseous mixture was continuously circulated through the catalyst bed at a flow rate of 10 l/min. The only products identified were water, carbon dioxide (probably produced by the reaction of water with carbon monoxide), and methane. Kinetic measurements in which the extent of conversion was estimated from the CO pressure drop yielded a rate constant of $11 \text{ E} - 4 \text{ h}^{-1}$.

Temperature K	p _{CO} mbar	p _{H2} mbar	k h ⁻¹
473	50	50	0.86 E-5
473	400	400	6.14 E-5

Table 4: Rate constants for the formation of methane from the reaction of hydrogen with carbon monoxide

Table 4 summarizes the rate constants obtained in a few runs in which the rate of formation of methane was measured. From the results it is apparent that the rate constant for the consumption of CO is approx. twice that of the formation of methane. This can be explained by the conversion of a fraction of the carbon monoxide into carbon dioxide by reaction with water.

The still preliminary data in Table 4 yield the rate equation

$$k = k_0 (p_{\text{CO}})^{1.2} \quad (IV)$$

To confirm this rate law more experiments are presently in progress.

One of the aims of the CAPRICE experiment in the TLK is the demonstration with tritium of the water/hydrogen conversion using a process step based on the water gas shift reaction. For the vaporization of water a newly designed vaporizer will be tested. Employing the rate constants determined above and assuming a residence time of 100 seconds for the gas in the water gas shift catalyst vessel of the CAPRICE experiment, the max. methane concentration in the exhaust gas of the catalyst vessel is estimated to be 100 ppm. After the catalyst vessel the reaction rate will be much lower because the temperature in the zone between the catalyst vessel and the diffusor is only little above that of the room. Furthermore, once the process gas is in the permeator, one of the reactants, i.e. hydrogen, is removed.

To study the catalyzed reaction between tritium and carbon monoxide and/or carbon dioxide a small, externally heated reactor containing 3.53 g of water gas shift catalyst was built. The reactor can be heated up to 200°C. It is enclosed by an evacuated second containment to exclude the possibility of permeation losses. The periodical circulation of gases is carried out with a tritium compatible MS 151 DC Metal Bellows pump. For gas analysis a gas chromatograph equipped with a small volume ionization chamber is available (detection limit for HT 0.3 ppm). In addition, Fourier transform infrared spectroscopy will be used for the identification of gaseous products. The gas cell has an optical path length of 100 mm and is provided with sapphire windows.

Staff:

M. Glugla

W. Jung

T. Le

R.D. Penzhorn

A.N. Perevezentsev

NDB 2 Neutronics Data Base - Benchmark Experiments

The neutronics data base task consists of the analysis and execution of bulk shield experiments (Subtask 1) and of the analysis and experimental study of the assembly gaps between adjacent blanket/shield segments.

Subtask 2: Shield Penetration Experiments

The objective of this subtask is the verification of calculational tools for shield penetrations. For the ITER shield design limits of the main parameters - the fluence of fast neutrons in the magnet coils, the number of atomic displacements in the copper stabilizer, and the maximum nuclear heat in the winding pack - have been formulated [1]. They are determined by the neutron and photon fluxes (Φ_n , Φ_γ) penetrating the shield. In a benchmark experiment the measurement $\Phi_n(E)$ and $\Phi_\gamma(E)$ have to be compared to the calculated energy-differential fluxes.

An uncertainty analysis of the NET shield [2] has shown that the evaluated nuclear data are the main source of inaccuracies of the calculated shield parameters, and that the main contributions arise from the iron data uncertainties. Therefore, the benchmark assembly was decided to consist of Fe. To investigate also the influence of an assembly gap as it is between two adjacent blanket segments, slab geometry with a variable plane gap was chosen as outlined in Fig. 1.

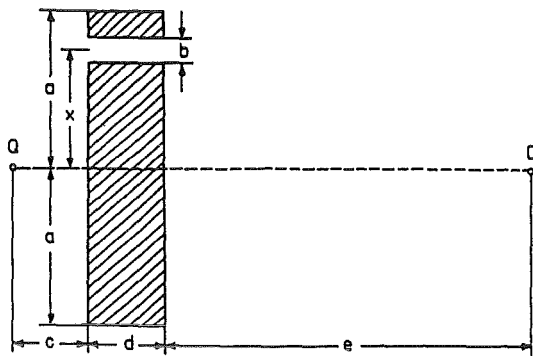


Fig. 1: Horizontal section of the benchmark geometry in the plane of the 14 MeV neutron source (Q) and the detector position (D).

Measurements without gap in the assembly were complemented by runs with $x + b = 10 \text{ cm} + 5 \text{ cm}$ and $20 \text{ cm} + 5 \text{ cm}$, respectively. The other geometry parameters were found to be at an optimum [3] for $d = 30 \text{ cm}$, $e = 300 \text{ cm}$, $c = 19 \text{ cm}$ and $a = 50 \text{ cm}$.

The $d - T$ neutron source strength was monitored by the associated α - particles. The neutron generator was operated in a pulsed mode, and for each detector event the pulse height and the time-of-arrival have been recorded. One detector used (liquid scintillator NE 213, $2'' \times 4'' \text{ } \varnothing$) [4] was sensitive to both, neutrons and photons. Low-energy neutrons ($30 \text{ keV} < E < 1 \text{ MeV}$) were detected by spherical

proportional chambers filled with hydrogen (pressure [MPa] + \varnothing [cm] = $1.0 + 4.0$, $0.4 + 4.0$, $0.1 + 3.2$). The pulse-height distributions obtained were transformed to $\Phi_n(E)$ and $\Phi_\gamma(E)$ [5,6]. $\Phi_n(t)$ can be used for an additional (independent) test of the neutron nuclear data. $\Phi_n(t)$ is needed for background reduction by use of time-windows for the acquisition of the γ -event pulse-height distributions. Examples of measured spectra are presented elsewhere [7].

The experimentally obtained flux spectra were compared to three-dimensional Monte Carlo calculations (code MCNP [8]) based on the nuclear data of the European Fusion File EFF-1. Some examples are displayed in Fig. 2.

More neutrons with $5 \text{ MeV} < E < 13 \text{ MeV}$ are observed than expected by the calculation. In $\Phi_n(t)$ these neutrons build up the spectrum between $90 \text{ ns} < t < 140 \text{ ns}$. They originate from multistep-direct inelastic scattering processes that are forward peaked [3], whereas in EFF-1 this inelastic scattering is treated as isotropic process. A neutron excess compared to the calculated flux is also measured in the low-energy range ($40 \text{ KeV} < E < 200 \text{ keV}$) of the spectrum.

The photon spectrum is dominated to two peaks at $E = 0.85 \text{ MeV}$ and $E = 1.2 \text{ MeV}$ from the de-excitation of ^{56}Fe and by a third peak at $E = 0.51 \text{ MeV}$ from pair-production by high-energy photons and subsequent annihilation of the positron. The calculation of the annihilation photon contribution needs a coupled neutron-photon-electron transport code, whereas the version of MCNP used treats neutrons and photons only.

Literature:

- [1] W. Daenner, ITER Expert Meeting on Shielding Experiments and Analysis, Garching (FRG), Febr. 12-14, 1990, ITER-IL-5-0-5.
- [2] A. Santamarina and T. Parish: Sensitivity and Uncertainty Analysis of the NET Magnet Neutronic Design Parameters to Uncertainties in Cross Section Data, CEA 917/333.
- [3] T. Elfruth, J. Hanke, K. Seidel and S. Unholzer: Specification and Optimization of the Experimental Set-up and Procedure, 1st Intermediate Report to NDB 2-2, TU Dresden, April 1992.
- [4] M. Tichy, H. Klein and J. Pulpan: Calibration of an NE 213 Scintillator, Report Physikalisch-Technische Bundesanstalt PTB-7.2-92-1, Braunschweig, July 1992
- [5] S. Guldbakke, H. Klein, A. Meister, J. Pulpan, U. Scheler, M. Tichy and S. Unholzer: Response Matrices of NE 213 Scintillation Detectors for Neutrons, 8th ASTM/EURATOM Symposium on Reactor Dosimetry, Vall Colorado (USA), August, 29 - September, 3, 1993

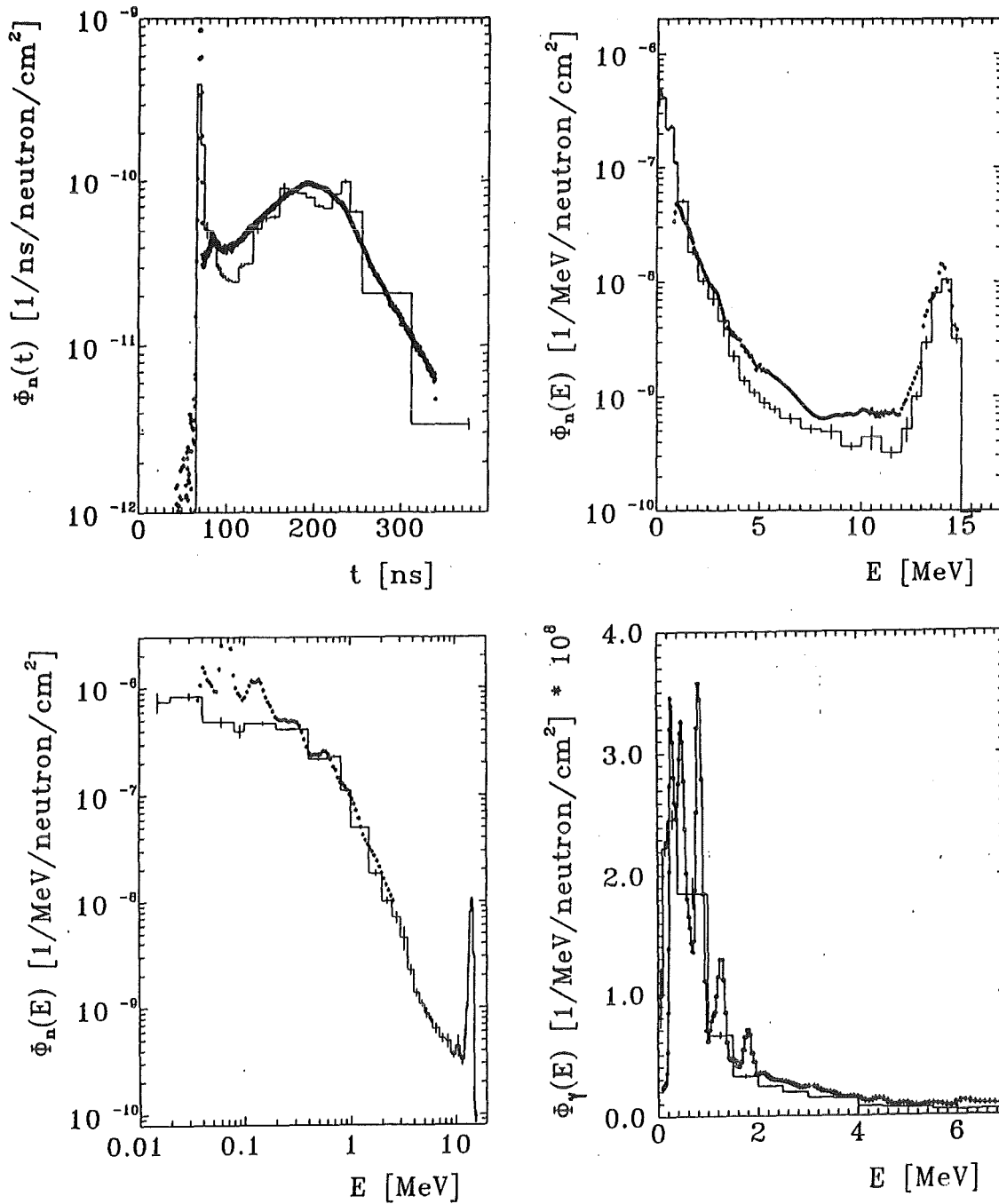


Fig. 2: Neutron and photon fluxes at the detector position normalized to one 14 MeV source neutron as function of energy and of time-of-arrival, respectively, for the assembly with gap at $x = 20$ cm and width $b = 5$ cm.

[6] D. Albert and W. Hansen: Auswerteverfahren zum Rossendorfer Rückstoßprotonenzählrohr-Spektrometer, Kernenergie 20 (1977) 95

[7] T. Elfruth, R. Schwier, K. Seidel and S. Unholzer: Measurement of Neutron and Gamma-Ray Spectra of a Shield Penetration Experiment, Progress Report on Nuclear Data Research in the Federal Republic of Germany, Period April 1992 to March 1993, edited by S.M. Qaim

[8] J.F. Briesmeister (Editor): MCNP - A General Monte Carlo Code for Neutron and Photon Transport, LA-7396, Los Alamos 1986

Staff:

W. Hansen
D. Richter
R. Schwier

K. Seidel
S. Unholzer
W. Vogel

Remote Handling / Maintenance

Introduction:

Due to the activation of most components of the NET /ITER basic machine, all operations of inspection, maintenance, connection and disconnection, assembly and disassembly will have to be carried out remotely from the very start of the physics phase. Hands-on or semi-remote maintenance will be possible only in limited areas and for some peripheral components.

The maintenance of the in-vessel components has been identified as a key problem. The preferred solution for NET and ITER (CDA) is the removal of divertor plates and protective tiles through equatorial ports by an articulated boom or an in-vessel vehicle and of blankets by a blanket handling device from top openings. The equipment for in-vessel maintenance will have to operate under extreme conditions of radiation and temperature. The large variety of operations to be carried out requires versatile and replaceable tools attached to different work units with large lifting capabilities. The high availability targeted by NET / ITER will require that in-vessel operations have to be carried out with relatively high speed.

Most of the KfK work concentrates on the development of an in-vessel handling unit (IVHU) with an articulated boom transporter (ABT) and different work units (task RHT 1). This system is primarily needed for the maintenance or replacement of in-vessel components during short term interventions.

The engineering design of the ABT has been completed (phase I of Subtask RHT 1-1).

The Experimental Device for In-Torus Handling EDITH is the prototype of this system (subtask RHT 1-2). It is required to demonstrate that the maintenance of plasma facing components can be carried out with the anticipated reliability and time. It is also needed to optimize the IVHU components and subassemblies and to test different control algorithms.

EDITH is a full scale ABT, supplemented by a full scale mock-up for divertor plate and protective tiles handling (subtask RHT 1-3) and a manipulator positioning unit (subtask RHT 1-4). The hardening of sensitive IVHU components for NET/ITER typical temperature and radiation levels is being performed in close cooperation with SCK/CEN Mol (subtask RHT 1-5).

Most of the work performed within task RHS 1 of the 1989-91 programme to standardize and qualify basic machine components for remote handling and to develop remote techniques to assemble and disassemble these items has been finished, e.g.:

- Electrical connectors (RHS 1-1),
- Pipe connectors (RHS 1-2),
- Fluid connectors (RHS 1-3),
- Welded connectors (RHS 1-4) and
- Welded vacuum lip seals (RHS 1-5).

In 1992-94 KfK concentrates its efforts on the development of cutting and welding tools for cryo-connectors (subtask RST 2-1, former subtask RHS 1-6).

Task RHB 1 (RH common subsystems) was started in 1992. The objective of this task is to develop different subsystems of common interest and specific applications in various tasks of the remote maintenance program.

Typical subsystems of this type are:

- A 3-D real time kinematic simulator (subtask RHB 1-1) and
- A RH workstation (subtask RHB 1-2).

The work for task RHB 1 is being performed in close cooperation between KfK and JRC Ispra.

A. Fiege

RHB 1 RH Common Subsystems

Subtask 1: 3-D Kinematic Simulator

The 3D kinematic simulator is intended as the basic simulation package for all major remote-handling tasks. This will require a wide range of functionality, including dynamics modelling, animated task simulation, task management and RH-user interfaces.

In task RHB 1-1, a study is being performed on requirements for kinematical simulation software available on the commercial market and from research establishments. The study concentrates on special requirements for fusion remote handling. The study is carried out in cooperation between KfK and JRC-Ispra. In the first period of the task, a requirements definition document was compiled. Apart from the requirements, the document additionally defines a list of possible candidates, test models and testing procedures.

Due to a change of personnel in the NET-Team and at JRC-Ispra, the requirements definition document (November 1992) was reopened for discussion and comments from the new personnel at JRC-Ispra.

A meeting took place at KfK on March 23rd 1993. It was agreed that the software candidates (CATIA, IGRIP, KISMET, ROBCAD) testing will be carried out at JRC-Ispra. The list of test models was shortened.

The development of the KfK simulation software KISMET (Kinematic Simulation, Monitoring and Off-Line Programming Environment for Telerobotics) during the first half year 1993 was highly influenced by new requirements from task RHB 1-1. Some of these new KISMET features are:

- User-friendly, MOTIF-like user interface, using panels, sliders and buttons.
- General inverse kinematics solution based on the Newton-Raphson algorithm, including the solution for kinematically underdetermined and overdetermined (redundant) mechanical structures. This allows for example cartesian control of 7-axis servomanipulators.
- Realtime multibody dynamics simulation, featuring direct (torque demand input, motion output) and indirect dynamics (motion input, required forces/torques output).
- Control system simulation, allowing for user-defined control structures.
- Simulation of elastostatic deformations due to weight, load and external forces.
- Elastodynamics simulation, allowing for deformable bodies.

Literature:

- [1] U. Kühnapfel, M. Becquet, RHB 1-1 - 3-D Kinematic Simulator Requirements Definition Document, Unpublished Report, Nov. 1992

Staff:

U. Kühnapfel
H.G. Krumm

Subtask 2: Remote Handling Workstation Development

The development of a Remote Handling Workstation (RHWS) for NET/ITER is based on a NET study contract whose results are documented in [1]. The development of workstation modules was started in other KfK projects and is now worked on under this task. The goal is to develop a general purpose support software tool which assists the remote handling operator during task preparation, training, and execution. The RHWS provides (1) the man-machine interface to the devices and the working environment and (2) operational aids supporting the operator in executing planned procedures correctly, controlling the devices, and working under spatial restrictions without direct view onto the scene. The RHWS [2,3] represents a multimedial handbook which is used off-line in the planning and training phase of work and which is connected to the device controllers during task execution. The RHWS leads especially to a homogenous man-machine interface and powerful operator support helping to minimize operator errors and maintenance time. The RHWS consists mainly of three components dedicated to the three operators' views onto the task:

1. KISMET (Kinematik, Simulator, Monitor, and programming Environment for Telem Manipulation) assists the operator with spatial representations of the work and the devices,
2. the DOIF-SS (Direct Operating Interface SubSystem) represents the device functions and assists the operator in controlling the devices,
3. and PEXOS (Procedure Editing, simulation, eXecution, and mOnitoring System) represents the working procedures to be performed (the multimedia handbook using also KISMET and DOIF-SS for presentation of different aspects of a procedure).

Based on KfK and KfK/JET cooperation experiences in the workstation field two documents were worked out which were discussed and are in discussion with the NET/ITER team and JRC-Ispra:

- the requirements definition document for a general purpose NET/ITER Remote Handling Workstation and
- the requirements definition document for a Remote Handling Workstation prototype. The purpose of RHWS prototype (RHWS-P) is to demonstrate the usability of key components or key subsystems in realistic experiments: EDITH and ROBERTINO. This means, the RHWS-P will be tailored to control two specific machines (EDITH and ROBERTINO), will be implemented on available hardware using available software, and its functionality will be reduced to key subsets, demonstrating the basic interfacing and controlling and the basic planning and simulation to demonstrate the cooperation of the RHWS subsystems and to demonstrate the basic support for the operator. The basic requirements will be fulfilled such that the RHWS-P could be enhanced step by step as needed to full functionality.

Major KISMET enhancements in the last year were: a new easily to use operating interface layout, an interface for using KISMET as a graphical master system to control directly the devices (using device model positions for move command generations), real time dynamics simulation, and an interface for simultaneous visualization of FEM calculation results.

The DOIF-SS manager coordinating the various application specific device operating panels was implemented and is being tested in different applications. This manager allows the definition of operator macros integrating different devices.

The first version of the PEXOS subsystem was finished which can describe a procedure network (consisting of work actions and states) by modified Petri nets with general and individual tokens (work resources). The graphical representation of the action/state network helps the operator to grasp more easily

the state of the work and allows to access multimedial information describing the work to be done by texts, drawings, photos, video sequences, audio output, graphical simulations by KISMET, and device panel explanations using the DOIF-SS (see Fig. 1). PEXOS also allows to start automated working sequences directly.

In the context of the remote handling procedure development at JET (using mock-ups e.g. for vessel port opening) a KfK delegate has implemented a JET specific camera DOIF-SS working together with KISMET. The mock-up experiments pointed out that KISMET support is indispensable. The procedure documentation was done in form of paperwork, an electronic multimedial support as provided by PEXOS together with KISMET is desirable, an application of PEXOS at JET is in preparation.

Literature:

- [1] Leinemann, K.: NET Remote Workstation, KfK-47852, Oct. 1990
- [2] Leinemann, K., Kühnapfel, U. Katz, F., Krumm H.-G., Olbrich, W.: KISMET based multimedia workstation for operational support in fusion plant remote maintenance. In: Ferro, Gasparotto, Knoepfel: Fusion Technology 1992, vol. 2, p. 1579-1583
- [3] Benner, J., Leinemann, K.: Supervision and automatic control of robotic systems in nuclear environments. Proc. 3rd Intern. Conf. on High Level Radioactive Waste Management, Las Vegas, April 12-16, 1992, pp.966-973

Staff:

K. Leinemann

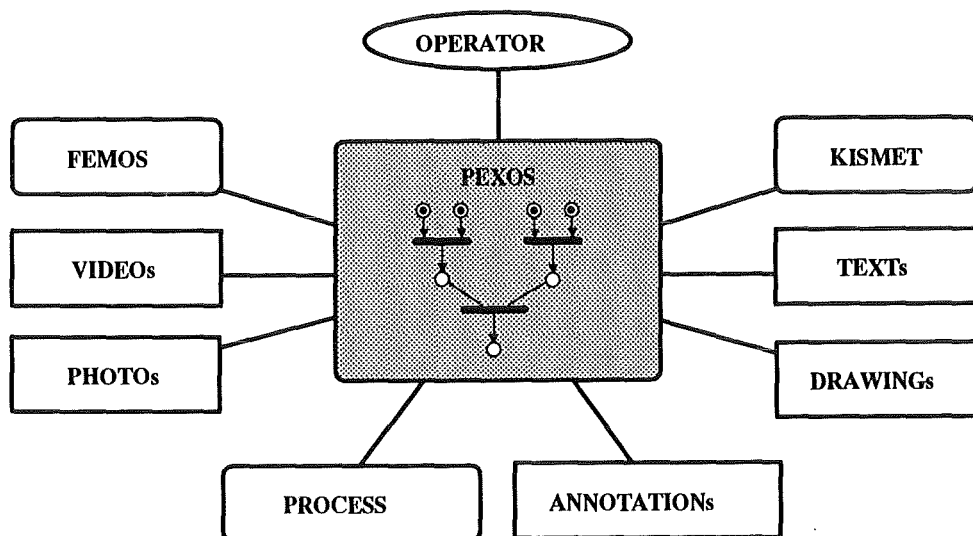


Fig. 1: PEXOS as interactive multimedia handbook/notebook. PEXOS represents the integrating workstation subsystem and the medium for task oriented information and services access.

RHT 1 Articulated Boom Transporter

Subtask 2: EDITH Prototype Articulated Boom

Aim of this subtask is the design, manufacture, testing and follow-up work of an articulated boom transporter (ABT) full scale prototype (EDITH) and a mock-up to perform NET/ITER-typical boom operating procedures and to demonstrate crucial maintenance operations (Figure 1) [1, 2, 3].

In continuation of the work performed during the last periods of reporting [4, 5, 6] the assembly and commissioning of EDITH was continued at the Remote Handling Laboratory of KfK. In addition the qualification tests are ongoing. The mock-up, representing a torus sector of the NET/ITER machine is finished and will now become prepared for tile handling. [7]

Mechanics

As to be seen in Figure 2 EDITH is composed of the support structure, four links, the endeffector-positioning unit (EPU), and an interim manipulator handling unit (MHU) to investigate e.g. armour tile replacement at the first wall.

The links are actuated by coaxial drive units which have undergone extensive measurements and some improvements, in particular with respect to their stiffness, before assembling them with the boom. Each drive unit has two redundant gear trains. Their motors are working in a

master/slave mode. The movement of the links is controlled by control components which give either position signals of the link joints to the position control system (multiturn resolvers) or stop the joints via the drive control system (limit switches) or mechanically if the other systems which have priority fail.

The front link of the ABT has been changed by eliminating the pitch and roll joints in order to simplify the link and to reduce its length and weight. The former task of these joints which was the compensation of deviations due to the dead weight of the boom and the payload will be overtaken, in case of using a MHU, by the roll joint of the manipulator positioning unit (MPU) and the MHU itself.

The EPU forms the permanently attached connection between the ABT and the end-effectors (Figure 2). It is required to reach the upper and lower torus regions and is based on a slide and trolley system. To achieve high position accuracy and repetitive accuracy, size and weight of the EPU were kept as small and low as reasonably possible by fabricating it as compact as possible and using for the large components an Al-alloy welded structure. Prior to its assembly with the ABT acceptance tests were performed externally. These included the validation of the stress analysis. The results were compatible with the computations. Further external load tests at the EPU and integral load tests with the ABT are ongoing in order to establish a data base for the

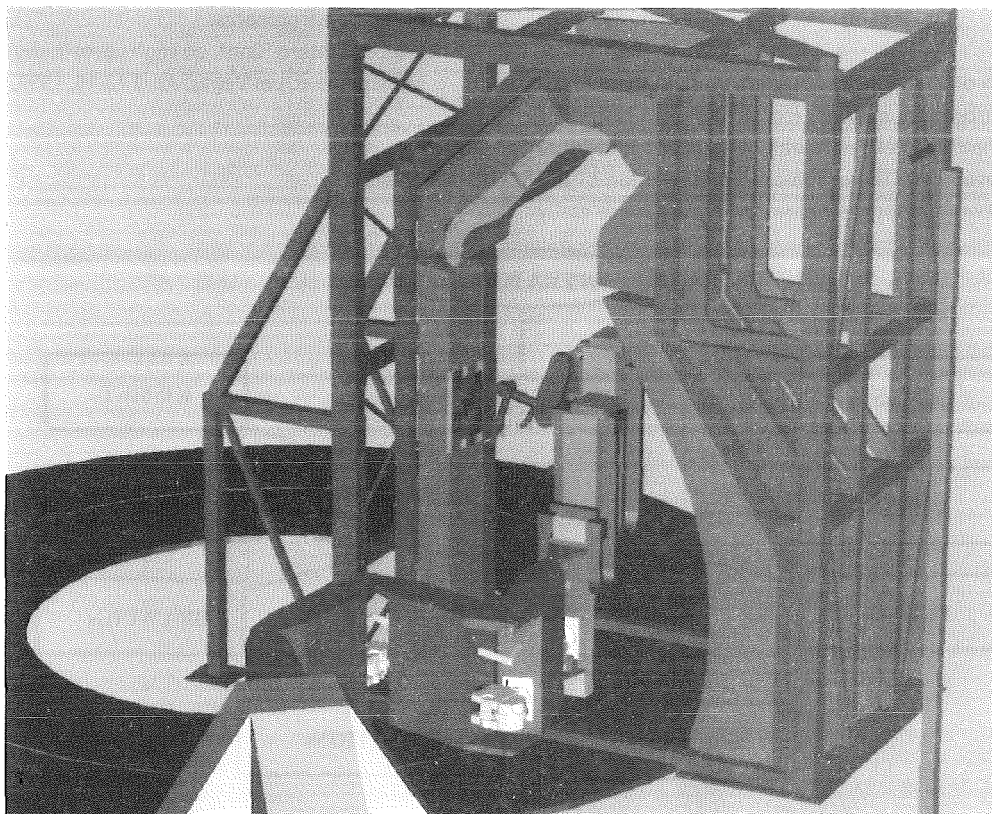


Fig. 1: Articulated boom replacing protective tiles located in the upper torus region of the mock-up

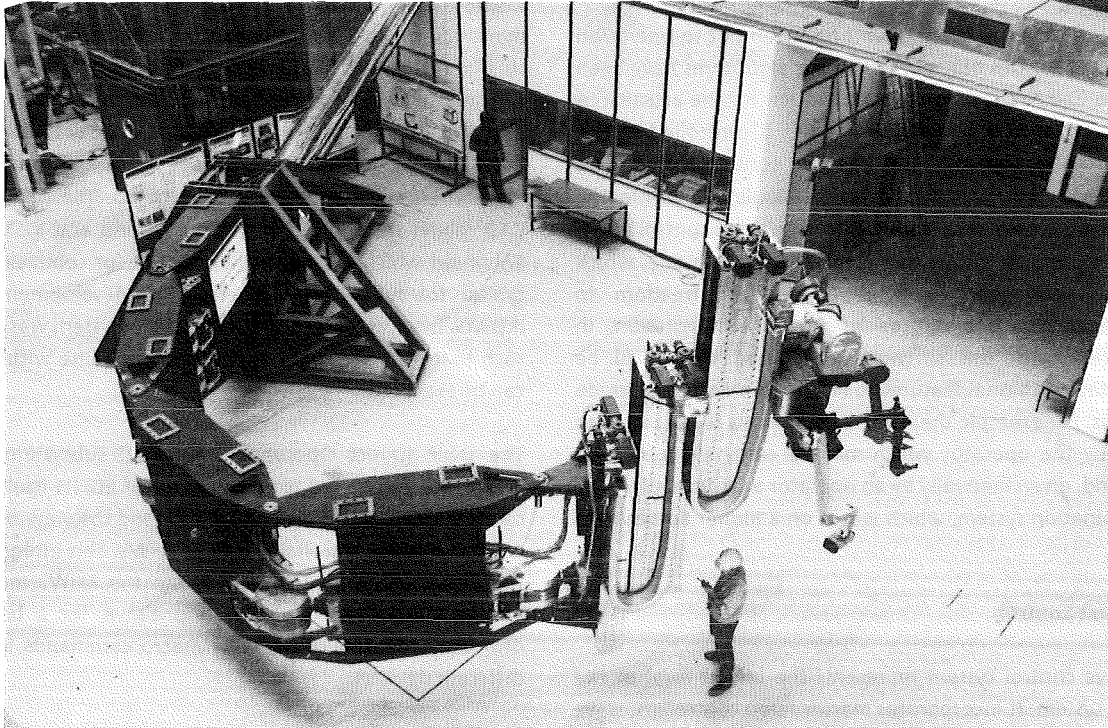


Fig. 2: Testbed EDITH with ABT, EEPU and attached MHU

control of the boom and here especially for the path planning.

The MHU, constructed as an interim solution for the demonstration of maintenance tasks in connection with EDITH is shown in Figure 3. It is composed of electric master/slave manipulators, available at KfK, which are connected by an adaptation unit to compensate the geometrical differences of the manipulators and allowing additionally a 180°-rotation of the MHU. Up to now the MHU is attached directly to the EEPU. Later on a manipulator positioning unit (MPU) will connect MHU and EEPU. Also the viewing system consisting of an overview camera and two camera systems for zooming the work site will be installed at the MPU. The latter ones are equipped with camera booms actuated electrically. They are already constructed and are made up of the subassemblies rotation unit, upper arm, forearm and swivel pitch head. They have four driven movement options. By means of one additional passive movement option the swivel-pitch can be kept in vertical position independently of the upper arm pitch. Until now the camera arms are mounted at the adaptation unit.

EDITH Motion Control System

Further tests of the motion control system (EMCS) have been processed. On the one hand the functionality of the control system itself has been tested. On the other hand tests have been carried out to destine the repetition accuracy of the articulated boom system. As result of these tests the specified repetition accuracy of 5 mm was confirmed. It was shown, that the point positioning error mainly depends on axis



Fig. 3: Interim manipulator handling unit with viewing system

positioning accuracy. Thus the improvement of axis positioning accuracy will also cause a better point positioning accuracy.

Integration of End-Effector Positioning Unit

The end-effector positioning unit has been put to operation with EMCS. For this only path planning algorithms have been implemented supporting resolved motion for the articulated boom part, as in a first step the EEPU is controlled in axis control mode. Actually the motion control software is adapted due to the demands of manipulation within the torus. So till end of 1993 it should be possible to control boom and EEPU simultaneously in a resolved motion mode, which supports movements with 3 degrees of freedom in positioning and one degree of freedom in rotation. In connection with this software adaptation there will be integrated additional features to ensure safe operation inside the torus. For example there will be soft limits for each axis to be set by the operator which may be easily changed by a command, given manually by an operator or automatically by an automation system, which works on a higher automation level.

Drive Unit Control

The drive control system represents the lowest level of the control system. It incorporates master servo controllers, slave servo controllers and electronic gear systems which are delivered, pre-tested and implemented. The servo controllers are based on standard controllers modified with some additional functions specified by KfK. Each servo controller includes the power amplifiers, the current controller, the electronic commutation, the speed controller and safety functions. One of these is monitoring directly the motor winding temperature and the controller heat sink temperature and limiting the peak torque available to prevent thermal overload.

Both master and slave motors are speed controlled. To prevent a mutual influence of both control loops due to mechanical coupling, the motion of the motors of each link is synchronized by a digitally controlled electronic gear. A second task of this device is the electric pre-loading of the mechanical part of the drive system to compensate mechanical backlash. Since the results of the according tests were successful electronic gears are not only applied at the ABT drive units but also at the drives of the EEPU.

Remote Handling Workstation

To support the tele-operator as flexible and complete as possible a general purpose remote handling workstation (RHWS) was developed and continuously enhanced (see task RHB1). The RHWS provides the man-machine interface and operational support functions based on spatial, functional, and procedural models of the work environment, the working devices, and the working procedures. In the context of this task the RHWS is applied to the EDITH project to assist the operator in in-vessel handling with EDITH [7,8]. Figure 4 shows the EDITH RHWS in the EDITH control room.

For the RHWS subsystem KISMET models of the EEPU, the tile handling unit, the KfK master-slave manipulators, the torus

mock-up, and the camera arms were developed or modified. KISMET now models also the bending of EDITH and the dynamics in real time enhancing the precision of the simulation. The KISMET simulation is actually used especially for design studies for tile handling and camera positioning. The procurement of a graphics/video overlay hardware for the KISMET video editor serving for easy and quick model verification and corrections was initiated. The software for CAD model transfer between CAD systems and KISMET was enhanced which is especially important for complex models typical for fusion environments. The development of an IRDATA interpreter for the EDITH control system was finished such that motion programs developed off-line with KISMET can be executed.

The DOIF (Direct Operating Interfaces) subsystem of the RHWS was completed for the control of EDITH itself and its camera/video system such that EDITH and the viewing system are completely controllable via the RHWS. This integration of the direct device control panels into the RHWS makes the interface more homogeneous and allows for a better co-ordinated usage (e.g. operator macro commands including different devices).

The RHWS subsystem PEXOS representing the work procedures for operator instruction and assistance and for task oriented co-ordination of hardware and software tools usage is ready for use including an enhanced more compact modelling technique ("individual tokens"). PEXOS allows for a structured multimedia description and simulation of work sequences by a network of actions and working states which is graphically visible for the operator and which provides access to the working step related information. Figure 4 shows the three computer displays for the three RHWS subsystems (procedures, device control panels, working scene graphics) and a group of video monitors. Video images can also be displayed on the computer screens in separate windows. The working place will additionally be equipped with the master arms of the master-slave manipulators. The master-slave manipulator operator will have available a variable subset of the workstation information on separate screens. The modelling of procedures that means the input of task specific data into the PEXOS database was started.

Dynamic Simulation

The AMBOSS dynamic simulation has been set up to examine critical remote handling tasks and to optimize control algorithms. Multibody dynamics of the transporter system are modelled utilizing the commercial analysis package ADAMS. A precise dynamic actuator model including backlash and static friction is introduced by applied forces, spring elements and differential equations [9].

Elastic deformation and structural oscillations are described by a six dimensional linear force deformation dependency. Stiffness matrices of the main links are extracted from FEM calculations [10]. Support structure and end-flange are modelled with similar estimated values.

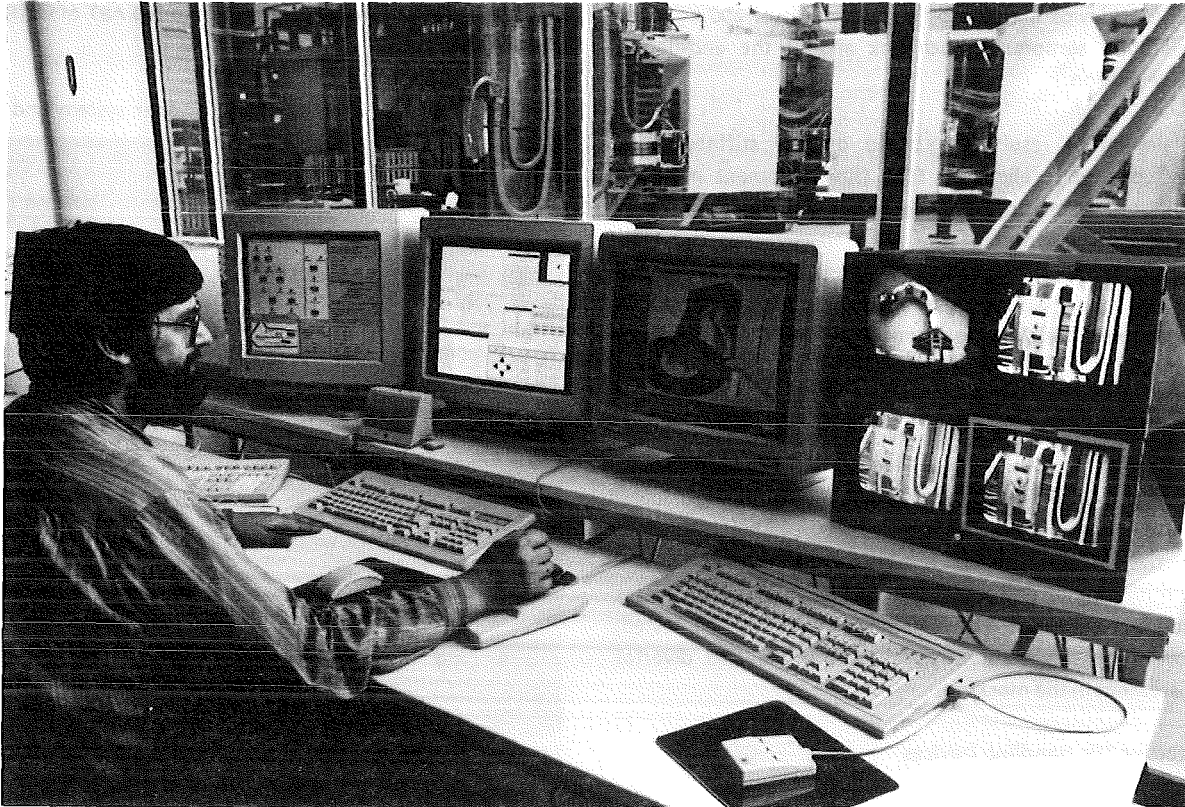


Fig. 4: EDITH remote handling workstation

The last working period concentrated on the verification of the structural model. Figure 5 compares static deformations

from a static simulation with those measured with the GMS-Laser theodolite system at the EDITH device. For the dynamic

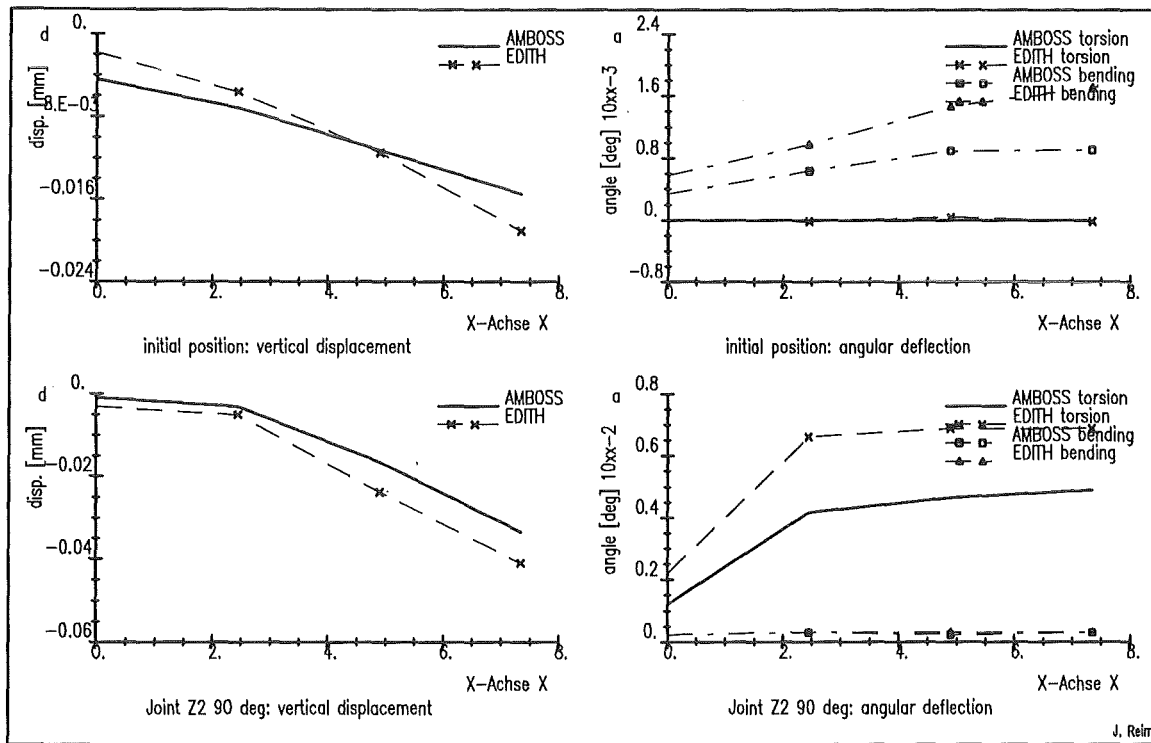


Fig. 5: Static deflections in simulation and experiment

case Table 1 shows the natural frequencies. In the experiment the EDITH device is excited by a sudden loss of 200 kg load. Acceleration sensors on each link and at the end-flange observe motion.

The simulation results are based on the stiffness data extracted from preliminary FEM (finite element method) calculations. Rising differences between experiments a rather low torsional stiffness of the links. Nevertheless the high accuracy of the preliminary calculated results prove the AMBOSS model structure and accuracy. Simulation in bowed boom positions point out that the FEM calculations assumed

Subtask 3: Divertor Plate and Armour Tile Handling

Objective of this subtask is the design, production and commissioning of protective armour tiles and divertor plates handling equipment. The equipment will then be tested, followed by the demonstration of the tile and divertor replacement in the mock-up.

Protective Tile Handling Devices

In agreement with the NET team two prototype devices were designed and fabricated for the replacement of protective armour tiles, a tile positioning device (TPD) and a tile detachment device (TDD). The TPD allows to grip a new tile from a magazine, to bring it to its position and to fix it there. With the TDD a damaged tile can be gripped, the fixation bored free and the tile removed. Both devices are handled by electric master/slave manipulators.

The TPD is composed of the gripper system and the screwing unit which allows the locking of the two tile fixation nuts simultaneously. The gripper system is based on a toggle lever system and actuated by a lifting magnet. To avoid uncontrolled unlocking the gripper is always closed in the currentless status. The two drivers of the screw driver units are actuated via spur wheel gears and a worm gear by a common electric motor. The torque of the drive unit is limited by slipping clutches. Experiments with the TPD were carried out on tile dummies mounted at a vertical wall as well as at a tilted wall. The tests showed satisfying results after an adjustment of the fixing elements according to the positioning accuracy of the master/slave manipulator. Additionally, the most suitable viewing and lighting positions

were determined. The tests will be continued by handling the device by means of the MHU attached to the ABT of EDITH in the mock-up.

The TDD (Figure 6) consists of the gripper system and the

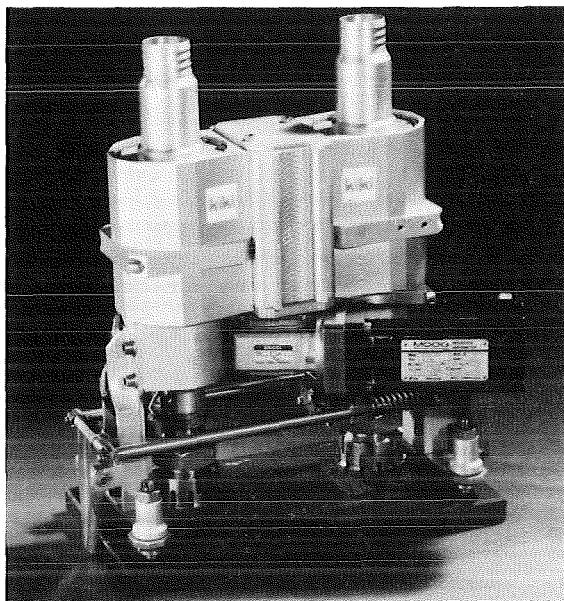


Fig. 6: Tile detachment device with gripped tile dummy

trepan system. The gripper is cam controlled via the feed motion of the spindle. During drilling the gripper can not be unlocked. The drill spindle positions are controlled by limit switches. The tubular drills are actuated by a common electric drive via a worm wheel gear and spur wheel gears. The feed motion of the diamond drill and the sintered carbid drill, respectively, is proportional to the drill spindle revolutions. The TDD is delivered. Experiments for drilling CFC-tiles and the suction of the drilling dust were launched.

Divertor Plate Handling Unit (DHU)

According to the NET task definition forms the work at the prototype devices for the divertor plate handling is postponed until a clarification of the ITER divertor design and maintenance concept.

Position		Z1-Z4: 0 deg	Z4 90 deg	Z3 90 deg	Z2 90 deg
EDITH experiment	1. Mode	4.2	4.4	4.0	3.5
	2. Mode	14.3	12.8	10.2	12.7
AMBOSS model	1. Mode	4.24	3.9	3.0	2.6
	2. Mode	14.9	14.9	11.7	10.5

Table 1: Natural frequencies [Hz] in simulation and experiment

Subtask 4: Manipulator Positioning Unit

To guarantee sufficient manoeuvrability of the MHU a manipulator positioning unit (MPU) composed of an additional link with electrically driven yaw joint was designed and specified for a call for tender to be accomplished by NET. Due to the fact that the order is suspended the MPU will not yet be available in 1992. In order to allow anyway first tile handling tests in the mock-up a simplified device was designed and is prepared for fabrication. It consists of one yaw joint similar the later MPU and is manually adjustable relatively to the working position.

Subtask 5: Pre- and Post Irradiation Testing of Boom Components

Motors, Lubricants, Cables

Based on the irradiation and the post-irradiation examinations of basic components for motors, the irradiation tests MOL F2-1, MOL F2-2, MOL F2-2/2 and the following qualitative post-irradiation examination of the motor components [11], weak points were identified. These are mainly:

- The fail-safe brake due to temperature sensitivity.
- Cables with respect to temperature and gamma irradiation sensitivity.
- Lubricants due to temperature and gamma irradiation sensitivity.
- Ball bearings with respect to temperature.

Due to the occurred difficulties during the irradiation, on-line measurements as foreseen in the test-specification were not always possible and also only a qualitative post-examination was useful. On the basis of the visual inspection after the irradiation and in connection with the good results of the irradiation tests at basic components, the motors are undergoing a modification at the suppliers followed by a further irradiation campaign end of 1993. The modifications are listed hereafter:

- The previous ball bearings will be substituted by special high temperature bearings. Their delivery time is the driving factor for the time schedule of the second irradiation campaign of motors.
- The original motor resolvers will be replaced by another type to become independent from the resolver supplier.
- The connection cables of the motors and resolvers will be substituted by KAPTON cables.

- At the fail safe brakes the cable inlets and outlets will be modified as well as the inlets and outlets at the windings and the motor housings.

Before an irradiation of the motors in a following campaign, the no-load current and no-load speed will be measured to check whether the motor characteristics have been changed by replacing components, which is not to be expected. If the characteristics will have been unchanged, the motors will be irradiated and the post-irradiation quantitative measurements will be evaluated on the basis of the original pre-irradiation tests. Otherwise the pre-irradiation tests will have to be repeated.

Resolvers:

The gamma hardening activities were successfully continued with temperature and irradiation tests for new insulation plastics of cables and thin copper wires to be used with a couple of modified resolvers. By a mechanical post-irradiation inspection of two multiturn resolvers having failed formerly in 1992 it turned out that, contrary to earlier experiences, their solder material being used for the electrical connections was partly corroded and the RADOX insulated wires showed defective insulation areas due to their mechanical twists and associated stresses.

As a consequence, two more still available and identically made but not yet irradiated resolvers are now going to become modified and, in order to fit the irradiation requirements will be equipped with thin KAPTON insulated wires instead of RADOX. Moreover, a flux-free tin-lead solder will come in use which has been successfully tested by two preceding irradiation campaigns.

The irradiation test is scheduled for September 1993 after the receipt of the named resolvers with modified stator elements from the supplier.

Inclinometers:

By an intermediate gamma irradiation campaign performed in February 1993 which reached an integral gamma dose of 80 mega rad, a ceramic film potentiometer, type 50ESA59318 - 5000 Ohms from PEWATRON, was irradiated at 70°C constant gamma heating temperature. From a subsequent investigation it could be shown that all mechanical and electrical parameters remained fully unchanged and from there, the continuation of the irradiation up to 1 giga rad is justifiable and seems to be hopeful.

Plastics:

A series of polyamide and polyethylene derivate wire insulating plastics, all available in form of highly polymerised 0.6 to 1 mm thick cladding became irradiated for the first time in March 1993. During a 1 giga rad gamma campaign insulating samples of NORYL, ULTEM, SILTEM, ARNITEL and a

NORYL/PEEK composition were gamma exposed in the BR2-reactor at Mol/Belgium.

The post irradiation analysis and testing is underway for the time being and final results are anticipated for the second half of 1993.

Literature:

[1] Suppan, A., et al.: The NET Articulated Boom: Preliminary Investigations and Justification for a Full Scale Prototype. KfK 4809, December 1990

[2] Kast, G.: Nuclear Fusion Project - Semi-annual Report of the Association KfK/Euratom - April 1989 - September 1989. KfK 4677, EUR 11397 EN, November 1989

[3] Suppan, A., et al.: EDITH - A Prototypical Boom System for NET/ITER. In: Ferro, Gasparotti, Knoepfel: Fusion Technology 1992, Proceedings of the 17th Symposium on Fusion Technology, Rome, 14-18 September 1992, Vol. 2, p. 1599-1603

[4] Kast, G.: Nuclear Fusion Project - Annual Report of the Association KfK/Euratom - October 1989 - September 1990. KfK 4774, EUR 13151 EN, September 1990

[5] Kast, G.: Nuclear Fusion Project - Annual Report of the Association KfK/Euratom - October 1990 - September 1991. KfK 4944, EUR 14015 EN, October 1991

[6] Kast, G.: Nuclear Fusion Project - Annual Report of the Association KfK/Euratom - October 1991 - September 1992. KfK 5099, EUR 14795 EN, October 1992

[7] Suppan, A., et al.: Experimental Device for In-Torus Handling - EDITH, Intermediate Report, KfK 5252, August 1993

[8] Leinemann, K., Kühnapfel, U., Katz, F., Krumm, H.-G., Olbrich, W.: KISMET Based Multimedia Workstation for Operational Support in Fusion Plant Remote Maintenance. In: Ferro, Gasparotti, Knoepfel: Fusion Technology 1992, Proceedings of the 17th Symposium on Fusion Technology, Rome, 14-18 September 1992, Vol. 2, p. 1579-1583

[9] Reim, J.: Dynamic Simulation of the NET In-Vessel Handling Unit, Fusion Engineering and Design 18 (1991), p. 471-476

[10] Krieg, R.; Wehner, E.; Hübener, J.; Suppan, A.: Design and Optimization of an Articulated Boom for the NET In-Vessel Handling Unit, Structural Mechanics in Reactor Technology: Transactions of the 10th Int. Conf., Anaheim, Calif., Aug. 14-18, 1989, Vol N, p. 91-96

[11] Suppan, A., Rahn, A., Englert, M.: Gamma Irradiation Tests with Motors for the NET/ITER In-Vessel Handling Equipment, Unpublished report, July 1993

Staff:

- J. Bernert
- H. Braun
- G. Dillmann
- B. Dolensky
- B. Haferkamp
- R. Heeg
- W. Hennhöfer
- W.E. Hörl
- J. Hübener
- H. Knüppel
- H.-G. Krumm
- W. Köhler
- H.-G. Krumm
- U. Kühnapfel
- K. Leinemann
- W. Link
- A. Ludwig
- G. Müller
- W. Müller
- W. Olbrich
- A. Rahn (KfK-AG Mol)
- J. Reim
- H.A. Rohrbacher
- M. Salaske
- U. Schygulla
- A. Suppan
- J. Woll

RST 2 Cutting and Welding Tools

Subtask 1: Tools for Cryoconnectors

The objective of this subtask is the commissioning of the cryogenic prototype connectors, the design and preparation of a set of specifications suitable for procurement of the prototype tools as well as of auxiliary equipment required for the remote disassembly/assembly of the connectors, the technical assistance in supervising the procurement (done by NET through industrial contract), and the follow-up commissioning and testing of the prototype tools.

In continuation of the work performed during the last period of reporting [1] the cryogenic prototype connectors were delivered and mounted at the FEROS test facility. The assembly and disassembly procedures were performed hands on under simulated remote handling conditions.

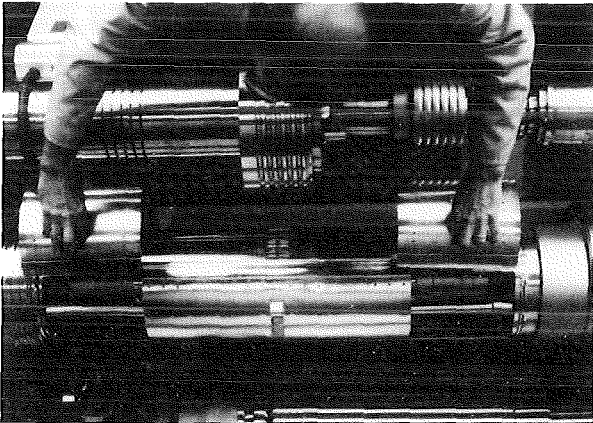


Fig. 1: Cryogenic prototype connector assembly/disassembly tests

The control and monitoring system of the FEROS test facility has been modified for the procurement, follow-up commissioning and testing of the prototype tools.

The CCD camera system design for the visualization of the welding process has been modified with respect to a better resolution, reliability, increase of the scale of magnification and reduction of the overall dimensions.

The new design will be implemented in the prototype welding tools.

Each weld of the cryogenic connectors is carried out in two passes to obtain a better final external surface and to facilitate a follow-on nondestructive examination (NDE) of the weld.

The NDE will be carried out by bringing into contact the NDE probe, placed on the orbital carriage, with the weld. Two NDE methods are under investigation: eddy current and ultrasonic testing.

The general design and the implementation of the NDE probes into the welding heads has been investigated. The expected maximum free space and overall dimensions of the probes have been considered for all three welding tools. The detectable sizes of defects as well as the designs of the calibration blocks and test samples have been determined.

The test specimens have been manufactured. The test program has been finalized. The placement of the probes in the orbital carriage of the welding tools has been determined.

For the present cryoconnector assembly/disassembly design a set of ten tools is proposed.

Three different families of tools are earmarked for carrying out the cryoconnector replacement cycle [2]:

- cutting tools (a total of three for the diameters 24, 50-160, 300 mm),
- welding tools (a total of three for the diameters 24, 50-160, 300 mm),
- clamping/aligning tools (a total of four: one to clamp the 300 mm pipe before welding, one to handle the 300 mm sleeve, one to handle the assembly of sleeves 50-160 mm to be replaced, one for bellow clamping, only for flexible connectors).

The design, the tool design description and the call-for-tender specification of the set of ten tools has been completed and submitted to NET along with a set of drawings for documents and preparation of the tool procurement.

Literature:

- [1] Kast, G., Nuclear Fusion Project, Annual Report of the Association KfK/Euratom, October 1991 - September 1992, KfK 5099, EUR 14795, October 1992.
- [2] Ferro, C., Gasparotto, M., Knoepfel, H., Fusion Technology 1992, Proceedings of the 17th Symposium on Fusion Technology, Rome, Italy, 14 - 18 September 1992, Volume 2, pp. 1574 - 1578.

Staff:

R. Gaa
L. Gumb
P. Heilmann
H. Krause
A. Schäf
M. Selig
D. Stern

Safety and Environment

Introduction:

Within the European Fusion Technology Programme 1992-94 the safety analyses for NET/ITER which are being performed in parallel to the design efforts address mainly two different areas:

Safety Assessment Studies

- Operational Safety (SEA 2)
- Reference accident sequences (SEA 3)
- Probabilistic risk studies (SEA 4)

and

Plant Related Studies

- Radioactivity inventories and source terms (SEP 1)
- Environmental impact of tritium and activation products (SEP 2)
- Waste management and decommissioning (SEP 3)

The KfK contributions to this program concentrate on:

- Analyses of reference accident sequences in superconducting magnets (subtask SEA 3-2),
- Identification and characterization of tritiated organic compounds in fusion devices (subtask SEP 1-3), and
- Calculations of individual and collective doses to the public for routine and accidental releases of tritium and activation products (subtask SEP 2-2).

A. Fiege

SEA 3 Analysis of Reference Accident Sequences

Subtask 2: Magnet System Safety

Within the subtask 3.2 KfK investigates the thermal and mechanical behaviour of magnet systems during accidents.

During the period reported here the validation of the MAGS [1] system was started. In this context some improvements have been introduced and some supplements have been added to the system. In terms of accident analysis calculations for the European SEAFP Study have been performed.

a) Thermal analyses for the magnet system

The EFFI module of MAGS was extended to provide also data blocks for forces and inductances. The former can be used as input for ABAQUS, the latter can be passed to a small module to compress the full inductance matrix according to the requirements of a special circuit analysis. Additionally a new module named HEXAN has been prepared. This module determines the quench front propagation along a conductor using a simple analytical formula instead of solving the balance equations of mass, momentum and energy for the helium coolant. The use of HEXAN reduces the precision of the results, however, the turn around time for a job, being only about 1% to 2% percent of a full analysis, allows parametric analyses almost impossible otherwise. This updated MAGS code system has been presented at the IAEA Fusion Safety Technical Committee Meeting in Toronto [2]. To include also the coil case into the MAGS analysis a mesh generator for the coil casing has been developed.

Concerning the validation of MAGS two efforts have been made. One is a comparative analysis to the computer code SARUMAN [3] and the other is the analysis of a conductor to conductor transversal quench propagation observed at the European coil in an LCT experiment in Oak Ridge.

The comparison with the SARUMAN code showed that the results are similar. SARUMAN needs less computing time but has also less detailed results compared to MAGS. For accident analyses which is the area of application for MAGS more detailed results are required and a higher computer effort seems to be justified.

The recalculation of the LCT experiment with the European coil has been done with great care and will be presented in a separate report. For the presentation here it can be stated that the analysis was successful and that the hydraulic conditions in the supply lines of the helium outside of the coil have great influence on the results. To illustrate the analysis in Fig. 1 a temperature relief plot is given. The data are plotted over the coil cross section analysed. One can see that the pancakes have a different number of turns. The temperatures of the shorter pancake are only slightly disturbed, in the longer, however, they are beyond the critical temperature of 7.5 K in the first and the second turn. As the

coil is made with two conductors in hand the figure shows that a transversal quench propagation has taken place.

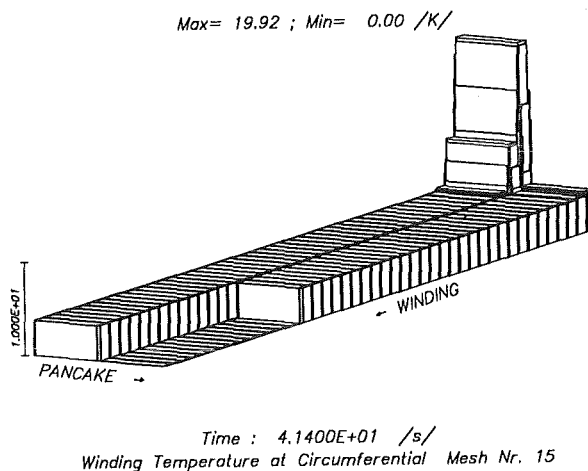


Fig. 1: Temperature relief plotted over the LCT coil cross section analysed. The pancakes have a different number of turns. In the longer pancake the temperatures are beyond the critical value of 7.5 K in the first and the second turn. As the coil is made with two conductors in hand the figure shows that a transversal quench propagation has taken place.

The analyses for the SEAFP task are reported every three months to the NET-Team [4]. The SEAFP design has much larger TF coils than the magnet systems proposed so far for NET/ITER. The stored energy of the system is now about 200 GJ compared to 40 GJ in the former designs. A basic question for the safety of the system is the expected temperature ramp in a coil in case of an unprotected growing quench. The analysis was done using the new module HEXAN. Fig. 2 shows the temperature of the hottest spot in a pancake versus time. From the figure one can see that it takes about 150 s to reach the failure temperature of the insulation of 600 K. This is roughly ten times longer than for the old designs. This shows that even though the stored energy is larger, there is more time for safety systems to cope with the problem.

b) Analysis of the mechanical behavior of the coil casings under accident conditions

The results gained for the NET/ITER design, reported in [5] have been presented at the 17th Symposium on Fusion Technology in Rome [6].

Similar studies have begun for the European SEAFP Study [4]. The SEAFP reactor design is roughly an enlarged NET design with a scaling factor of about two. Although the design is not very detailed yet the mechanical structure of the magnets seems to be very similar to the NET device. The work performed so far is concentrated on both the stability of the central vault under TF-coil fault loading and the possibility of missile generation caused by mechanical failure of the magnet structure.

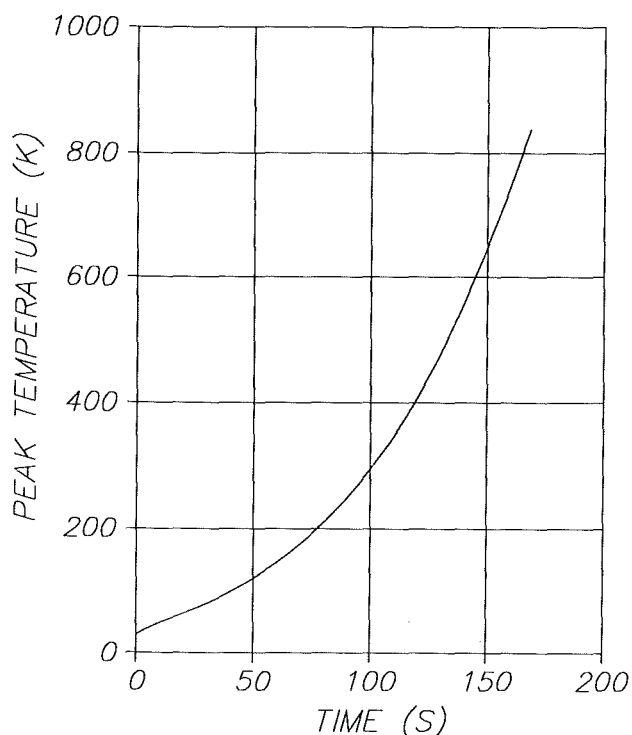


Fig. 2: Temperature in the hottest spot of a SEAFP TF coil during an unprotected growing quench.

The most critical part of the coil structures under fault loads for the NET design [6] was the central vault. This vault is composed of the wedge shaped inboard legs of the TF coils. It is well suited to bear high axisymmetrical loads without additional interlocking between the individual coil legs. But non-axisymmetrical loads, as produced by faults in the TF-coils, lead to bending moments which try to deform the circular arch. Since the interface between the neighbouring coil legs do not allow for transmission of tensile stresses, gaps may open leading to instability of the central vault.

Calculations have been performed for a) an electrical short at the busbar of a TF-coil during a fast discharge and b) a discharge of a coil due to a sequence of faults while all other coils remain charged.

In both cases considered circumferential tensile stresses occur at the wedge interfaces, leading to gaps and subsequent instability. Even the use of shear keys at the upper and lower end of the vault would not guarantee a global vault stability. Therefore an interlocking device along the individual coil legs forming the central vault will be needed, as required in the earlier ITER design. The actual design, however, does not contain such details.

The safety analysis of large magnet systems has to consider the possibility of missile generation. One source could be a mechanical failure which results in a loose fragment accelerated in the strong magnetic field. A realistic modelling of the mechanical and electro magnetic processes leading to a missile would be rather complicated. Therefore in a first step limiting cases with some hypothetical assumptions were

treated to estimate whether a missile generation could be possible.

The results of this study are summarized in [4].

It was shown that the formation of missiles and the resultant damage of neighbouring structures can be excluded for the actual design of the SEAFP magnets.

This has to be checked for future more advanced designs. Also dynamic effects and large displacements of the moving arch will have to be taken into consideration.

Literature:

- [1] R. Meyder
MAGS: A code system to analyse 3D thermal failure propagation of a forced cooled superconducting coil. KfK Unpublished Report, May 1992
- [2] G. Bönisch, G. Hailfinger, R. Meyder
MAGS: A computer code system to analyse the 3d quench propagation in forced flow cooled superconducting magnet systems. IAEA Technical Committee Meeting, Toronto, June 1993; to be published in Journal of Fusion Energy.
- [3] L. Bottura
Quench analysis of superconducting magnets. A numerical study. The NET Team c/o Max Planck IPP, Boltzmannstr. 2, D-8046 Garching, October 1991.
- [4] R. Meyder, S. Raff
SEAFP Task A5, Magnet System Safety Analysis, Unpublished report, June 1993
- [5] Contribution to Nuclear Fusion Project Annual Report of the Association KfK/Euratom, October 1992, KfK 5099
- [6] S. Raff, Y.S. Hoang, R. Krieg
'Investigations concerning the mechanical integrity of the NET/ITER coil structure under fault conditions' Proc. of the 17th Sympo. on Fusion Technology, Rome, September 14-18, 1992, Vol. 2, p. 1754-58, Amsterdam, North Holland, 1993

Staff:

- G. Bönisch
- B. Dolensky
- G. Hailfinger
- Y.S. Hoang
- R. Krieg
- S. Kuhn
- R. Meyder
- S. Raff

Proposal of a Concept and Reliability Analysis for a Magnet Protection System

The unavailability for the current switch down in case of a demand in the magnet coils of a fusion demonstration plant must be decreased by a few orders of magnitude as compared to the one of experimental facilities. The safety requirements to prevent initiation of event sequences which might lead to the release of energy and radioactivity by the plant must be fulfilled with the same standards as applied in a nuclear fission power plant. On the basis of this proven technology a general usable magnet protection system will be proposed, which achieves some considerable improvements by the use of an additional microprocessor supported system in the failure detectability as compared to the conventional protection systems [1]. The principle is given in Fig. 1.

One of the plant variables for quench detection in a super conducting magnet system is the current in the conductor coils. This current will be permanently monitored by detectors. The resulting analog signals will be processed in redundant analog processing units. Independent single failures in the measuring and in the processing channels will be supervised by comparators arranged between the redundant channels.

In this arrangement each channel is controlled by two comparators. The individual signal is also surveyed by limit values. In case of exceeding a limit value an initiation signal is transmitted to the logic part of the system. The analog part of the signal processing is identical to the conventional

protection system according to KTA 3501. The advantage is, that the essentially fix wired system possesses a very low unavailability in the order of magnitude of 10^{-7} per demand. The disadvantage is, the system is only able to supervise minimum or maximum values, respectively. The values could also represent gradients or values dependent on other parameters, but it is always a single value. The necessary precautions against the Common Mode situation are very demanding and mainly based on administrative precautions and an extensive quality assurance.

The advantage of the protection system compared to the conventional systems is the improvement in the failure detectability. Unavailability values $\leq 10^{-9}$ per demand are achieved. New in the present system is the on-line testability of the measuring chains including the sensors and the high safety against Common Modes. The on-line test is based on the assumption that the sensor signal level is known and can be tested during each shut-down and during the operating phase. The high reliability for the initiation of a safety action is based on the proven classical technology. The improvements in the failure detectability will be achieved by combination with a microprocessor supported digital system. The transfer of safety functions to the digital microprocessor system is not considered here. According to the current safety regulations as valid in the nuclear fission power plants this would not be accepted due to problems in the proof of digital systems reliability. This might change, however, in the future.

The protection system was designed to cope with the quench of superconducting coils. But it is quite obvious, that the basic

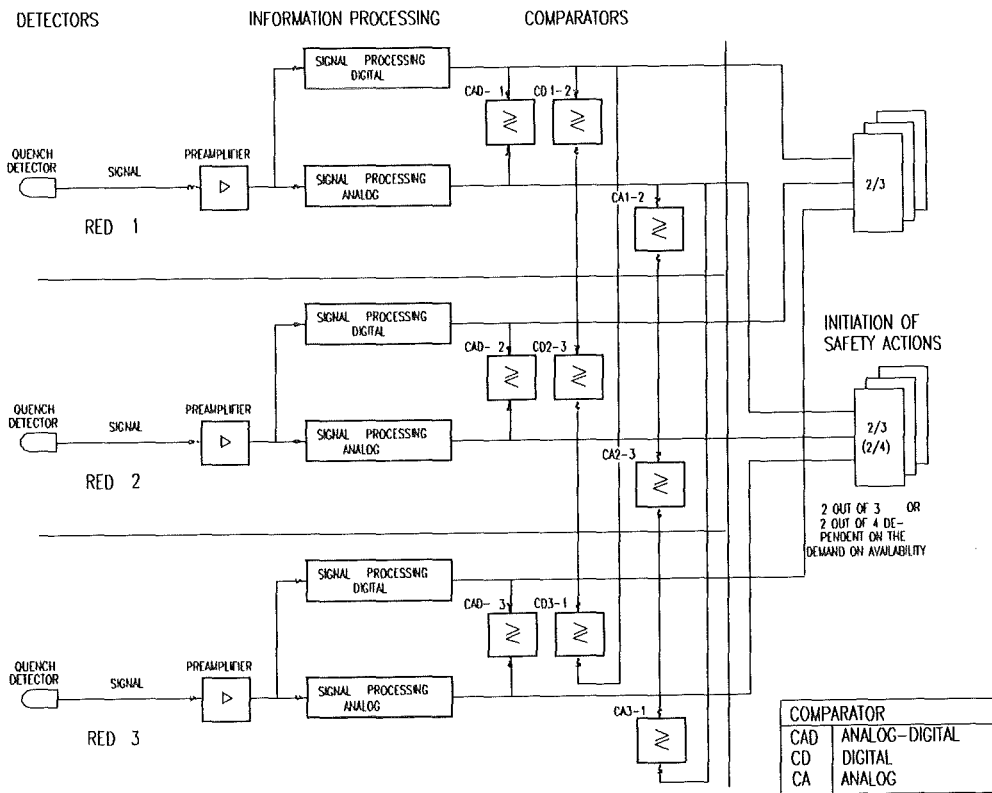


Fig. 1: Protection System for a certain initiation criteria (quench)

concept of the system is also applicable for initiations of safety actions in general in a fusion power plant.

Literature:

- [1] H. Schnauder, E. Pamfilie; Proposal of a concept and reliability analysis for a fusion plant magnet protection system, KfK 5192, Mai 1993

Staff:

H. Schnauder

SEP 1 Radioactive Inventories and Source Terms

Subtask 3: Tritiated Organic Compounds

Source terms of organic and/or inorganic tritiated species that escape from facilities operating with tritium need to be evaluated for the safety analysis of these installations. To possibilitate the calculation of doses the tritiated compounds have to be identified and the sources quantified.

In a first literature survey an attempt was made to identify the tritiated species that may be released into the environment during normal or accidental operation of tritium handling facilities. Particular attention was focused on facilities related to the fuel cycle of a fusion reactor. More than 110 publications from the literature were examined and evaluated.

An important source of a variety of tritiated compounds are the products from the interaction of atomic hydrogen, energetic hydrogen ions and combinations of these with graphite, the classical first wall protection material of a fusion reactor. In numerous laboratory studies on the interaction of hydrogen radicals and ions with carbon it was observed that besides methane - the main product - other saturated and unsaturated hydrocarbons with up to eight carbon atoms are produced in lower yields. The relative product distribution observed in laboratory experiments when hydrogen atoms and ions react with carbon is similar to that measured in the exhaust gas of JET. The total amount of products and their relative distribution changes drastically when the graphite in the torus is covered by beryllium. From this it is clear that the chemical composition of the first wall will have a significant impact on this source term. Hydrocarbons of high molecular weight can have a high specific tritium concentration. They can accumulate in components working on a cryosorptive basis. Depending upon their tritium content, they can undergo radiochemical reactions that give rise to new gaseous, liquid and solid products.

Because much work has been published on the reactions of tritium with other single gases as well as on the self-radiolysis of certain tritiated compounds, the first survey concentrated on these simple radiochemical systems.

In the presence of oxygen tritium gives rise to water and to the intermediate species T_2O_2 and O_3 . The steady state concentration of O_3 , a very reactive compound, is proportional to the concentration of tritium to a power of 0.6. The self radiolysis of tritiated water is enhanced by such gases as CO, CO_2 and N_2 . Certain adsorbers are capable of accelerating the self radiolysis of water.

The reactions between tritium and carbon monoxide are complex. They can take place whenever tritium and CO are stored together. The products include numerous oxygen containing saturated and unsaturated hydrocarbons as well as water etc. Among the oxygen containing compounds formaldehyde, acetaldehyde, methane and methanol can be cited as main products. Smaller amounts of higher molecular weight aldehydes, alcohols, and organic acids and their derivatives, cyclic ethers have also been reported. In mixtures containing relatively small amounts of CO two types of not well identified polymeric solids are formed. The product distribution, which is a function of the partial pressures of the reacting gases can be influenced by additives such as ammonia, methane or oxygen. Several adsorbers have been observed to catalyse the reaction between tritium and carbon monoxide.

The self radiolysis of carbon dioxide tritium mixtures yields CO, CT_4 , C_2T_4 and T_2O as well as a white carbonaceous polymer.

Tritium is capable of inducing reactions with hydrocarbons. Not only isotopically exchanged molecules are formed but also higher olefinic and saturated tritium substituted hydrocarbons. As is the case with other radiochemical reactions, certain adsorbers enhance the reactions and influence the product distribution.

The main product of the reaction of tritium with nitrogen is ammonia. In the presence of moist air highly corrosive nitric acid is rapidly formed.

In the future more attention will be directed towards the radiochemistry of more complex systems of relevance to the fusion fuel cycle both during normal operation as well as during accident conditions.

Staff:

W. Leifeld

R.-D. Penzhorn

N. Perevezentseva

SEP 2 Environmental Impact of Tritium and Activation Products

Subtask 2: Doses to the Public

The computer code UFOTRI for assessing the off-site consequences of accidental tritium releases has been further developed in several of its submodels; the extensions and modifications are documented in [1]. The photosynthesis model, which calculates the actual transfer rate of tissue free water tritium into organically bound tritium has been compared with first experimental results, obtained at KfK [2]. Due to the importance of the OBT in nutriment plants, a more detailed photosynthesis model will be developed together with the scientists who perform the plant experiments. Further plant experiments such as the exposure of winter wheat with HTO (closed chamber) and measurements of key plant parameters (e.g. leaf stomata resistance and leaf area index) in the open field will provide a data base for testing the new model.

To have a rough estimate of the radiological impact from nuclides not yet implemented in COSYMA [3], a simplified version of COSYMA has been generated which allows dose assessments with about 290 nuclides. As a result of the reduction in complexity, only long term effective dose values can be obtained. A modified set of equations from the German regulatory guidelines [4] has been implemented which allows a rough estimation of the dose from the ingestion pathways for all the 290 nuclides.

With the newly developed evaluation program DOSELOOK [5] it is possible to scale and easily combine precalculated dose values of unit releases of up to 290 fusion/fission relevant nuclides for 5 exposure pathways - external irradiation from the ground and cloud, inhalation during plume passage, inhalation of resuspended material and ingestion of contaminated foodstuffs - to get dose estimates for source terms with non-unit release rates.

For accidental releases, both computer codes UFOTRI and COSYMA (partly simplified) have been applied for investigations on worst case release scenarios. Based on updated source terms of activation products, dose calculations have been performed for unit releases of corrosion products from water coolant loops, first wall erosion products, tungsten dust from diverter erosion, activated copper, activated niobium alloy and of different coating materials (boron carbide, beryllium, graphite and tungsten). Additionally, releases of 1g ($3,7 \cdot 10^{14}$ Bq) of tritium in HT/HTO form has been investigated and compared with the releases of the activation products. The results have been presented in June 1993 at the IAEA Technical Meeting on Fusion Reactor Safety, Toronto [6].

The computer code NORMTRI for estimating the doses from tritium releases under normal operation conditions, has been established in a first version. It is based on a so-called 'statistical Gaussian dispersion model' [7]. This means, for all different dispersion situations during the considered time

period, a double Gaussian distribution of the released radionuclides is assumed within the plume. The data file contains meteorological parameters such as wind speed, wind direction, stability classes and rain intensities for one year. Tritium concentrations in foodstuffs are calculated dependent on the tritium concentrations in air and precipitation, with the relative air humidity as the steering factor. The dose from exposure of HT is a result of the deposited HT which is converted rapidly into HTO, and will be reemitted again into the atmosphere. Therefore the tritium concentration in foodstuffs is determined solely by the converted HTO. The inhalation dose results of the incorporation of both HT during plume passage and HTO reemitted after HT deposition.

Dose assessments during normal operation conditions have been performed for corrosion products from the first wall of the primary coolant loop and for tritium in both chemical forms (HT/HTO) by using COSYMA and NORMTRI, respectively. The results of dose calculations for normal operation effluents (activation products and tritium) have been presented in Toronto 1993 [6].

Dose assessments for the International Thermonuclear Experimental Reactor - Engineering Design Activities (ITER-EDA) for tritium and activation products, released under accidental as well as under normal operation conditions, are presently under way.

Within BIOMOVs II (BIOSheric MOdel Validation Study - phase II) a working group has been established with the aim of testing and validating tritium transfer models. During the third BIOMOVs II workshop in November 1992 the results from two release scenarios have been compared and discussed. The results will be documented in a BIOMOVs report (mid 1994). Based on the discussions during this third workshop, a new case study, now with real measured data (Savannah River Site, US), will be established at the fourth BIOMOVs-II meeting at the end of 1993 (September/October) in Vienna. Then not only model intercomparison but also model testing and model validation will be possible.

The work on developing models for the assessment of doses to individuals and the public resulting from contamination of waterbodies after an accidental release of radionuclides has been started recently. It has been outlined that a model chain covers the processes such as run-off, transport of radionuclides in large river systems and the behaviour of radionuclides in lakes. A first version of the integrated model chain will be ready at the end of 1993. At present basic transport models (1-D and 2-D) are available for hydrological investigations. Cs-137 will be the main nuclide in the developing and testing phase of the model chain (Chernobyl data).

Literature:

- [1] Raskob, W.
Description of the New Version of the Tritium Model UFOTRI Including User Guide

KfK-report 5194, Kernforschungszentrum Karlsruhe, to be published 1993

- [2] Diabate, S.
Personal communications, KfK, 1993

- [3] COSYMA: A New Program Package for Accident Consequence Assessment.
Joint report by Kernforschungszentrum Karlsruhe GmbH and National Radiological Protection Board Commission of the European Communities, Report EUR-13028 EN (1991)

- [4] Der Bundesminister für Umwelt, Naturschutz und Reaktorsicherheit
Allgemeine Verwaltungsvorschrift zu § 45 StrlSchV: Ermittlung der Strahlenexposition durch die Ableitung radioaktiver Stoffe aus kerntechnischen Anlagen oder Einrichtungen.
Bundesanzeiger vom 21.02.1990, Bonn, (1990)

- [5] Meyer, D. and Raskob, W.
User Guide for the PC-Program DOSELOOK KfK, unpublished internal report (to be printed 1993)

- [6] Raskob, W.
Dose Assessments for Releases of Tritium and Activation Products Into the Atmosphere in: Proc. of the 'IAEA Technical Meeting on Fusion Safety' Toronto, 7.6.93 - 11.6.93, to be published in: Journal of Fusion Energy

- [7] Hübschmann, W. and Raskob, W.
ISOLA V - A FORTRAN 77-Code for the Calculation of the Long-Term Concentration Distribution in the Environment of Nuclear Installations
Report KfK-4606, Kernforschungszentrum Karlsruhe (1990)

Staff:

J. Ehrhardt

I. Hasemann

W. Raskob

Long Term Program for Materials Development

Introduction and Overview:

In the frame of the structural materials Long Term Programme KfK makes major contributions to the development and qualification of martensitic steels within the task areas MANET and LAM.

The second heat of the MANET type steel, MANET-II, has been fully characterized according to task MANET 1.1, and an improvement has been attained as compared to the first heat with respect to practically all mechanical properties.

A new task on diffusion welding (MANET 3.2) to facilitate the manufacturing of special coolant channel geometries was taken up, but no results are available yet.

Within the established task MANET 2.3 mechanical and thermal fatigue tests were continued with an emphasis on the influence of hold times in tension or compression and a comparison of MANET-I and -II fatigue behaviour. It was found that, in contrast to austenitic materials, compression hold times cause a pronounced reduction in the number of cycles to failure. Concerning thermal fatigue a fundamental deviation from isothermal fatigue behaviour has been reported earlier. No significant differences could be found between MANET-II and MANET-I. To cover the full range of possible load conditions thermal fatigue was also studied with an overlay of in-phase or out-of-phase mechanical load.

Remarkable progress has been made in the compilation of post-irradiation data on ductile-to-brittle transition in the frame of task MANET 3.4. From a total of almost 90 subsize notch specimens irradiated to different dose levels at different temperatures the influence of several parameters could be evaluated by instrumented impact testing and subsequent SEM investigations:

- Pre-irradiation heat treatment has a pronounced effect both on DBTT and USE that is maintained during irradiation, i.e. the shifts Δ DBTT and Δ USE are practically independent of tempering treatment.
- There is a combined effect of irradiation temperature and dose in the sense that moderate neutron doses of 10 to 15 dpa already lead to a saturation of significant deterioration in fracture toughness behaviour unless there is a limitation of damage by annealing effects.
- This compensation effect needs temperatures as high as about 500°C. On the other hand, from the lowest achieved irradiation temperature (ca. 300°C) it is not yet clear whether the irradiation induced shift in the above-mentioned quantities represent the worst case to be expected.

A further irradiation is therefore in preparation to investigate the effect of low irradiation temperature, the time-evolution of the dose effect, and the behaviour of other martensitic

ferritic alloys with a potential to reduce the radiation embrittlement issue.

A proper fusion neutron source still being unavailable, the dual beam simulation technique of KfK is a valuable research tool, especially when mechanical loading is synchronously applied as has been done within task MANET 5. By comparison with post-irradiation fatigue experiments where the irradiation-induced microstructure is already fully developed, and with unirradiated specimens, the following results have been obtained: At a test temperature of 420°C under in-beam conditions a slowing down of the cyclic softening behaviour is observed that can directly be attributed to irradiation hardening. For post-irradiation fatigue the effect is even more pronounced and has, in addition, the strongest influence on fatigue life. These tests have been complemented by SEM and TEM investigations. SEM of the fracture surfaces could not establish significant differences, and TEM investigations so far have confirmed the small influence of helium on the failure mode at the mentioned temperature. Nevertheless He bubbles are considered as main contributors to hardening.

Under task LAM 2.1 activation calculations have been continued on all elements contributing to long-term radioactivity in form of alloying constituents and of tramp impurities. Emphasis has been on an optimization of the martensitic steel resulting in an OPTIFER version for which the dose rate can realistically be expected to be reduced by one order of magnitude. A further decrease is possible if one succeeds to arrive at a lower impurity level for some critical elements like Nb and Ag. The effect of impurities could also be demonstrated for the group of Vanadium alloys: Under realistic assumptions on the manageable impurity contents the theoretically extremely low activation is increased by orders of magnitude and then ranges not far below an OPTIFER type alloy.

The metallurgical aspects of OPTIFER have been treated with in task LAM 3.2. Five experimental heats of this alloy have been provided, and the characterization has been started. Work on the preceding alloy, called CETA, has been completed and reported.

H.D. Röhrig

LAM 2.1 Low-Activation Fusion Materials Development

1. Systematic Investigations of All Stable Elements for the Effect of Sequential (x,n) Reactions

A reliable estimate of materials activation in future fusion reactors requires the inclusion of all kinematically allowed reactions and subsequent reaction chains. While one-step neutron-induced reactions have been sufficiently covered in the past, all previous calculations neglected the so-called sequential (x,n) reactions, which have shown to produce often important contributions to the induced radioactivity and/or the related surface γ -dose rates, decay heats and biological hazards.

In order to improve activation calculations the libraries KFKSPEC and KFKXN were updated to match with the European Activation File version 2 which covers now all stable and radioactive nuclides with $T_{1/2} \geq 0.5$ days in the mass range $1 \leq A \leq 210$. Together with the European reference code FISPACT and the KfK code PCROSS systematic activation calculations were performed for all stable elements from hydrogen to bismuth ($1 \leq Z \leq 83$). As a result we found in 34 of all 81 single-element cases (Tc and Pm have no stable isotopes) an increase of, at least, one of the above mentioned radiological quantities due to sequential (x,n) reactions. In the following 17 cases the effect was greater than one order of magnitude: Li, N, O, F, Ne, Na, Mg, V, Cr, Mn, As, Y, Xe, Cs, Pt, Au, Tl.

2. Importance of alloying elements and impurities for the long-term activation of alloys

For the development of low-activation alloys in general two aspects are important: The first is to select the base material and necessary alloying elements according to their long-term activation, i.e. with a short life-time period of activity. For iron-based alloys - be it austenitic or ferritic-martensitic steels - the minimum achievable long-term activation is governed by the decay characteristics of pure Fe. In commercial austenitic and ferritic steels important alloying elements like Ni, Mo, Nb and Al worsen the situation because they contribute strongly to the long-term activation. Therefore in a first step of optimisation these elements have been replaced in ferritic-martensitic stainless steels by elements like Ta, W and Ce, leading to alloys of Fe Cr W Ta Type (CETA- and OPTIFER alloys). Based on the chemical analysis of the European reference alloys MANET II and "OPTIFER 1a real" the dose rates have been calculated and plotted in Fig. 1. In comparison the long-term activation of the latter alloy is reduced by roughly one order of magnitude which reflects a similar reduction of the Nb content.

This example demonstrates the second important aspect when developing materials with reduced or low activation, namely the role of impurity elements. Our calculations have shown that a few crucial elements like Nb, Mo, Ag, Bi and some rare earth elements cause a high long-term activation. If one takes into account that with modern steel production

techniques these impurities can be limited to low concentrations, a further reduction of long-term activity to the level indicated as "OPTIFER 1a target" can be expected.

A very interesting confirmation of the effect of impurities for the long-term activation can be observed for the group of Vanadium alloys. Vanadium, Cr and Ti are known to have a very low long-term activation under fusion reactor irradiation. This can be observed in the dose-rate plot of a "V-5Cr-5Ti pure" alloy in Fig. 1. If, however, even very low

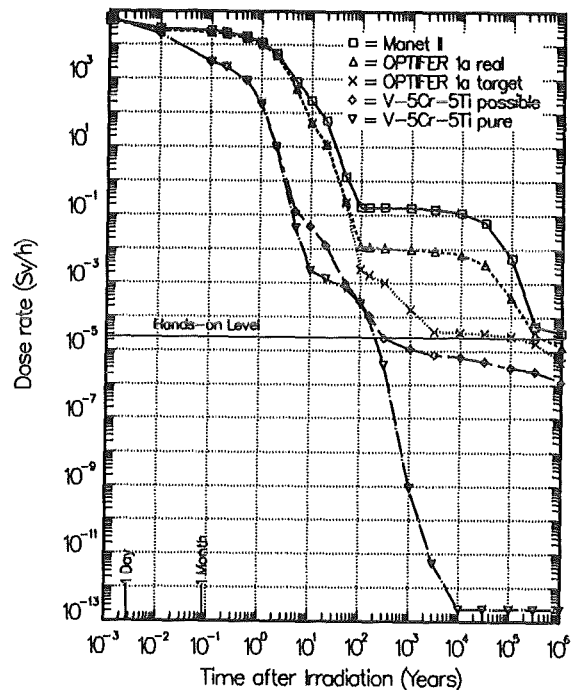


Fig. 1: Comparison of calculated surface γ -dose rates versus time after irradiation for different types of alloys. Explanation see text. The results refer to neutron irradiation in the first wall of a DEMO fusion reactor. A first wall 14 MeV neutron load of 12.5 MWyr/m² was assumed.

impurity concentrations - manageable with sophisticated fabrication methods - are taken into account, our calculations show a drastic increase of 6-7 orders of magnitude for the alloy "V-5Cr-5Ti possible" in long-term activation approaching the level of the optimized Fe-based steels. As a conclusion the impurity control of sensitive elements is even more important for the so-called Low-Activation-Alloy groups based on V, Cr, or Ti.

Literature:

- [1] S. Cierjacks, P. Oblozinsky, S. Kelzenberg, K. Ehrlich; Activation Calculations for Single Elements and Alloys Including Sequential (x,n) Reactions; Progress Report on Nuclear Data Research in the Federal Republic of Germany (to be published).

- [2] S. Kelzenberg, P. Oblozinsky; Influence of Sequential (x,n) Reactions on Production of Long-Lived Radionuclides in Fusion Reactors; Contributed paper to the IAEA Meeting on Activation Cross Sections for the Generation of Long-Lived Radionuclides of Importance in Fusion Reactor Technology, Del Mar near San Diego, California, USA, April 29-30, 1993.
- [3] K. Ehrlich, S. Kelzenberg, A. Möslang, L. Schäfer and M. Schirra; Assessment of Vanadium Alloys for ITER Application; (to be published). Mechanical Properties at Elevated Temperatures.
- [4] S. Cierjacks, P. Oblozinsky, S. Kelzenberg, B. Rzehorz; Development of a Novel Algorithm and Production of New Data Libraries for the Treatment of Sequential (x,n) Reactions in Fusion Materials Activation Calculations; Fusion Technology, Nov. 1993.

Staff:

K. Ehrlich
S. Kelzenberg
E. Daum
A. Möslang
G. Bürkle

LAM 3.2 Development of Low Activation Martensitic Steel

Structural material in the region of the first wall and the blanket is activated by neutron exposure during reactor operation. This may cause problems if such components must be repaired or stored in a repository. For this reason the Nb, Mo and Ni alloying constituents with high susceptibility to activation, in CETA-grade steel were replaced by W, Ta, and Ce, which are elements less prone to being activated.

The characterization of this first low activation martensitic steel had been finished and the results were reported [1]. In a second step the mechanical properties, especially the ductile brittle transition temperature (DBTT) of the impact energy of such steels, will be improved by modifying the chemical composition and optimizing the heat treatment. Beyond this we are trying to minimize the radiologically unacceptable impurities of the steel. The characterization of five new heats, called OPTIFER, has been started by metallurgical examinations and investigation of the mechanical properties.

Literature:

- [1] K. Anderko, K. Ehrlich, L. Schäfer, M. Schirra: CETA, ein Entwicklungsschritt zu einem schwach aktivierbaren martensitischen Stahl. KfK-Bericht 5060 (1993)

Staff:

L. Schäfer
M. Schirra

MANET 1.1 Characterization and Optimization of MANET-II-Steel

For application as structural materials of the first wall and of blanket structures, ferritic steel grades constitute a good alternative to austenitic steel grades because of their more advantageous thermal characteristics and irradiation properties.

The characterization of six heats of MANET-II-grade steel has been finished. The investigation of the metallurgical properties, the metallographical examinations and some mechanical properties, especially the creep rupture tests, has been reported [1]. Fig. 1 shows the creep-rupture strength of four heats of the MANET-II-grade steel in dependence of a time-temperature parameter P. Above $P = 24$ the creep-rupture strength of the MANET-II-grade steel is superior to MANET-I because of its higher ratio of the elements nitrogen to aluminum.

The evaluation of the V-notch impact bending properties has been reported [2]. An improvement with respect to strength, ductility, toughness and DBTT of MANET-II (evaluated from instrumented impact tests) has been achieved in comparison to MANET-I. Fig. 2 shows the impact energy of four heats of the MANET-II-grade steel in dependence of the test temperature. The DBTT is about 0 °C. A report has been published describing experiments of the influence of

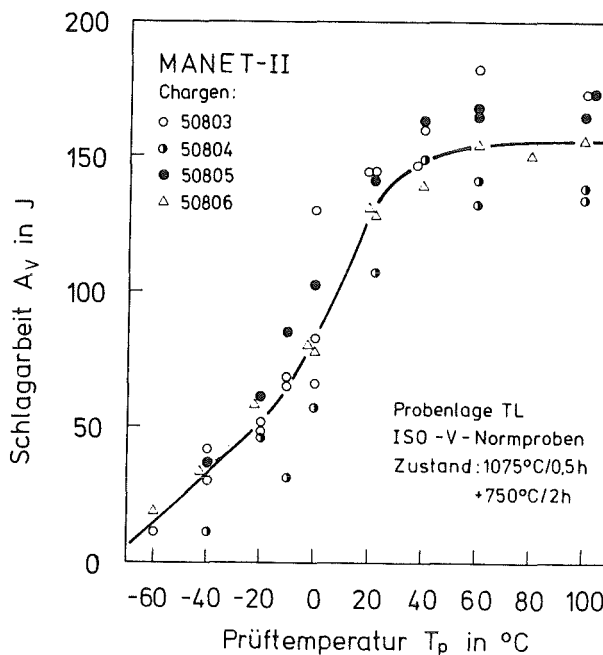


Fig. 2: Impact energy of four heats of the MANET-II-grade steel in dependence of the test temperature

deltaferrite on the tensile and creep-rupture properties for six martensitic steels containing 9-14 % Cr [3].

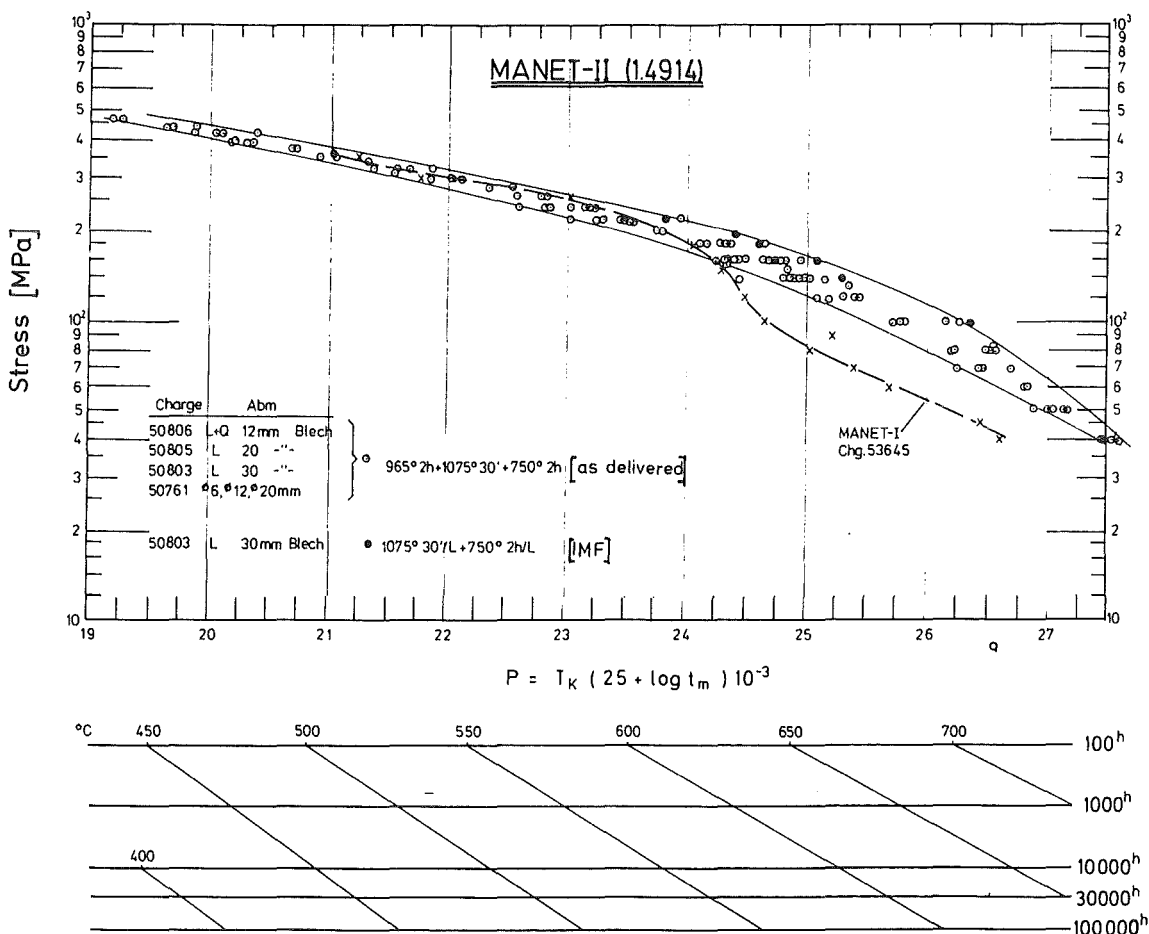


Fig. 1: Creep-rupture strength of four heats of the MANET-II-grade steel in dependence of a time-temperature parameter P.

Literature:

- [1] M. Schirra et al.: MANET - II, Untersuchungsergebnisse zum Umwandlungs- und Vergütungsverhalten und Prüfung mechanischer Eigenschaften. KfK-Bericht 5177 (1993)
- [2] L. Schäfer, W Meyer: MANET-II, Kerbschlagergebnisse, KfK-Unpublished report (3/93)
- [3] M. Schirra, S. Heger: Der Einfluß des δ -Ferrit-Gehaltes auf die Vergütungseigenschaften und das Zugfestigkeits- und Zeitstandverhalten eines CrNiMoVNb-Stahles mit 9-14% Chrom. KfK-Bericht 5080 (1993)

Staff:

W. Meyer
L.Schäfer
M. Schirra

MANET 2.3 Diffusion Welding

Within the framework of activities directed to developing materials for high loaded blanket structures of a DEMO fusion reactor a technique of diffusion bonding is to be found which allows structural plates with coolant channel geometry to be made from MANET 2. A qualified contractor ready to assume this task is IKE, Stuttgart. First, the welding parameters will be determined for small specimens and thereafter a larger component will be manufactured by welding.

The material has been provided and the specimen parts have been manufactured in the KfK Central Workshop. The welding tests were carried out in the middle of this year. All samples have, after welding, undergone a heat treatment at 750°C for two hours in vacuum. Post-weldment tests comprised He-leak testing, metallographic examination and bending tests with specimens manufactured from welded material and - for comparison - from base material.

First evaluations show a good weldability of MANET with the diffusion welding method. The best results were obtained for specimens with finish-ground contact surfaces (roughness $\leq 3 \mu\text{m}$) and welding temperatures of 980 or 1050°C. The resistance to failure during bending until 90° was the same as for base material. In a further test series components (diam. 320 mm) with a prototypical First Wall cooling channel geometry shall be diffusion-welded.

Staff:

G. Reimann

MANET 3.2 Pre- and Post-Irradiation Fatigue Properties

Thermal cycling of large components is a serious problem for the designer. The structure considered in the present case is the first wall of a fusion reactor. Its surface, in the actual design concept, will be subjected to radiation heating from the plasma facing side which may lead to severe thermal stresses. Due to the discontinuous operational mode, thermal cycling will generate oscillating temperature gradients. These, depending on the loading conditions, will cause elastic or elasto-plastic reversed deformation, giving rise to thermal fatigue which at present is considered as the most detrimental lifetime phenomenon for the structure considered. The investigations of MANET 3.2 are devoted to this problem.

The studies to be reported within MANET 3.2 are:

- The influence of temperature and hold-times in tension and compression upon isothermal low-cycle fatigue behaviour of MANET I at 450 °C and 550 °C and a strain rate of 3×10^{-3} /s on solid hourglass specimens.
- Isothermal fatigue at 200 °C and 550 °C as well as thermomechanical fatigue between 200 °C and 550 °C on hollow hourglass specimens from MANET I.
- Comparison between MANET I and MANET II samples under thermal fatigue loading conditions.

1. Isothermal Fatigue of MANET I

The experiments to study creep-fatigue interaction damage have been extended to tests with hold-time in the compression phase of the cycle. Fig. 1 shows the results for two strain

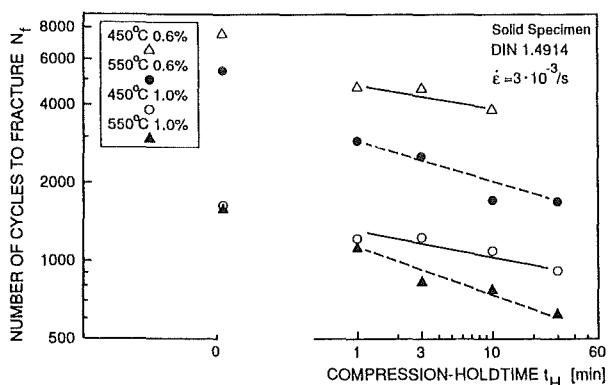


Fig. 1: Number of cycles to fracture vs. hold-time in compression as function of strain range and temperature for solid specimens of MANET I.

ranges (0.6 and 1.0 %) at 450 °C (open symbols) and 550 °C (closed symbols). Therefrom it is obvious that already for a hold-time of one minute the number of cycles to fracture N_f is significantly decreased, especially for $\Delta\epsilon t = 0.6$ %. At 550 °C

the reduction of the N_f -value is somewhat more pronounced as compared to 450 °C.

For comparison results of experiments with hold-time in tension are plotted in Fig. 2. It can be seen that for a dwell-

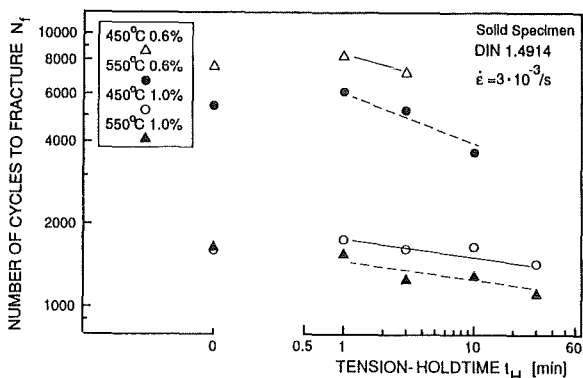


Fig. 2: Number of cycles to fracture vs. hold-time in tension as function of strain range and temperature for solid specimens of MANET I.

time of one minute no reduction of N_f occurs. The numbers of cycles to fracture are generally higher for tension dwell-time tests as compared to compression hold-time experiments. The N_f -value for instance for a compression hold-time of one minute ($\Delta\epsilon t = 1$ % and $T = 450$ °C) is about 1200 in comparison to the tension hold-time value which is ≈ 1800 . The corresponding results for $t_H = 30$ minutes are 900 (compression) and 1400 (tension).

The results aforementioned show that under comparable loading conditions compression hold-times on MANET I cause a more pronounced reduction of the number of cycles to fracture which is in contrast to results of hold-time tests on austenitic materials.

2. Thermal fatigue of MANET

2.1 Thermomechanical fatigue of MANET I

Thermomechanical out-of-phase and in phase fatigue tests between 200 °C and 550 °C were conducted with overlaid mechanical strains. During both thermomechanical fatigue tests the temperature cycle will lead to a strain portion. This strain will intensify the mechanical strains for out-of-phase or diminish it for in phase tests and therefore both quantities together are denominated as "effective strain range".

For comparison also isothermal fatigue tests at 200 °C and 550 °C were performed and evaluated.

Under all loading conditions MANET I samples show cyclic softening. From the beginning of the test a degressive reduction of the load range can be detected, changing into a near linear decreasing behaviour of the load range. This change depends strongly on the strain range and in case of isothermal fatigue tests also from test temperature.

While evaluating the fatigue tests it was observed that the behaviour of the load range is describable by a two parametric allometric function: $F = \beta \cdot N^\alpha$, with load range F and number of cycles N . The parameter β is the start value of the allometric function and α will be named as "softening exponent". Generally the adaptation of this function to load range values and to the softening process of MANET I was very good, as can be seen from Fig. 3.

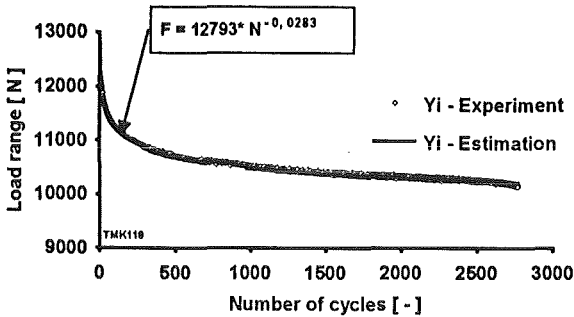


Fig. 3: Experimental load range compared with estimated load range by the allometric function from isothermal fatigue MANET I at 200 °C with 0.8 % total strain range.

The cyclic softening process under thermomechanical fatigue conditions is influenced by the phase situation. This effect is shown in Fig. 4 where the allometric "softening exponents" α

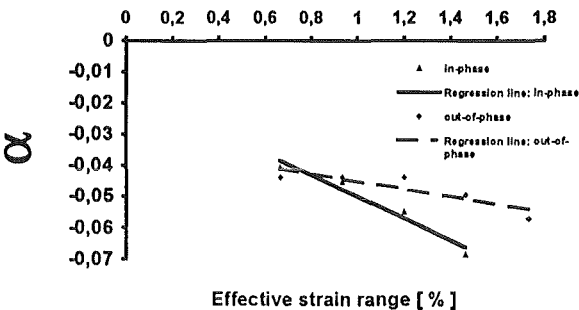


Fig. 4: Relation between effective strain and the "softening exponent" α of allometric functions at in phase and out-of-phase thermomechanical fatigue.

are plotted versus effective strain range for in phase and out-of-phase thermomechanical fatigue conditions.

With increasing effective strain range the cyclic softening decreases faster, i.e. reaching smaller α - values under in phase loading than under out-of-phase loading conditions.

2.2 Thermal fatigue of MANET II

The two heats - MANET I and MANET II - of a ferritic - martensitic Cr - steel are under investigation. This steel has the German Steel Denomination Nr. 1.4914. The MANET I material had just been described elsewhere. The MANET II material is a 20 mm thick sheet with the Heat Nr. 50805 and

the chemical composition: C, 0.10; Cr, 10.3; Ni, 0.65; Mo, 0.57; V, 0.19; Nb, 0.14; Si, 0.14; Mn, 0.75; B, 0.0075; N, 0.031 and Zr, 0.028 wt%.

Hollow hourglass shaped specimen from MANET I and MANET II were fabricated - in case of sheet material perpendicular to the rolling direction and in the centerline of the sheet - and then heat treated. The resultant microstructure is a fully tempered martensite. As was shown earlier, the carbides are lying along prior austenite grain boundaries and lath boundaries, while smaller carbides are contained in the matrix.

MANET I and MANET II samples had been thermally fatigued by triangle temperature cycles with constant heating and cooling rates of ± 5.8 K/s in a range of a fixed low temperature T_L (200 °C) and a variable high temperature T_H (550 °C to 700 °C).

Due to the fact, that the thermal fatigue testing device is not enabled to control neither the total mechanical strain range $\Delta \epsilon_{t,m}$ nor the stress range $\Delta \sigma$, quantities like $\Delta \sigma$, $\Delta \epsilon_{t,m}$ and the plastic mechanical strain $\Delta \epsilon_{p,m}$ change with number of cycles. Hence only the measured values at $N_f/2$ are taken for any comparison.

The small thermal elongation of the ferritic - martensitic steels causes total mechanical strain of both heats between 0.2 % and 0.8 % during triangular thermal fatigue experiments. From the data sets of thermally cycled hourglass samples of MANET I and MANET II the total mechanical strain ranges $\Delta \epsilon_{t,m}$ at $N_f/2$ are plotted versus the number of cycles to failure N_f in Fig. 5. By increasing ΔT , $\Delta \epsilon_{t,m}$ at $N_f/2$ increases

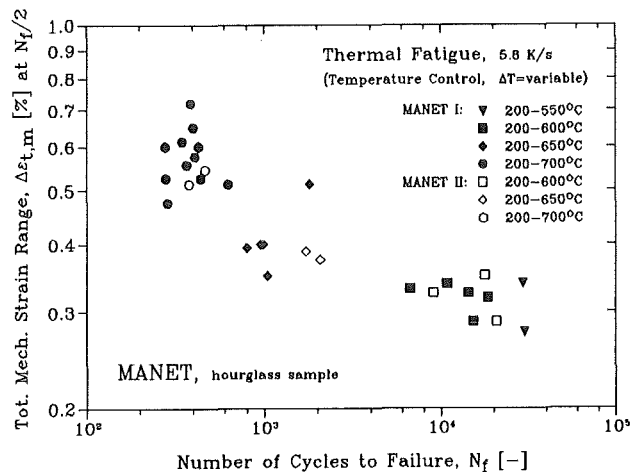


Fig. 5: Comparison of thermal fatigue data of the ferritic - martensitic steels MANET I and MANET II in a $\Delta \epsilon_{t,m}$ at $N_f/2$ versus N_f diagram.

and leads to smaller N_f -values. This effect is mainly driven by the ΔT - influence on the plastic mechanical strain $\Delta \epsilon_{p,m}$ - values at $N_f/2$, which is plotted versus N_f for MANET I and MANET II in Fig. 6. The $\Delta \epsilon_{p,m}$ -values at $N_f/2$ range from 0.02 % up to 0.5%.

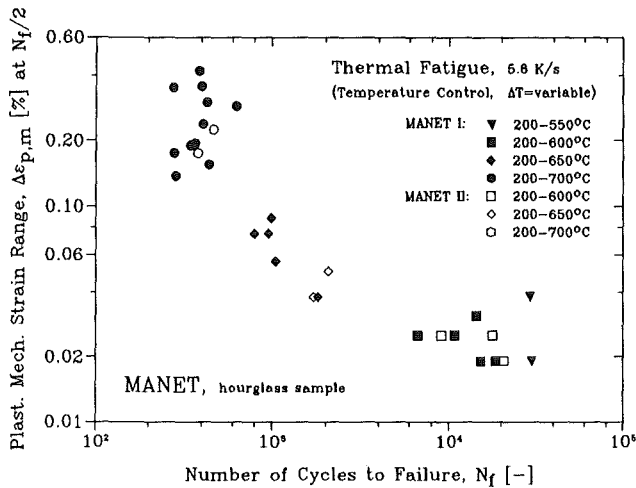


Fig. 6: Comparison of thermal fatigue data of the ferritic-martensitic steels MANET I and MANET II in a $\Delta\epsilon_{p,m}$ at $N_f/2$ versus N_f diagram.

With increasing ΔT the amount of plastic mechanical strain range increases due to the growing compressional creep contribution at each high temperature cycle.

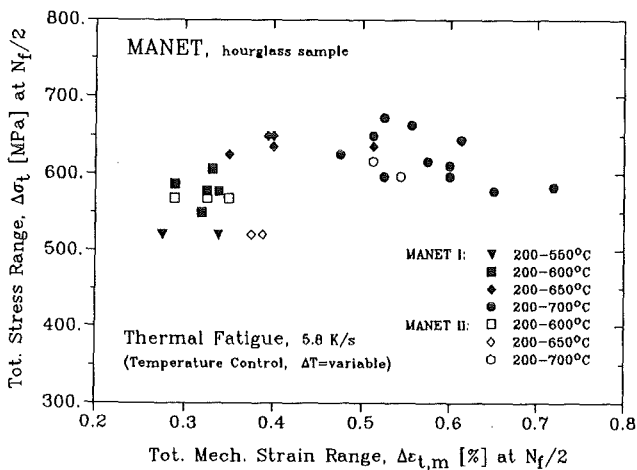


Fig. 7: Comparison of thermal fatigue data of the ferritic-martensitic steels MANET I and MANET II in a $\Delta\sigma_t$ at $N_f/2$ versus $\Delta\epsilon_{t,m}$ at $N_f/2$ diagram.

In Fig. 7 are compared the total stress ranges $\Delta\sigma_t$ at $N_f/2$ from MANET I and MANET II, obtained during thermal fatigue. The $\Delta\sigma_t$ - values at $N_f/2$ of MANET I increase up to a maximum value of about 670 MPa with increasing ΔT and $\Delta\epsilon_{t,m}$ at $N_f/2$. The MANET II - values reach only $\Delta\sigma_t$ - values at $N_f/2$ of about 610 MPa under the same conditions.

Literature:

[1] C. Petersen, I. Alvarez-Armas and A.F. Armas: Thermal Fatigue on Steels for ITER and DEMO, held at 2nd Conference: "The Effect of Irradiation on Materials of Fusion Reactors" at St. Petersburg, GUS,

22.-24.9.1992, to be published in Plasma Devices and Operation.

[2] R. Gersinska, C. Petersen, D. Rodrian, W. Scheibe and R. Schmitt:

Low Cycle Isothermal and Thermal Fatigue, to be published in the Proceedings of the IEA Workshop on "Ferritic-Martensitic Steels", Tokyo, Japan, October 26.-28.1992.

[3] F. Wolter and C. Petersen:

Einrichtung zur Thermomechanischen Ermüdung metallischer Werkstoffe, Proceedings of Tagung Werkstoffprüfung 1992, Bad Nauheim, FRG, Dec. 3.+4. 1992, eds. Deutscher Verband für Materialforschung und -prüfung eV, (1992), pp. 83-92.

[4] I. Alvarez-Armas, A.F. Armas and C. Petersen:

Recovery and Precipitation Formation in a Martensitic Stainless Steel under Thermal Fatigue Hold Times, Proceedings of FATIGUE '93, Montreal, Canada, May 3.-9.1993, Vol. II, eds. J.-P. Bailon and J.I. Dickson, (1993), pp. 903-908.

[5] I. Alvarez-Armas, A.F. Armas and C. Petersen:

Thermal Fatigue of a 12 % Chromium Martensitic Stainless Steel, accepted for publication in Fatigue & Fracture of Engineering Materials & Structures for (1993).

[6] F. Wolter and C. Petersen:

Thermomechanische Ermüdung eines martensitischen Stahles vom Typ 1.4914, Proceedings of the Annual Meeting on Nuclear Technology '93, Köln, Germany, 25.-27.05.1993, pp. 401-404.

[7] C. Petersen:

Thermische Ermüdung mit Haltezeiten an dem martensitischen Stahl Werkstoff Nr. 1.4914, Abstract in Proceedings of Hauptversammlung 1993 of the Deutsche Gesellschaft für Materialkunde, Friedrichshafen, Germany 1.-4.6.1993, p. 39.

[8] F. Wolter and C. Petersen:

High Temperature Thermomechanical Fatigue of 1.4914 Type Steel, Proceedings of 12th International Conference on Structural Mechanics in Reactor Technology, Stuttgart, Germany, 15.-20.8.1993, Pap.: L01/2.

[9] C. Petersen:

Thermal Fatigue on MANET II, to be held on the 6th International Conference on Fusion Reactor Materials, Stresa, Italy, 27.9.-1.10.1993, Pap.: ICFRM6/L006.

Staff:

C. Petersen

D. Rodrian

W. Scheibe

R. Schmitt

H. Schneider

W. Schweiger

(F. Wolter)

MANET 3.4 Pre- and Post-Irradiation Fracture Toughness

In the course of the irradiation program FRUST/SIENA 138 KLST V-notch specimens (3 x 4 x 27 mm, notch depth 1 mm) were irradiated in the HFR in Petten (Netherlands) at dose levels of about 5dpa, 10dpa and 15dpa. The irradiation temperatures were in the range from 280 °C to 480 °C. Up to now 87 specimens have been tested in an instrumented Charpy impact system in a Hot Cell [1, 2, 3]. Eight different pre-irradiation heat treatments were applied to the specimens. In the first step of the evaluating procedure changes of the impact properties caused by variations in structure and by irradiation embrittlement were investigated. The impact properties were described as a pair of two values: Ductile to Brittle Transition Temperature (DBTT) and Upper Shelf Energy (USE).

1. Effect of heat treatments on the impact properties

The heat treatments of the MANET-I specimens were performed at 950-980 °C/2h + 1075 °C/0.5h + tempering in the range from 600 °C to 780 °C/h. The results show a linear dependency of DBTT on the tempering temperature: the higher the tempering temperatures the lower the DBTT. The USE is increasing exponentially with rising values of the tempering temperature. Δ DBTT and Δ USE are shift values which describe the difference between the unirradiated and irradiated condition of a material. The results of the Charpy impact tests with the MANET-I specimens show clearly, that Δ DBTT as well as Δ USE are independent of the tempering treatment.

2. Effect of irradiation temperature on the impact properties

Both Δ DBTT and Δ USE are increasing exponentially with abating irradiation temperatures. At irradiation temperatures above 500 - 520 °C a nearly total compensation of the irradiation induced embrittlement is to be expected.

3. Effect of irradiation dose on the impact properties

The results show a saturation of the embrittlement above dose levels of about 10 to 15dpa.

4. Model of the DBTT depending on the heat treatment and irradiations parameters

The results can be fitted by a set of empirical equations describing - for a certain validity range - the DBTT of KLST MANET-I V-notch specimens as a function of pre-irradiation heat treatment and irradiation parameters:

$$DBTT_{irr} = DBTT_{unirr} + \Delta DBTT$$

$$DBTT_{unirr} = 30\text{ °C} - (T_A - 600\text{ °C})/3$$

$DBTT_{unirr}$: Ductile to brittle transition temperature in the unirradiated condition

T_A : Tempering temperature in °C

$DBTT_{irr}$: Ductile to brittle transition temperature after irradiation

$$\Delta DBTT = 4900K e^{-(T_{irr}/370K)^{2.5}} (1 - e^{-N/2.5})$$

Δ DBTT: Irradiation induced shift of the ductile to brittle transition temperature

T_{irr} : Irradiation temperature in K

N: Irradiation dose in dpa

The plot of the Δ DBTT function is shown in Fig. 1. The model for the USE is similar to the DBTT model. All experiments and results are described and discussed in [4, 5, 6, 7].

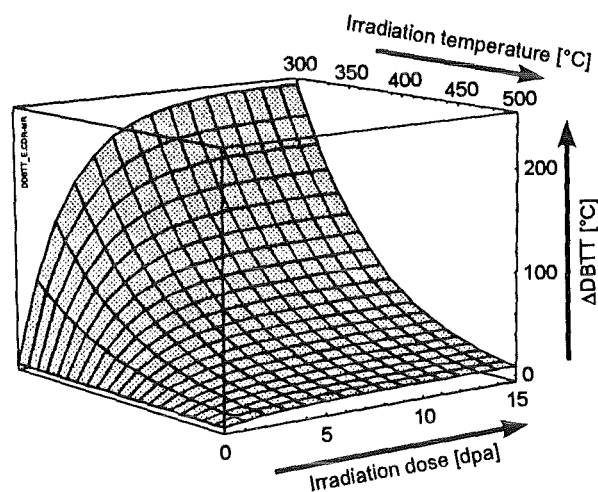


Fig. 1: Δ DBTT model depending on irradiation dose and temperature

Literature:

- [1] M. Rieth, B. Dafferner, C. Wassilew: "Ein flexibles System zur Durchführung, Auswertung und Analyse von instrumentierten Kerbschlagbiegeversuchen", Jahrestagung Kerntechnik 1993, 25.-27. Mai, Köln.
- [2] M. Rieth, B. Dafferner, C. Wassilew: "Ein modulares Softwarepaket für die Analyse, Auswertung und Verwaltung von instrumentierten Kerbschlagbiegeversuchsdaten", Jahrestagung Kerntechnik 1993, 25.-27. Mai, Köln.
- [3] C. Wassilew, M. Rieth, B. Dafferner: "Verfahren zu Störgrößenkompensation bei instrumentierten Kerbschlagbiegeversuchen", Kernforschungszentrum Karlsruhe, KfK 4796, Oktober 1990.

- [4] C. Wassilew, B. Dafferner, M. Rieth, A. Krütter: "Effect of Neutron Irradiation on the Dynamic Fracture Toughness Behaviour of the 12 % Chromium Steel MANET-I Investigated Using Subsize V-Notch Specimens", Presentation on the Fifth International Conference on Fusion Reactor Materials (ICFRM-5), Clearwater, Florida, USA, 17.-22- November 1991.

- [5] C. Wassilew, K. Ehrlich: "Effect of Neutron Irradiation on the Dynamic Fracture Toughness Behaviour of the 12 % Chromium Steel MANET-I Investigated Using Subsize V-Notch Specimens" Journal of Nuclear Materials, September 1992, 191-194, 850-854.

- [6] C. Wassilew, B. Dafferner, M. Rieth, A. Krütter: "Effect of Neutron Irradiation on the Dynamic Fracture Toughness Behaviour of the 12 % Chromium Steel MANET-I Investigated Using Subsize V-Notch Specimens", Institut für Materialforschung II, Projekt Kernfusion, Kernforschungszentrum Karlsruhe, Unpublished report, April 1992.

- [7] M. Rieth, B. Dafferner, C. Wassilew: "Der Einfluß von Wärmebehandlung und Neutronenbestrahlung auf die Kerbschlageigenschaften des martensitischen 10,6 % Cr-Stahls MANET-I" Institut für Materialforschung II, Projekt Kernfusion, Kernforschungszentrum Karlsruhe, KfK 5243, Sept. 1993

Staff:

B. Dafferner
A. Krütter
O. Romer
H. Ries
M. Rieth
C. Wassilew †

MAT 5 Ion-Beam Irradiation Fatigue and Creep Fatigue Tests

The Dual Beam Facility of KfK, where α -particles (≤ 104 MeV) and protons (≤ 40 MeV) are focussed onto a target, was developed as a research tool for materials within the European Fusion Technology Programme. This high energy Dual Beam Technique allows the simulation of fusion neutrons by the systematic variation of hydrogen, helium and damage production in thick metal and ceramic specimens as well as the simulation of Tokamak relevant thermal and mechanical loads in proposed plasma-facing materials.

A specific feature of next step tokamak fusion devices are the plasma burn and off-burn periods. Depending on the operating conditions and the thermal conductivity of plasma facing structural components, these oscillating temperature gradients will cause thermal fatigue or creep fatigue which under neutron irradiation are considered to be one of the main lifetime-limiting failure modes. After several years of development novel experiments can be performed at the cyclotron facility of KfK (for technical description see previous annual report), which allows a close simulation of realistic fusion conditions by simultaneous irradiation and fatigue loading.

The effect of irradiation on mechanical properties is studied in the fast majority by means of postirradiation experiments. This means that the irradiation induced microstructure is fully developed before the mechanical test is started. However, realistic fusion conditions with simultaneous irradiation and fatigue loading can lead to an inherently different material response. Therefore, we have focussed in this reporting period the experimental activities also on the comparison between postirradiation and in-beam fatigue results. The material used for these investigations was the ferritic/martensitic 12% Cr steel MANET-I in the tempered condition.

1. In-beam fatigue versus unirradiated fatigue

Strain controlled isothermal in-beam fatigue tests have been performed on hollow fatigue specimens with the following loading conditions:

Temperature	420 °C
Environment specimen outside	vacuum (10^{-3} Pa)
Environment specimen inside	purified He-gas
Inner surface heat flux	(0.7-1.0) MW/m ²
Damage production rate	(2-3) $\times 10^{-6}$ dpa/s
Helium production rate	(6-8) $\times 10^{-4}$ appm He/s
Fatigue mode	continuous push-pull cycling (R=-1)
Strain rate $\Delta\epsilon_t$	(0.5-1.0)%
Strain rate	$8 \times 10^{-4} \text{ s}^{-1}$

Fig. 1 shows the total strain amplitude $\Delta\sigma_t$ (a) and the plastic elongation $\Delta\epsilon_{pl}$ (b) as function of number of cycles N for typical in-beam fatigue and unirradiated control tests. At all strain loads in the unirradiated reference specimens (dashed

lines) $\Delta\sigma_t$ continuously decreases with increasing N, i.e. cyclic softening occurs, a common feature of ferritic steels.

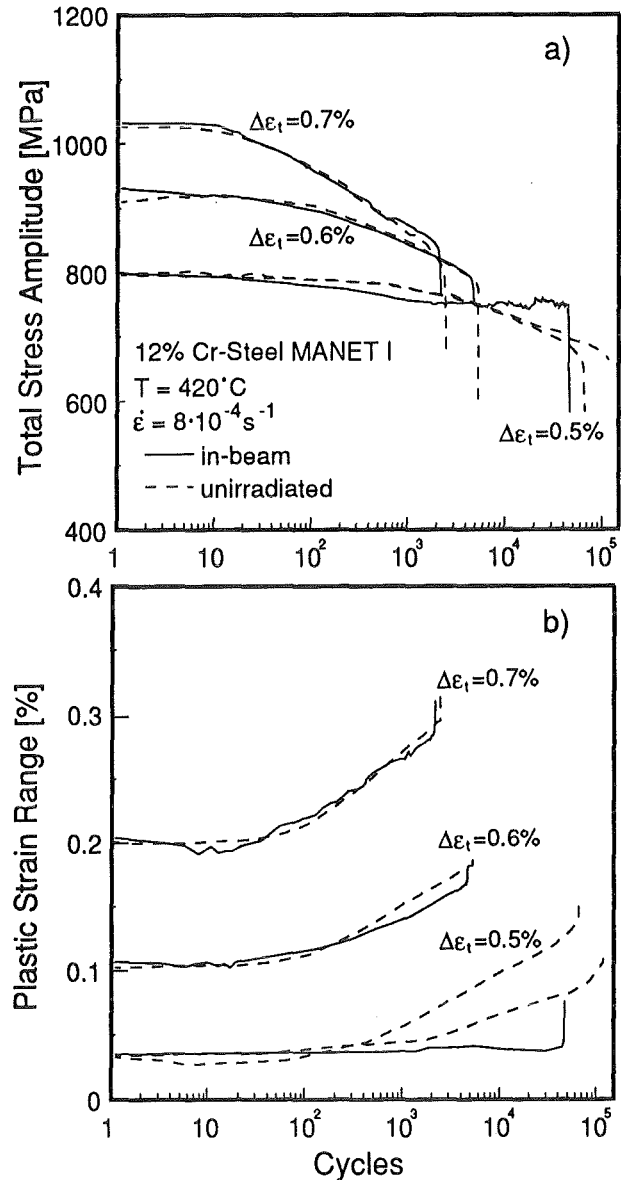


Fig. 1: Development of the (a) total stress amplitude $\Delta\sigma_t$, and the (b) total plastic elongation $\Delta\epsilon_{pl}$ in strain controlled in-beam and out-of-beam fatigue experiments at 450 °C

At higher strain loads ($\Delta\epsilon_t > 0.6\%$) the fatigue life N_f under in-beam conditions (solid lines) is similar to that of unirradiated reference tests. However, below $\Delta\epsilon_t = 0.6\%$ the fatigue life is sufficiently high, and under in-beam conditions the total stress amplitude $\Delta\sigma_t$ will get influenced during irradiation. That is $\Delta\sigma_t$ deviates more and more from the reference tests, indicating a radiation induced slowing down of cyclic softening. Because $\Delta\sigma_t$ is strongly connected with changes of the microstructure, the observed difference between in-beam and out-of-beam tests can directly be related to irradiation induced hardening. This hardening accelerates crack propagation and consequently reduces fatigue life.

The plastic strain amplitude $\Delta\epsilon_{pl}$ reflects the amount of inelastic deformation within one cycle and for a given strain load $\Delta\epsilon_t$ a decrease of $\Delta\sigma_t$ is synonymous with an increase of $\Delta\epsilon_{pl}$ and vice versa. A comparison between Fig. 1a) and b) shows, that this feature does not only hold for unirradiated, but also for in-beam irradiated specimens. In addition, the in-beam fatigue experiments done at $\Delta\epsilon_t = 0.5\%$ directly confirms the general consensus of the present knowledge, that under strain load conditions not the plastic deformation but the stress amplitude seems to be responsible for crack propagation.

2. Postirradiation fatigue versus in-beam fatigue

Under in-beam conditions at $\Delta\epsilon_t = 0.5\%$ a number of cycles to failure of $N_f = 42,000$ cycles, a He-concentration of 400 appm and a damage dose of nearly 2 dpa has been reached (Fig. 2). This N_f is only about a factor of two below the

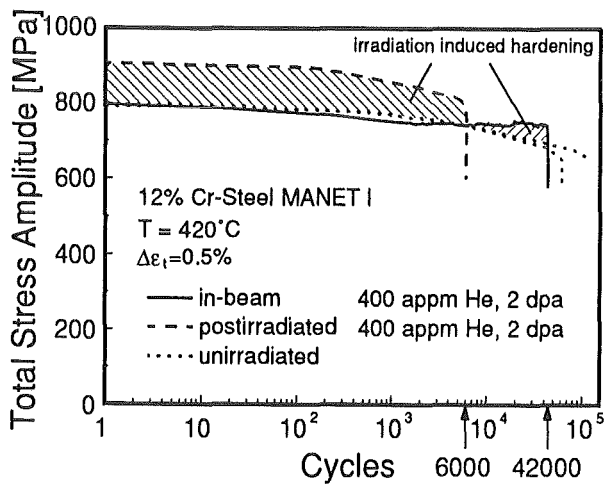


Fig. 2: Development of $\Delta\sigma_t$ during strain controlled fatigue tests. The hatched areas show the difference between in-beam and postirradiation experiments.

average N_f -value of unirradiated reference tests, but seven times higher than N_f of comparable postirradiated specimens. The hatched areas in Fig. 2 show that the time evolutions of the total stress amplitudes $\Delta\sigma_t$ under in-beam fatigue loading are completely different from those of postirradiation experiments. Obviously in contrast to in-beam conditions in postirradiated specimens the irradiation induced microstructure and consequently also the irradiation hardening is completely developed before the fatigue test is started.

Within the fracture-mechanics methodology the fatigue-crack-propagation da/dN can be represented in the so-called long crack, low-stress regime by $da/dN \sim (\Delta K)^n \sim (\Delta\sigma_t)^n$, where a is the crack length, ΔK the stress-intensity-factor fluctuation, and n a material constant (typically 2.25 for martensitic steels). It becomes clear, that at a given strain load crack propagation is in the end governed by $\Delta\sigma_t$, and that preexisting hardening (postirradiation tests), where irradiation hardening acts already on the first cycle, has the strongest effect on fatigue life. A comparison between in-

beam and postirradiation fatigue properties confirms the general consensus of the present data, that at least at 420 °C conventional postirradiation tests are a conservative approach to in-situ conditions.

3. Microstructural investigations

The SEM-analysis of the fracture surface could not establish significant differences between fatigue tested unirradiated, postirradiated and in-beam irradiated specimens, even at helium contents of 400 appm. Under all conditions at 420 °C, the rupture mode remained ductile and transcrystalline.

Fig. 3 shows the TEM micrographs of irradiated and fatigue tested specimens. During fatigue testing a distinct subcell structure (Fig. 3a) has been developed similar to unirradiated specimens. Under postirradiation conditions the relatively high density of dislocations doesn't change during irradiation and almost all He-bubbles are pinned at those sinks (Fig. 3c). In fatigue tests following such irradiations the trapped He-bubbles act as barriers and compared to in-beam tests a somewhat higher fraction of dislocations remains in the matrix. An important feature of the present TEM investigations is, that in MANET steels at 420 °C even after in-beam fatigue loading the majority of He-bubbles can be still observed in the bulk and that excessive bubble nucleation at inner surfaces like precipitates or lath boundaries does not occur (Fig. 3b).

This observation is not obvious because the originally high density of dislocations, acting as sinks in the matrix for bubble nucleation, is reduced during the early stage of in-beam fatigue testing due to the formation of dislocation walls and subcells. In addition it has been speculated, that the cyclic motion of dislocations can sweep small He-clusters and bubbles lying on their glide planes onto inner surfaces where they will accumulate and significantly contribute to embrittlement. However, the TEM investigations both on postirradiated and in-beam specimens so far have confirmed the small influence of helium on the failure mode at 420 °C.

While the fracture mode is only marginally affected by He-implantation, He-bubbles are presently considered as main hardening contributors above about 400 °C and therefore seem to be responsible for the observed fatigue life reduction. The irradiation induced hardening observed under in-beam and postirradiation conditions can be quantitatively understood in the frame of a hardening model assuming a modified Orowan-type barrier model, and the observed diameters and densities of the He-bubbles are in good agreement with the predictions of that model.

Literature:

- [1] A. Möslang, S. Baumgärtner, G. Bürkle, R. Lindau, G. Przykutka, and K. Ehrlich; "In-Situ Fatigue Experiments on the Karlsruhe Dual Beam Facility: Capabilities and first results"; in Fusion Technology 1992, p. 1439; Eds. C Ferro et al, North Holland (1993)

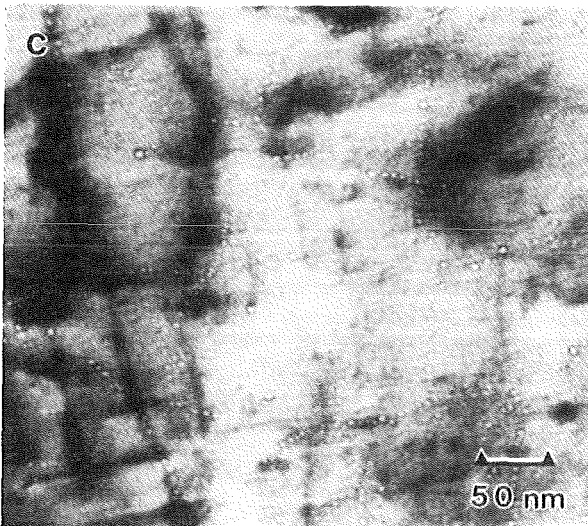
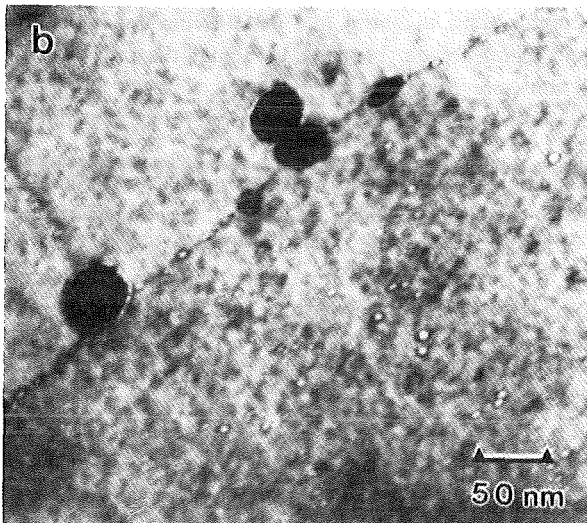
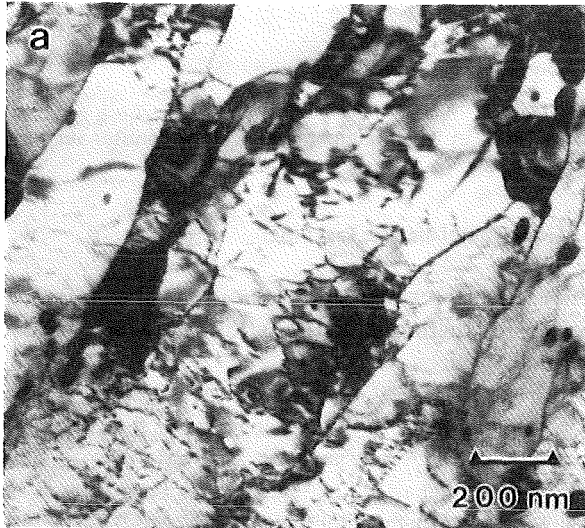


Fig. 3: TEM micrographs of MANET-I irradiated (400 appm, 2 dpa) and fatigue tested ($\Delta\epsilon_f = 0.5\%$) at 450 °C.
a) subcell formation
b) Helium bubble morphology after in-beam fatigue
c) Helium bubble morphology after postirr. fatigue

- [2] B.N. Singh, M. Eldrup and A. Möslang, "Effects of Hot Implantation of Helium in Copper on Bubble Formation within Grains and on Grain Boundaries"; 16th Int. Symposium on the Effects of Radiation on Materials; Denver, USA, 21-25 June 1992
- [3] R. Lindau and A. Möslang; "In-Situ-Ermüdungsexperimente an der Karlsruher Zweistrahlanlage: Ergebnisse bei 450 °C; Jahrestagung Kerntechnik 1993, 25-27 May 1993, Köln; Proceedings.
- [4] G. Albertini, F. Carsughi, M. Ceretti, R. Coppola, F. Fiori, A. Möslang and F. Rustichelli, "Small Angle Neutron Scattering (SANS) Investigation of Irradiated MANET Steel"; IX Int. Meeting on Small Angle Scattering, 27-30 April 1993, Saclay; Proceedings.

Staff:

S. Baumgärtner
G. Bürkle
R. Lindau
A. Möslang
D. Preininger
G. Przykutka

Test Blanket Development

Introduction:

Within the European Fusion Technology Program blanket development is divided in work for the ITER machine and work for the DEMO-reactor within the Long Term Program. After establishing two European working groups KfK has concentrated its efforts on the development of test blankets for ITER. By test blankets we understand blankets for the next step towards a commercial power station, so called DEMO relevant blankets. In the DEMO-reactor, the potential of a fusion machine to produce electricity shall be tested for the first time. Consequently the test blankets have to be designed for DEMO relevance in terms of breeding rate, temperatures and pressure. Structural materials, maintainability, reliability and safety have to satisfy the more stringent requirements of power production in comparison with driver or shielding blankets for the ITER machine. The boundary conditions mentioned above cannot be satisfied full scale and at the same time in the test positions available in ITER. Therefore the definition of test objects and the testing program is one of the main objectives of KfK besides the proof of DEMO relevance of the KfK blanket design alternatives.

The European Test Blanket Development Groups mentioned above deal with two development lines, one with solid breeder helium cooled, the other with liquid metal breeder and either liquid metal (selfcooled) or water cooled blankets. Both KfK developed designs, the selfcooled lithium-lead blanket and the helium cooled, breeder out of tube, blanket are accepted alternatives within the European test blanket development program - see BS-DE and BL-DE tasks. A part of the work defined by the partners - KfK, CEA, ENEA and JRC Ispra - consists of common work, relevant to all blanket designs, whereas the design work itself remains independent for the time being. It is foreseen to reduce the number of blanket alternatives to two in 1994/95, one solid breeder and one liquid metal breeder design, which will finally be tested in ITER.

The Solid Breeder Blanket Tasks (BS)

Solid breeder design, already mentioned above (DE-D-1), includes besides the design work proper, also small scale thermomechanical and fabricability tests. The KfK solid breeder material program has concentrated, in agreement with the European partners, on lithium orthosilicate. The program tasks include preparation, characterization, irradiation and postirradiation examination as well as measurement of the physical, chemical and mechanical properties. Of special interest are the in and out of pile tritium release studies, performed at KfK and within the common breeder development program in several European reactors. The KfK breeder program is described in tasks BR-D-1 through D-8. The main non nuclear testing facility to prove the feasibility of KfK's solid breeder design will be the helium

loop HEBLO, in which elements as well as canister sections may be tested - see NN-D-1.

The Liquid Metal Blanket Tasks (BL)

Design activities (DE-D-1) concentrate on a solution featuring an inboard / outboard selfcooled blanket with a helium cooled first wall.

Of great importance to the development of the selfcooled blanket is the knowhow and the data base of magneto-hydrodynamic behaviour of liquid metal flow acquired in theoretical and experimental studies of task MH-D-1. The test facility MEKKA and the cooperation with Argonne National Laboratory play a central role in MHD development. The liquid metal breeder blankets are so far the only blanket alternatives, including solid breeder blankets which allow a sufficiently high tritium breeding rate, not using beryllium.

In addition to design and MHD activities KfK studies the physico-chemical behaviour, task PC-D-1, especially corrosion of structural materials in the lithium lead eutectic (Pb-17Li) and the behaviour of impurities (Polonium) including methods of clean-up. Newly taken up is the irradiation of electrically insulating coatings. The Pb-17Li loops TRITEX and PICOLO are the main testbeds for the experimental studies.

H. Sebening

BS DE-D 1 Solid Breeder Test Blanket Design

1. Demo Blanket Design Work

The new design of the Demo blanket based on the use of beryllium pebbles was presented in the previous annual report [1]. Since then, further neutronic and thermohydraulic calculations have been performed. Originally it was assumed that in the back part of blanket only ceramic breeder material is used. However, detailed thermal calculations showed that the resulting temperature would have been too high. Therefore also for the back region a mixed bed of 2 mm beryllium pebbles and 0.1 - 0.2 mm Li_4SiO_4 has been chosen for the present design (zone 2, see Fig. 1). Furthermore, the Li^6 enrichment has been decreased to 25 % so that the Li_4SiO_4 pebbles are the same for two blanket zones. In the front part the bed arrangement (zone 1, Fig. 1) is the same as before (60 % of 2 mm Be pebbles + 15 % of 0.1 - 0.2 mm Li_4SiO_4 and 5 % of 0.08 - 0.018 mm Be pebbles, the rest 20 % being helium).

The three-dimensional neutronic calculations have been performed as usual, with the Monte Carlo computer code MCNP. The heat transfer correlation used to calculate the breeder temperatures have been obtained by extrapolation of correlations from measurements performed with aluminum pebbles replacing the beryllium pebbles [2]. Fig. 1 shows the temperatures calculated for the equatorial plane of the outboard blanket. All of them are within acceptable limits.

As shown in Ref [3] the steady state tritium inventory in the breeder material can be calculated with a good approximation by integrating the tritium residence time in the breeder between the minimum and the maximum

breeder temperature. The tritium residence time as a function of temperature has been measured in-situ for the reference Li_4SiO_4 pebbles (Schott 89/3 tempered) in presence of the reference purge gas ($\text{He} + 0.1 \% \text{H}_2$) in the FRJ-2 reactor [4]. The resulting total tritium inventory in the breeder material is 30 g. Also this is a quite acceptable value.

A further improvement is given by the new arrangement of the manifolds feeding the helium to the cooling tubes of the first wall and the breeder region (Fig. 2). The two completely separated cooling systems and the separate cooling of the two sides (in the toroidal direction) of the breeder region are maintained. However, the manifold arrangement is such that two blanket slices adjacent in the poloidal direction are always cooled by tubes belonging to separate cooling systems. This has been deemed necessary to maintain the blanket temperatures at acceptable levels by a sudden loss of coolant from one of the two systems.

Table 1 shows the main results of the performed calculations.

The calculations of the loads in the box of the outboard blanket segment due to the electromagnetic forces caused by a major disruption have been improved to account for the fracture mechanics properties of the structural material [5]. The method to assess the effect of the ferromagnetic behavior of the structural material Manet on the electromagnetic forces caused by a disruption has been improved [6].

2. Fusion Water Cooled Ceramic Blanket for ITER with Li_4SiO_4 Pebbles

Following a suggestion of the European ITER Home Team KfK was working for the months May to July 1993 at a water

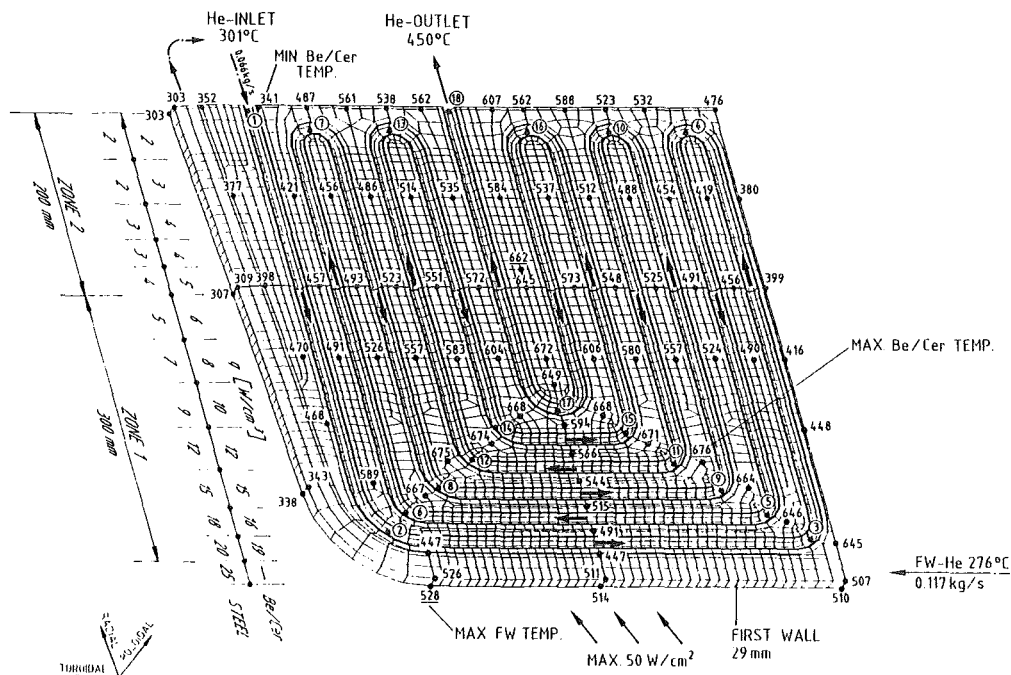


Fig. 1: Isometric view of a radial-toroidal equatorial slice of the outboard blanket segment showing the results of the temperature calculations

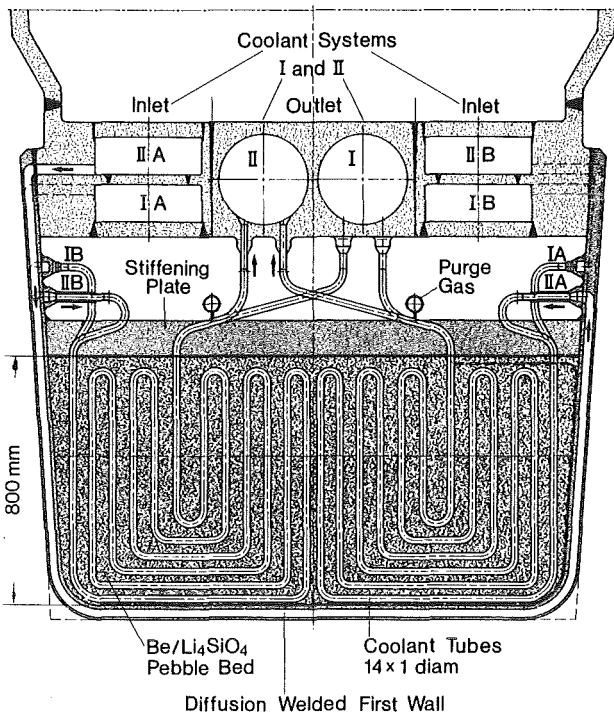


Fig. 2: Radial-toroidal section of the outboard blanket segment at the equatorial plane showing the new arrangement of the feeding tubes of the two separate cooling systems.

cooled ceramic blanket to offer as an alternative more conservative design of the presently prepared by the ITER Central Team.

The present design is derived from the design prepared by the NET team during the CDA phase, but it has been adapted to the new ITER geometry and boundary conditions. Namely, average neutron load = 1 MW/m², fusion power = 1.5 GW, max. First Wall heat flux = 25 W/cm². Temperatures and stress calculations have been performed for the F.W. also for the case with av. neutron load = 2 MW/m², fusion power = 3 GW and max. heat flux = 50 W/cm². In both cases the power excursion to 5 GW for 10 sec has been investigated. The structural material is solution annealed 316L stainless steel. The proposed ceramic breeder material is made of 0.3 - 0.6 mm lithiumorthosilicate (Li₄SiO₄) pebbles for which a lot of experience is available at the Karlsruhe Nuclear Center.

Fig. 3 shows an equatorial cross section of the outboard blanket. The first wall is cooled by water flowing in double walled poloidal tubes. Also the outer tube containing the cooling water and the breeder material is double walled (Fig. 4).

The neutronic calculations have been performed with the Monte Carlo code MCNP. The calculations account for the strong heterogeneity effects due to the presence of water. The resulting tritium breeding ratio is 1.05. The maximum burn-up of lithium for an average fluence of 1 MWa/m² is 3.5

<p>Breeder and multiplying material:</p> <p><u>region with higher power density:</u> mixed bed of 2 mm Be-pebbles and 0.08 - 0.18 mm Be and 0.1 - 0.2 mm Li₄SiO₄ pebbles (25 % Li⁶ enrichment)</p> <p><u>regions with lower power density:</u> mixed bed of 2 mm Be-pebbles and 0.1 - 0.2 mm Li₄SiO₄ pebbles (25 % Li⁶ enrichment)</p> <p><u>Coolant temperature:</u> inlet = 250 °C, outlet = 450 °C</p> <p><u>First wall max. temperature:</u> 530 °C</p> <p><u>Pebble bed temperatures:</u> min. = 341 °C, max = 676 °C</p> <p><u>Total blanket power:</u> 2500 MW (+ 300 M in the divertor)</p> <p><u>Real tridimensional tritium breeding ratio (assuming ten 3 x 1 m ports on outboard blanket):</u> 1.07</p> <p><u>Tritium production rate:</u> 370 g/d</p> <p><u>Tritium inventory in the breeder mat.</u> = 30 g</p> <p><u>Peak burn-up in Li₄SiO₄:</u> 6.5 %</p> <p><u>Peak fluence in beryllium:</u> 17000 appm He</p> <p><u>Peak fluence in MANET:</u> 70 dpa</p>

Table 1: Main characteristics of BOT Helium Cooled Solid Breeder Blanket for DEMO Reactor. Solution with Beryllium Pebbles.

% which is in the range of the irradiation data already available today for Li₄SiO₄.

Table 2 shows the results of the thermohydraulic calculations for the first wall and the blanket. The water inlet temperature of 200 °C has been chosen to ensure that the first wall remains above 200 °C even during the dwell time (ITER Central Team suggestion). The calculated temperatures are acceptable for the breeder material and the beryllium. To avoid vapor formation during the transients the water pressures have to be increased. If after an initial operation, these transients can be excluded, the water pressures in normal operation can be decreased to the lower values indicated in the brackets.

The stress calculations for the steady state show that in both the cases (fusion power=1.5 and 3 GW) the primary and secondary stresses in the first wall are acceptable according to the ASME norms. For the transient conditions the limitation is given by fatigue. The fatigue calculations have been performed for 10⁵ cycles for the steady state fusion powers of 1.5 GW and 3 GW, plus 10² cycles due to the 5 GW

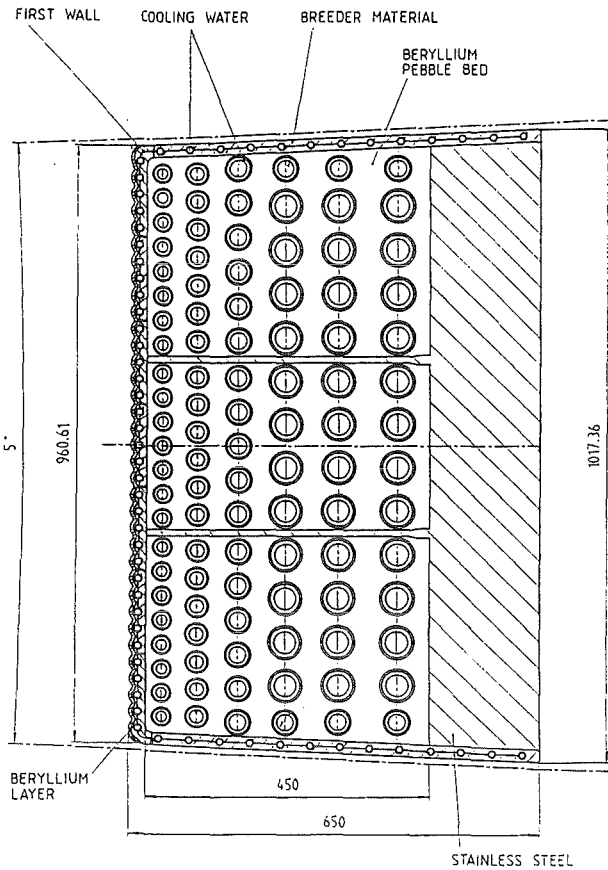


Fig. 3: Equatorial cross section of the outboard blanket segment

transients. The contribution to the fatigue damage given by the transients is small. Both cases are acceptable. The present design of the breeder region is not suitable for 3 GW operation, however it can be modified by decreasing the breeder tube diameters and increase their number so that acceptable temperatures are obtained for the case with 3 GW as well.

If the water inlet temperature in the first wall and blanket would be reduced to 170 °C, according to the TAC-2 suggestion, then the water pressure in the first wall and in the blanket could be reduced to 5.0 and 2.2 MPa, respectively.

The neutronic and thermal calculations allow to estimate the tritium inventory in the breeder material by on-line tritium release. This value is 80 g. In the case of a water inlet temperature in the blanket of 170 °C (outlet temperature = 200 °C) the tritium inventory would increase to 167 g. The end of life tritium inventory in the beryllium is 780 g. However, even at a temperature transient of up to 700 °C, various hours at this high temperature would be required to release more than about 40 g of tritium from the beryllium.

Calculations performed with the code IVA3 show that, in case of failure of the cladding and water leak in the region of the hot breeder material, the pressure build up in the breeder tube is limited by the coolant water pressure

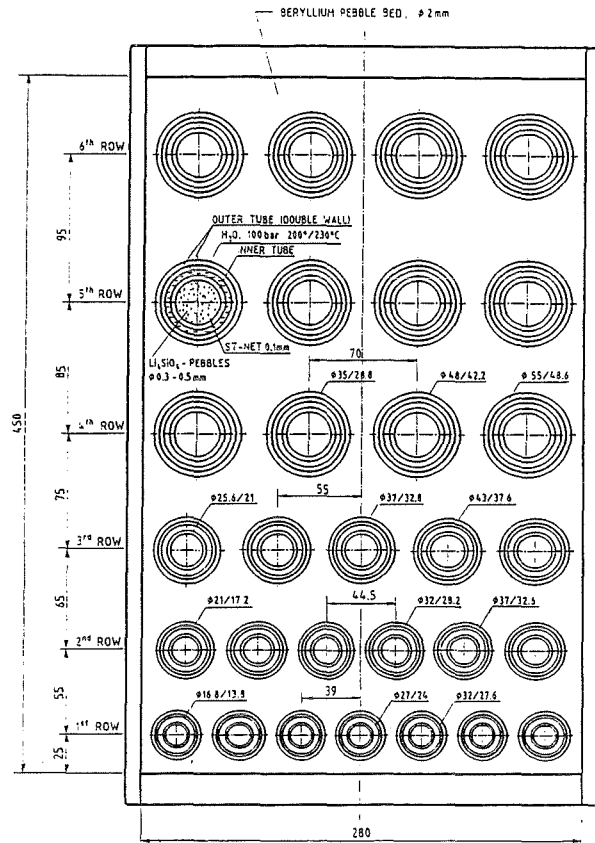


Fig. 4: Central portion of the equatorial cross section of the outboard blanket segment

	Av. neutron load = 1 MW/cm ² Max. F.W. heat flux = 25 w/cm ² Fusion power = 1.5 GW		Av. neutron load = 3 MW/cm ² Max. F.W. heat flux = 50 w/cm ² Fusion power = 3 GW	
	Steady state	Transient to 5 GW 10 sec	Steady state	Transient to 5 GW 10 sec
FIRST WALL				
Water inlet temp. (°C)	200	200	200	200
Water outlet temp. (°C)	229	277 (max)	260	280
Required outlet pressure (MPa)	6.5 (3.0)	6.5	7.0 (5.0)	7.0
Required inlet pressure (MPa)	7.5 (4.0)	7.5	8.0 (6.0)	8.0
Max. Temp. (°C)	271	423	354	445
BREEDER BLANKET				
Water inlet temp. (°C)	200	200	Design must be modified:	
Water outlet temp. (°C)	230	237 (max)	smaller breeder tube diameters and greater	
Required outlet pressure (MPa)	3.5 (3.0)	3.5	number of tubes, to	
Required inlet pressure (MPa)	3.7 (3.2)	3.7	obtain acceptable	
Breeder max. temp (°C)	710	815	breeder material	
Beryllium max. temp (°C)	350	385	temperatures.	

Table 2: Results of thermohydraulic calculations

Calculations with a tridimensional computer code for a similar first wall and blanket segment box show that, even with a disruption with a current quench time of 2 ms, the stresses in

the FW and box are acceptable provided there is a toroidal electrical connection of the blanket segment at the plasma facing side of the box.

Literature:

- [1] Nuclear Fusion Project Annual Report on the Association KfK/EURATOM Oct. 91 - Sept. 92., KfK 5099, EUR 14-795EN (Oct. 92.)
- [2] M. Dalle Donne, A. Goraieb, and G. Sordon, J. Nucl. Mater. 191 - 194 (1992), 149
- [3] M. Dalle Donne et al., Demo-relevant Test Blankets for NET/ITER, BOT Helium Cooled Solid Breeder Blanket, Vol. 2, KfK-4929 (1991).
- [4] W. Krug et al., In-pile Tritium Release from Ceramic Breeder Materials in TRIDEX Experiments 1-6. Fusion Eng. Design, 17 (1991), 65 - 71.
- [5] L.V. Boccaccini, Fracture Mechanics Assessment of the Karlsruhe Demo Blanket during Plasma Disruptions, 2nd Int. Workshop on Electromagnetic Forces and Related Effects on Blankets and Other Structures Surrounding the Fusion Plasma Torus, Tokai, Ibaraki, Japan, 15 - 17. Sept. 1993.
- [6] P. Ruatto, Electromagnetic Forces Computation for a Ferromagnetic Blanket Structure during a Plasma Disruption, *ibid.*

Staff: (ITER-Blanket)

L. Boccaccini
St. Böhmer
F. Dammel
M. Dalle Donne
B. Dolensky
U. Fischer
H. Jacobs
P. Norajitra
G. Reimann
H. Reiser
F. Scaffidi-Argentina
K. Schleisiek

Staff: (DEMO-Blanket)

L. Boccaccini
E. Bogusch
M. Dalle Donne
U. Fischer
K. Müller
P. Norajitra
K. Philipp
D. Piel
G. Reimann
H. Reiser
P. Ruatto

BS BE-D 1 Beryllium

Modelling of Swelling and Tritium Release in Irradiated Beryllium

1. Introduction

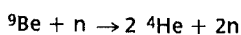
The operating conditions in the blanket of the DEMO Fusion Reactor [1] (fast neutron fluence $\approx 2.5 \times 10^{22}$ n/cm²s ($E_n > 1$ MeV), operation time ≈ 20000 h, helium content ≈ 17000 appm) dictate the necessity of evaluating beryllium behaviour under fast neutron irradiation conditions typical of the next generation of fusion reactors. To our knowledge, no computer codes are as yet available which describe the possible processes occurring during beryllium irradiation. It was thus decided to develop a mechanistic code to predict the performance of beryllium in the blanket up to high neutron fluences.

A code, previously written at the Institute for Transuranium Elements in Karlsruhe for analysing the behaviour of fuel pellets in fission reactors [2], was modified to model all the relevant processes which are thought to affect gas behaviour and swelling in beryllium.

To evaluate the performance of the new computer code calculations for a wide range of irradiation conditions were carried out. Additionally, a first analysis for the KfK BOT Solid Breeder Blanket [1] was also performed. The aim of this study is to describe the analytical approach used in the new code and to discuss the results obtained.

2. Computer Code Model

The gas kinetics and dynamics of the helium-induced swelling in beryllium have been described by a system of reaction-rate differential equations. All the relevant effects occurring in irradiated beryllium under stationary or transient temperature conditions have been considered on a microscopic (lattice and subgranular volume elements), structural (metallographic features of the material) and geometrical (specimen design parameters) point of view. The beryllium specimen was ideally considered as an arrangement of spherical grains in which helium generated by the reaction:

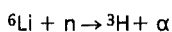
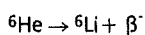
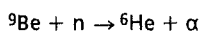


(which has a neutron energy threshold of 1.85 MeV), migrates to the free surfaces and/or precipitates into intragranular bubbles. These can also migrate (at much lower rate than the free atoms) through the grains to the grain boundaries to form grain-face bubbles and grain-edge bubbles (intergranular bubbles) usually larger than the intragranular ones. Bubbles may grow by capture of gas and coalesce to create larger bubbles with a lower restrain capillarity pressure. The growth of intragranular and intergranular bubbles causes a plastic deformation of the lattice resulting into material swelling. For relatively large volume increases, grain-face and grain-edge bubbles can become interlinked

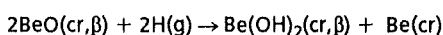
and merge into an open porosity network through which the gas can escape from the specimen. The modelling of the interlinkage of intergranular pores and bubbles is based on percolation theory [3].

The developed mathematical model is expressed by a system of seven reaction-rate differential equations which describe the helium short and long-range transport. These equations, which account for the concentrations of the gas in dynamical solution, in intragranular bubbles, grain-face bubbles and grain-edge bubbles, consist of a sum of terms which represents a source or loss-rate of the respective concentration due to a distinct mechanism. A more detailed discussion of their expression is given in [2]. The reaction-rate equations are integrated by using the three bubble radii r_i , r_f , r_e of the intragranular, grain-face and grain-edge bubbles respectively, calculated from additional expansion equations resulting from the interplay of all forces (i.e. gas pressure, capillarity stresses, internal stresses, etc.) acting on the intragranular, grain-face and grain-edge bubbles respectively. A major part of the present work consisted in reformulating the constitutive relations used in these equations and select the parameters specific to beryllium, the most important of which are listed in Tab. 1.

The model used to describe the behaviour of tritium is formally identical to that of helium. The only important difference is due to an additional rate-equation accounting for the chemical trapping of the tritium by oxygen impurities. Furthermore, in the case of tritium no distinction was made between bubbles on grain-faces and bubbles on grain-edges which, for calculations purposes, were considered as a single population. Schematically, the tritium behaviour is described as follows: once it has been generated by the chain of reactions



it can diffuse in the lattice, or be captured by physical traps (such as intragranular helium bubbles, closed porosity, grain boundaries, etc. as in the case of helium), or it may react with beryllium oxide to form beryllium hydroxide by the chemical reaction:



the STP formation enthalpy of which is ≈ -0.7 eV.

Experiments conducted up to the present time [4] [5] [6], show that in beryllium irradiated at relatively low temperatures and fluences, tritium is mainly captured by "chemical traps" as beryllium hydroxide, whilst for highly irradiated beryllium tritium appears to be mainly trapped in helium bubbles. At intermediate temperatures and fluences both the above mechanisms are important.

Properties	Physical laws		Ref.
Solid surface tension [dyn/cm]	$\gamma = 3130.24$	$T < 780 \text{ }^\circ\text{K}$	[13]
	$\gamma = 1960 - 1.5 \times (T - 1560.16)$	$T < 1560 \text{ }^\circ\text{K}$	[14]
	$\gamma = 1960$	$T \geq 1560 \text{ }^\circ\text{K}$	
Grain boundary surface energy [erg/cm ²]	$\gamma_{gb} = 1076.08$	$T < 780 \text{ }^\circ\text{K}$	[15]
	$\gamma_{gb} = 686 - 0.5 \times (T - 1560.16)$	$T < 1560 \text{ }^\circ\text{K}$	
	$\gamma_{gb} = 686$	$T \geq 1560 \text{ }^\circ\text{K}$	
Self-diffusion coeff. [cm ² /s]	$D_{v\perp} = 0.52 \times \exp(-18916.15/T)$	$T \geq 838 \text{ }^\circ\text{K}$	[16]
	$D_{v\parallel} = 0.62 \times \exp(-19844.55/T)$	$T \geq 838 \text{ }^\circ\text{K}$	
	$D_v = 3.14 \times 10^{-6} \times \exp(-9105.03/T)$	$T < 838 \text{ }^\circ\text{K}$	
Surface-diffusion coeff. [cm ² /s]	$D_{v\perp} = 0.52 \times \exp(-18916.15/T)$	$T \geq 838 \text{ }^\circ\text{K}$	
	$D_{v\parallel} = 0.62 \times \exp(-19844.55/T)$	$T \geq 838 \text{ }^\circ\text{K}$	
	$D_v = 3.14 \times 10^{-6} \times \exp(-9105.03/T)$	$T < 838 \text{ }^\circ\text{K}$	
Bubble-diffusion coeff. [cm ² /s]	$D_b = (3\lambda^3/2\pi r^3 f)D_v + (3\lambda^4/2\pi r^4)D_s$		[17]
Helium-diffusion coeff. [cm ² /s]	$D_{He} = 3.1 \times 10^{-2} \times \exp(-25817.8/T)$	$T \geq 873 \text{ }^\circ\text{K}$	[18]
	$D_{He} = 9.889 \times 10^{-13} \times \exp(-4718.87/T)$	$T < 873 \text{ }^\circ\text{K}$	
Tritium-diffusion coeff. [cm ² /s]	$D_T = 9.18 \times 10^{-3} \times \exp(-7702.89/T)$	$T \geq 873 \text{ }^\circ\text{K}$	[6]
	$D_T = 1.73 \times 10^{-5} \times \exp(-2225.16/T)$	$T < 873 \text{ }^\circ\text{K}$	
Thermal creep rate [1/s]	$\dot{\epsilon}_t = 0.02 \times \sigma^{3.6} \times \exp(-26000/T)$		[19]
Irradiation creep rate [1/dpa]	$\dot{\epsilon}_i = 3.2 \times 10^{-12} \times \sigma$		[20]
Vapour pressure [atm]	$\log p = 6.186 + 1.454 \times 10^{-4} \times T - 16734/T$		[21]

Table 1: Beryllium, helium and tritium properties

At present a first version of the code based on the above-mentioned assumptions is available, and is being validated by comparison with a large number of experiments. First results using this code are given below.

3. Results

Beryllium in-pile irradiations [7] [8] [9] [10] [11] have been considered for our calculations. A comparison of the calculated swelling with in-pile experimental data for a wide range of irradiation conditions (i.e. irradiation temperatures from 60°C to 700 °C, neutron fluences from 2.1×10^{21} n/cm² s ($E_n > 1$ MeV) to 5.0×10^{22} n/cm² s ($E_n > 1$ MeV), helium contents from 500 appm to 26100 appm) is shown in Fig. 1.

This data covers the range of irradiation temperatures and neutron fluences applicable to the DEMO blanket. Experimental data for combined high temperatures and fluences is, as yet, unavailable. The agreement between calculated swelling and experimental data is excellent (mean error +0.9%, standard deviation 13.3%), whereby the error is probably due to the relatively large uncertainty in the

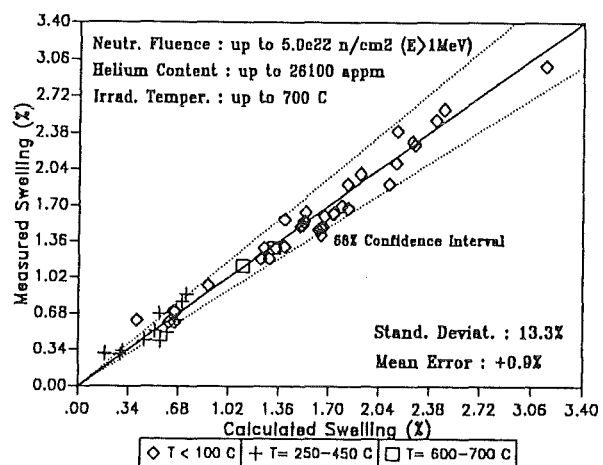


Fig. 1: Comparison of calculated and experimental swelling data for in-pile irradiated beryllium [7] [8] [9] [10] [11]

experimental conditions (i.e. fast flux, helium generation rate, volumetric heat generation, etc.). A further cause of

uncertainty is due to material properties (i.e. creep law, helium diffusion coefficient, etc.) which are affected by the manufacturing processes and impurity content.

Data on tritium release is available from the post-irradiation annealing results of Baldwin (for both moderately irradiated 99% dense and highly irradiated 100% dense beryllium) [4] [5], and from the SIBELIUS experiment for a low-irradiated 98% dense beryllium [12], which cover a wide range of temperatures and oxygen impurity content. In Baldwin's experiments [5] [6] beryllium contained a relatively high quantity of oxygen (1.5-2.0 wt% BeO), and the initial irradiation at low temperature (75 °C) was followed by out-of-pile annealings at temperatures from 300 to 900 °C. As it can be seen from Fig. 2, for temperatures up to 700 °C the

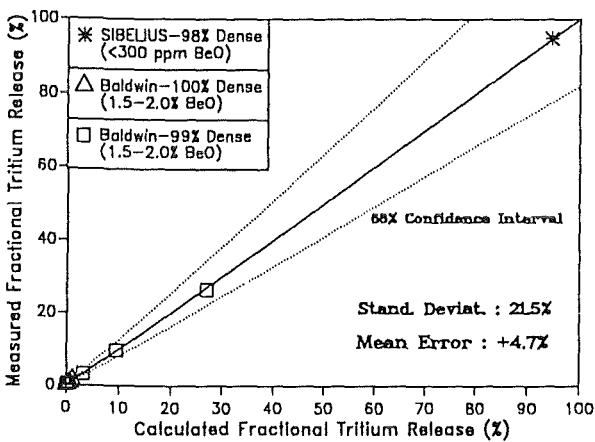


Fig. 2: Arrhenius plot of the cumulative out-of-pile annealing fractional tritium release in the experiments of Baldwin [5] for 99% dense beryllium as compared to calculated results.

tritium release is mainly governed by a single energy thermally activated (chemical) process, as demonstrated by the linear trend of the fractional release shown in the Arrhenius plot.

In the SIBELIUS specimens, due to the very low oxygen content (BeO < 300 ppm) and low irradiation fluence (6.0×10^{20} n/cm²), the tritium release is predominantly due to atomic diffusion through the lattice, with both chemical and He-bubble trapping of tritium playing a minor role. Data for in-pile tritium release from irradiated beryllium is not yet available. As it can be seen from Fig. 2 and Fig. 3, the agreement between calculated and experimental out-of-pile annealing data for the end of each annealing step is good (mean error +4.7%, standard deviation 21.5%).

In order to evaluate beryllium swelling and tritium release during normal reactor operating conditions, a first calculation for the proposed KfK BOT DEMO blanket [1] was performed. Calculations for beryllium pebbles under a variety of irradiation temperatures and fluences appropriate to the DEMO blanket have been carried out. The results are shown in Fig. 4.

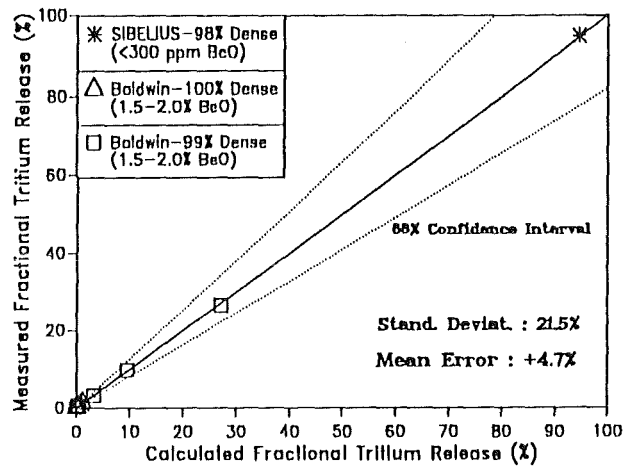


Fig. 3: Comparison of cumulative fractional tritium release calculations to experimental data for out-of-pile annealed beryllium [5] [6] [12].

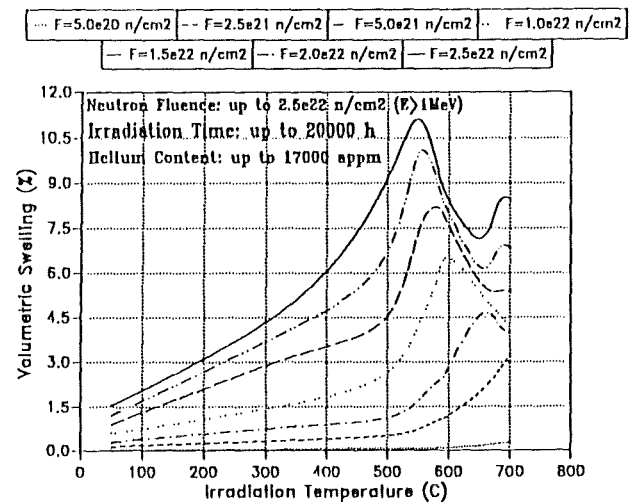


Fig. 4: Volumetric swelling vs. irradiation temperature at different fast neutron fluences for the DEMO BOT [1] beryllium as predicted by ANFIBE.

It can be noticed that swelling initially increases with irradiation temperature; for high fluences, however, this trend is inverted due to release of helium. At higher irradiation temperatures the initial trend of the swelling behaviour is found again due to the rapid coalescence of the gas bubbles and to the reduction of the mechanical strength of the material.

With regard to the release of tritium, as shown in Fig. 5, the approximately linear dependence of the logarithm of release on $1/T$ up to about 450 °C (temperature at which an upswing in helium release is observed), suggests that a single thermally activated process is operating up to this temperature. Above 450 °C release is controlled by tritium trapped in helium bubbles, as indicated by the departure from linearity of the fractional-release curve in the Arrhenius plot. Although the effective mechanism governing the release of tritium in irradiated beryllium is so far uncertain, the experiments [5] [6]

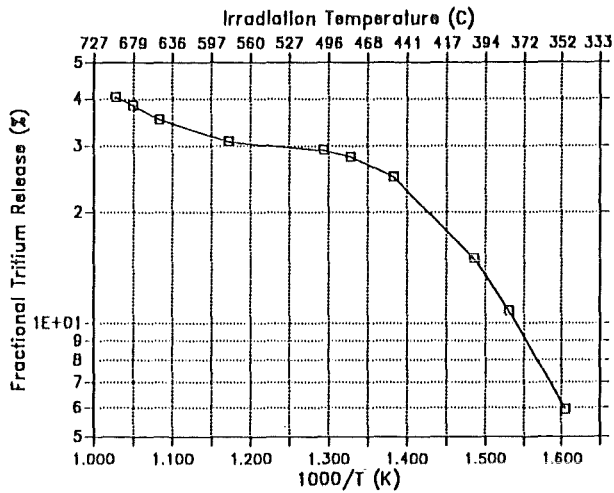


Fig. 5: Arrhenius plot of the cumulative in-pile-irradiation fractional tritium release vs. irradiation temperature for the DEMO BOT [1] beryllium as predicted by ANFIBE.

performed up to this time seem to confirm that the above-mentioned conclusions are fundamentally correct.

4. Conclusions and Future Work

The ANFIBE code describes satisfactorily the beryllium swelling and tritium release in in-pile tests. However, to improve the reliability of the code predictions, further in-pile experiments at high temperatures and neutron fluences are clearly required. Additional code development is also needed in order to describe both the behaviour of beryllium at temperatures higher than 700 °C where, as it has been noted experimentally, a "burst" release of the tritium associated with a "breakaway" swelling occurs [5] [6], and the behaviour of beryllium with fabrication open porosity.

Literature:

[1] M. Dalle Donne et al., "Conceptual Design of a Helium Cooled Solid Breeder Blanket Based on the Use of a Mixed Bed of Beryllium and Li₄SiO₄ Pebbles", Proc. 17th Symp. Fusion Technology, Rome 14. - 18. Sept. 1992, p. 1326.

[2] C. Ronchi and J. Van der Laan, EUR Report, 11387 EN (1988).

[3] C. Domb and M.S. Green, Phase Transitions and Critical Phenomena, Vol. II, (Academic Press, London, 1972) p. 197.

[4] G.R. Longhurst, Tritium Behaviour in ITER Beryllium, EG&G Idaho Report, EGG-FSP-9304 (1990).

[5] M.C. Billone, Private Communication (1993).

[6] M.C. Billone et al., Fusion Technol. 19 (1991) 1707.

[7] J.M. Beeston, Properties of Irradiated Beryllium: Statistical Evaluation, EG&G Idaho Report, TREE-1063 (1976).

[8] J.M. Beeston et al., J. Nucl. Mater. 122 & 123 (1984) 802.

[9] E. Koonen, Study on Irradiation Effects and Swelling of Irradiated Beryllium, CEN/SCK Report, Reactor Safety Analysis BR2 Department, (1989).

[10] J.M. Beeston et al., Gas Retention in Irradiated Beryllium, EG&G Idaho Report, EGG-FSP-9125 (1990).

[11] V. Levy, Rapport Final du Contrat SBB-BS1, CEA Report, Centre d'Etudes de Saclay, N.T. SRMA 92-1955 F.A 3591-532 (1992).

[12] W. Dienst et al., Tritium Release of Li₄SiO₄, Li₂O and Beryllium and Chemical Compatibility of Beryllium with Li₄SiO₄, Li₂O and Steel (SIBELIUS Irradiation), KfK Report, Kernforschungszentrum Karlsruhe, 5109 (1992).

[13] Brush Wellman Inc., Private Communication (1992).

[14] Ullmann's Encyclopedia of Industrial Chemistry, Vol. A4, (VCH, Weinheim, 1985) p. 12

[15] L. Murr, Interfacial Phenomena in Metals and Alloys, (Addison-Wesley Publishing Company, Reading, 1975) p. 130.

[16] J.M. Dupoy et al., Mém. Scientif. Rev. Metallurg. 63 (1966) 481.

[17] C Ronchi, J. Nucl. Mater. 84 (1979) 55.

[18] A.G. Bepalov et al., Tr. Fiz.-Energ. Inst. (1974) 443.

[19] M.C. Billone: Private Communication (1992).

[20] W.G. Wolfer and T.J. McCarville, An Assessment of Radiation Effects in Beryllium, Presented at the Sixth Topical Meeting on the Technology of Fusion Energy (San Francisco, 1985).

[21] N.P. Pinto, Beryllium Science and Technology, (Plenum Press, New York, 1979) p. 342.

Staff:

M. Dalle Donne
 C. Ferrero
 C. Ronchi
 F. Scaffidi-Argentina

BS BR-D 1/D 2 Preparation and Characterization of Ceramic Breeder Materials

The preparation of lithium containing monosilicates, especially Li_4SiO_4 are under development to be used as breeder materials within the European Fusion Program. The development was concentrated on the annealing of lithium orthosilicate spheres fabricated by melting. Because of the rapid quenching from the melting temperature the pebbles exhibit internal stress and may also contain cracks. If the pebbles contain a slight excess of silica (2.2 wt%) annealing and recrystallization above 1024 °C can lead to healing of microcracks and finally to an improvement of the mechanical properties. On the other hand pebbles with a excess of 2.2 wt% SiO_2 show a dendritic structure as an indication of a supercooled liquid. During annealing above 1024 °C the crystalline phase of Li_4SiO_4 and the silicon rich liquid exist together and the pebbles tend to stick together.

To prevent the pebbles from sticking together the annealing was performed in a high temperature fluidized bed. It consists of a vertical, heated tube with an expansion vessel at the upper end to reduce the gas velocity. A gas stream with a temperature of 500 °C is blown via a frit into the lower section of the vessel to keep the pebbles in turbulent movement. The annealing experiments were carried out with an amount of 400 g of Li_4SiO_4 pebbles with diameters in the range from 300 to 630 μm . At polished and etched cross sections of the pebbles the change of the microstructure was examined before and after the annealing. The disappearance of the dendritic structure was chosen as a criterion for a successful annealing.

The experiments showed that it is difficult to reach a homogeneous fluidization and a homogeneous change in microstructure with the given diameter range of the pebbles. Heavier pebbles with a larger diameter stayed in the lower part of the reaction tube. Because of the lower temperature in this part the microstructure remains unchanged during annealing. The optimization of the process parameters led to the following values:

heating rate:	380 °C/h
annealing time:	1 h
max. temperature	
at the furnace wall:	1150 °C
in the reaction tube:	1020 - 1030 °C
gas flow rate:	3 - 5 m^3/h
cooling rate:	400 °C/h

Annealing experiments with these process parameters led to recrystallization of almost all pebbles in the diameter range between 300 and 500 μm but to no agglomeration (Fig. 1).

Consequently it is possible to anneal Li_4SiO_4 pebbles fabricated by melting successfully in the fluidized bed if the range of diameters is narrow enough to guarantee a complete fluidi-

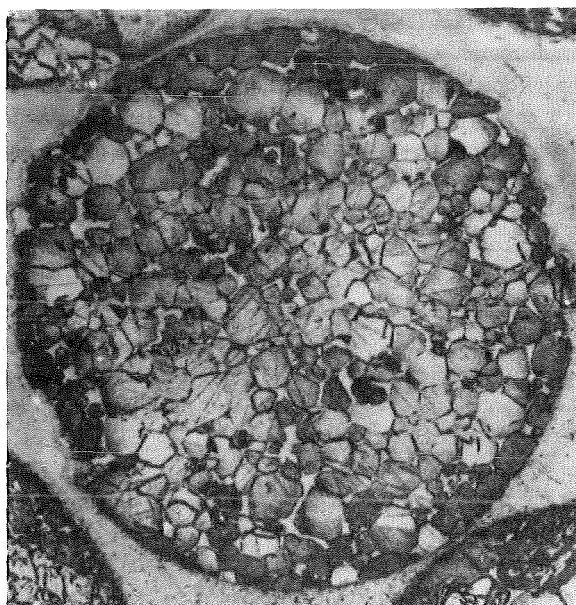
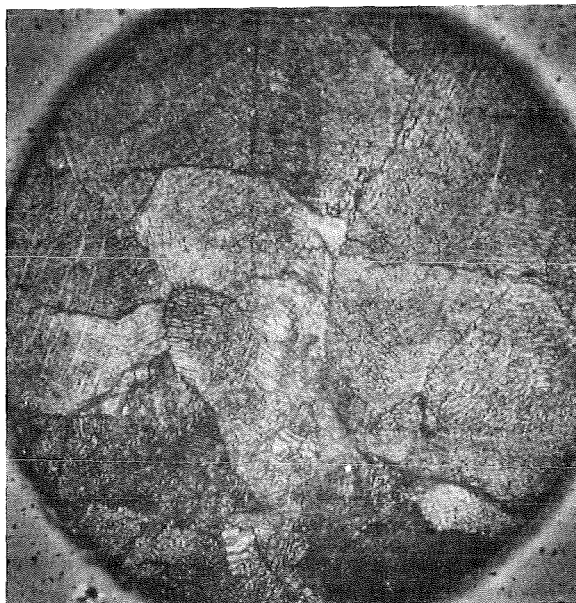


Fig. 1: Microstructure of the Li_4SiO_4 pebbles before and after annealing in the fluidized bed (200 : 1).

zation of the bulk material in the constant temperature zone of the reaction tube.

Staff:

E. Günther
 R. Hanselmann
 J. Heger
R. Knitter
 W. Laub
 U. Maciejewski
 C. Odemer
H. Wedemeyer

BS BR-D 3 Irradiation Testing and Post Irradiation Examination

Post Irradiation Examination

The investigation of the effects of irradiation on physical properties and integrity, microstructure and thermo-mechanical performance of breeder ceramics was the main purpose of the ALICE type irradiations. Irradiations of ALICE type so far were performed in the past in OSIRIS for needs of CEA and for needs of European partners in the frame of the fusion projects.

In the irradiation experiment ALICE 03 pebbles of Lithiumorthosilicate and - zirconate from KfK were irradiated besides other Lithiumcompounds of the European partners. The fabrication and characterization of the 6 KfK samples is documented in [1]. The irradiation was performed under Helium in special capsules between 15. Nov. 1990 and 15. January 1991.. The capsules containing the KfK material are specified in Tab. 1. Capsule A was a bigger container with 15 mm diameter, whereas the capsules B, C1, C2, C3 & C4 were smaller ones with only 6 mm dia. Capsule A with a volume of 8 cm³ was filled with Lithiumorthosilicate-pebbles for measurement of the thermal conductivity of the pebble bed. As can be seen in Fig. 1 (A) the pebbles were found molten after dismantling the capsule at KfK Hot Cell FKL. In the melting zone near the central thermocouple temperatures of ≥ 1250 °C should have been reigned (cif. Fig. 2). The contents of the smaller (15 mm dia) capsules can be seen in Fig. 1: the pebbles were intact. Fig. 3 shows a ceramographic cross section of capsule A: it shows the molten center, surrounded by columnar grains, in the outer clad near region we can perceive a ring of intact pebbles.

The irradiation data for ALICE 03 are for the time being not available at KfK. It was assumed that the maximum temperature in the capsule was at least 1300 °C. With an average thermal conductivity of 0.014 w/cm² K in the pebble bed [2] it was calculated by an analytical formula for the temperature distribution in the capsule that the linear rod power must have been at/or above 165 w/cm.

The measurement of T-release of the pebbles of capsules B and C1 to C4 (Tab. 1) is performed. Results will be published.

Literature:

- [1] E. Günther, R. Knitter, H. Wedemeyer. KfK Unpublished Report Dec. 1990
- [2] H. E. Häfner, K. Philipp. KfK Unpublished Report Aug. 1992

Fabricated by	Capsule No.	Material	Irradiation temperature	Action
Schott	A	Li ₄ SiO ₄ + 2,2 % SiO ₂	450 °C	(■) T, K, R, P, W, S, X
Schott	B	Li ₄ SiO ₄ + 2,2 % SiO ₂	650 °C	■ T, K, R, P
Schott	C1	Li ₄ SiO ₄ + 2,2 % SiO ₂ + 1 % Al ₂ O ₃	650 °C	■ T, K, R, P
HITEC	C2	Li ₂ ZrO ₃	650 °C	■ T, K, R, P
KfK	C3	Li ₄ SiO ₄	650 °C	■
KfK	C4	Li ₄ SiO ₄	650 °C	■ T, K, R, P

Legend

- dismantled
- T T-Release Measurement
- K Ceramography
- R Scanning Electron Microscopy
- P Mercury Porosimetry
- W Measurement of thermal conductivity
- S Strength against thermal shock
- X X-Ray diffraction studies

Status of the Action

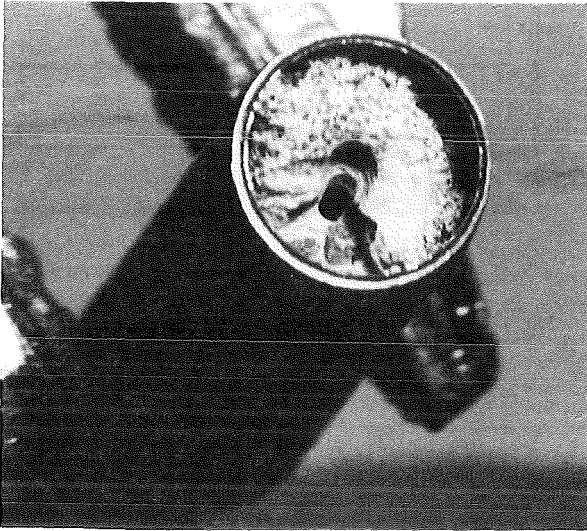
- Specimen ready for examination
- Examination performed

Table 1: KfK-capsules of ALICE 03

Staff:

- E. Kaiser
- D. Knebel
- R. Pejsa
- O. Romer
- H. Steiner
- P. Weimar
- F. Weiser
- H. Ziegler
- L. Dörr

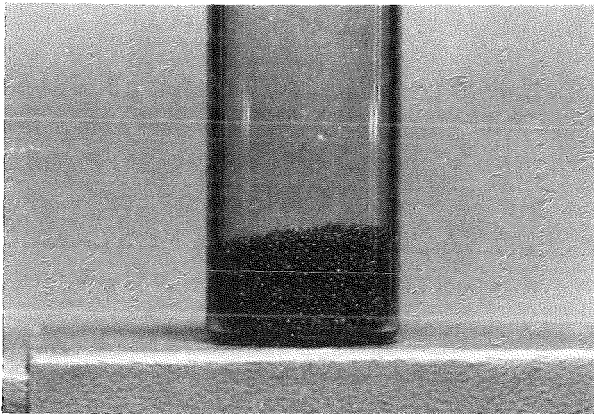
ALICE 03 Fig 1: Visual Inspection of the KfK-pebbles after Dismantling



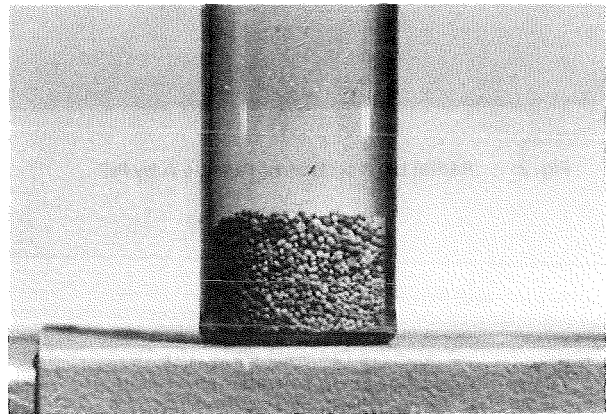
A
Schott $\text{Li}_4\text{SiO}_4 + 2,2\% \text{SiO}_2$



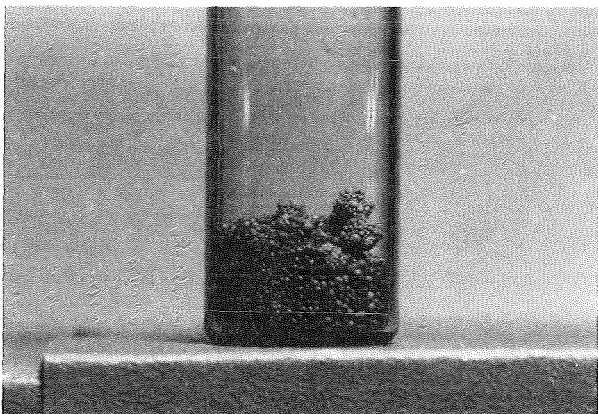
C2
HITEC Li_2ZrO_3



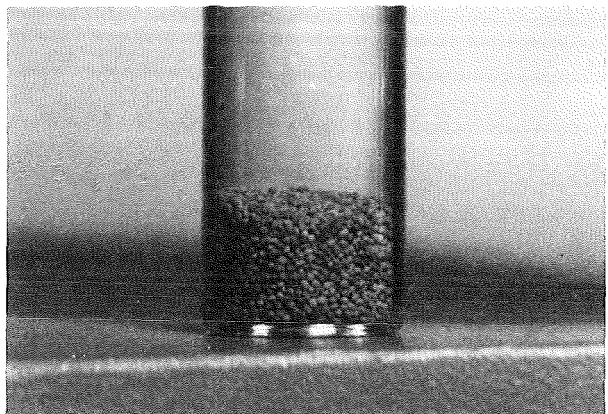
B
Schott $\text{Li}_4\text{SiO}_4 + 2,2\% \text{SiO}_2$



C3
KfK Li_4SiO_4



C1
Schott $\text{Li}_4\text{SiO}_4 + 2,2\% \text{SiO}_2 + 1\% \text{Al}_2\text{O}_3$



C4
KfK Li_4SiO_4

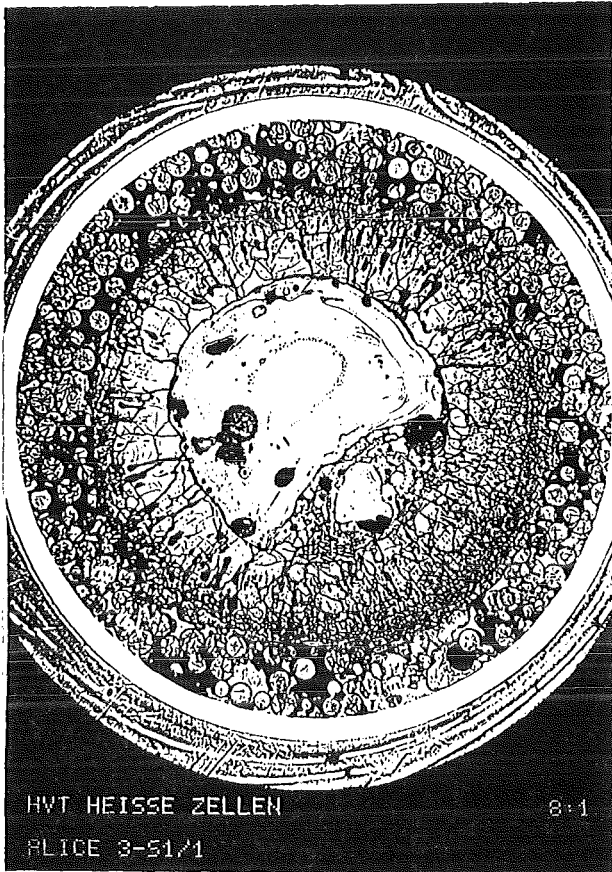


Fig. 2: Radial cross section of capsule A by PIE

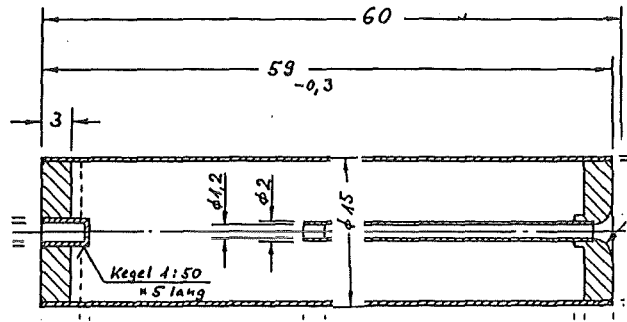


Fig. 3: Axial cut of capsule A with dimensions

BS BR-D 4 Tritium Release

In assessing the performance of ceramic breeders, tritium release is an important aspect. KfK concentrates on lithium orthosilicate and metazirconate. Purged inpile and out-of-pile annealing tests are performed.

The main goal of the purged inpile tests SIBELIUS, performed April to October 1990 at CEN Grenoble, was to study the compatibility of breeder ceramics /Be/ steel in a neutron environment. Results from inpile tests and from PIE concerning compatibility and tritium release, especially from beryllium [1, 2] have been discussed in previous annual reports. Spare samples from the SIBELIUS irradiation are now used to study tritium release from beryllium over long times (12 months) at different temperatures (380, 450, 550 and 650 °C) [3].

In the CORELLI-1 inpile test, performed May to July 1991 at CEN Grenoble, orthosilicate pellets with different grain sizes (7 and 80 µm) were tested by KfK. Whereas out-of-pile annealing, performed before the inpile test, indicates a faster release from the small grains, inpile tests, surprisingly, demonstrated a faster release from the large grains. PIE and tritium annealing tests of the irradiated CORELLI-1 samples firstly proved that the samples have not been mixed up during handling and confirmed the inpile observation of faster release from the large grains [4].

In the second joint European medium-burnup (3 % total Li) inpile test EXOTIC-6, performed at the HFR Petten from May 1991 to March 1992, reference breeder materials of the participating laboratories were tested [5]. Both KfK samples, Li_4SiO_4 and Li_2ZrO_3 pebbles survived the 200 FPD irradiation without visible damage. Because of the pretty large radial temperature difference (up to 180 °C) between the center and the boundary of the samples, a careful estimation of the temperature distribution and an iterative procedure is required to determine relevant tritium residence times [6]. The residence times of both samples determined in this way were found to be in acceptable agreement (factor three) with previous low-burnup inpile tests (TRIDEX). In addition, there were no indications that the residence times increased with burnup to 3 % [6].

The high-burnup (up to 10 % total Li) joint European inpile tests EXOTIC-7, to be performed at the HFR Petten 1994 with samples enriched to about 50 % Li^6 is in preparation. Mixed beds of Be and orthosilicate spheres will be tested by KfK.

The extensive annealing studies with a variety of samples from the joint European, closed capsule, fast/thermal neutrons irradiation COMPLIMENT have been finished, a report is in preparation.

A closed capsule irradiation of Be and orthosilicate pebbles to study irradiation-induced swelling and embrittlement of Be and tritium release of Be and orthosilicate to be performed in the first half of 1994 is in preparation at HFR Petten.

Literature:

- [1] H. Werle, "Tritium Release from Beryllium Irradiated in the SIBELIUS Experiment", 17th SOFT, Rome, 1992.
- [2] W. Dienst, D. Schild, H. Werle, "Tritium Release of Li_4SiO_4 , Li_2O and Beryllium and Chemical Compatibility of Beryllium with Li_4SiO_4 , Li_2O and Steel (SIBELIUS Irradiation)", KfK 5109 (Dez. 1992).
- [3] L. Dörr, T. Eberle, H. Werle, "Long-time Tritium Release from Irradiated Beryllium (SIBELIUS Irradiation)", Workshop on Beryllium for Fusion Application, Karlsruhe, October 1993.
- [4] E. Günter, H. Wedemeyer, H. Werle, "Influence of Grain-Size on Tritium Release from Lithium Orthosilicate (Irradiation CORELLI-1)", Second Int. Workshop on Ceramic Breeder Blanket Interactions, Paris, September 1993.
- [5] H. Kwast et al., "The Effect of Purge Gas Composition on the Release of Tritium from Ceramic Breeder Materials Irradiated in EXOTIC-6", 17th SOFT, Rome, 1992.
- [6] H. Werle, KfK, Unpublished Report, August 1993

Staff:

T. Eberle
J. Lebkücher
M. Möschke
H. Werle

BS BR-D 5 Irradiation Testing and Post-Irradiation Examination

1. Mechanical Properties

Compressive strength measurements were performed on breeder pellets of the COMPLIMENT irradiation experiment. 3 or 4 pellets were available of each sample column examined. Large strength reductions under neutron irradiation were observed for all breeder materials. The damage dose which was nominally constant (1.8 dpa) showed a wide variation (1.35 - 3 dpa) which, however, had no obvious influence on the strength decrease. Therefore the percentage strength reduction of the breeder materials investigated (Fig. 1) is presented in dependence on the lithium burnup, which was different on purpose for ELIMA 02 and DELICE 03 (0.4 % and 1.4 % Li). The initial strength values were in the range of about 200 to 300 MPa.

Fig. 1 gives an obvious ranking of the different breeder

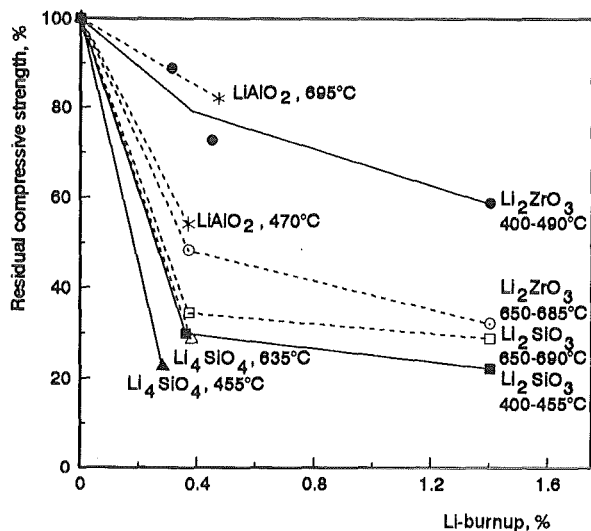


Fig. 1: Percentage decrease of the compressive strength of ceramic breeder materials at different Li-burnup.

materials concerning the irradiation sensitivity of their fracture strength, and that in the sequence lithium aluminate, zirconate and silicates, the latter compounds being most sensitive. This may be due to the specific character of the silicate lattice bonding. One could suppose that the strength degradation of the silicates is mainly caused by lattice damage, and thus not directly dependent on the Li-burnup as indicated in Fig. 1. But the rather high homologous sample temperature under irradiation ($T_{irr}/T_m \approx 0.45$ and 0.6 K/K), suggests coarse defect aggregates being responsible instead of point defects. Of course, the tritium supply from Li-burnup could advance the formation of voids or even gas bubbles in this connection. Such influence is more obvious from the Li₂ZrO₃ results, which show the fracture strength being degraded with increasing Li-burnup as well as with increasing irradiation temperature, now in the range of

$T_{irr}/T_m \approx 0.35 - 0.5$ K/K where formation but no considerable healing of coarse defect aggregates can be expected.

2. Corrosion Behaviour

Chemical attack of the Cr-Ni stainless steel cladding was investigated on some breeder rod samples of the COMPLIMENT irradiation experiment. Reaction rates derived from the maximum penetration depths are given in Fig. 2. For

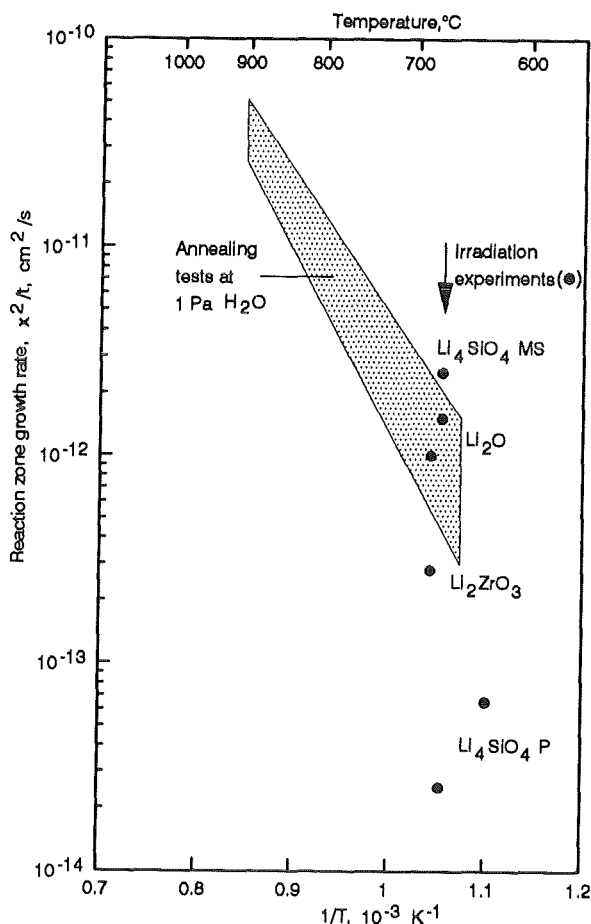


Fig. 2: Comparison of the chemical attack of ceramic breeder materials on Cr-Ni steel capsules under neutron irradiation with that in annealing tests at 1 Pa H₂O partial pressure

most of them (like "Li₄SiO₄P" or even below 10⁻¹⁴cm²/s) it seems probable that the cladding attack was limited to the effect of tritium water generated by the breeding process, if steel passivation and, on the other hand, local concentration of the attack is taken into consideration. But for the four samples with higher reaction rates additional influences have to be considered. One could suppose that they contained oxidizing impurities (H₂O, CO₂) that intensify local attack and render the reaction product layer more permeable, which is especially indicated by a marked, deep diffusion zone with distinct etching and hardening effects. Only the reaction rates of these samples come into or near the band of results of comparable laboratory annealing tests at 1 Pa H₂O partial pressure (see Fig. 2) [2]. Consequently, one can expect tritium water vapour pressures far below 1 Pa for similar breeder

material/cladding configuration and temperature level, and the annealing test results at 1 Pa H₂O can be regarded as conservative data.

Literature:

- [1] W. Dienst, H. Zimmermann; Strength change and chemical reactivity of ceramic breeder materials near operation conditions, 6th Int. Conf. on Fusion Reactor Materials, Stresa, September 27 - October 1, 1993, Paper D004
- [2] P. Hofmann, W. Dienst; Fusion Technology 1992, C. Ferro, M. Gasparotto, H. Knoepfel (editors), 1993, Elsevier Science Publishers B.V., p. 1374

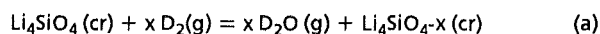
Staff

W. Dienst

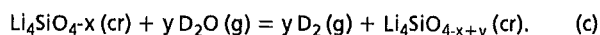
H. Zimmermann

BS BR-D 8 Thermochemistry of the Reaction of Lithium Orthosilicate with Hydrogen

The formation of water vapor on exposure of lithium orthosilicate to hydrogen was observed to occur at temperatures such as anticipated in conceptual blanket design studies. In the case of this lithium ceramic material there is evidence that an oxygen deficient layer is formed at the ceramic surface. This layer is capable of reducing water to hydrogen. The following reactions are assumed to occur between the lithium orthosilicate surface and deuterium



together with



In this investigation the reaction of lithium orthosilicate with hydrogen was studied by mass spectrometric analysis of the effusates from a reaction Knudsen cell. Several long-term experimental runs comprising the measurement of the partial pressures of D_2 , D_2O , Li , and LiOD were performed in the temperature range $945 < T < 1173$ K and an average deuterium pressure of $(6.3 \pm 0.6) \times 10^{-5}$ bar. The reaction of deuterium with lithium orthosilicate causes first a rapid build-up of the deuterium partial pressure and subsequent slow decrease to nearly constant values. The oxygen partial pressure, which is calculated from the D_2O and D_2 pressures shows, of course, the same time dependence. In spite of the very low partial pressures of Li and LiOD at this temperature, the corresponding data were obtained with reasonable precision. The partial pressure of lithium under the deuterium pressure mentioned above is orders of magnitude higher than that over lithium orthosilicate in the absence of deuterium.

Since the steady state condition is approached very slowly, a sample was pretreated with D_2 for 17 days at a temperature about 48°C higher than that of the actual experiment, i.e. 995 K. The average deuterium pressure of this experiment was $(6.4 \pm 0.1) \times 10^{-5}$ bar. Under these conditions all partial pressures remain essentially constant. From the result of this experiment an estimate on how close equilibrium was approached in the other runs was possible.

The equilibrium constants for the main sublimation process of Li_4SiO_4 (K_1), for the formation of gaseous D_2O from the elements (K_2), and for the reaction of gaseous D_2O with deuterium-pretreated Li_4SiO_4 under formation of gaseous LiOD (K_3) are summarized in Table 1.

The measured partial pressures of D_2 , D_2O , Li , and LiOD and that of the calculated oxygen partial pressures are given as function of temperature in Table 2 and Fig. 1. The temperature dependence of the equilibrium constants defined in Table 1 is also given in Table 2. The reasons for conducting experiments at comparatively low and constant

$\log K_1 = 2 \log p(\text{Li})/\text{bar} + 0.5 \log p(\text{O}_2)/\text{bar} + \log a(\text{Li}_2\text{SiO}_3) - \log a(\text{Li}_4\text{SiO}_{4-x})$
$\log K_2 = \log p(\text{D}_2\text{O})/\text{bar} - \log p(\text{D}_2)/\text{bar} - 0.5 \log p(\text{O}_2)/\text{bar}$
$\log K_3 = 2 \log p(\text{LiOD})/\text{bar} - \log p(\text{D}_2\text{O})/\text{bar} + \log a(\text{Li}_2\text{SiO}_3) - \log a(\text{Li}_4\text{SiO}_{4-x})$

Table 1: Definition of equilibrium constants

$\log K_1 = -(42.067 \pm 0.757) \times 10^3/T + (10.787 \pm 0.725)$
$\log K_2 = (13.258 \pm 0.005) \times 10^3/T - (3.021 \pm 0.004)$
$\log K_3 = -(20.381 \pm 2.070) \times 10^3/T - (7.125 \pm 1.983)$
$\log p(\text{D}_2)/\text{bar} = (0.462 \pm 0.118) \times 10^3/T - (4.641 \pm 0.113)$
$\log p(\text{D}_2\text{O})/\text{bar} = -(1.473 \pm 0.330) \times 10^3/T - (4.974 \pm 0.316)$
$\log p(\text{Li})/\text{bar} = -(13.437 \pm 0.155) \times 10^3/T + (4.049 \pm 0.149)$
$\log p(\text{LiOD})/\text{bar} = -(10.927 \pm 0.870) \times 10^3/T + (1.076 \pm 0.834)$
$\log p(\text{O}_2)/\text{bar} = -(30.385 \pm 0.894) \times 10^3/T + (5.377 \pm 0.857)^*$

*) calculated

Table 2: Equilibrium constants (see Table 1) and partial pressures as function of temperature

temperature as well as at constant pressure are the following: 1) attainment of steady state conditions becomes possible after a sufficiently long equilibration time without undue loss of material, 2) data can be obtained in or close to the temperature region of operation of a blanket, and 3) results of good precision and accuracy are achieved.

In this study on the thermochemistry of the reaction of hydrogen with lithium orthosilicate experimental results down to 945 K were obtained, i.e. 245 K lower than in previous measurements. The equilibrium of the reaction between H_2 and Li_4SiO_4 with formation of water vapor and a "reduced layer" is given by the stoichiometric coefficient x in the activity of the produced solid and approaches asymptotically steady state conditions. The data given in Fig. 1 and in Table 2 refer to this state and therefore apply to a prolonged exposure of Li_4SiO_4 to hydrogen in a blanket.

The endothermic reaction enthalpy for reaction (a) was found to be low, which implies that the reaction between hydrogen and lithium orthosilicate can play a role at temperatures well below the range of the present measurements, provided the reaction rates are sufficiently high.

The temperature at which the sum of the pressures of Li and LiOD reach 10^{-7} bar was found to be 1210 K; at this

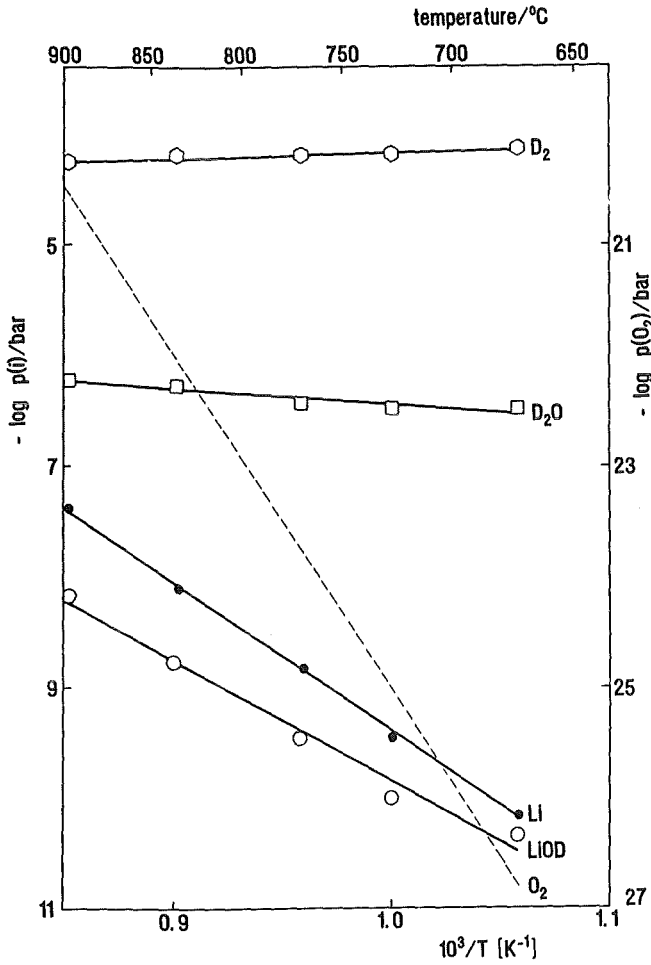


Fig. 1: Plot of partial pressures as function of inverse temperature within the range 945 - 1173 K. The average deuterium pressure was 6.31 ± 0.04 E-5bar

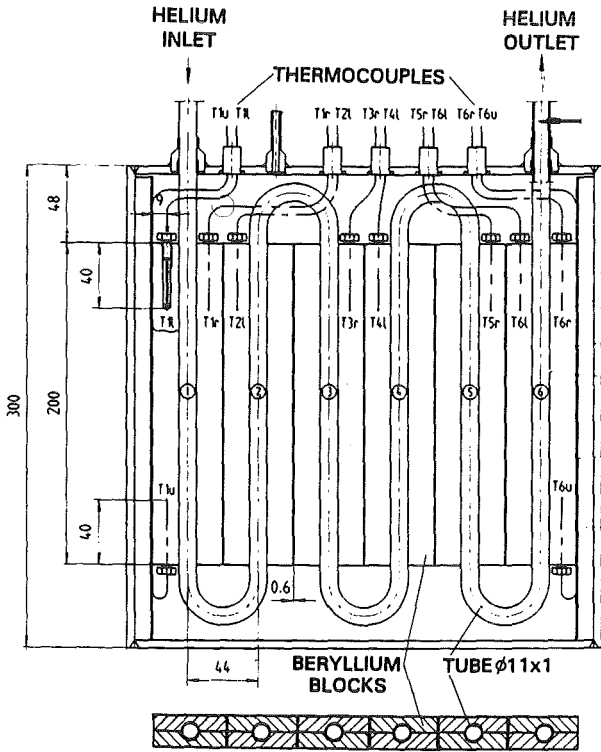
temperature the contribution of LiOD amounts to only about 10 % of the total condensable lithium bearing species.

Staff:

- H.R. Ihle
- R.-D. Penzhorn
- P. Schuster

BS NN-D 1 Helium Blanket Test Loop

The Helium Blanket Test Loop (HEBLO) was commissioned without major difficulties in November 1992. It has been used since January 1993 to test beryllium plates with cooling tubes integrated in them. The test piece represented in Fig. 1 and 2



TUBE SECTION ①, ④ and ⑤ : BEST BRAZING CONDITIONS
 TUBE SECTION ②, ③ and ⑥ : NOT WETTED BY BRAZE

Fig. 1: Beryllium plates with brazed-in helium tubes as test piece for temperatur transient tests.

comprises twelve beryllium plates of 200 mm length each, brazed pairwise with each other and with a leg of the cooling tube coil. The test piece was manufactured by W.C. Heraeus, Hanau, using a brazing technique which had previously been optimized for this plate geometry and tested extensively. The test piece accomodates ten thermocouples in total which are in excellent contact with the beryllium bodies. Moreover, the gas temperature is measured at the inlet and at the outlet.

The first test series is designed to comprise roughly 1000 temperature cycles; 700 cycles of them have already been completed. On the average, temperature amplitudes of 160 K have been achieved at maximum temperatures of 440 °C. Fig. 3 shows the measured development of the helium temperature and of the temperature in the beryllium plate at the gas inlet side (broken lines) during a temperature cycle of 650 seconds duration. The beryllium temperature has been plotted (as solid line) which was calculated with the ABAQUS code assuming that an ideal thermal contact between the cooling tube and the beryllium metal has been established

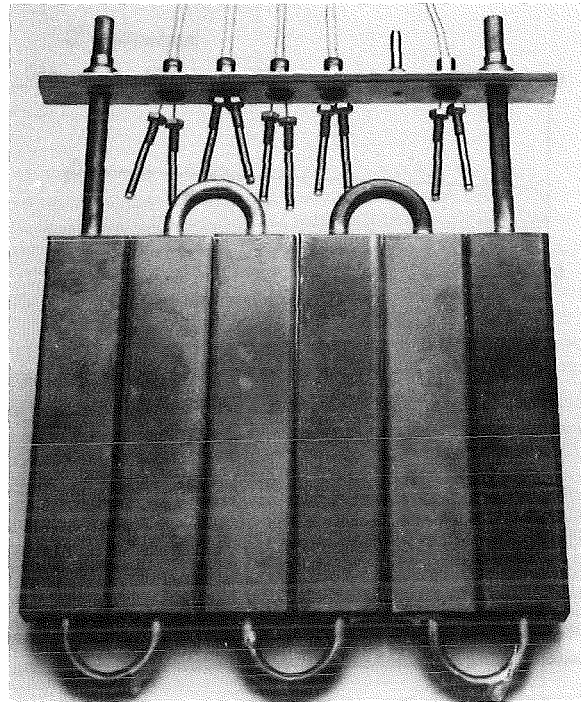


Fig. 2: Beryllium test piece during fabrication at W.C. Heraeus.

through the braze layer. The agreement between the measured and calculated temperature plots is very good.

It is indicated in Fig. 1 that for some tube sections - including the area of cooling gas outlet - wetting of the cooling tube by the brazing alloy was artifically avoided. It is intended to determine in this way the thermal resistance in case of non-observance of the optimum brazing conditions.

Figure 4 shows the gas and beryllium temperatures on the gas outlet side (broken lines), also measured during one temperature cycle. In the post-test calculation of the temperature plot the heat resistance around the brazed joint was subjected to variations until the best agreement was reached between the calculation and the measurement. This occurred at a mean heat transfer coefficient $\alpha=0.3 \text{ W/cm}^2\text{K}$.

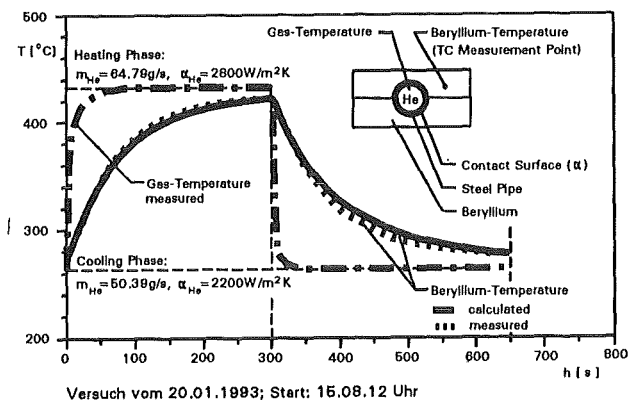


Fig. 3: Transient temperature plots recorded at the gas inlet under optimum brazing conditions

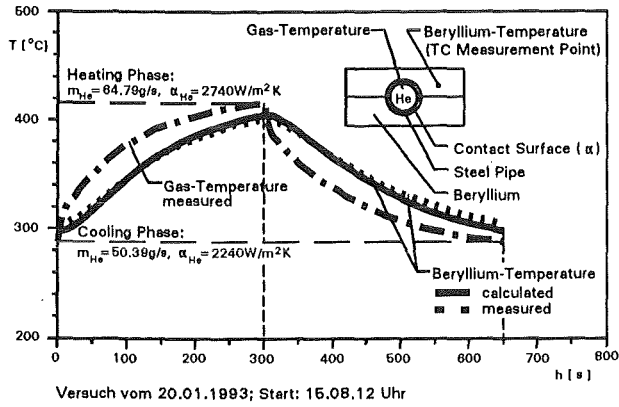


Fig. 4: Temperature plots recorded at the gas outlet in the absence of tube wetting by the brazing alloy.

In the course of previous testing (700 cycles) the typical development of all temperature values measured and hence probably also the condition of the brazed connection remained unchanged. After completion of the tests in HEBLO the beryllium parts will be subjected to a post-test examination with the manufacturing firm (including strength and crack examinations and metallographic examinations).

Staff:

- M. Dalle Donne
- H. Deckers
- H. Lehning
- K. Müller
- D. Piel
- H. Reiser

BS NN-D 2 Irradiation Experiments and Non Nuclear Tests

Pebble Bed Thermal Conductivity Measurements with Irradiated Pebbles

At IMF III an equipment has been built for measurement of the thermal conductivity on small irradiated pebble beds which allows a direct comparison to be made of the values applicable to irradiated and non-irradiated materials [1]. The main feature which is typical of the measuring equipment consists in miniaturisation; 3 to 4 cm³ of an irradiated material are already sufficient for measurement of its thermal conductivity. The equipment has been tested and is a proven device which, following some modifications, has provided thermal conductivity values on non-irradiated Li₄SiO₄ spheres which agree well with the values indicated in the literature [2]. Meanwhile, the equipment has been installed in the Hot Cells and is ready for first measurements to be made on activated material.

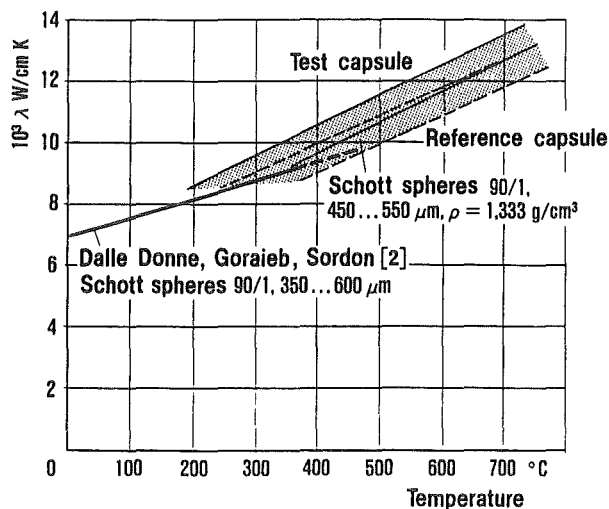


Fig. 1: Thermal conductivity values measured on Li₄SiO₄ spheres in helium atmosphere

Literature:

- [1] H.E. Häfner, K. Philipp, Apparatur zur Messung der Wärmeleitfähigkeit an kleinen bestrahlten Kugelschüttbetten, unpublished KfK report
- [2] M. Dalle Donne, A. Goraieb and G. Sordon, Measurements of the effective thermal conductivity of a bed of Li₄SiO₄ pebbles of 0.35-0.6 mm diameter and of a mixed bed of Li₄SiO₄ and aluminium pebbles, Journal of Nuclear Materials 191-194 (1992)

Staff:

H.E. Häfner
K. Philipp
R. Vouriot

Heat Transfer and Technological Investigations on Beds of Beryllium and Li₄SiO₄ Pebbles

1. Introduction

The Karlsruhe solid breeder blanket design for the DEMO is based on the use of a mixed bed of 2 mm beryllium pebbles and of smaller pebbles of either 0.1 - 0.2 mm Li₄SiO₄ or a mixture of 75 % 0.1 - 0.2 mm Li₄SiO₄ and 25 % 0.08 - 0.18 mm beryllium pebbles [5]. The packing factor of the 2 mm beryllium pebbles is about 60 %. The bigger pebbles form the structure of the bed. The smaller pebbles are poured in the already settled bed of bigger pebbles and occupy about 50 % of the remaining place available in the bed. The resulting packing factor is about 80 %. This kind of arrangement offer various advantages:

- a) The volume ratio beryllium/Li₄SiO₄ is between 4.3 and 3 and the mixing between beryllium and Li₄SiO₄ is very thorough and without steel in between. This arrangement is very advantageous from the neutronic point of view.
- b) The direct contact of the highly heat-conducting bigger beryllium pebbles and the high packing factor, obtained by the choice of two quite different pebble diameter ranges, gives a pebble bed with high thermal conductivity. The arrangement with the smaller beryllium pebbles is used in the front of the blanket where the higher power densities are expected, while the other is used in back region.
- c) The neutron irradiation induced swelling of the beryllium pebbles should increase the contact surface between them and thus increase the thermal conductivity of the bed. This has the effect to decrease the bed temperatures and to reduce the amount of beryllium swelling [5].

The blanket design for NET [6] and the previous DEMO-blanket design [4] were based on the use of beryllium plates and Li₄SiO₄ in diameter range of 0.3 - 0.6 mm. This concept remains valid and quite interesting in the case one does not expect large beryllium swellings. However no information is available for the behavior of the Be/Li₄SiO₄ mixed pebble beds. For this reason a series of heat transfer and technological investigations have been initiated in Karlsruhe for the 0.1 - 0.2 mm Li₄SiO₄ pebbles and their mixtures with bigger and smaller beryllium pebbles. The Li₄SiO₄ pebbles have been developed in collaboration between KfK and the firm Schott-Glaswerke Mainz and the beryllium pebbles have been made by the firm Brush Wellman.

The results of the experiments performed so far are reported below. Namely:

- a) Measurements of the thermal conductivity and of the wall heat transfer coefficient of a bed with 0.35 - 0.6 mm Li₄SiO₄ pebbles, to extend the temperature range of validity of the heat transfer correlation already available

[4] (bed 1), of a bed of 2 mm beryllium pebbles (bed 2), of a mixed bed with 2 mm beryllium and 0.1 - 0.2 mm Li_4SiO_4 pebbles (bed 3) and of mixed bed with 2 mm beryllium and 0.1 - 0.2 mm Li_4SiO_4 + 0.08 - 0.18 mm beryllium pebbles (bed 4).

- b) Thermal cycle tests for bed 1, 3, and 4.
- c) Annealing tests of Li_4SiO_4 pebbles at 650 °C and measurement of the failure loads of the Li_4SiO_4 pebbles before and after annealing.

2. Heat Transfer Tests

The experimental apparatus and the evaluation of the experimental results have been presented earlier [3]. In ref. [3] also the results of preparatory experiments with 2 mm aluminum pebbles in place of the beryllium pebbles were given.

2.1 The bed of Li_4SiO_4 pebbles

Fig. 2 shows the measured effective thermal conductivity of

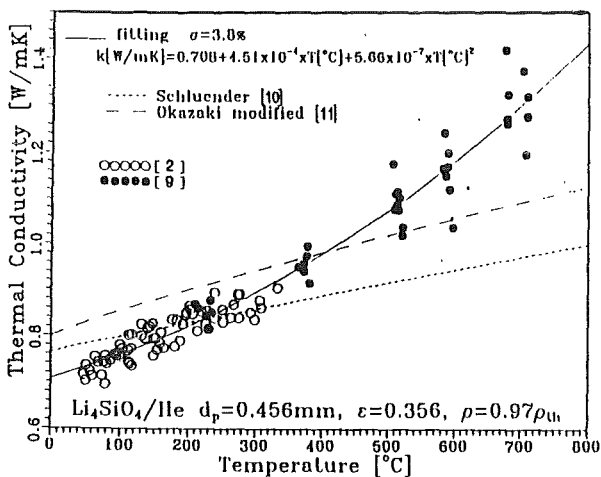


Fig. 2: Effective thermal conductivity of the bed of 0.35 - 0.6 mm Li_4SiO_4 pebbles (bed 1).

the bed of Li_4SiO_4 pebbles versus the bed average temperature. The average diameter of the pebbles is 0.456 mm and the void fraction 35.6 %. The density of the pebbles is 97 % of theoretical i.e. 2.32 g/cm³. No effect was observed on the measured data of the differential thermal expansion between bed and the bed containment wall ("interference"). Besides the data already published in ref. [3] other experimental points are shown in the diagram. These have been obtained in a smaller, but similar, experimental apparatus which allowed to perform experiments at higher temperatures [7]. The data may be correlated in the temperature range 40 - 720 °C by the equation given in Fig. 2. The data agree reasonably well with the Schlünder correlation [8] for temperatures up to 380 °C, however they are higher for the higher temperatures. Fig. 2 shows the prediction of the modified Okazaki correlation [9] as well.

For the heat transfer coefficient at the bed wall a value of 0.6 W/cm²K, as predicted by the Schlünder correlation [8], is recommended [3]. The measured pressure drop coefficients, which lay in the laminar flow region, agree very well with the correlation of ref. [10].

2.2 The beryllium pebble bed and the mixed beds

Preliminary tests were performed in a plexiglas annulus about 12 cm high and having the same cross section of the test section (annular cross section with $R_1 = 0.8$ cm and $R_2 = 5.1$ cm). These tests showed that, after vibration, a packing factor of 63.3 % was achieved with the 2 mm beryllium pebbles. Afterwards, the 0.1 to 0.2 mm Li_4SiO_4 pebbles were poured into the bed. The small pebbles flowed quite well in between the bigger pebbles, filling about half of the remaining volume. The resulting filling factor of the Li_4SiO_4 pebbles was 17.5 % of the total bed volume. After filling with small pebbles and slightly vibrating, the height of the pebble bed did not increase showing that the contact between the beryllium pebbles is maintained.

The actual heat transfer measurements were performed in the steel test section which was filled up to a height of 483 mm. The test section was placed vertically so that no separation between the two kinds of pebbles occurred. The packing factors were the same as in the plexiglas annulus.

In the case of the mixed bed with small beryllium pebbles (bed 4) the filling arrangement was the same: after filling the test section with the 2 mm Be pebbles the previously mixed smaller Be and Li_4SiO_4 pebbles (volume ratio 1 to 1) were poured into the bed. The packing factors were about the same as in Be/ Li_4SiO_4 mixed bed (bigger particles 63.3 %, smaller ones 17.6 %).

The ratio of the smaller Be and Li_4SiO_4 pebbles was chosen 1 to 1 rather than 1 to 3 as in the beryllium design of ref. [5], to have a greater range of the total volume ratio Be/ Li_4SiO_4 (7 to 3 as against 4.3 to 3), in case the extrapolation from the bed with aluminum pebbles to the case with beryllium would produce too optimistic thermal parameters. The ratio 7 rather than 4.3 gives higher thermal parameters of the bed but practically has no effect on the tritium breeding ratio.

Table 1 shows a resumé of the heat transfer measurements for the beds 2, 3, 4. The data are correlated with equations of the type:

$$k, \alpha = C_0 \left(1 + C_1 \frac{\Delta l}{l} \right) (1 + C_2 T_m) \tag{1}$$

where k is the bed thermal conductivity and α its heat transfer coefficients to the wall, T_m [°C] the average temperature of the bed and $\Delta l/l$ the "interference", i.e. the difference between the thermal expansion of the bed and that of the confinement walls. This is given by:

$$\frac{\Delta l}{l} = \alpha_{Be} (T_m - T_o) + \alpha_{st} T_o - \alpha_{st} \frac{R_2 T_{W2} - R_1 T_{W1}}{R_2 - R_1}$$

where $l = R_2 - R_1$ is the thickness of the bed, R_1 and R_2 the inner and the outer radius of the annular cross section of the test section, T_o the room temperature, T_m the average temperature of the bed, T_{W1} and T_{W2} the inner and the outer temperature of the confining walls and α_{Be} and α_{st} the thermal expansion coefficients of beryllium and of the confinement walls of stainless steel respectively. The coefficients C_0, C_1, C_2 are given in Table 1 for the three beds

Bed effective thermal conductivity [W/mk]							
Pebble bed no.	No. of experiments	C_0	C_1	C_2	Standard deviation %	Temp. range (°C)	Interference range %
2	23	2.293	353	6.358×10^{-4}	10.6	30 - 590	0 - 0.24
3	21	4.721	206.4	0	14	40 - 490	0 - 0.16
4	18	5.478	320.2	0	13	30 - 520	0 - 0.16
Wall heat transfer coefficient [W/cm ² °C]							
2	23	0.06438	287.6	3.379×10^{-3}	18.8	90 - 690	0 - 0.24
3	21	0.0932	196.8	1.654×10^{-3}	8.8	60 - 550	0 - 0.16
4	18	0.2120	383.1	9.239×10^{-4}	13	50 - 580	0 - 0.16

2: 2 mm Be pebbles; packing factor 63.3 %
 3: 2 mm Be + (0.1 - 0.2 mm) Li_4SiO_4 ; packing factors 63.3 % + 17.5 %
 4: 2 mm Be + (0.1 - 0.2 mm) Li_4SiO_4 + (0.08 - 0.18 mm) Be pebbles; packing factors: 63.3 % + 8.8 % + 8.8 %
 For the definition of C_0, C_1, C_2 see equation (1).

Table 1: Resume of heat transfer results

investigated. The linear dependence of the heat transfer parameters on $\Delta l/l$ was already observed in the case of the experiments with aluminum and aluminum plus Li_4SiO_4 pebbles [3].

As expected, both the thermal conductivity and the wall heat transfer coefficients are considerably higher for the mixed beds, especially in the case of the small beryllium pebbles (bed 4).

3. Thermal Cycle Tests

A series of thermal cycle tests have been performed on the bed 2 (2 mm Be), 3 (2 mm Be + (0.1 - 0.2) mm Li_4SiO_4) and 4 (2 mm Be + (0.1 - 0.2) mm Li_4SiO_4 + (0.08 - 0.18) mm Be). The experimental apparatus has been described in an earlier paper [11]. Fig. 3 shows the test section containing the pebbles to be tested. The temperature of the pebble bed center and of tube wall were measured during the test. After a certain number of cycles the pressure drop of helium flowing through the bed was measured. The pressure drop increase gave an indication of the amount of broken particles. Fig. 4 shows a typical temperature diagram during a test. As the cooling is given by the quick immersion of the test section in cold water, the temperature decrease in the wall is much faster than that at the bed center.

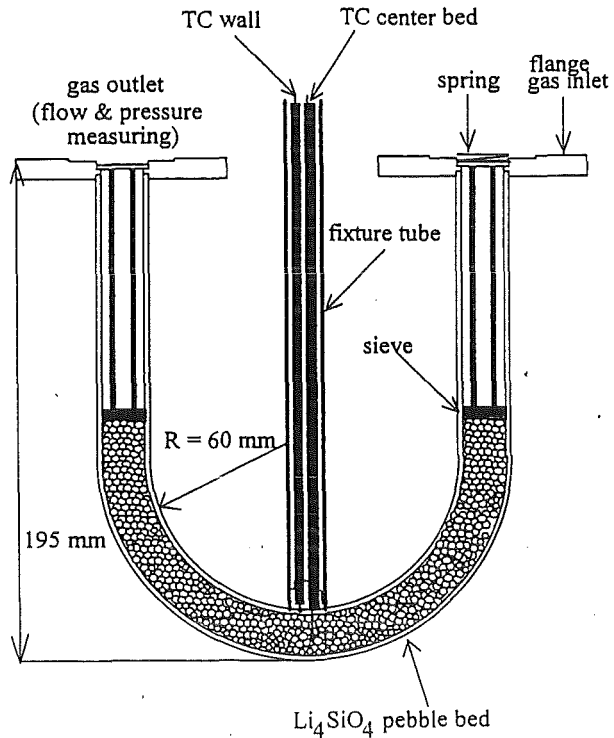


Fig. 3: Test section for the thermal cycle tests.

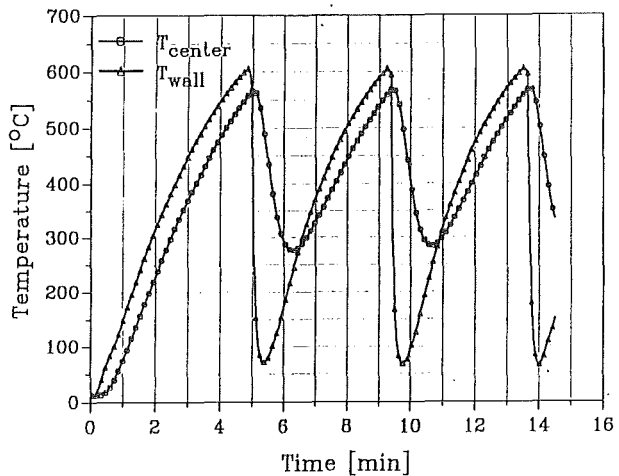


Fig. 4: Typical temperature diagram during a thermal cycle test.

A test with 50 cycles was performed for the Li_4SiO_4 bed, at the end of which it was found that about 2 % for the particles were broken. As in previous tests, it was noticed that the broken particles were on the periphery of the bed in the region nearest to the outer wall, where the temperature gradients with time are the highest. The measurement of the temperatures at bed center and at the wall allowed to calculate the temperature and the temperature gradient with time in the bed during the cooling phase where the temperature gradients are the highest (Fig. 4). The determination of the amount of broken particles at the end of the test allowed to calculate the critical radius beyond which the particles are broken. Fig. 5 shows the temperature gradient versus the temperature for various radii for the

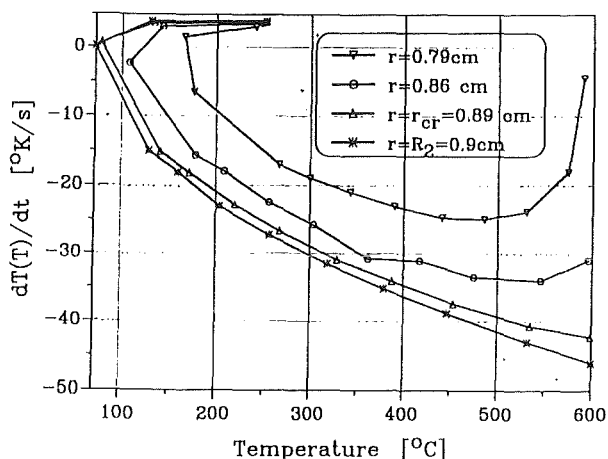


Fig. 5: Temperature gradient versus temperature at various radii of the bed of Li_4SiO_4 particles, r_{cr} = radius beyond which the particles are broken. R_2 = outer diameter of the bed.

Li_4SiO_4 bed. The line for $r = r_c$ = critical radius gives the combination of temperature gradient and temperature at which the breaking of the pebbles would have occurred. With the present experimental data is not possible to establish with certainty which is actually the critical temperature gradient. However, there are indications from irradiation experiments, that the Li_4SiO_4 become less brittle in a temperature range between 450 and 650 °C.

Indeed, experiments performed in the OSIRIS reactor at power densities of 215 W/cm³ (referred to pebble bed volume), i.e. about 5 times higher than the peak value expected in the Demo blanket [4], and in presence of strong temperature gradients in time given by reactor scrams, showed that a considerable portion of the particles irradiated at temperatures of 400 - 450 °C were broken, while the particles irradiated at 650 - 700 °C were intact. From Fig. 3 one can see that this temperature range correspond to a temperature gradient of about 38 to 42 °C/sec. The line for $r = 0.86$ cm shows that in any case the critical temperature gradient should be greater than 34 °C/sec. These gradients are considerably higher than the peak values expected in the KfK Demo-blanket (≈ 20 °C/sec).

A test with 1000 thermal cycles was performed with the bed with 2 mm Be + (0.1 - 0.2 mm) Li_4SiO_4 pebbles (bed 3). Although in this case the thermal wave propagated much faster in the pebble bed due to its high thermal diffusivity, the curve dT/dt versus T for the critical radius, i.e. the radius above which the Li_4SiO_4 pebbles were broken, was almost identical to the one for the bed of Li_4SiO_4 pebbles only. The bed with 2 mm Be and the smaller Li_4SiO_4 and Be pebbles (bed 4) was subjected to a test with 500 cycles only, because it was noticed that for the bed 3 a steady state situation, i.e. no further break of ceramic particles, as indicated by the pressure drop measurements, was established after 450 cycles. Also here the dT/dt versus T curve for the critical radius was almost identical to the previous ones. This indicated that the resistance to the temperature gradients of the bigger (0.3

- 0.6 mm) Li_4SiO_4 pebbles is about the same as that of the smaller (0.1 - 0.2 mm) ones. A further indication of the tests is that what breaks the particles is not the outside pressure of the constraining steel walls, but it is rather the temperature gradient over the time. Indeed, the smaller Li_4SiO_4 pebbles are affected much less by the wall pressure than the bigger ones. In the mixed beds the structure of the bed is made up by the bigger beryllium pebbles, which take the major part of the wall pressure. Nevertheless, with or without beryllium pebbles the breaking characteristics of the Li_4SiO_4 were about the same. No failure of beryllium pebbles occurred during the thermal cycles.

An important result of these experiments was that, although the bed was kept in place by a wire net with mesh size of about 50 μm , no broken particles were coming out of the bed although some broken particles were as small as 10 μm and the helium was flowing through the bed at velocities considerably higher than those foreseen in the Demo-blanket.

The results of these tests show a much better behavior of the orthosilicate pebbles than that found in a recent experiment by JAERI, where, after 50 cycles in the temperature range 400 to 800 °C and with temperature gradients of 20 °C/sec, 30 % of the Li_4SiO_4 pebbles were broken [12]. This poor performance is probably due to the fact that these particles were made by sintering and had a density considerably lower than the present pebbles (93 % as against 97 - 99 % of theoretical). Furthermore the present particles have a slight excess of SiO_2 , which, after a proper tempering process, is forming a sort of cement at the grain boundary, making them stronger [7].

4. Long Term Annealing Tests

Long term annealing tests were started to examine the behaviour of pebbles and pebble bed mixtures under condition of reactor operation. A temperature of 650 °C was chosen for the tests. Specimen were placed in a quartz tube inside a little furnace of 30 mm tube diameter, which is located in an inert gas box. The sweep gas in the quartz tube is helium, containing 0.1% hydrogen. The atmosphere in the box is kept at low oxygen (< 0.5 ppm) and water (< 0.2 ppm) levels by cleaning systems. Heating and cooling rates are restricted to 50 °C/h in order to avoid any possibility for thermal cracking of specimen. Always after 6 days the annealing process was interrupted by controlled cooling of the specimen to room temperature for taking test samples. Mechanical tests were conducted on 10 pebble samples of each of the pebble charges contained in the furnace. Some additional pebble samples were also taken for investigation of structural changes that may have occurred during the treatment.

The first test run started contains the samples listed in Tab. 2 with exception of charge 2. The uniform beds constitute only of Li_4SiO_4 pebbles with the given specifications, whereas the mixed beds consist of a mixture of beryllium pebbles and

Charge	bed	Li ₄ SiO ₄ pebbles Ø mm	Li ₄ SiO ₄ pebbles addition	Be pebbles Ø mm
1	uniform	0.10-0.20	+ 2% SiO ₂	-
2	uniform	0.35-0.60	+ 2% SiO ₂	-
3	mixed	0.10-0.20	+ 2% SiO ₂	1.50-2.30
4	mixed	0.10-0.20	+ 2% SiO ₂ + 0.4% TeO ₂	1.50-2.30

Table 2: Specification of pebble beds for long term annealing tests

Li₄SiO₄ pebbles. Charge 2 was annealed in a separate test with similar conditions but at 800 °C [13].

The mechanical strength is examined by a simple test, in which a continuously increasing weight load is imposed by a piston to a single pebble until it breaks. The load is made by a water container that gradually fills with water. The pebble is placed on a balance that measures the load. The force, at which the pebbles break, averaged through 10 tests, is taken as a measure of the mechanical strength. Detailed description of the tests is given in [4]. Tests with samples of charge 1, 3 and 4 were conducted using pebbles of 0.2 mm diameter, those with charge 2 by selecting pebbles of 0.5 mm diameter. The definition of diameters is necessary because the force, at which the pebbles break, strongly depends on the diameter of pebbles.

The influence of the thermal treatment is described in Tab. 3.

Charge	before annealing	650 °C 144 h	650 °C 288 h	800 °C 1340 h [11]	bed
1	1.6	1.0	0.9		uniform
2	6.4	-	-	7.1	uniform
3	1.6	1.1	1.1		mixed
4	2.8	1.1	1.1		mixed

Table 3: Influence of long term annealing on pebble strength (means values of force [N] out of 10 tests at which the pebbles break)

The second column shows the mechanical strength of the pebbles before thermal treatment, the next columns the values after annealing.

The small pebbles show a drop to lower values during the first step of annealing, but not so the larger pebbles that were annealed before the test at 1030 °C to reduce the scatter in the mechanical strength [4]. This annealing procedure was not applied to the small pebbles because in this case a reduction of mechanical strength was observed after the annealing process. During annealing crystal growth occurs up to a size of 10 - 40 µm, which reaches the order of the radius of the small pebbles, and leads to early cracking of the material.

In former long term annealing tests under the same conditions it was observed that larger pebbles also show a drop in mechanical strength to about half of the initial value after the first annealing step, if those pebbles were not subjected to proper treatment at 1030 °C before [13]. In this

case pebbles showed still the original detritic structure without grain growth. This structure is typical for the small pebbles also.

It is important to note that beryllium contained in the mixed bed does not influence the mechanical strength of the lithium orthosilicate pebbles. Charge 1 and 3 arrive at about the same mechanical strength after 144 and 288 hours of annealing. The annealing tests conducted so far do not indicate a further decline of the mechanical strength with increasing annealing time.

5. Conclusions

The results of the tests performed for the new design of the DEMO-relevant Solid Breeder Blanket developed at KfK are very encouraging. The new design is based on the use of mixed beds formed by large (2 mm) beryllium pebbles and either smaller Li₄SiO₄ pebbles or a mixture of smaller Li₄SiO₄ and beryllium pebbles.

The results of the heat transfer experiments have confirmed what was already found by previous experiments using aluminum pebbles. Namely that the heat transfer parameters of the mixed beds (bed thermal conductivity and wall heat transfer coefficient) are considerably better than those of a bed of mere beryllium pebbles and of a mixture beryllium and Li₄SiO₄ pebbles of the equal diameter.

The results of the thermal cycles tests indicate that, for both the smaller and the bigger Li₄SiO₄ pebbles, the critical temperature gradient over the time is about 38 - 42 °C/sec which is considerably higher than the peak values expected in the DEMO blanket (≈ 20 °C/sec). The results of the annealing and failure tests indicate that the presence of beryllium does not affect the failure load of the small Li₄SiO₄ pebbles.

Literature:

- [3] M. Dalle Donne, A. Goraieb, and G. Sordon, J. Nucl. Mater. 191 - 194 (1992), 149
- [4] M. Dalle Donne et al., Demo-relevant Test Blankets for NET/ITER, BOT Helium Cooled Solid Breeder Blanket, Vol. 2, KfK-4929 (1991).
- [5] M. Dalle Donne et al., "Conceptual Design of a Helium Cooled Solid Breeder Blanket Based on the Use of a Mixed Bed of Beryllium and Li₄SiO₄-Pebbles", Proc. 17th Symp. Fusion Technology, Rome, 14.-18. Sept. 1992, P. 1326
- [6] M. Dalle Donne et al., Fusion Technol. 14 (1988), 1357.
- [7] H.E. Häfner, K. Philipp, private communication, Kernforschungszentrum Karlsruhe, 1992.
- [8] E.V. Schlünder, Proc. 7th Heat Transfer Conf., Munich, Vol. 1 (1982), p. 195

- [9] M. Dalle Donne and G. Sordon, Fusion Technol. 17 (1990) 597.
- [10] Verein Deutscher Ingenieure, VDI-Wärmeatlas (VDI-Verlag Düsseldorf, 1984), p.Le1.
- [11] G. Schumacher et al., Fusion Eng. Design 17, (1991), 31.
- [12] H. Yoshida et al., Proc. 17th Symp. Fusion Technology, Rome, 14. - 18. Sept. 1992, p. 1547.
- [13] H. Wedemeyer, E. Günther, R. Knitter, Proc. Jahrestagung Kerntechnik, 5. - 7. May 1992, p. 445 - 448

Staff:

M. Dalle Donne

A. Goraieb

H.E. Häfner

R. Huber

R. Schmidt

B. Schmitt

G. Schumacher

G. Sordon

A. Weisenburger

BS NN-D 3 Irradiation Experiments and Non Nuclear Testing

Tritium Recovery from a DEMO Solid Breeder Blanket

The main task of a Tritium Extraction System (TES) for a helium cooled Li_4SiO_4 DEMO blanket is the tritium recovery from a purge gas stream of about $105 \text{ m}^3/\text{d}$. On the basis of several TES proposals published for a NET/ITER solid breeder blanket, a new concept has been developed which is especially appropriate to cope with large purge gas streams.

As tritium is expected to appear in two chemical forms (HT and HTO) two specific process steps are needed for its removal from the primary purge gas loop (cf. Fig. 1):

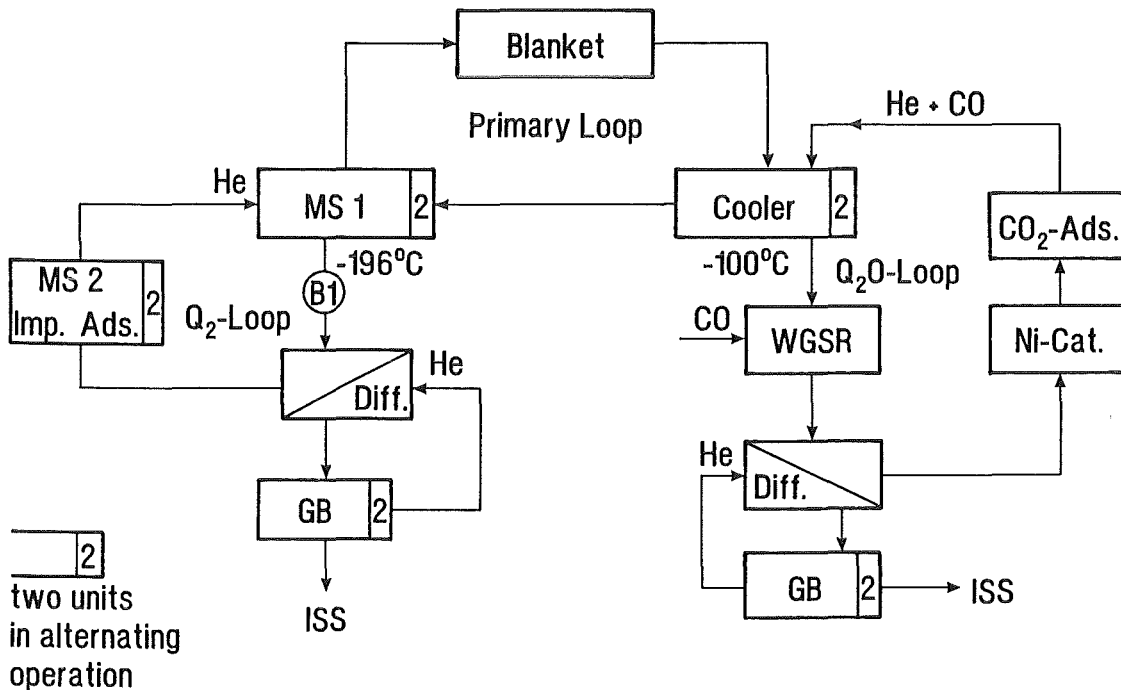
- a cooler to freeze out Q_2O at -100°C ($\text{Q} = \text{H}, \text{T}$), and
- a molecular sieve bed to absorb Q_2 at -196°C .

Only these components including some additional devices for the gas preconditioning like compressor and precooler, are subjected to the high gas flow rates mentioned above. All further processing is done in relatively small secondary loops during and after warmup of the cooler and the molecular sieve bed. Two identical units of these components must be available for continuous operation of the TES: while the first cooler/molecular sieve is being loaded, the second unit will be in the deloading/regeneration mode.

Some operation parameters of the DEMO blanket and the main requirements of the TES are compiled in Table 1.

Tritium Production Rate	370 g/d = 62 mol/d	
Mass Flow of He Purge Gas	0.22 kg/s = $4.8 \cdot 10^6$ mol/d	
Average Helium Pressure	p(He) = 80 kPa	
Swamping Ratio	He: H_2 = 1000 : 1	
Purge Gas Component	Mass Flows and Concentrations	
	TES Inlet	TES Outlet
He	4.8·10 ⁶ mol/d ≈ 99.9 %	4.8·10 ⁶ mol/d ≈ 99.99 %
H ₂	4.7·10 ³ mol/d ≈ 0.1 %	500 mol/d ≈ 100 ppm
HT*)	93 mol/d ≈ 19 ppm	< 10 mol/d < 2 ppm
HTO + H ₂ O*)	31 mol/d ≈ 6.5 ppm	3 mol/d ≈ 0.6 ppm
*) It was assumed that 50 % of the tritium is released from the breeder pebbles as HTO; by isotope exchange, some of the HTO is further converted into H ₂ O at HT		

Table 1: Some parameters of the DEMO blanket and requirements for the tritium extraction system (TES)



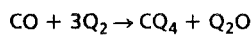
KfK Proposal

Fig. 1: Schematic flow sheet of blanket tritium extraction system

Short Description of the Secondary Loops

Q₂O-Loop: The Q₂O released from the cooler during warmup is transferred within the closed Q₂O-loop to a water gas shift reactor (WGSR) where it is converted to CO₂ and Q₂ by addition of CO and by the use of a copper chromite catalyst (T=200°C). The hydrogen isotopes are then removed from the gas stream by a Pd/Ag diffusor. The back pressure side of the diffusor is integrated into a small helium loop (diffusor loop) which serves to continuously transport the permeated hydrogen isotopes to a metal getter bed for storage.

The next component is a nickel catalyst bed (T=500°C) which has the task to crack tritiated methane that can be formed with a small yield by the reaction



The CO₂ adsorber (e.g. modernite) downstream of the nickel catalyst is used to remove the CO₂ formed by the water gas shift reaction.

All chemical process steps occurring in the Q₂O-Loop have been verified in laboratory tests with hydrogen and tritium [1]. In addition, the feasibility of the complete loop will be demonstrated in a technical scale by the CAPRICE tests in the Tritium Laboratory Karlsruhe (TLK).

Q₂-Loop: When the molecular sieve bed containing 5400 kg zeolite 5A is heated up the co-adsorbed helium (22 Nm³) will be released first, then the hydrogen isotopes (max. 54 Nm³), and finally a small amount of gaseous impurities which are unknown with respect to species and quantity. These gases are transferred into the buffer vessel B1 (volume: 150 m³, prepressurized with 400 mbar of helium) and then circulated through a Pd/Ag diffusor. At the same time the gaseous impurities and eventually some small amounts of residual water are removed by the molecular sieve bed MS2.

The cycle time of the molecular sieve bed MS1 is expected to be 24 hours, with 12 hours for sorption and 12 hours for desorption, regeneration, and cooldown. Further details are described elsewhere [2].

Conclusions

The main feature of the Tritium Extraction System described here is that only two main components are subjected to the large gas flow rate of the purge gas: the cooler and the molecular sieve bed. The process steps of Q₂O reduction and Q₂ separation from helium and gaseous impurities are carried out in secondary loops, where the technical components as well as the gas flow rates can be much smaller than in the primary purge gas loop. Future work will be concentrated above all on the technical aspects of the large molecular sieve bed, of the cooler, and of a Pd/Ag diffusor for gas flow rates of up to 50 Nm³/h.

Literature:

- [1] M. Glugla, R.-D. Penzhorn, J.L. Anderson, J.R. Bartlit, R.S. Willms, Tritium Experiments with an Integral Catalytic Fuel Cleanup Loop, 4. Topical Meeting on Tritium Technology in Fission, Fusion, and Isotopic Applications, Albuquerque, N.M., Sept.29 - Oct.4, 1991
- [2] H. Albrecht, Tritium Recovery from the KfK DEMO Blanket, Int. Workshop on Physics and Technology of Tritium for Fusion Reactors, Varenna, Italy, Sept. 6 - 14, 1993

Staff:

H. Albrecht

BL DE-D 1 Liquid Metal Test Blanket Design

Subjects of this task are the design of liquid metal blankets for the application in a DEMO reactor, the development and the design of blanket test modules in NET/ITER, and, for both cases, the conceptual design of suitable external loops for heat- and tritium extraction.

In the past, work concentrated on a self-cooled PbLi blanket with a poloidal-toroidal-poloidal flow geometry /1/. The main challenge of self-cooled blanket design is to overcome the high magneto-hydrodynamic (MHD) pressure drop and a degraded heat transfer caused by the influence of the magnetic field on liquid metal flow. Although recent results in the MHD area (compare BLMH-D-1) show that MHD is no longer a critical issue for the pursued self-cooled concept, other criteria have led to a change in the reference blanket concept. As described in the previous annual report /2/, reliability is considered as critical issue because the operation of the tokamak reactor requires that all segments are functionable. Malfunction of one segment requires an exchange and causes a long downtime of the machine and has to have, therefore, a very low probability. The desire to improve the reliability of blanket segments have led to a novel design employing helium as coolant for the First Wall (FW) and using Pb-17Li as breeder and coolant for the bulk structure, the "Dual Coolant Blanket". This concept was described in detail in the previous annual report /2/. The design work on this concept, which is considered now as reference concept, has been continued.

Dual Coolant Blanket for a DEMO reactor

With support from industry the detailed design of the inboard and central outboard segments was elaborated including the design of the supply tubes at the blanket top. Of special interest were manufacturing issues.

Work also concentrated on a comprehensive thermo-hydraulic layout for inboard and outboard blankets for a mean neutron wall load of 2.2 MW/m² and a mean/-maximum surface heat flux of 0.4/0.5 MW/m².

Compared to the design described previously /2/ the following modifications are proposed (see Fig. 1):

- Use of two independent helium circuits for the FW cooling to avoid that the malfunctioning of one loop with a delayed plasma shutdown results in unacceptable temperature increases in the structural material which necessitate a blanket exchange.
- Integration of the helium supply ducts in the grid structure of the blanket box (steel plate design with leak detection systems using).
- Demountable support and shielding structure in order to minimize the masses of structural material to be discarded after a blanket segment exchange.

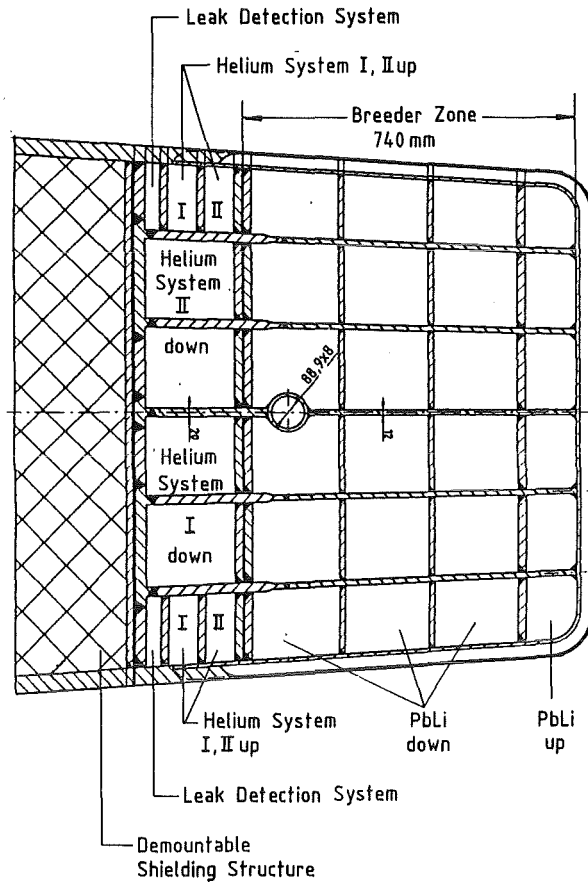


Fig. 1: Cross section of the outboard blanket segment for a DEMO-reactor

- Minimization of the helium pressure losses in the first wall by varying the velocity in each pass corresponding to the increase of helium temperature.

Alternative Convertible Blanket for ITER

In response to recent blanket proposals from the Joint Central ITER Team which were not acceptable for several reasons for the European Home Team, an alternative European design (CEA-KfK-ENEA) was proposed which aimed to combine important requirements of the European blanket development strategy with some features of the more advanced ITER design.

A "convertible" blanket was proposed which allows to switch from the shielding configuration of the Basic Performance Phase (BPP) to the breeding configuration of the Enhanced Performance Phase (EPP) by simply changing the liquid metal without replacing the blanket structure. PbLi is proposed for the EPP and PbMg or PbBi, depending on the coolant, for the BPP. As structural material the stainless austenitic steel 316 LN is used for an average neutron wall load of 1 MW/m².

The blanket box has many similarities with that of the Dual Coolant Concept: the stiff blanket box, the toroidal FW cooling using two independent cooling circuits, a double containment of the liquid metal to the plasma, a leak tolerant

blanket adequate shielding is ensured by optimizing the vacuum vessel.

- tritium control: The tritium is removed from the PbLi in a process unit outside the vacuum vessel. In order to reduce tritium permeation into the coolants permeation barriers are highly desirable for both blanket concepts.
- power excursions: The ITER requirements of 10 power excursions at 170 % of nominal power for 10 sec cause temperature increases which do not result in unacceptable stresses.
- LOCA conditions: First assessments show that a failure of a FW cooling system is tolerable for a delayed plasma shutdown, see also the contribution for BLSA-D2.
- plasma disruptions: Calculations for ITER specific plasma disruptions show that electrical box currents in the blanket cross-section are significantly reduced if the blanket segments are electrically connected at the FWs.
- reliability: The principle of double containment or double welds is applied to reach a high degree of failure tolerance. Single failures do not necessitate the immediate blanket segment exchange nor lead to severe damage to other components.
- ferritic/martensitic steel as structural material: The use of ferritic/martensitic steel could extend the operational regime to much higher reactor values (average neutron wall load = 2 MW/m², neutron fluence = 5 MW a/m²) if the DBTT shift is no longer an essential draw back. An assessment of the current and planned R&D work indicates that the corresponding database could be provided in the required ITER time schedule.

Staff:

F. Dammel
H. Deckers
U. Fischer
H. John
S. Malang
K. Müller
P. Norajitra
G. Reimann
J. Reimann
H. Reiser
K. Schleisiek

Literature

- [1] S. Malang, J. Reimann, H. Sebening (comp.): Status report. DEMO relevant Test Blankets for NET/ITER, Part 1: Self-cooled Liquid Metal Breeder Blanket, KfK 4907, October 1991, Volume 1: Summary
- [2] G. Kast (comp.): Nuclear Fusion Project, Annual Report of the Association KfK/Euratom, October 1991 - September 1992, KfK 5099 (Oct. 92).
- [3] S. Malang, J. Reimann, L. Barleon, U. Müller: MHD-Work on Self-Cooled Liquid Metal Blankets for Fusion Reactors under Development in KfK, The Seventh Intern. Beer Sheva Seminar on MHD Flows and Turbulence, Jerusalem, Israel, February 14-18, 1993

BL PC-D 2 Active and Inactive Impurities and Clean-up of Molten Pb-17Li

In a molten Pb-17Li blanket impurities may cause safety and operational problems. The aim of the work is to characterize the different impurities, to study their transport behavior in a blanket, and to find methods for the removal from the liquid metal. While corrosion products are the main impurities, attention has to be given also to the behavior of lithium.

1. Behavior of Lithium

More studies were done concerning segregation effects of Pb and Li in the eutectic [1]. Capsule tests in temperature gradients were performed. If the initial Li-concentration was below the eutectic composition, a lead phase was formed. With an initial concentration higher than the eutectic, a Li-rich phase is formed. Fig. 1 shows an example. Capsules with

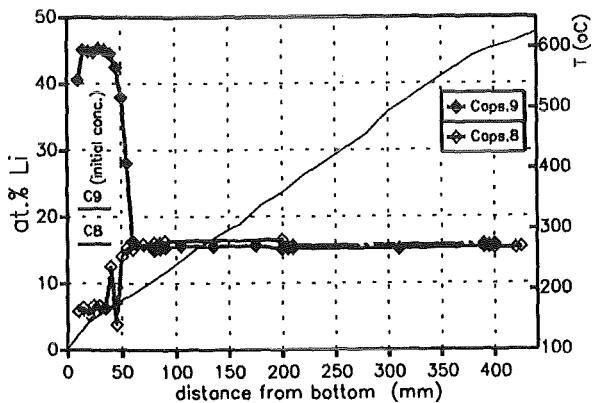


Fig. 1: Li-distribution in capsules, heated in a thermal gradient for 760 hours

different initial concentrations were heated horizontally in thermal gradients. The experimental program will continue to find the boundary conditions for segregation effects.

2. Pb-17Li Loop TRITEX

TRITEX is a pumped Pb-17Li loop from ferritic steel [2]. After run V, the loop was completely dismantled. More than 100 samples from different parts of the facility were analyzed. The total amount of corrosion products was 100 grams. 90 % of these were deposited in form of particles at following positions:

- ferritic core of the electro magnetic pump 26 g
- crusts at valves and experimental volumes of the loop 12 g
- crusts from the drain tank 50 g.

Crusts contained 5 to 20 % particles. Only 10 grams corrosion products were found in 100 kg Pb-17Li, corresponding to 100 wppm. This fraction was partly dissolved. Several kinds of magnetic and non-magnetic particles with different compositions were identified.

Fig. 2 shows crusts in the drain tank. Corrosion products

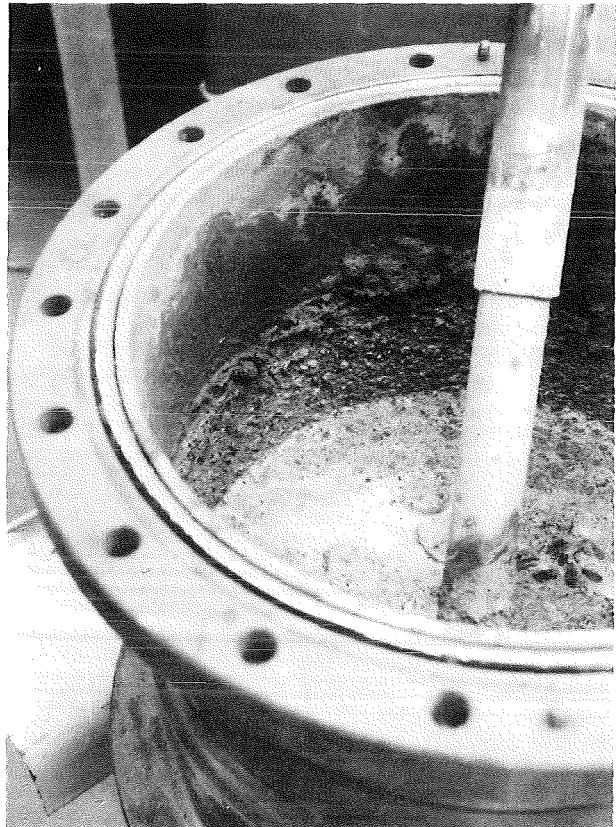


Fig. 2: Photo of the drain tank with crust deposits.

found there indicate, that a large fraction was floating in the Pb-17Li and drained to the tank. It should be possible to remove these particles from the molten eutectic.

3. Cleaning of TRITEX

Draining the eutectic at temperatures between 300 and 400 °C, from a ferritic stainless steel system or from Mo surfaces leaves 200 to 500 grams per square meter adhering at the surface. This corresponds to a layer of 20 to 50 microns. Of course this is not a homogenous layer.

In preparation of experimental phase VI, the complete facility TRITEX was cleaned. A mixture with 1 to 2 % acetic acid and less than 1 % hydrogen peroxyd was circulated through pipes and expansion volumes at 80 °C for several hours. The purification process was controlled by analyzing the solution. This mixture does not attack fresh ferritic steel. But in case of TRITEX a thin surface layer was dissolved. A report describing this purification is under preparation.

Literature:

- [1] H. Feuerstein et al., Intern. Conf. on Liquid Metal Systems, Karlsruhe, Germany, March 16-18, 1993
- [2] H. Feuerstein et al., J. of Nuclear Materials 155-157 (1988) 520

Staff:

J. Beyer

H. Feuerstein

L. Hörner

S. Horn

G. Kieser

BL EI-D 1 Electrical Insulation and Coatings

In order to reduce the magneto-hydro-dynamic pressure drop the duct walls of the liquid metal (Pb-17Li) breeder blanket must be electrically insulated. Two methods are developed:

- Use of so called Flow Channel Inserts (FCI) consisting of an insulating ceramic layer sandwiched between two thin protecting metal sheaths and
- the direct coating of the duct wall by insulating materials.

Development of electrical insulations includes choice of materials, manufacturing methods, thermomechanical and compatibility tests and the assessment of irradiation behaviour. (Subtask BL EI-D 1 includes former subtasks BL PC-D 1 and BL CO-D 1).

1. Flow Channel Inserts

Flow Channel Inserts (FCI), a laminated element (steel-ceramic-steel), shall be fitted loosely into the coolant ducts of liquid metal cooled blanket. They avoid electrical short circuits through the steel structure of the blanket. The electrical potential is induced in flow channels arranged perpendicular to the magnetic field.

Work on fabrication and testing of flow channel inserts (FCI) was continued. In the field of fabrication, the following activities were performed:

- In addition to the coating of the steel sheets with a ceramic layer by plasma spraying [1], thin ceramic layers were generated by CVD. On the base metal sheet first a layer of Ti(CN) was deposited by CVD, followed by an Al₂O₃-layer of about 10 µm thickness as the insulating layer.
- Diffusion bonding of the metal-ceramic sandwich structures with the plasma sprayed ceramic layers was successfully performed at a bonding temperature of 1050 °C and bonding pressure of 200 MPa.

In the field of testing, the following work was done:

- A device for performing thermal cycling as test of the bonding strength of the FCI-structures was completed.
- Nondestructive testing of bonding quality of the FCI's was performed by high-resolution ultrasonic testing of the diffusion bonded samples. The bonding looks well.
- The bonding strength of the ceramic layer on the base metal was tested by bonding tests, where the ceramic layer was on the tensile side of the bonding bar. No flaking or cracking of the ceramic layer could be detected during up to 100 bonding cycles. The tests

were not continued beyond this number of cycles because of the plastic deformation of the steel sheet.

Literature:

- [1] G. Kast, Ed., Nuclear Fusion Project: Annual Report of the Association October 1991 - September 1992, KfK 5099, 1992, 128

Staff:

F. Bauer
 R. Hanselmann
 J. Heger
 W. Laub
 C. Odemer
H.-J. Ritzhaupt-Kleissl

2. Direct Electrical Insulation

In a liquid metal cooled blanket the MHD pressure drop has to be reduced by electrical insulation of the blanket walls. The development of direct insulating layers on MANET steel with the ability of self-healing was started with the so-called hot-dip aluminizing process and the optimization of the thermal treatment. The adhesive strength between the steel and the formed intermetallic Al-Fe layer is good. The Al content is around 60 at% and the layer has a thickness of about 70 µm, see Fig. 1.

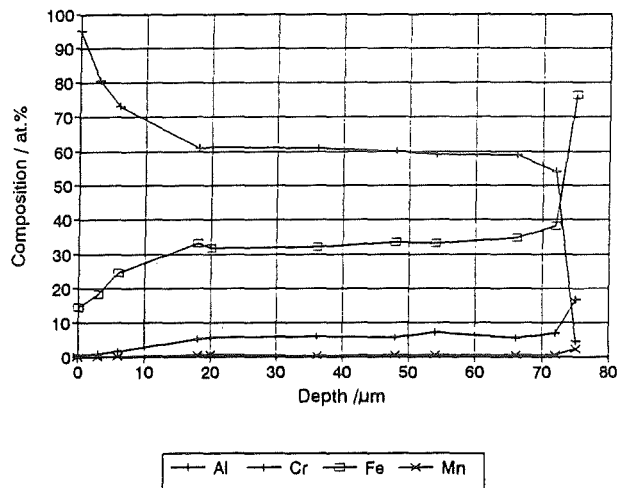
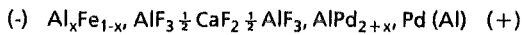


Fig. 1: The concentration depth profile of hot-dip aluminized MANET steel which was measured with EDAX on the polished cut of the specimens

An Al₂O₃ scale is foreseen as electrical insulator which is compatible with Pb-17Li and is produced on the Al-Fe layer by high temperature oxidation of the alloy. Compatibility tests in flowing Pb-17Li at 450 °C were carried out on cylindrical MANET steel specimens which were hot-dip aluminized and oxidized. In the test section of the PICOLO loop six of these specimens were mounted in series. After the exposure up to

8000 h no corrosion effects on the surface of the layers could be observed and the adhesive strength between the steel and the intermetallic layer is still good. However, the formation of the oxide scale has to be improved in order to get uniform and sufficiently thick layers.

In the case of oxide cracking or peeling off self-healing is expected by additional Al_2O_3 formation on the free Al-Fe alloy. Therefore, thermodynamic studies in the Al-Fe system were started to predict the conditions for this desired reaction. The system is characterized at 800 °C by a broad bcc $\alpha\text{-Fe(Al)}$ solid solution range followed by AlFe , a CsCl-type superlattice structure with a homogeneity region of 25 - 51 at% Al, and by the compounds Al_2Fe , Al_5Fe_3 , and Al_3Fe . Gibbs energy measurements are being made in the Fe rich region of this system by the EMF method on solid galvanic cells of the second type with CaF_2 single crystals in the arrangement:



Preliminary experiments yield stable cells between 873 and 1073 K. $\text{AlPd}_{2+x} - \text{Pd (Al)}$ was selected as the reference electrode which is thermodynamically stable and remains solid in the applied temperature range. The thermodynamic activities of Al were measured as a function of temperature so far for three concentrations which give at 1000 K: $a_{\text{Al}} = 0.00026$ for $x_{\text{Al}} = 0.20$, $a_{\text{Al}} = 0.0026$ for $x_{\text{Al}} = 0.30$, and $a_{\text{Al}} = 0.0032$ for $x_{\text{Al}} = 0.324$. The activities of Fe will be calculated by integration of the Gibbs-Duhem equation when sufficient experimental data for other concentrations in the Al-Fe system are available.

Electrical conductivity measurements on aluminized and oxidized specimens in the stagnant Pb-17Li alloy are prepared to start.

An electrochemical oxygen meter with yttria-stabilized zirconia electrolyte was already tested in stagnant Pb-17Li between 470 and 830 K and is at the moment applied in the expansion chamber of the PICOLO loop at 550 K.

The lithium content of vanadium based alloys was assessed. First tests to plate vanadium alloys with aluminide gave encouraging results, layers of sufficient thickness and excellent bonding on the substrate were achieved.

Literature:

- [1] H.U. Borgstedt, C. Guminski, "Solubility of Vanadium in the Liquid Metals Lithium and Sodium", 5th Internat. Symp. on Solubility Phenomena, Moskva, GUS, July, 8-10, 1992.
- [2] H. Glasbrenner, H.U. Borgstedt, Z. Peric, "Compatibility of Insulating Materials in Pb-17Li Alloy", Material Behaviour and Physical Chemistry in Liquid Metal Systems II, Karlsruhe, March 16-18, 1993.

- [3] H..U. Borgstedt, "Liquid Metal Corrosion of Vanadium Alloys", Workshop on Vanadium Alloys, JRC, Ispra, Italy, 5.-6.7.1993.

Staff:

H.U. Borgstedt
G. Frees
H. Glasbrenner
H. Kleykamp
W. Laumer
Z. Peric

3. Irradiation Behaviour of Insulating Coatings

The studies of the radiation induced electrical degradation (RIED) of alumina have been continued [1]. The results of a comprehensive review of related publications are represented in Fig. 1. Electrical conductivity of Al_2O_3 is plotted versus an equivalent neutron dose, which also allows the representation of irradiation experiments with electrons and protons, as well as versus the dpa values calculated for Al_2O_3 (according to U. Fischer, KfK).

The range of the diagram is limited by the line of $4 \times 10^{-2} (\Omega\text{m})^{-1}$ on the one hand and by the line of $7.2 \times 10^{22} \text{ n/cm}^2$ (corresponding to 45 dpa) on the other hand. Both lines indicate the range of maximum acceptable increase in the conductivity of an Al_2O_3 insulating layer of 10 μm in thickness in a liquid metal blanket channel for the prevention of MHD pressure loss and the maximum neutron dose reached of the DEMO-LM blanket after an operating time of 20000 h. The conductivity values may not exceed the conductivity limiting lines before reaching the neutron dose limit.

The Al_2O_3 experiments taken from recent publications and shown in Fig. 2 were carried out at temperatures ranging from 347 to 797 °C and voltages (d.c. and a.c. voltages of 100 Hz) applied of 50 - 5000 V/cm. As is obvious, a maximum neutron dose of about 10^{21} n/cm^2 (which corresponds to about 0.5 dpa) is reached. The curves cannot be interpreted systematically, as not all important parameters are known. Nevertheless, some important information can be obtained from the curves:

- At comparable electric fields and damage values, increase in electrical conductivity strongly depends on the irradiation temperature. A maximum value is found to exist at 590 °C (curves 5 - 7). Even at 590 °C (curve 6), saturation seems to occur before the conductivity limit is reached. For this reason, there is hope that the conductivity limit will not be exceeded at the wall temperature of 450 °C assumed for the DEMO blanket.
- The irradiation results obtained with obviously similar parameters vary by several orders of magnitude (curves 3 and 4).

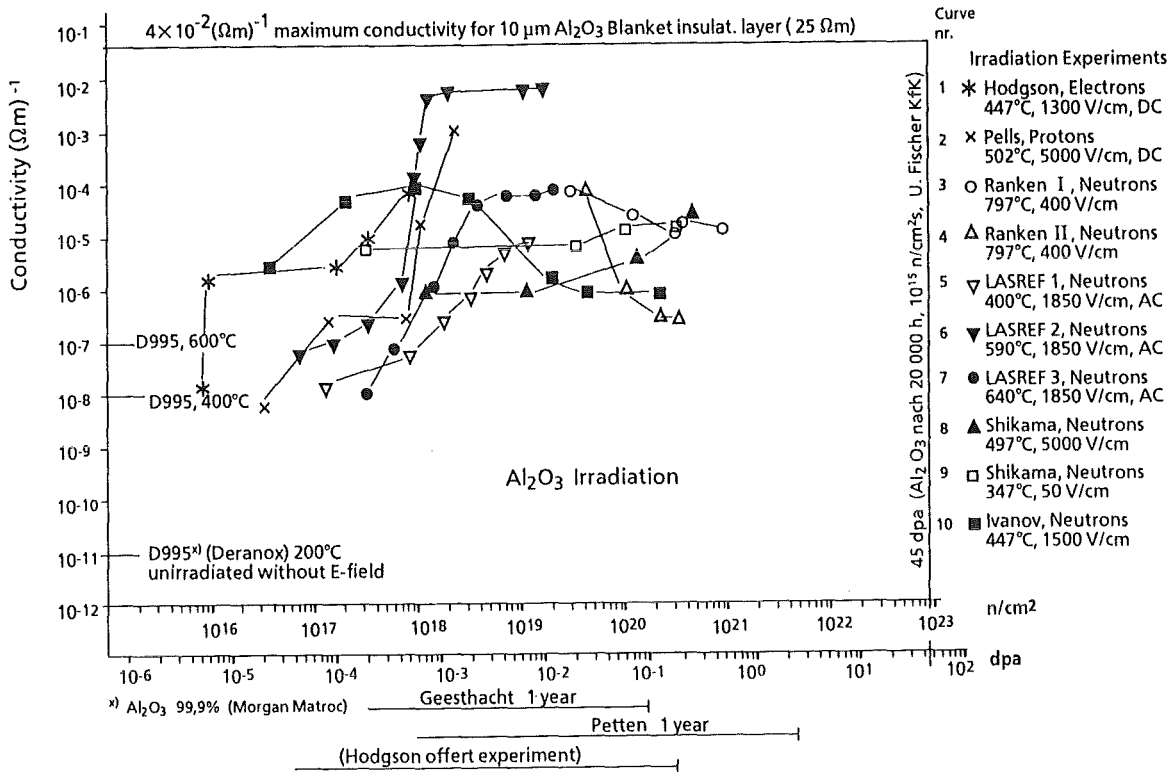


Fig. 2: Al_2O_3 Irradiation Experiments

- Influence of the type of radiation on the results cannot be defined clearly. It is excluded by the curves 1 and 10. Curves 2 and 8, however, indicate that the effects produced by irradiation with protons are greater than those achieved by an irradiation with neutrons.

According to the present knowledge, the increase in electrical conductivity during irradiation and in the presence of an electric field is caused by colloid formation. In the damage zone between 10^{-3} and 0.5 dpa, this colloid formation exhibits a certain saturation character and tends to decrease. For damage above 0.5 dpa, it is not sure, whether this property is preserved. It is therefore necessary to penetrate into damage zones above 0.5 dpa. Such experiments can be carried out with different kinds of radiation. The following possibilities have been considered:

Taking into account the capacity of the irradiation facilities in question as well as the boundary conditions with regard to time, the following irradiation strategy is envisaged:

Long-term irradiations up to DEMO-relevant damage will be carried out at HFR/Petten. The following arguments speak for this decision:

- Irradiation with fast neutrons is fusion reactor specific;
- the maximum fast neutron fluxes of the HFR and the DEMO blanket are of the same order of magnitude;

Facility	Kind of Radiation	Particle Energy [MeV]	Displacement Rate [dpa/s]
HFR-Petten	neutrons	≥ 0.1	$3.0E-7$
KfK Dual-Beam fac.	protons	40	$2.4E-7$
KfK Dual-Beam fac.	alphas	104	$2.6E-7$
CIEMAT-Madrid	electrons	2	$1.6E-8$

Table 1: Al_2O_3 irradiation possibilities

- the ratio of ionization rate to damage rate nearly corresponds to that obtained under blanket conditions;
- HFR has a good availability time ratio;
- HFR will probably also be available for irradiation experiments for a long term.

At first, use of two irradiation capsules with about 3 specimens each is planned. Pure Al_2O_3 serves as the reference material. If available, some of the specimens may be made of alternative materials, e.g. Al_2O_3 with specified impurities or directly coated manet. Irradiation temperature of all speci-

mens amounts to 450 °C. The axial neutron flux distribution leads to a small variation of the damage rate over the capsule height. With the experiments being prepared and carried out swiftly, damage values considerably exceeding the values available at the moment may be reached by the end of 1994.

At the KfK Dual-Beam facility, 20% of which is available only for the irradiation of insulating ceramics, no high damage values will be attained within acceptable periods of time. Therefore, this facility should be applied above all for fundamental and parametrical investigations using proton and alpha radiation, where generally smaller damage values are sufficient. Direct access to the facility and direct availability of the results allow the test programme to be conceived in a flexible manner. Possible test parameters are the material composition, the irradiation temperature, and the damage rate.

To study material degradation as a function of the type of radiation, additional experiments to be performed at the KfK Dual-Beam facility using protons and at the CIEMAT facility (Hodgson, Madrid) using electrons, respectively, will be planned if funds will be granted.. Special attention must be paid to the conditions prevailing which should be nearly identical (material, temperature, damage rate).

Literature:

- [1] G. Schmitz, K. Schleisiek, IRS; H. John, IATF;
"Proposal for the Irradiation of Al_2O_3 with High-Energy Particles for the Determination of the Variation of Electrical Conductivity in the Presence of an Electric Field", Internal Note, KfK-IRS, July 93

Staff:

H. John

G. Schmitz

BL MH-D 1 Liquid Metal MHD

In designing a self-cooled liquid metal blanket based on the poloidal-toroidal flow concept, the magnitude of the MHD pressure drop and the character of the velocity distribution in the first wall coolant channels, that result from 3-dimensional MHD effects associated with the required right angle bends in the coolant flow, represent important design issues. To address these issues and to verify the relevant models used in the design, MHD experiments were conducted in order to get basic information about pressure drop and velocity distribution in the cooling channels of this concept and to validate numerical codes developed at KfK to describe MHD-flow in complex geometries.

Additionally, advanced blanket concepts based on flow in parallel poloidal channels are investigated (compare the contribution to BLDE-D1). The advanced design concepts rely heavily whether or not the heat transfer in MHD flow can be improved by turbulence.

Multichannel U-bend Experiments

In electrically coupled multichannel ducts with a U-bend geometry MHD effects cause strong uneven distributions of flow rates Q_i and pressure drop Δp_i . In order to investigate these multichannel flow effects screening tests were performed in Riga with InGaSn as liquid metal at the end of 1991 and detailed Experiments were conducted in the MEKKA facility with NaK at the end of 1992. The documentation of the screening tests was recently completed [1], first results of the detailed experiments are described below; for details, see [2].

A test section with 5 parallel channels was used, see Fig. 1.

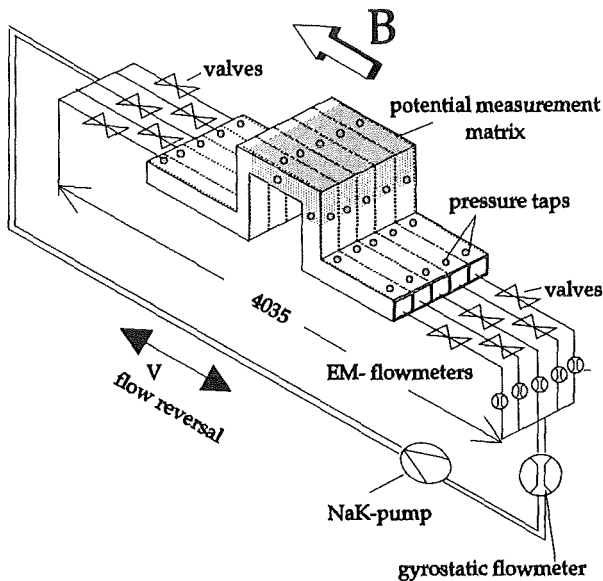


Fig. 1: Schematic set up of multichannel test section

These channels were electrically coupled because of the use of dividing stainless steel walls.

Figure 2 shows the redistribution of the individual flow rates

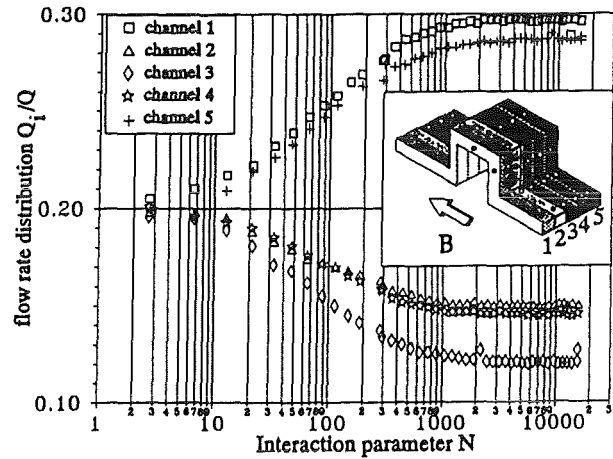


Fig. 2: Flow rate for increasing magnetic field; $k = 5$; $\Delta p_i^* = \text{const.}$

for the case that the magnetic field B (respectively the Hartmann Number M) is increased, starting from zero. During this experiment, the pump power was kept constant and the throttles in the individual channels were completely opened. With increasing M , the flow rate decreases (due to increasing MHD pressure drop) and with this the Interaction parameter N , defined by $N = a\sigma B^2/(\rho\bar{u})$, increases (a is the half channel width, σ and ρ the electrical conductivity and density of the NaK and \bar{u} the average duct velocity). For a negligible influence of the magnetic field the normalized flow rate in each of the five channels is about 0.2, as expected. With increasing N , the flow rates redistribute such that the values in the outer channels become significantly larger than those in the inner channels. This redistribution is terminated in these experiments at about $N = 1000$.

Figure 3 shows characteristic results for the case that the flow

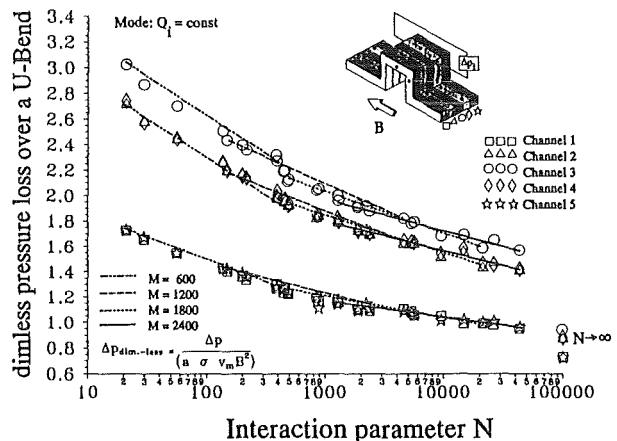


Fig. 3: Pressure drop distribution for $Q_i = \text{const.}$ (Detailed Experiments)

rates Q_i of the five individual channels was kept constant. The pressure drops are the smallest in the outer channels and the largest in the middle channel. The values decrease with increasing N . The values predicted by a theoretical analysis

based on the Core Flow Approximation (valid for $N \rightarrow \infty$) are not reached yet in the experiments. However, the predicted ratios of the pressure drops in the individual channels agree well with the theoretical results. A correlation is developed presently to describe the pressure drop for arbitrary values of M and N .

Figure 4 shows first results of measured and calculated electrical potential distributions on the outer wall surfaces. These distributions reflect the electrical current distribution inside the liquid metal. With the additional knowledge of the pressure distribution, the flow rates in the radial ducts and in the first wall layers can be determined. A good agreement is observed in the radial ducts with respect to the existence of fully developed flow. From the results for the toroidal ducts one can presume that less fluid than predicted is flowing in the first wall layer and more fluid flows in the side layers at

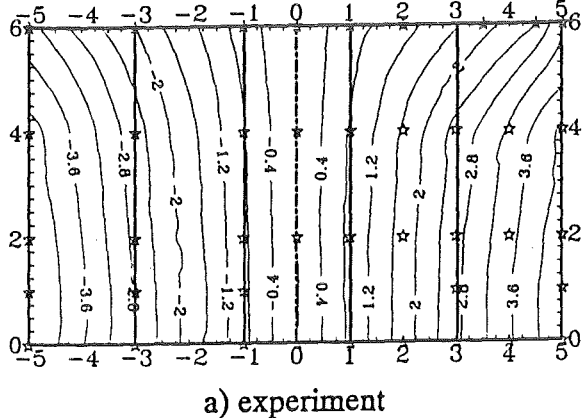
the outer channel walls. More detailed analyses will be performed in the near future.

A measure to reduce significantly the multi channel effects is to decouple electrically the individual channels in the radial parts of the U-bend. This method was applied in the design of the KfK self-cooled PbLi blanket and the effectivity of this measure was proven previously in the screening tests. Again, more detailed experiments with such a test section have just started in the MEKKA facility.

Poloidal-radial manifold experiments

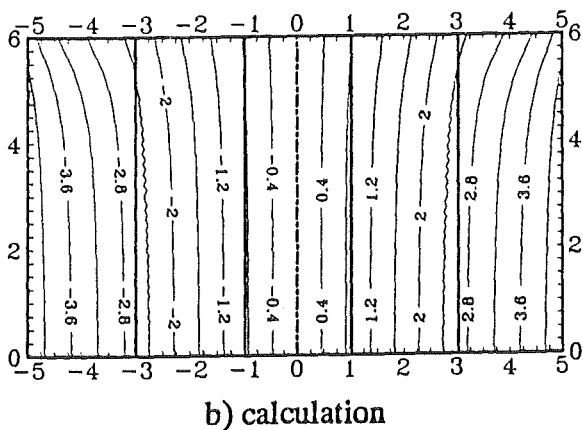
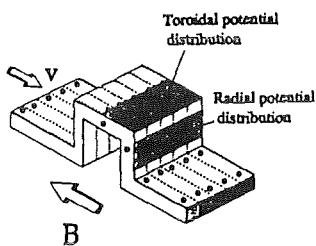
The KfK self-cooled PbLi blanket uses large poloidal ducts for distributing/collecting the liquid metal flow into /from perpendicular radial channels. A significant fraction of the total blanket pressure drop ($\approx 20\%$) was estimated for these

Radial potential distribution



Boundary conditions:

- $M = 2406$
- $N = 14800$
- $C = 0.0374$
- $Re = 1.62E-03$
- $B_m = 3.59 T$
- $\Theta = 0^\circ$



Toroidal potential distribution

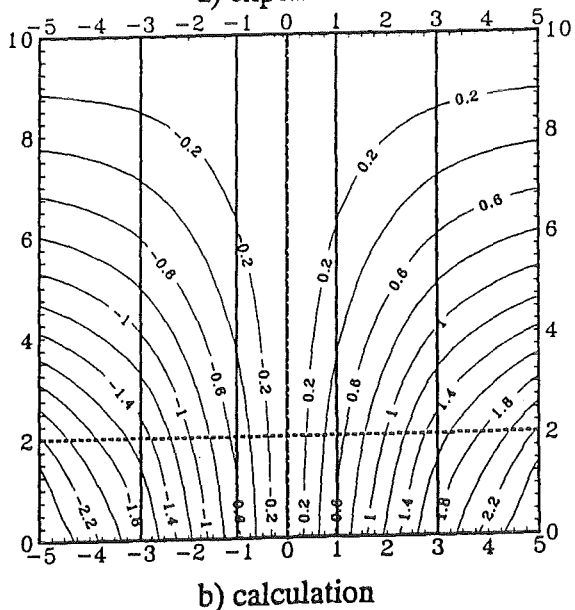
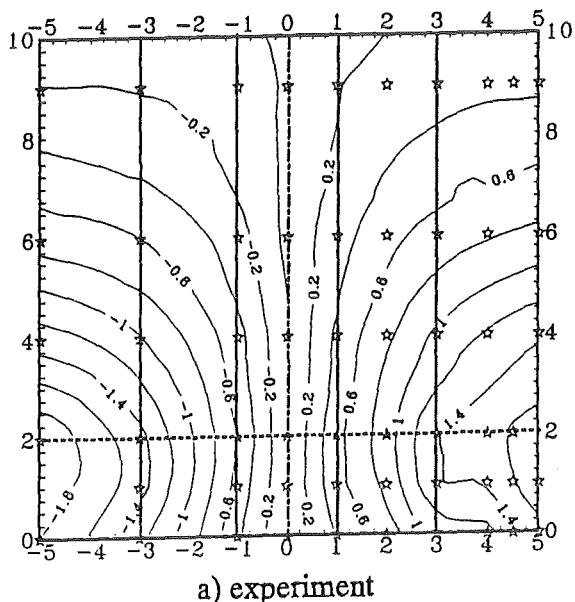


Fig. 4: Topography of surface potential distribution in KfK multichannel experiment

flow geometries. In order to predict these pressure drops more accurately, screening test using Hg as liquid metal were performed in cooperation with the Latvian Academy of Sciences in Riga. Figure 5 shows schematically the test section with flow directions for the case of flow distribution.

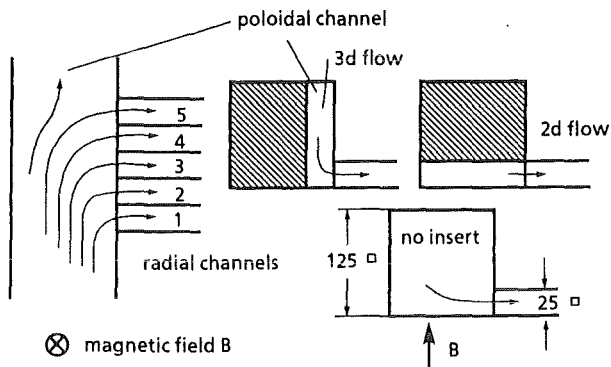


Fig. 5: Schematic set-up of manifold test section

Experimental parameters were Hartmann number M , Interaction parameter N , number of radial channels, wall conductivity, flow geometry in the poloidal channel and flow direction (distributor and collector case). Although the maximum achievable values of M and N were quite low compared to DEMO conditions, the results should be suitable for extrapolation.

The MHD heat transfer experiment WTM-1

The goal of this experiment is to get a deeper understanding of heat transfer of MHD flow in cooling ducts perpendicular to the magnet field direction, to confirm the model of laminar heat transfer used in our design calculations up to now and to investigate measures to promote heat transfer of MHD flow in a parameter range relevant for fusion application [3].

In this experiment the side wall (wall parallel to the field) of a rectangular test section is heated over a length of 500 mm using a radiation heater (Fig. 6). The test section with a cross

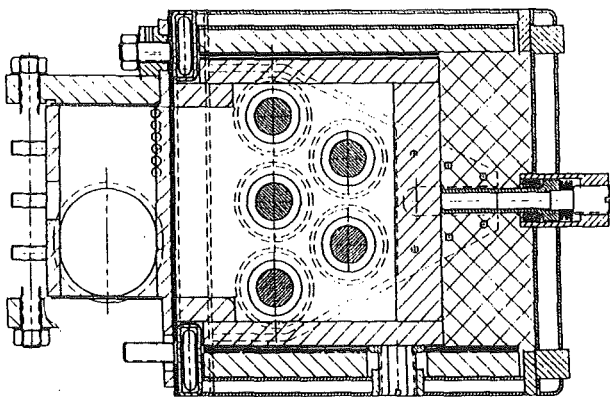


Fig. 6: Radiation heating the duct side wall of the WTM-experiment

section of 80 mm x 40 mm is made of stainless steel, the Hartmann walls are 1 mm the side wall 6 mm thick.

With the radiation heater a homogeneous heat flux of up to 20 W/cm² can be reached. The design of the test section allows to move the heater along its axis thus enabling to investigate heat transfer at least at two positions without removing the test section from the liquid metal loop. At the first position, heat transfer of a simple rectangular channel, in the second position, heat transfer of a channel with electrical turbulence promoters will be investigated. These turbulence promoters are copper stripes embedded in the Hartmann walls. The temperature rise along the heated wall is measured by thermocouples.

The fabrication of the test section is almost finished. The experiments will start end of 1993.

The GALINKA facility:

To explore the potential of an enhancement of the heat transfer the new facility GALINKA (GALium Indium facility Karlsruhe) was designed and built in which the different methods to produce turbulence in MHD-flow and the effect on heat transfer will be studied systematically under fusion relevant condition. This facility is a horse track design, where all components of a liquid metal loop, pump, flow through meter, heat exchanger and the test section itself are housed in a box, which is placed within the magnet. The eutectic alloy Indium-Gallium-Tin is used as liquid metal, the box is made of electrically insulating material.

Since MHD-flow in electrically insulated ducts is of high interest in the frame of a self-cooled liquid metal concept for ITER first experiments are conducted in the electrically insulated test section of GALINKA.

Pressure drop and velocity fluctuations were measured as a function of the Interaction Parameter N for different Hartmann numbers M (Figs. 7 and 8).

The results show that the MHD pressure drop agrees rather well with the prediction and that strong velocity fluctuations at rather low frequencies exist indicating a strong vorticity character of the flow.

MHD - Theoretical Work for blanket relevant flows

All theoretical methods for describing MHD-effects in liquid metal blankets for fusion relevant parameters are based on an asymptotic theory, which is valid especially for strong magnetic fields. Several numerical codes have been developed on the basis of the assumption that $M, N > 1$. The most general one for calculating MHD flows in ducts of arbitrary geometry in locally variable magnetic fields is described in [6].

The special case of MHD flows in conducting radial - toroidal - radial U-bends, which are important elements of any toroidal blanket concept has been analyzed in [8]. The most

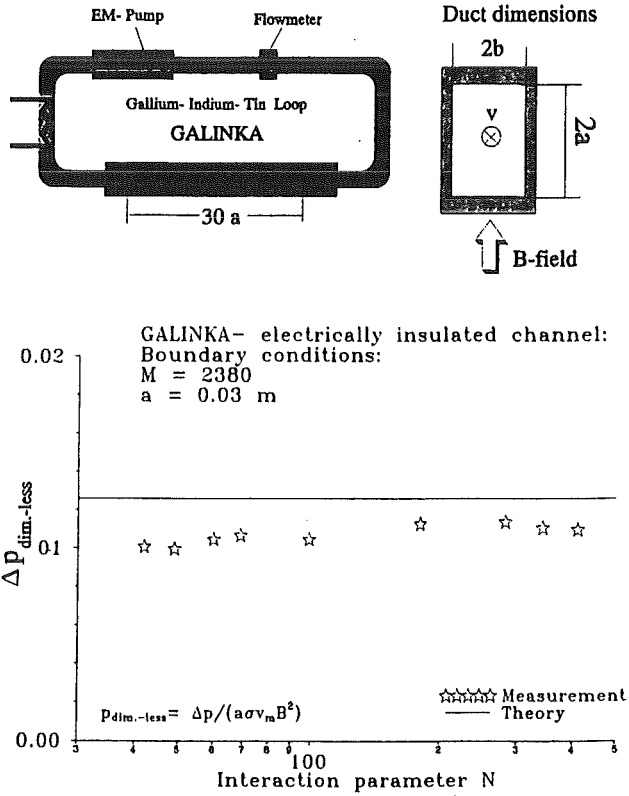


Fig. 7: Pressure drop measurements in the electrically insulated test section of the GALINKA facility

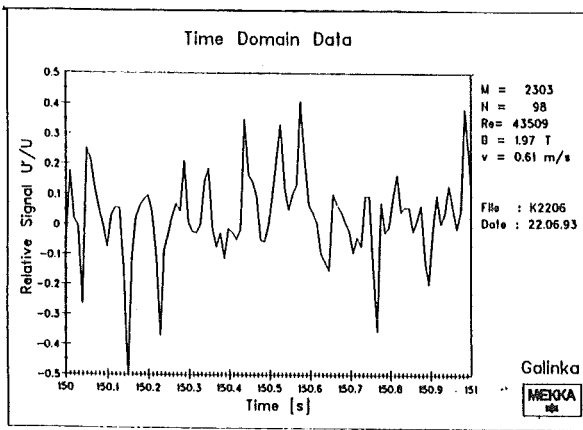


Fig. 8: Velocity fluctuations in the test section of GALINKA

interesting feature of the flow structure is shown in Fig. 9. The core of the toroidal duct has no component of velocity in magnetic field direction (the main flow direction) due to the strong interaction with the magnetic field. The whole volume flux is confined to thin boundary layers along the four toroidal walls, which are aligned with the field. However, the core in the toroidal duct is not stagnant, but shows a motion in planes perpendicular to magnetic field lines. The interaction of the toroidal core with the layers finally leads to a kind of helical motion as sketched in figure 9 for the streamline E→M. Theoretical results for a single 90° bend have been compared to experimental results. The

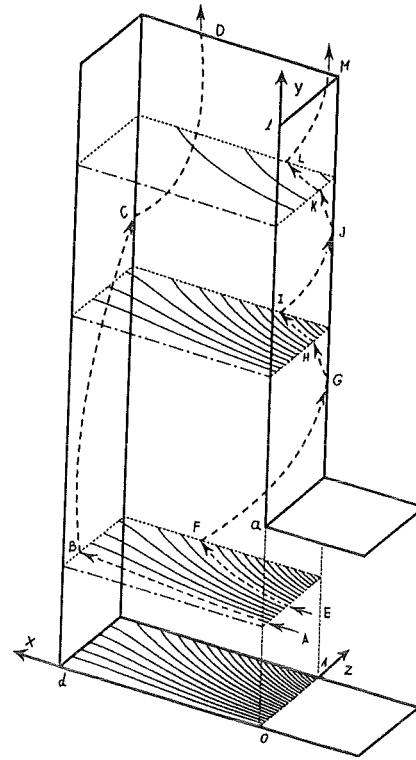


Fig. 9: Isolines of potentials and flow structure in a part of a U-bend

comparison, which shows good agreement for wall potential and pressure drop at large M and N is given in [9].

The electrical coupling of several channels, which are separated by conducting walls has been analyzed in [10]. The analysis shows interesting flow structures near the dividing wall and only minor increase in pressure drop due to multi channel effects.

MHD effects in ducts with insulating coatings [7] have been considered in order to provide materials scientists with sufficient data for required insulation properties.

Three-dimensional heat transfer calculations have been performed on the basis of assumed fully developed laminar MHD flow in ducts of circular and rectangular cross section [11]. Figure 10 shows that the thermal conditions in a poloidal concept of blanket are of boundary layer type ($T_w \sim \xi^{1/3}$) since the dimensionless wall temperatures are restricted to values of $T_w < 10^{-2} \cdot 10^{-1}$) depending on the used liquid metal and wall material.

The full numerical simulation of MHD-flows describes the complete flow structure including inertia and viscosity. Straight rectangular ducts and 90° bends can be calculated with the current version. Fig. 11 shows the pressure drop due to inertia in a straight insulating duct with decreasing magnetic field at $x=3$ for $M=100$, $N=25$ and $N=1000$. In Fig. 12 velocities in several cross sections of a bend are presented at $M=50$ and $N=100$.

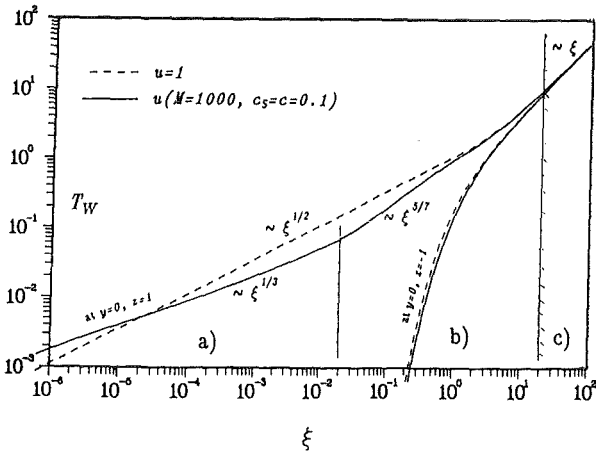


Fig. 10: Developing of wall temperature behind the entrance of a heated section. A fully developed laminar MHD velocity profile is assumed.

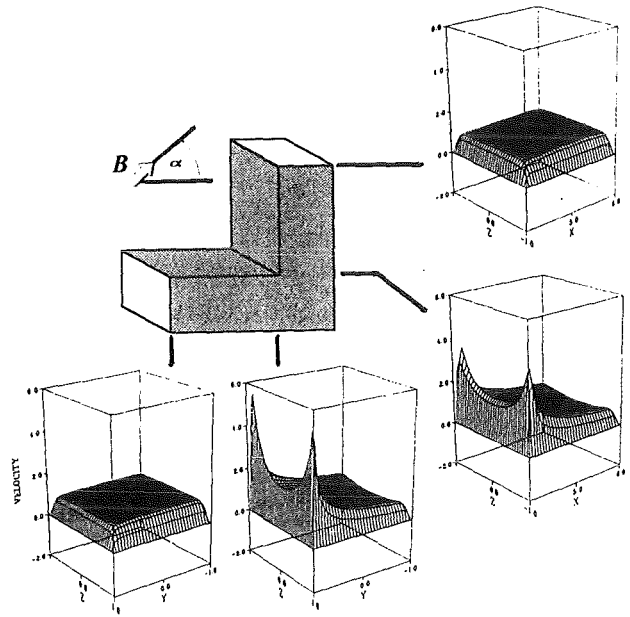


Fig. 12: Velocities in a bend, $M=50, N=100, \alpha=45^\circ$

$$B = f(x) \uparrow$$

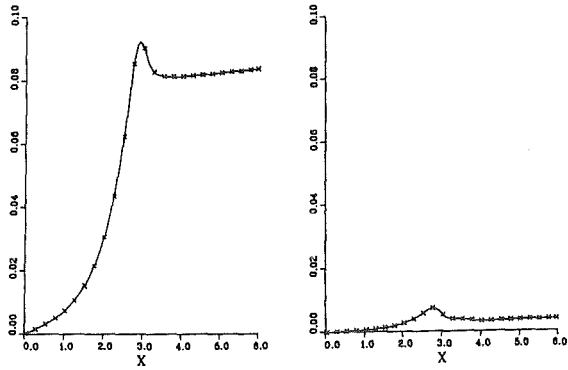
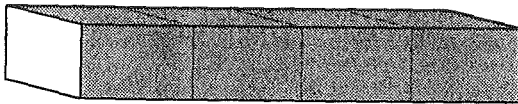


Fig. 11: Pressure drop due to inertia $M=100, N=25$ (left), $N=1000$ (right)

Literature:

[1] J. Reimann, S. Molokov, I. Platnieks, E. Platacis: "MHD Flow in Multichannel U-Bends: Screening Experiments and Theoretical Analysis", KfK 5102, Februar 1993

[2] J. Reimann, L. Barleon, S. Molokov, I. Platnieks, E. Platacis, R. Stieglitz: "First Results from Different Investigations on MHD Flow in Multichannel U-Bends", The Seventh Intern. Beer Sheva Seminar on MHD Flows and Turbulence, Jerusalem, Israel, February 14-18, 1993

[3] S. Malang, L. Barleon, L. Bühler, H. Deckers, S. Molokov, U. Müller, P. Norajitra, J. Reimann, H. Reiser, R. Stieglitz: "MHD-work on self-cooled liquid metal blankets under development at the Nuclear Research Center Karlsruhe". 7th Beer-Sheva Internat. Seminar on

MHD Flows and Turbulence, Beer-Sheva, IL, February 14-18, 1993.

[4] L. Barleon, L. Bühler, S. Molokov and R. Stieglitz: "MHD-Flow through a right angle bend", The Seventh Int. Beer Sheva Seminar on MHD Flows and Turbulence, Jerusalem, Israel, February 14-18, 1993

[5] L. Bühler: Additional magnetohydrodynamic pressure drop at junctions of flow channel inserts. Fusion Technology 1992: Proc. of the 17th Symp., Roma, I, Sept, 14-18, 1992.

[6] L. Bühler: "Magnetohydrodynamische Strömungen flüssiger Metalle in allgemeinen dreidimensionalen Geometrien unter der Einwirkung starker, lokal variabler Magnetfelder". KfK-5095, Februar 93, Dissertation, Universität Karlsruhe 1993.

[7] L. Bühler, S. Molokov: "Magnetohydrodynamic flows in ducts with insulating coatings". KfK-5103, Jan. 93, 7th Beer-Sheva Internat. Seminar on MHD Flows and Turbulence, Beer-Sheva, IL, Febr. 14-18, 1993.

[8] S. Molokov, L. Bühler: "Numerical simulation of liquid-metal flows in radial-toroidal-radial bends. KfK 5160.

[9] L. Barleon, L. Bühler, S. Molokov, R. Stieglitz: "Magnetohydrodynamic flow through a right angle bend." 7th Beer-Sheva Internat. Seminar on MHD flows and Turbulence, Beer-Sheva, IL, Febr. 14-18, 1993.

[10] J.S. Molokov: "Fully developed liquid-metal flow in multiple rectangular ducts in a strong uniform magnetic field". KfK 5075.

[11] L. Bühler: "Convective-diffusive transport in laminar MHD-flows. KfK 5241.

Staff:

L. Barleon

L. Bühler

E. Höschle

R. Kirchner

H. Kreuzinger

L. Lenhart

K.J. Mack

J. Reimann

R. Stieglitz

R. Vollmer

BL SA-D 1 Reliability Assessment

Helium Cooled Solid Breeder Blanket

The solid breeder blanket consists of 48 outer and 32 inner blanket segments. The cooling system for the outer and for the inner blanket are composed of two 50% systems each. Every 50 % system is further subdivided into independent redundant cooling cycles. The redundancy is 2 out of 3 for the inner cooling system and 5 out of 6 for the outer system. That means one system in a 50 % system can fail without the necessity to shut down the plant.

The availability analysis [1] takes into consideration all pipes, collectors, valves, steam generators (SG) including vessels and blowers. The size of the SG's is 180 MW for the outer and 170 MW for the inner cooling cycles. For this configuration the availability determined is > 98 %. The result is influenced with more than 99.9 % by the inner blanket cooling system. That means the unavailability for the outer blanket cooling system is in the order of magnitude of 10^3 lower than the value for the inner blanket cooling system.

The overall availability of > 98 % is sufficiently high at the present state of the project, but in general there exists a certain potential for further improvements in the availability if necessary.

The Dual Coolant Concept

The blanket system according to the dual coolant concept is also based on 48 outer and 32 inner blanket segments. The energy from the LiPb cycles will be transferred by double-wall steam generators according to the concept of the liquid metal cooling system [2]. The medium in the gap between the inner and the outer tubes is NaK.

For the 32 cycles of the inner blanket LiPb cooling system a 1 out of 2 redundancy is foreseen. This leads to a power of 30 MW per cycle. For the 48 cycles of the outer LiPb blanket cooling system a 2 out of 3 redundancy is planned. This results in a power of 35 MW/cycle.

For the inner blanket He-cooling system four systems are assumed according to the 1 out of 2 principle, and for the outer blanket He cooling six systems according to the 2 out of 3 principle. The power per redundant cycle is equal for the inner and for the outer blanket cooling and considered with 80 MW. The main SG data are listed in the Tab. below [1].

By an additional consideration of the SG vessels, pipes, collectors, valves and pumps, the overall availability will result in a value of 96 %. Here is also a special potential for improvements of the availability if necessary.

Data for the LiPb and the He Steam generators

Primary Medium Blanket	LiPb		He	
	inner	outer	inner	outer
Power per unit [MW]	30 35		80	
Redundancy per segment	1/2 2/3		1/2 2/3	
$t_{p\ in}$ [°C]	425		350	
$t_{p\ out}$ [°C]	275		260	
$p_{p\ in}$ [bar]	2		80	
$t_{H_2O\ in}$ [°C]	250		170	
$t_{H_2O\ out}$ [°C]	286		286	
$p_{H_2O\ in}$ [bar]	70		70	
Steam quality [x]	0.7		0.3	
Tube OD-ID [mm]	24/20-30/26		23/19	
Tube material	Austenit		Incoloy	
Transfer area [m ²]	422 492		2275	
Δp_{prim} [bar]	0.1 0.1		0.16	
Δp_{H_2O} [bar]	1.1 1.1		1.4	
Failure rate [10 ⁻⁶ /h]	5.8 6.8		11.0	

Literature:

- [1] H. Schnauder, Verfügbarkeit für die Kühlkreisläufe bei einem He-gekühlten Feststoffblanket und einem LiPb- und He-gekühlten Dual Coolant Concept, Unpublished Report in preparation
- [2] H. John, H. Schnauder, E. Bogusch, J. Wehling; Reliability investigations and improvements of the cooling system of a self-cooled liquid metal breeder blanket; SOFT 92, September 14-18, Rom

Staff:

H. Schnauder

Probabilistic analysis of welded joints in blanket design

A crucial point in the reliability analysis of blanket systems is the influence of the failure of welds on the system reliability of the whole blanket. Input data e.g. failure probability of welds per unit length for the different welds are necessary to perform a system reliability analysis. Non-destructive inspection is used to ensure proper quality of the weldments. It is well-known that detecting, locating and sizing of flaws in welds can only be performed with some uncertainty depending on the welding procedure, the geometry of the weld, the flaw type and the material. These uncertainties can be assessed with the help of probabilistic fracture mechanics. As a result, the reliability of a certain weld can be given in

terms of a failure probability which depends on the uncertainties in the inspection procedure (detecting, locating and sizing uncertainties), on the loading conditions of the weld, and also on the sensitivity of the inspection procedure.

Preliminary calculations were performed to establish a reference example which can be updated if real data are available. The reference weld was chosen to be the double-weld between two segments of the self-cooled liquid metal breeder blanket with helium cooled first wall. Typical results are shown in figure 1. The acceptance level indicates the sensitivity of the inspection procedure and has to be chosen in such a way that the probability of false acceptance (i.e. accepting a weld which contains a prohibitively large flaw which may cause failure) is minimized as well as the probability of false rejection (i.e. rejecting a weld which does not contain dangerous flaws which results in unnecessary costs for repair). Figure 1 shows that these two requirements

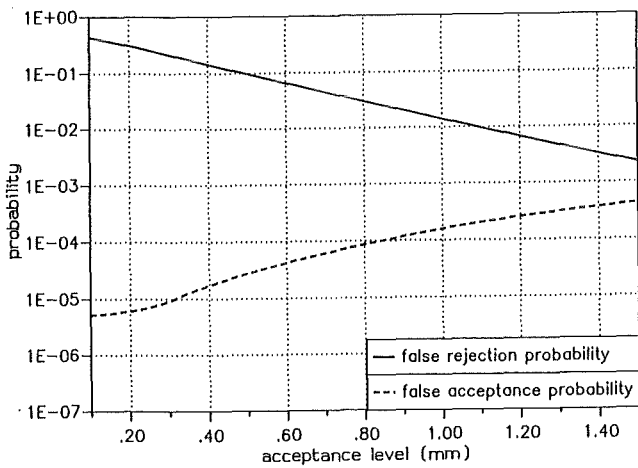


Fig. 1: Influence of the sensitivity of the inspection procedure on different probabilities.

are contradictory. The choice of an adequate acceptance level can be performed using critical values of false acceptance and false rejection probabilities.

The numerical values of the calculated probabilities in Figure 1, however, serve only illustrative purposes because important input quantities for the analysis are yet unknown and therefore have to be assumed or taken from the literature. In order to obtain realistic values, sample weldings which are presently produced will be evaluated and used to update the input quantities of the fracture mechanics model.

With the resulting probabilities of failure for individual welds it is then possible to perform a system reliability analysis for a whole blanket system.

Staff:

H. Riesch-Oppermann
S. Zhang

BL SA-D 2 Safety Analysis of Self-cooled LM Breeder Blankets

a) Electromagnetic Forces

Investigations for a rigidly fixed self-cooled liquid metal blanket have shown that the eddy current damping effect may be neglected [1]. The stresses calculated for the outboard blanket segment are in an acceptable range. For these calculations the design disruption (linear decay of 20 MA within 20 ms) and perfect insulation of each blanket segment have been assumed. Furthermore, the inductive coupling with the vacuum vessel has been neglected.

In another study the behaviour of the liquid metal blanket with a gas cooled first wall during a plasma disruption has been compared with that of the gas cooled ceramic breeder blanket. Here the inductive coupling with the vacuum vessel has been taken into account. Special attention has been given to the influence of the electrical connection of the first wall segments and to the question whether an internal insulation of the liquid metal blanket is necessary.

For the eddy current computations the 3D FEM code CARIDDI has been applied. The same initial and boundary conditions have been chosen for the different blankets. Again the design plasma disruption has been assumed. The same vessel and shield has been used and the inboard blanket has not been modelled. The resulting eddy current is split into two parts. One, the box current, is circulating in the blanket box, the other one, the toroidal current, flows in the first wall in toroidal direction. Because of the alignment of the toroidal current and the time constant magnetic field this part of the current does not produce any Lorentz forces. So the mechanical loading of the blanket during a plasma disruption is mainly depending on the magnitude and flow pattern of the box current.

Firstly it proves that the results for both blanket concepts do not differ significantly. The internal insulation of the liquid metal blanket has no significant influence on the maximum of the box current. Because the insulation emphasises the resistive behaviour of the blanket, the maximum box current is occurring a little bit earlier. But this may be neglected with respect to the mechanical loading.

The electrical connection of the first wall segments and its electrical properties are strongly influencing the magnitude of the box currents. The maximum current - and consequently the maximum forces - are reduced by a poloidally continuous connection of the first wall segments to the factor 3 and even more. Furthermore the maximum occurs later. For these results the global electrical resistance of the first wall in toroidal direction has been adjusted to approximately 0.5 m Ω .

Assuming a rigidly fixed blanket the electrical connection yields a decisive reduction of mechanical stresses in the

blanket caused by the disruption. Nevertheless a more detailed stress analysis is needed.

b) Blanket Selection Criteria

Safety and reliability related criteria for the evaluation of different blanket concepts have been elaborated [2]. They refer to the procedures proposed by the European Blanket Coordination Group for the "DEMO Blanket Selection Exercise" in 1994.

In the report a short survey is given of important studies on criteria for the comparison of different blanket options. Since these previous studies give a very wide picture when taken all together, an attempt has been made to elaborate a consistent list of criteria and to outline an evaluation procedure. Hence, for the evaluation of blanket concepts the following tasks are being proposed:

- Characterization of the toxic inventories and potential source terms including tritium, activation products, and chemical toxins
- Characterization of the possible energy sources for mobilization of toxic materials, including high pressure fluids, the decay heat, and possible chemical reactions
- Identification of the fault tolerance including the response to mixing of different media, loss of coolant accidents, loss of flow accidents, plasma disruption, off-normal magnetic loads, loss of vacuum accidents, loss of site power, earthquakes
- Assessment of the radioactive effluents under normal operation and accidental conditions
- Quantification of the recycling possibility and waste hazards
- Quantification of reliability and availability.

In two ad-hoc working groups (one group for safety, and one for reliability/availability) with members of CEA, ENEA and KfK the activity in establishing blanket selection criteria was continued in the framework of the European Fusion Technology Program. Due to the still existing deficiencies in the blanket designs and the limited resources special effort was undertaken to reduce the amount and depth of the investigations considered to be necessary for a comparison of different blanket concepts. The elaborated proposals were submitted to the Blanket Project Leaders and the Blanket Coordination Group.

c) Accident Analysis (ITER Blanket)

On request of the NET-Team an alternative blanket concept for ITER has been investigated based on austenitic steel (316 L) as structural material, a Pb alloy as shield/breeder material, and helium as coolant (s. BL DE-D1). The first wall which is similar to that of the DEMO dual coolant concept is designed

for an average neutron wall load of 1 MW/m². The rectangular first wall cooling channels of 2.5 x 2.5 cm² in size are connected to two independent helium systems. The quasi-stagnant Pb alloy inside the blanket box is cooled by helium flowing in an array of hairpin-shaped tubes.

For this blanket concept a preliminary analysis of the first wall behaviour during loss of coolant accidents (LOCA) has been carried out using the General Electric code TIGER V. This code allows to calculate the temperatures in complex structures with internal heat sources and convective heat transport in arbitrary internal channels. To limit the input and calculational effort, the real geometry was transformed into a simple 3-dimensional model in the following way: The rectangular first wall channels were turned by 90° into the poloidal direction, thus the coolant is flowing upward like the overall direction of the flow in the single passages of the first wall. Only the first row of the breeder cooling tubes is included in the model. The flow direction of the He in this channels is downward. Heat conduction and surface heat transfer is taken into account in the radial and toroidal direction, convective heat transport in the cooling channels in the poloidal direction. The helium inlet temperature is 250 °C, the outlet temperature of the first wall channels 329 °C. The surface heat load amounts to 20 W/cm² with a local peak value of 25 W/cm².

In the calculations it was assumed that at the start of the LOCA cooling of the first wall is instantaneously interrupted either in one or in both helium cooling systems. According to the "Safety and Reliability Related Blanket Selection Criteria" plasma shut down was assumed 1 s after LOCA occurrence. At that time, the neutron power in the blanket disappears instantaneously, and the first wall heat load decreases linearly down to zero in 20 s. In a first step the poloidal position of the maximum first wall temperature was determined with the average surface heat load of 20 W/cm².

Then the calculation was repeated with a local peak heat load of 25 W/cm² in that area.

As a representative result of the analysis, Fig. 1 shows for the two LOCA cases the history of the maximum first wall temperatures during the LOCA. The peak values are reached 12 and 15 s, respectively after the start of the LOCA. The difference between the peak values of the two cases is only about 11 K. This means that heat transfer between neighbouring channels does not play an important role. Consequently, the concept with two separate cooling systems will not induce significant advantages in the case of a LOCA. Of course, this conclusion applies only to the design investigated, i.e. to a channel pitch of 3 cm and austenitic steel as structural material.

In the case of a LOCA in both cooling systems the maximum first wall temperature increases to about 520 °C. The stress analysis of the first wall for these conditions has not yet been carried out, but it is expected that the transient will not cause severe damage to the blanket.

Literature:

- [1] Th. Jordan, "Kopplung der elektromagnetischen und strukturdynamischen Probleme beim Fusionsreaktor blanket", KfK 5236, 1993
- [2] W. Kramer, R. Meyder, H. Schnauder, Safety and Reliability Related Criteria for the Evaluation of Different Blanket Concepts, Part 1: Basic Considerations, KfK Unpublished Report (Jan. 1993)

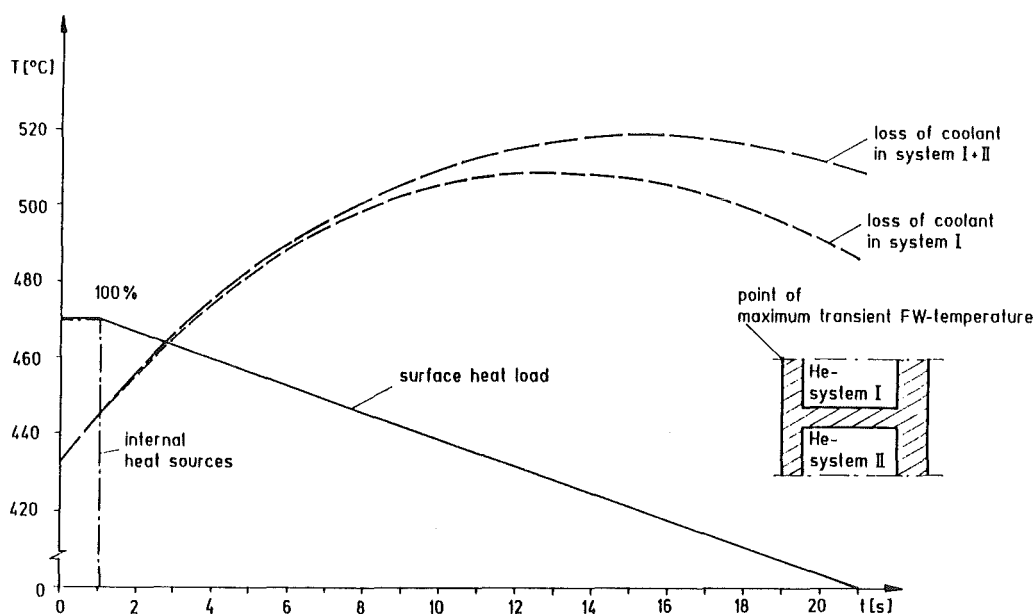


Fig. 1: Maximum first wall temperature under LOCA conditions

Staff:

F. Dammel

T. Jordan

K. Kleefeldt

W. Kramer

R. Krieg

R. Meyder

K. Schleisiek

Development of ECRH Power Sources

Introduction

The major goal of the gyrotron development program at KfK is the design, construction and test of high-power gyrotron oscillators for electron cyclotron wave applications in thermonuclear fusion experiments. For the next generation of fusion devices such as ITER, millimeter wave generators operating at long pulses up to cw with an rf output power in excess of 1 MW per unit at frequencies around 140 GHz are needed. In order to fulfill these requirements development work is still necessary. The ECRH development is the subject of cooperation between KfK Karlsruhe (power generation and millimeter-wave diagnostics), IPF University of Stuttgart (millimeter-wave transmission and diagnostics) and IPP Garching (plasma experiments).

Measurements at IPP Garching

A new Russian 140 GHz, 0.5 MW, 1.1 s gyrotron with a built-in quasi-optical mode converter and radial output coupling was installed at the Stellarator W 7-AS and tested together with the Russian group. Radial output coupling of the rf power in a Gaussian ($TE_{0,0}$) mode has three significant advantages for high-power operation. First, the linearly polarized $TE_{0,0}$ mode is directly usable for low-loss transmission as well as for effective interaction with the fusion plasma; thus no further mode converters are needed. Second, the converter separates the electron beam from the rf wave path, so that the electron collector is no longer part of the output waveguide as in the case of an axially arranged tube. Hence, the collector can be designed especially for handling the high electron beam power. In addition, energy recovery with a depressed collector becomes possible. Third, the influence of rf power reflected from the output window and the load (long-line effect) is significantly reduced, especially for modes rotating in the opposite direction from the design mode. The KfK gyrotron diagnostics system (100 MHz resolution) together with a frequency-time-interval analyzer allows instantaneous frequency measurements during a single pulse [1]. The measurements show a very stable single mode operation of the Russian tube (Fig. 1). No frequency hopping owing to the

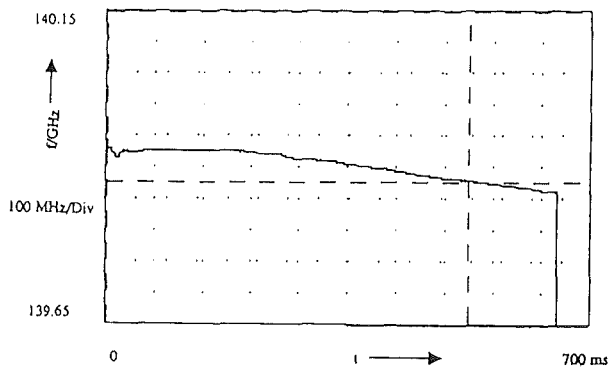


Fig. 1: Frequency of the 0.5 MW gyrotron versus time. The 50 Hz ripple is due to the cathode heater.

long-line effect has been observed.

KfK $TE_{10,4}$ -Gyrotron with Axial Output Coupling

Within the first KfK superconducting gyrotron magnet with a 100 mm bore hole only a tube with an axial output coupling could be installed in a reasonable way. Therefore, the first experiments had to be done with an axially arranged tube. The high power density due to the electron beam hitting the surface wall limits the maximum pulse length to a few msec. As rf-output windows an adjustable double disc sapphire window (DDW), a single disc sapphire window (SDW1) and a fused silica single disc window (SDW2) have been used. The electrical thickness of all the window discs is 5 half wavelengths at 140 GHz. The relative permittivity of sapphire is 9.4 and of the fused silica 3.8. Two different resonators with quite different quality factors have been investigated experimentally. The longer resonator with the length of the cylindrical section equal 12 mm has smooth transitions towards the input and output taper in order to reduce mode conversion [2]. The influence of the curved transitions increases the effective resonator length to about 16 mm. This resonator has been optimized for an average velocity ratio $\alpha=1.1$ (the shorter one for $\alpha \geq 1.5$). Both resonators are designed for maximum efficiency at an rf-output power of 0.5 MWe [3], [4].

Fig. 2 shows the calculated power reflection coefficient as a

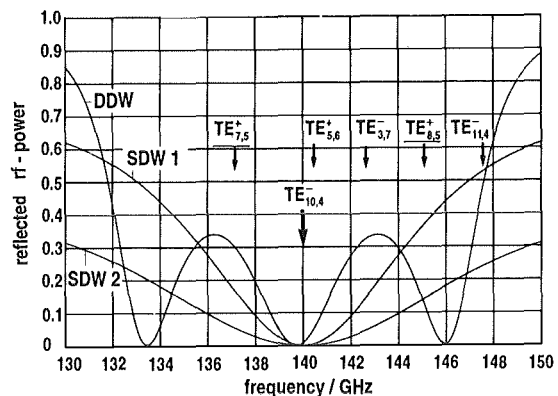


Fig. 2: RF-power reflected from different output windows

function of the frequency for the three different windows used. The distance between the discs of the double disc window is 4.41 mm, a value for which single mode operation of the $TE_{10,4}$ -mode was possible. As a consequence of the higher reflectivity of the sapphire windows, resonator modes located as far as the $TE_{11,4}$ at 147.4 GHz appeared to be competitors of the $TE_{10,4}$ mode. The mode competition problem was significantly reduced when the gyrotron was operated with the fused silica window. All modes indicated in Fig. 2 by arrows appeared as competitors when operated with the sapphire windows. However, only the underlined ones have been observed as competitors with the fused silica window.

In contrast to the design of the first tube the maximum achievable velocity ratio was limited to about 1.1. Above that value instabilities of the electron beam and a strong increase of the current to the modulation anode appeared. A reason for that seems to be an unusually large velocity spread leading to electron reflections already at this low value of the velocity ratio. One possible contribution to the enhanced velocity spread has been identified as a fabrication error. With the short resonator a maximum output power of 520 kW has been measured. However, in this case above 450 kW a slight contribution of the TE_{11,4} mode was observed. Fig. 3

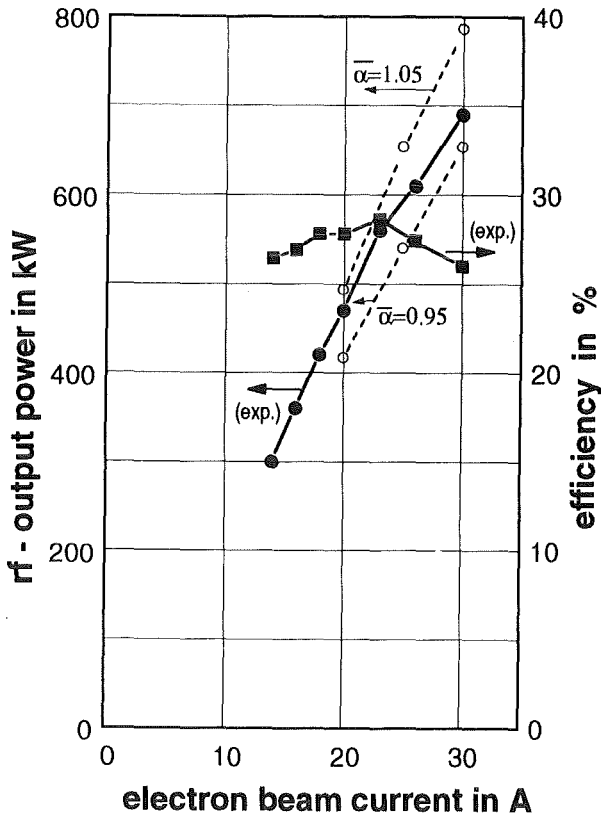


Fig. 3: Output power and efficiency for the TE_{10,4}-mode (long cavity) versus beam current

shows the rf-output power and the corresponding efficiency as a function of the electron beam current measured with the longer resonator. The optimized magnetic field distribution with a field strength of 5.6 T at the resonator was kept constant, whereas the beam voltage and the voltage of the modulation anode, which determines the velocity ratio have been adjusted for maximum output power. Care was taken to ensure that single mode operation occurred. A maximum output power of 690 kW was measured at 87.0 kV with an electron beam current of 30 A corresponding to an output efficiency of 26% [5]. When the internal losses in the resonator (~ 5%), the uptaper and collector (~3%), the output window (~1%), the external waveguide line (~1%) and the beam energy reduction due to the voltage depression (~5%) is taken into account, then the electronic efficiency is calculated to be about 31%. A maximum output efficiency of even 28.6% has been measured at an electron current of 23 A and an rf-output power of 560 kW. The corresponding electronic efficiency is about 33%. The achieved efficiencies

are in reasonable agreement with the calculated values, [6] [10] when velocity spread is taken into account.

A measurement of the mode content of the waveguide modes with a wavenumber spectrometer resulted in a purity of the TE_{10,4} mode better than 98%.

Frequency Step Tuning

One of the main advantages of ECW-heating of fusion plasmas is the well localised energy deposition of the microwave beam. By tuning the frequency of the generator it is possible to heat and stabilize different well defined areas of the plasma. In gyrotrons the frequency can be varied by changing the operating mode. Different modes can be excited by (fast) tuning of the beam voltage or (slow) variation of the magnetic field. Azimuthal neighbouring modes are suitable for frequency step-tuning in a gyrotron as their radial structure is very similar to that of the main mode. Subject to this condition the coupling of the electron beam and the rf wave in a gyrotron resonator is comparable for these modes. This behaviour is shown in Fig. 4 for the TE_{10,4}

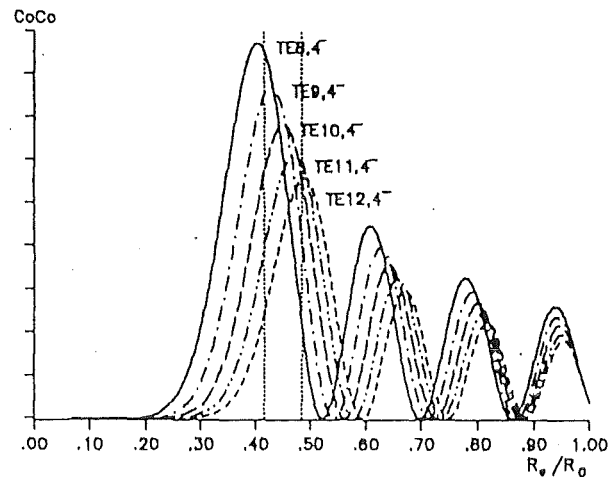


Fig. 4: Coupling coefficient for beam-wave interaction

mode and its neighbours. Although the frequency spacing of approximately 7.4 GHz of these modes is probably too large to fulfill the requirements for fusion plasma applications, investigations with respect to single mode operation and output power can be performed. A necessary broad band window is developed [11].

By increasing and decreasing the magnetic field (~ 5.3%) we optimized the tube to oscillate in the TE_{11,4} (147.4 GHz) and TE_{9,4} (132.6 GHz) mode respectively. In the TE_{9,4} mode we achieved 420 kW rf power at 25 A (to be compared with TE_{10,4}: 600 kW). We observed strong mode competition with the TE_{8,4} (124.96 GHz) and TE_{11,3} (126.24 GHz) modes. It is assumed that this effect is supported by a high amount of reflection of these modes at the window (up to 35%) which is tuned to 140.0 GHz. Taking realistic beam properties and window reflections into account the measured peak output

power of the TE_{9,4} mode is in reasonable agreement with numerical calculations [10].

Fig 5 shows the oscillating area of the TE_{11,4} mode in the

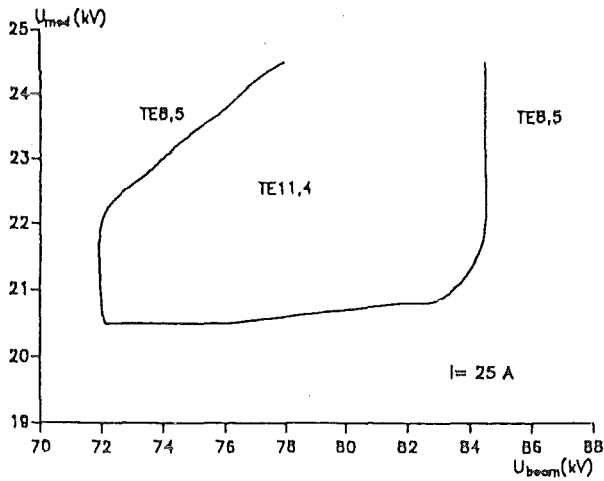


Fig. 5: Oscillating area of the TE_{11,4} mode

U_{mod} - U_{beam} plane. Several frequencies spaced by approximately 60 MHz have been observed for the TE_{11,4} mode, corresponding to different longitudinal modes of the long-line cavity formed by the gyrotron resonator and the (reflecting) window. The maximum output power in this mode was 300 kW.

TE_{10,4} gyrotron with radial output coupling and advanced quasi-optical mode converter

In the next version of the modular TE_{10,4}-mode gyrotron the rotating TE_{10,4} cavity mode is converted to a linearly polarized Gaussian beam by an advanced mode conversion system designed according to [7]. It consists of a helically cut quasi-optical aperture antenna with a deformed feed waveguide and three beam-forming mirrors (see Figure 6). The rotating mode is converted by the feed waveguide section into a mode mixture that assures an almost sidelobe-free radiation pattern when launched through the antenna aperture. After being refocused by a quasi-parabolic mirror, that corrects the phase in the transverse plane, an astigmatic Gaussian beam is obtained. Two further mirrors remove the astigmatism and direct the rf beam through the output window. The beam waist has a radius of 22 mm (1/e² drop of power density) and is located about 12 cm outside the window. The single disk window is made of pyrolytic BN with a permittivity of about 4.7. The transmission capacity of the edge cooled disk is estimated to be around 500 kW for up to 0.3 s. The electron gun and the beam tunnel from the axially arranged tube are used unchanged. The collector and superconducting magnet have been fabricated and tested. After assembly and bake-out of the tube, first tests are expected in September 1993.

Coaxial Cavity Gyrotron

The main advantages of coaxial gyrotron cavities compared to conventional cylindrical cavities are lower voltage

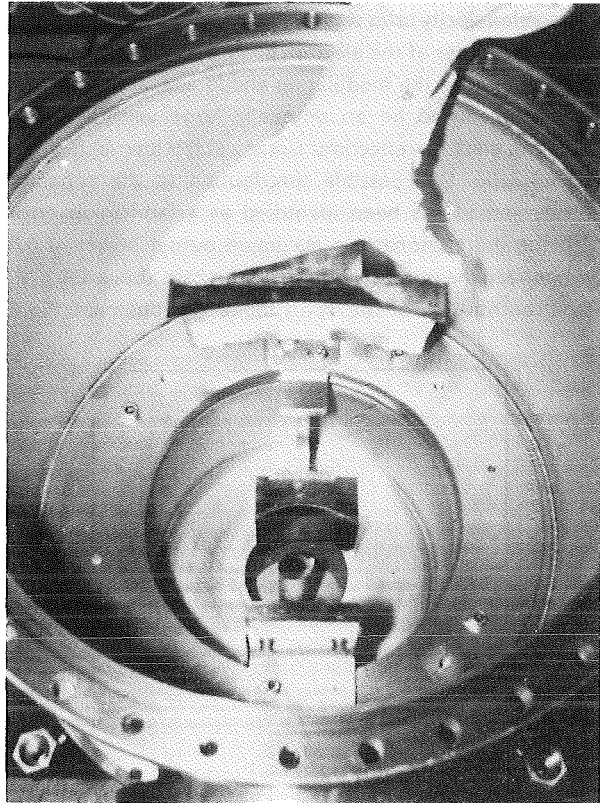


Fig. 6: Photograph of the gyrotron tank with the advanced quasi-optical mode converter

depression in the electron beam (i.e. 2.1 kV instead of 8.4 kV in conventional cavities) and better ability of mode selection. Very high operating modes can be utilized leading to lower ohmic losses in the cavity (≤ 1.5 kW/cm² at 2 MW output power). Therefore, a 2 MW cw gyrotron employing two 1 MW cryogenically cooled windows for ITER seems to be feasible. KfK has started in collaboration with IAP Nizhny Novgorod the design of a first experimental 1.5 MW 140 GHz short pulse coaxial cavity gyrotron with axial tube output for studies on mode competition (use of different mode selection schemes) and cavity output mode purity. Table 1 summarizes

Inverse electron gun

U	= 90 kV	R _{cavity}	≈ 29.8 mm
I	≤ 50 A	R _c /R _i	≈ 4
η	≥ 33 %	R _{beam}	≈ 10 mm
P	≈ 1.5 MW	Q _r	≈ 2000
α	≈ 1.3 (=v _⊥ /v _∥)	Q _{ohm}	≈ 75000
δv _⊥	≤ 30 % (operating regime)	P _{max}	≤ 1.5 kW/cm ²

Pulse length: τ = 300 μs

High order cavity mode: μ ≈ 90 (Bessel zero)

Table 1: Parameters of first experimental 1.5 MW, 140 GHz short pulse gyrotron with coaxial cavity (1994)

the main features of this tube. The inverse electron gun allows support and cooling of the inner cavity rod from the gun side and thus opens the possibility to install a dual-beam quasi-optical mode converter with an advanced dual-cut launcher together with two output windows in a later phase of the development (see Fig. 7). The two coherent Gaussian rf

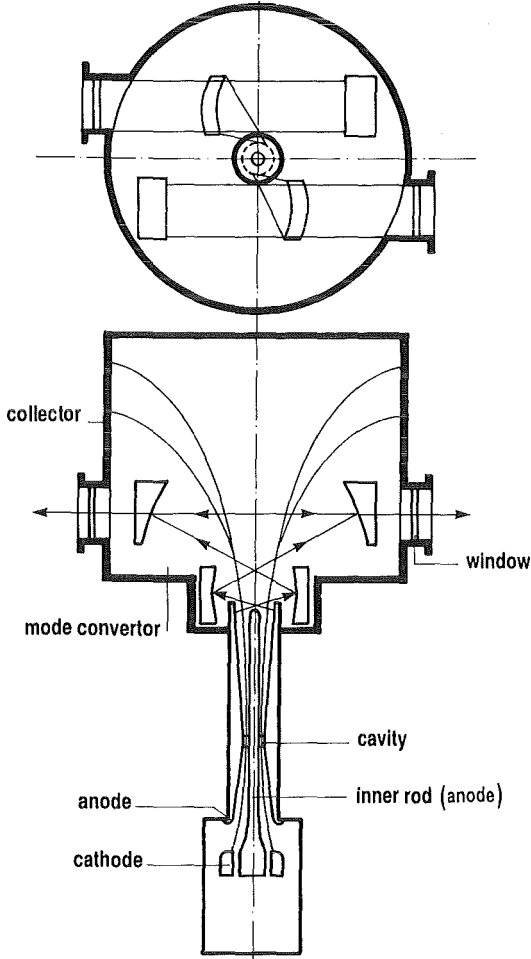


Fig. 7: Schematic arrangement of the coaxial cavity gyrotron

output beams can be combined again to a single beam for low loss transmission to the plasma torus.

Measurements of the Properties of Electron Beams

The measurement of the real properties of the electron beam is necessary not only for checking the limits of validity of the available numerical codes but also for a better understanding of the behaviour of a gyrotron tube and for being able to perform a reliable gyrotron design. The method of retarding fields is used for measuring the velocity distribution of the helical gyrotron electron beams. This method requires a special experimental set-up [8] as shown in Fig. 8.

As a consequence of the high power density of the electron beam, the measurements have to be performed at scaled down parameters. In order to prove the validity of extrapolating the measured values towards the operating parameters the experimental arrangement has been

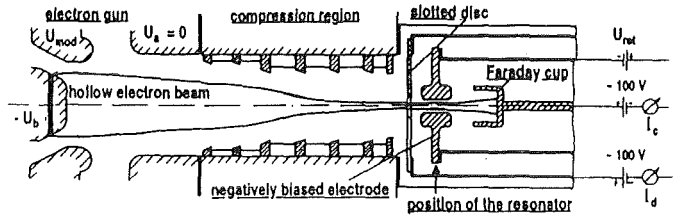


Fig. 8: Schematic arrangement of the velocity spread analyzer

modified to allow measurements over a wide range of scaling factors k_s . The scaling factor k_s gives the value by which the voltages applied at the gun are reduced. In addition, to have unchanged electron trajectories the beam current I_b and the magnetic field $B(z)$ have to be scaled down by $(k_s)^{1.5}$ and $(k_s)^{0.5}$ respectively. The retarding field method can be applied to measure the distribution of the current in dependence of the longitudinal and transverse velocity, $\beta_{||}$ and β_{\perp} because the motion within the retarding region is adiabatic and therefore the retarding field acts only on the longitudinal momentum leaving the transverse momentum unaffected.

Out of the measured current distributions the experimental values which are of interest for the gyrotron operation, as the relative transverse energy t_{\perp} , the average velocity ratio α and the velocity spread $\delta\beta_{\perp}$, are evaluated.

Two guns of the MIG-type optimized for a 140 GHz, TE₀₃-gyrotron have been examined. One of the guns has been designed to have a laminar and the other one a non-laminar electron flow [9]. Both guns are designed for an electron current of 8 A at 70 kV.

The experimental value of t_{\perp} and α are somewhat higher than the value calculated with the EGUN code. However, they are still within the estimated error margin of $\pm 10\%$. At low beam currents the experimental value of $\delta\beta_{\perp}$ is quite close to the numerically calculated value of about 5%. The spread $\delta\beta_{\perp}$ increases with the beam current and attains at a beam current of 8 A a value of about 10%. In order to prove the validity of extrapolating the results up to the gyrotron operating region, tests have been done at scaling factors of 5, 10 and 20 for different gun parameters. The experimental result of $\delta\beta_{\perp}$ as a function of beam current are given in Fig. 9. These results indicate that the measured $\delta\beta_{\perp}$ is, within an estimated accuracy of about $\pm 15\%$, independent of the scaling factor. This is a strong indication that the beam parameters measured at scaled down parameters can be extrapolated up to the gyrotron operating region. Up to about the design value of the electron current both guns have a similar velocity spread. Above about 10 A the non-laminar gun shows a significantly stronger increase of $\delta\beta_{\perp}$ with current than the laminar gun. This confirms the results of numerical calculations that the non-laminar flow is more sensitive to space charge forces than the laminar flow.

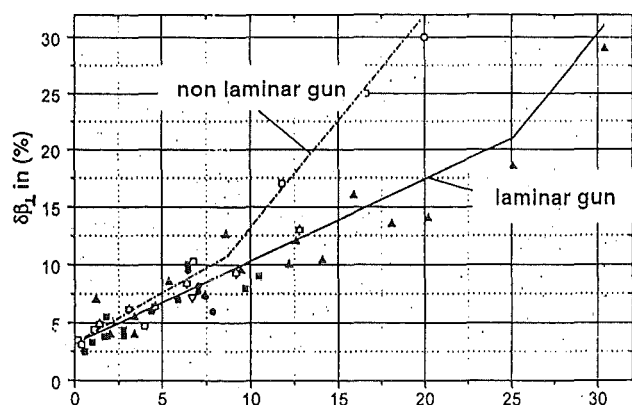


Fig. 9: $\delta\beta_{\perp}$ beam current for both guns measured with $k_z = 5, 10$ and 20

Literature:

[1] G. Gantenbein, T. Geist, G. Hochschild, Würzburg 1988, Proc. SPIE Vol. 1240, 221-222 and T. Geist, M. Thumm, W. Wiesbeck, Conf. Dig. 16th Conf. on Infrared and Millimeter Waves, Lausanne 1991, Proc. SPIE Vol. 1576, 274-275

[2] O. Dumbrajs, M. Thumm, J. Pretterebner, D. Wagner, Int. J. Infrared and Millimeter Waves, 13 (1992), 825-840

[3] E. Borie, G. Gantenbein, B. Jödicke, G. Dammertz, O. Dumbrajs, T. Geist, G. Hochschild, M. Kuntze, H.-U. Nickel, B. Piosczyk, M. Thumm, Int. J. Electronics, 72, 687-720 (1992)

[4] E. Borie, O. Dumbrajs, R.K. Gupta, A. Möbius, B. Piosczyk, H. Wenzelburger, Conf. Dig. 14th Int. Conf. Infrared and Millimeter-Waves, Würzburg 1989, Proc. SPIE Vol. 1240, 213-214

[5] B. Piosczyk, M. Kuntze, E. Borie, G. Dammertz, O. Dumbrajs, G. Gantenbein, A. Möbius, H.-U. Nickel, M. Thumm, Fusion Technology 1992, C. Ferro, M. Gasparotto, H. Knoepfel, eds., Elsevier Science Publisher B.V. 1993, Vol. 1, pp 618-622

[6] E. Borie et al., Proc. 8th Joint Workshop on Electron Cyclotron Emission and Electron Cyclotron Resonance Heating, Gut Ising, Germany, 1992, Vol.2, pp. 539-548

[7] J. Pretterebner, A. Möbius, M. Thumm, Conf. Dig. 17th Int. Conf. Infrared and Millimeter Waves, Pasadena 1992, Proc. SPIE, Vol. 1929, 462-463.

[8] B. Piosczyk, Conf. Dig. 17th Int. Conf. Infrared and Millimeter Waves, Pasadena 1992, Proc. SPIE, Vol 1929, 494-495, B. Piosczyk, Conf. Dig. 18th Int. Conf. Infrared and Millimeter Waves, Colchester, Sept. 1993;

[9] B. Piosczyk in C. Edgcombe (ed.), "Gyrotron Oscillators - their Principles and Practice", Taylor & Francis Ltd. London, 1993

[10] G. Gantenbein, Dissertation, Universität Karlsruhe, June 1993, KfK-Bericht Nr. 5229

[11] H.-K. Nickel, U. Ambrosy, M. Thumm, Conf. Dig. 17th Int. Conf. Infrared and Millimeter Waves, Pasadena 1992, Proc. SPIE Vol. 1929, 462-463

Staff:

- W. Baumgärtner
- E. Borie
- H. Budig
- G. Dammertz
- U. FeiBt
- G. Gantenbein
- P. Grundel
- A. Hornung
- S. Illy ab 01.05.1993
- S. Kern (Uni Karlsruhe)/ab 1.4.1993
- M. Kuntze
- R. Lehm
- A. Möbius
- N. Münch
- H.-U. Nickel (Uni Karlsruhe)
- B. Piosczyk
- G. Redemann
- M. Thumm
- R. Vincon
- A. Wien (Uni Karlsruhe)

High Power Windows

The actual candidate material for gyrotron windows is sapphire. In order to assess the resistance with respect to spontaneous failure the inert strength is necessary. In a first test series 4-point bending bars 3.5 x 4.5 x 45mm were cut out of an original sapphire disc. Whilst the disc surfaces remained polished the side faces of the specimens were only ground as usual in testing ceramic materials. The measured strength data are shown in Fig. 10 in Weibull representation (circles). The two Weibull moduli σ_0 and m are given in the plot. In order to estimate the influence of the cutting and grinding procedure during preparation of the bending specimens a second series of strength tests was carried out with discs of 25mm diameter and 2mm thickness in a ring-on-ring testing device (inner ring 11mm outer ring 22mm diameter). In these tests only the original polished surface can contribute to the strength. The results are entered in Fig. 10 as squares. A possible influence of the residual stresses generated during grinding and polishing was checked by measuring additional specimens which were annealed before the tests. The strength values (open squares in Fig. 10) show no significant influence of annealing.

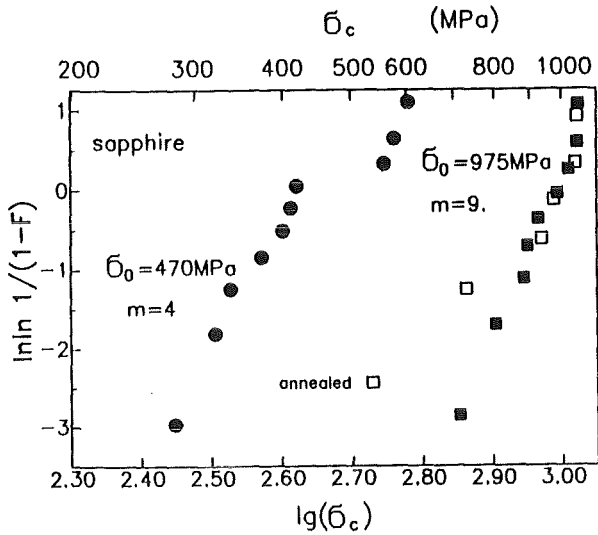


Fig. 10: Strength data of sapphire bars (circles) and discs (squares)

As the consequence of these first strength measurements with different types of tests it is recommended to perform all future strength measurements in ring-on-ring test with unannealed specimens.

Staff:

T. Fett

Plasma heating in nuclear fusion reactors by feed of millimeter waves from gyrotrons calls for effective and reliable high-vacuum tight window systems with preferably 1 MW power transmission as a major prerequisite.

At KfK the concept is being pursued of a single-disk window made from monocrystalline Al₂O₃ (sapphire) with edge cooling by bubble boiling in liquid nitrogen (77 K). The relevant development work has been continued by IMF III according to schedule during the period of reporting.

The design calculations have been performed with the ABAQUS finite element programm supported by the CAD program BRAVO for network preparation. In an extensive study the influence of different parameters on the transmitted power has been analysed [1, 2].

Three different power distributions have been chosen for the calculations (Fig. 11):

1. a profile of a fundamental Gaussian wave beam;
2. a distribution flattened by a phase-modulation mirror in order to reduce the peak power density in the center of the window [3];

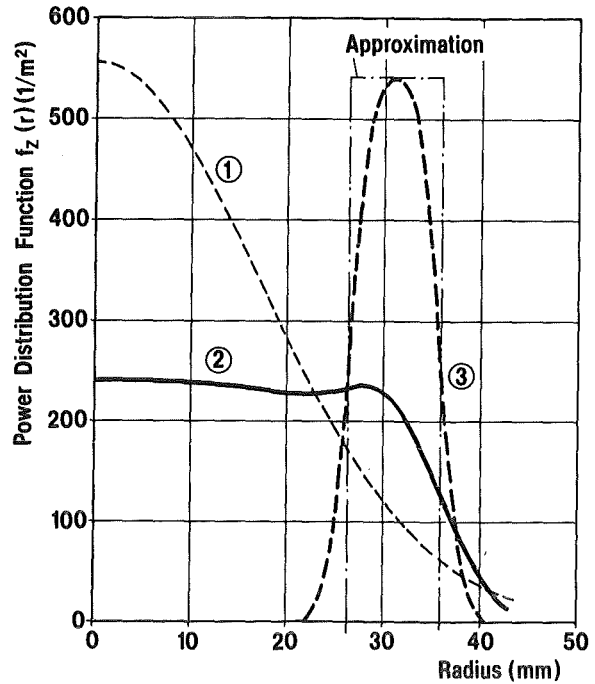


Fig. 11: Distribution of power density.

3. an annular shaped power distribution [4], which becomes possible by a coaxial gyrotron cavity.

With a power absorption factor $\tan \delta = 3.15 \times 10^{-12} \times T^{3.3}$ (at 140 GHz) presently available for a Ti-doped sapphire [5], and a thickness of the disk of 1.76 mm (6 mm at the edge) the maximum transmittance obtained for the window is shown in Fig. 12, i.e.

- about 500 kW for a Gaussian mode,
- 700 kW for a flattened profile, and
- 1 MW for an annular shaped power distribution [6].

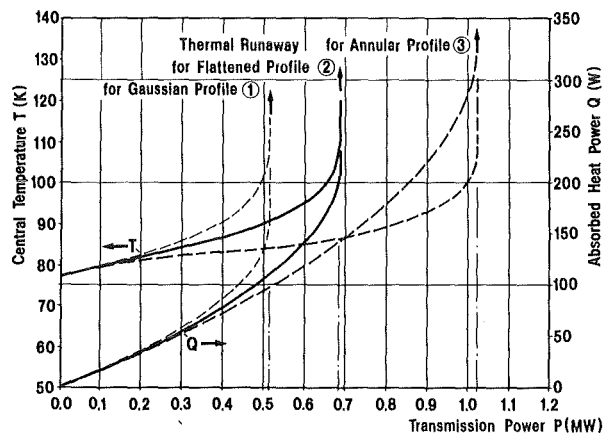


Fig. 12: Central temperature and heat absorption as a function of transmitted power.

It is actually not the heat transfer to the coolant at the edge of the window which sets the limit, but it is the radial heat

conduction in the disk itself which causes the so-called thermal runaway.

40 tests series have been performed in the meantime using the test equipment built in 1991 which served to test the concept and to verify the model computations: 22 of the test series with an electrically heated copper simulator and 18 with an original sapphire window also heated electrically.

In experiments with an electrically heated copper disk we found a very good agreement of the measured with the calculated temperature distributions. By contrast, deviations appeared in the tests involving sapphire disks - see Fig. 13 -

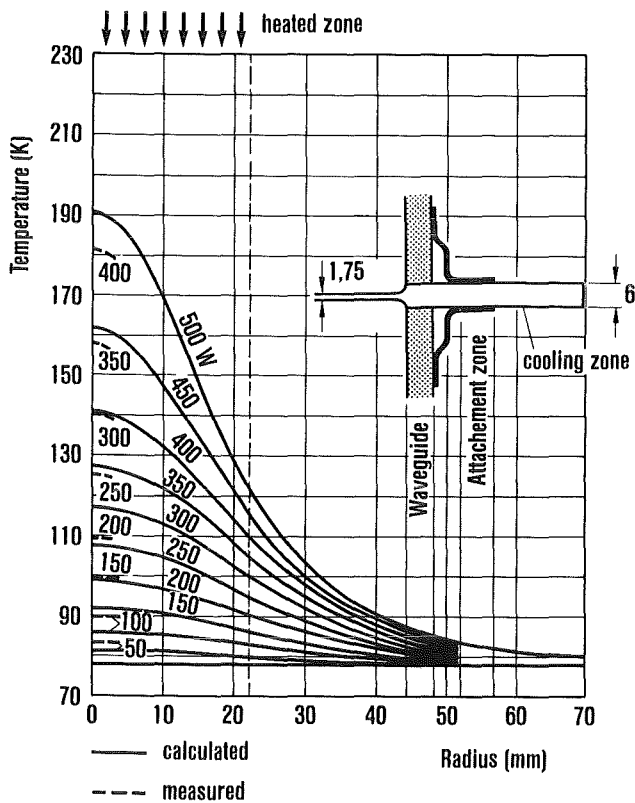


Fig. 13: Radial temperature distribution in the sapphire disk.

which allow to conclude that the thermal conductivity of the sapphire used is little as assumed. All the results obtained during the tests are contained in two internal KfK reports [7, 8].

In addition to development work on single-disk windows with edge cooling by liquid nitrogen a study was performed at IMF III which related to a gas-cooled double-disk window [9]. It appeared from that study that expenditure for this alternative window concept would be considerable.

Literature:

[1] P. Norajitra, E. Bojarsky, H. Reiser, H.E. Häfner, Cryo-cooled High-power Window for High-frequency Plasma Heating, KfK-Report 4930, September 1991

[2] H.E. Häfner, E. Bojarsky, P. Norajitra, H. Reiser, Cryo-cooled Windows for High Frequency Plasma Heating, 17th Symposium on Fusion Technology, Roma/Italy, September 1992

[3] N.L. Aleksandrov, V.I. Belousov, A.V. Chrikov, G.G. Denisov, D.A. Lukovnikov, V.I. Malygin, M. Yu. Shmelyov, D.V. Vinogradov, Quasi-Optical Millimeter-Wave Components at IAP, Institute for Applied Physics, Nizhny Novgorod, 4th Russian-German Meeting on ECRH and Gyrotrons, May 1992

[4] A. Sh. Fix, P. Sushilin, Output Window RF Power Capacity Increasing by means of RF Wave Transverse Structure Optimization, Institute for Applied Physics, Nizhny Novgorod, 4th Russian-German Meeting on ECRH and Gyrotrons, May 1992

[5] R. Heidinger, Dielectric Measurements on Sapphire for Electron Cyclotron Wave Systems, 6th International Conference on Fusion Reactor Materials, Stresa/Italy, 27.09-01.10.93

[6] H.E. Häfner, E. Bojarsky, K. Heckert, P. Norajitra, H. Reiser, Liquid Nitrogen cooled Window for High Frequency Plasma Heating, 6th International Conference on Fusion Reactor Materials, Stresa/Italy, 27.09-01.10.93

[7] H.E. Häfner, K. Heckert, K. Philipp, R. Vouriot, Zwischenbericht über Versuche für ein kryogen gekühltes Hochleistungs Fenster zur HF-Plasmaheizung, unpublished KfK Report, February 1992

[8] H.E. Häfner, Kühltechnische Untersuchungen zu einem Flüssigstickstoff-gekühlten Einscheibenfenster zur HF-Plasmaheizung, unpublished KfK Report, March 1993

[9] H.E. Häfner, Kryofenster für HF-Plasmaheizung, Kühltechnische Betrachtungen zu einem gasgekühlten Doppelscheibenfenster, unpublished KfK Report, February 1993

Staff:

- E. Bojarsky
- H.E. Häfner
- K. Heckert
- K. Müller
- P. Norajitra
- K. Philipp
- H. Reiser
- R. Vouriot

TRIT-1 Tritium Supply and Management

One gram of tritium was delivered to KfK in December 1992 and stored in the Institute of Radiochemistry.

From end September to the beginning of October 1993 a total of 3,5 g T₂ will be delivered to KfK in batches of 0.09; 0.9 and 2.5 g. These batches will be measured with the newly installed calorimeter, built by the KfK Engineering Department.

A final batch of 5.5 g T₂ will be delivered to KfK during April/May 1994 completing the total order of 10 g given to Ontario Hydro, Canada.

First filling of tritium into the process systems of the tritium Laboratory Karlsruhe is planned for October/November 1993.

A starting protium/tritium mixture with 0.09 vol % T₂ will be used for leak tightness measurements. Later on tests with higher tritium concentrations will be performed.

Staff:

G. Jourdan

Studies for ITER / NET

Introduction:

By granting study contracts to KfK, ITER/NET draws upon special expertise available in the laboratory. In contrast to the technology tasks which extend over a longer period of time and consist in most cases of experimental work, study contracts are agreed on short notice and are of limited duration. In the year under review the KfK has spent approximate two manyears for this kind of arrangements. Subjects scatter widely according to the need arising from the design activity for ITER/NET.

Extended Jacket Material Characterization of the Model Coil

The current material testing program under the framework of the NET contract No. NET 92-287 covers the efforts done in conjunction with the cryogenic crack growth tests of small cracks and the preliminary investigations about the impact of the insulation layer on an existing surface crack. The investigations concerning with small cracks required the manufacturing of small surface flaws on the specimens surface which may serve as a crack starter under cyclic loading. Two type of holes were introduced in this context. Firstly, machined holes of 0.1 mm diameter with a depth of 0.2 mm could be achieved by high speed mechanical drilling. Secondly, by electro discharge method (EDM) a small hole of 0.3 mm diameter could be produced. These two type of flaws were the initial step of the present cryogenic crack growth tests. Crack propagation and the microscopic examination of the broken halves of the specimens were completed within this work. In addition, the simulation of the "short crack" propagation were investigated according to a conservative measurement at constant high K-max value, which at near threshold ΔK range eliminates the unknown amount of the crack closure. This is believed to represent a conservative approach for the crack growth rate in engineering components, thus important for the cyclic loaded jacket material of the future superconductors.

In this context we believe that fatigue crack growth rate (FCGR) studies of small cracks is of special importance since in material fatigue, when crack size approaches that of the microstructure or the extent of local crack tip plasticity, or when cracks are physically small (typically smaller than 0.25 mm), crack-tip field characterization models may no longer apply.

The emanation of cracks from small surface defects was simulated with the small hole mechanically drilled into the surface. A pin holded flat specimen C-1 (316LN plate material) with a 0.1 mm hole was cycled at $R=0.1$ with a peak load of 20 kN at 12 K. No crack initiation could be observed up to 625229 cycles and at a corresponding peak stress of 714 MPa. After warm up, the specimen was removed and the cross section reduced to 20 mm². In this way higher stresses could be applied to the specimen in the next run. After cool-down, cycling of the specimen was continued at a peak stress of 900 MPa. No crack initiation could be observed until a sudden specimen failure occurred at 555860 cycles. The hole remained intact up to this final cycle number and no sight of a crack initiation could be detected after microscopic inspection of the fractured surface. It is assumed that failure start occurred from the corner of the rectangular cross section.

A similar behaviour was shown by the test carried out with the specimen C-2 and an EDM-machined 0.3 mm diameter hole. After 600000 cycles with a peak stress of 714 MPa ($R=0.1$) the stress was increased to 950 MPa. After additional 90000 cycles crack emanation was observed and crack growth of this specimen could be determined with the usual procedure [1]. According to these results it appears that

higher stresses are necessary for the crack initiation from an already existing flaw such as manufacturing related scratches. An EDM type flaw, however, simulates a most severe defect in a structure. These investigations figure out in principle the structural safety potential of cyclic loaded material when the nominal stresses are below 2/3 of the yield strength. Practically to emanate a crack from a preexisting very small material defect high cyclic stresses are necessary (in the range of ca. 1000 MPa) to achieve ΔK levels of about 6-10 MPa \sqrt{m} . This stress intensity factor range is on the other hand necessary for substantial crack emanation in a life period below a million cycles.

A quite different behaviour can be expected for very small already emanated cracks. To simulate this "short crack" behaviour on the basis of the proposal [2] given by R. W. Hertzberg, the specimen C-6 was tested with constant K-max = 20 MPa \sqrt{m} at 12 K. Figure 1 gives the cyclic load control

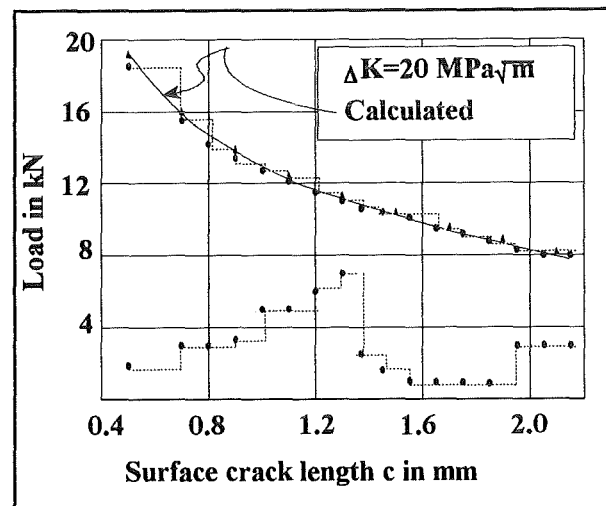


Fig. 1: Peak load vs. crack length c of the 316 LN plate material test procedure carried out at 12 K. The dotted line gives the step by step changed load levels during the test. The solid line gives the calculated ΔK -line of the specimen for 20 MPa \sqrt{m} .

procedure of the specimen. After decreasing the ΔK level to ca. 7 MPa \sqrt{m} the ΔK level was increased again to check the base line FCGR of the 316 LN plate material at $R=0.1$ determined recently [1] by measurements with C-2, C-3, and C-4 given in Fig. 2. Figure 3 gives the results of this test in form of a dc/dN vs. ΔK diagram. The lowest value of the stress intensity factor range indicates a R value as high as 0.63, corresponding to a high crack growth rate. In Fig. 3 the line of the plate material findings at $R=0.1$ is also given and the drastic increase of the FCGR can be seen with such a variation of test method. The curve determined at constant K-max, ΔK decreasing procedure indicates the absence of the crack closure effect and gives the detrimental impact on the 316LN plate material FCGR properties.

The second important problem about the influence of an insulating layer on the surface crack propagation were investigated with the same material at 12 K. These tests were performed under four-point bending mode. For the four

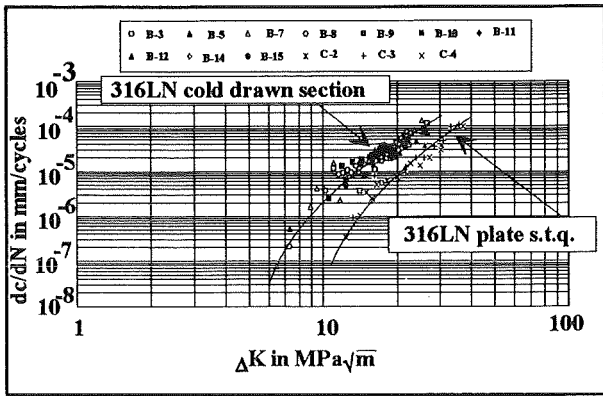


Fig. 2: dc/dN vs. ΔK plots of two 316 LN materials with different conditions determined at 12 K and at a load ratio of $R=0.1$. The runs B3...B15 give the results determined with the cold drawn U-section material. The runs C2...C3 are the tests with the solution treated and quenched plate material.

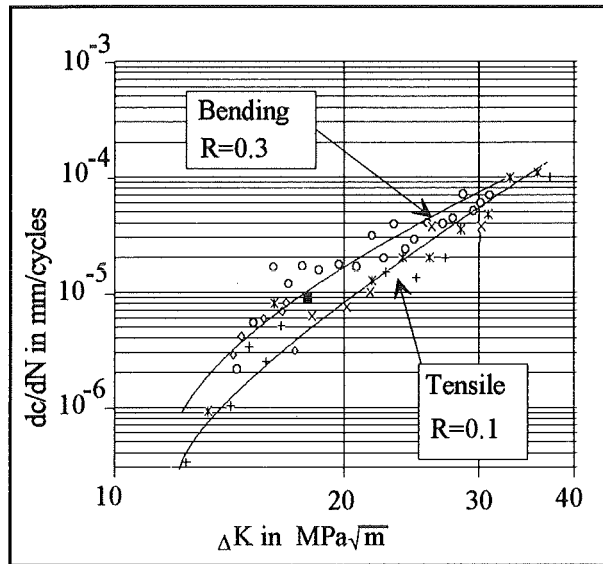


Fig. 4: dc/dN vs. ΔK of the 316 LN plate material for bend and tensile load tests at 12 K. Solid square point gives the result of the influence of an insulation layer.

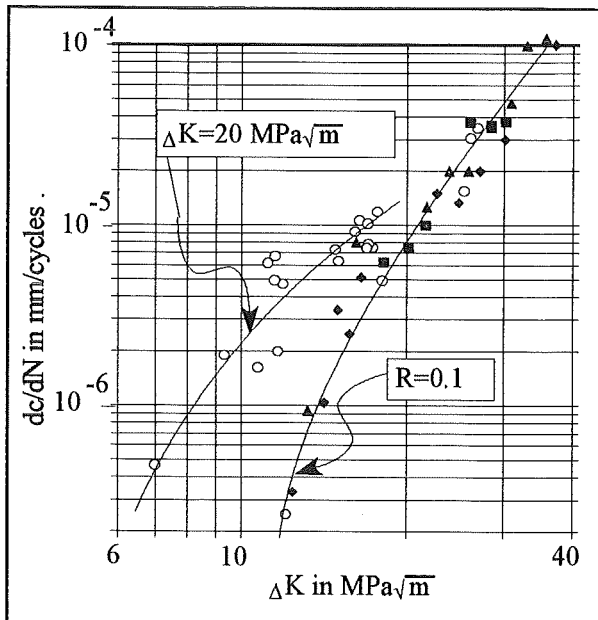


Fig. 3: dc/dN vs. ΔK of the 316 LN plate material "short crack" test obtained by constant K_{max} , ΔK decreasing method at 12 K

point cyclic bending tests, bars of size 110x17x5 mm were used. The upper and lower span length positions were 40 mm and 90 mm, respectively. To manufacture an insulation layer around the cyclic bend sample, a 6 mm wide standard glass fabric tape was overwrapped with two wet layers around the bar covering the already initiated crack on the metallic surface. The two component epoxy resin (type EA-2, Tokyo Sokki Kenkujo Co., TML) was cured at 295 K for 24 hours. After cryogenic cyclic loading the bond between fabric and metal showed no detectable failure.

Results of surface FCGR at 12 K produced by cyclic four point bending tests are given in Fig. 4. For comparison, the cyclic tensile data of 316 LN plate material are also shown. The higher FCGR of the cyclic bend bar loading results from the

high load ratio ($R=0.3$) necessary for this test. The influence of the insulation layer processed on an already initiated crack is shown by the solid square point. During the cycling, the crack beneath the insulation layer propagates with almost the same rate as in the case of the specimen without an insulation layer.

Literature:

- [1] A. Nyilas, B. Obst and A. Ulbricht: Simulations on jacket material failure of NET-superconductors by surface crack growth in 316 LN type materials at 12 K, To be published in the proc. of ICMC held on July 93 in Albuquerque, USA
- [2] W. A. Herman, R. W. Hertzberg, C. H. Newton and R. Jaccard, A re-evaluation of fatigue threshold test methods. "Fatigue 87", EMAS, Ltd. (1987) UK pp. 819-828

Staff:

A. Nyilas
H.P. Raber

Crack Growth in the NET First Wall

The first wall (FW) of a fusion machine operating as a pulsed Tokamak reactor as planned during the CDA-phase of the ITER (International Thermo-Nuclear Experiment Reactor programme (and former in the NET design studies) is subjected to periodically changing high heat fluxes. These loads are inducing a changing inhomogeneous temperature field in the component. As a part of whole blanket box, the FW is prevented from free expansion and free bending. Hence, global and local thermal stresses are applied. Under normal conditions one load cycle may be defined as the time span from start-up operation to the end of shut-down/dwell time. As some 50.000 cycles of operations are planned to be performed, fatigue of the FW has to be considered. The dominant failure mechanism of the component will probably be the interaction of some fracture and fatigue mechanism.

On the one hand, there will be fatigue growth of existing cracks under repeated load. The respective flaws may be generated in the fabrication processes during machining or as defects of welds. On the other hand, the FW is subjected to severe loadings under off-normal conditions (plasma disruptions, run-away electrons). During these events new cracks may be initiated, that will propagate further as fatigue cracks. Failure of the component has to be defined, at least, if any crack penetrating the wall under stable crack growth reaches the plasma facing surface of the FW. Due to the high vacuum conditions needed in the plasma chamber, no leak whatsoever can be tolerated.

Furthermore, cracks of a critical size will fail spontaneously. If the FW is subjected to overloads as they are applied under the dynamic conditions of disruption events, spontaneous failure, even of small cracks, cannot be excluded.

The study was performed for a water-cooled austenitic stainless steel FW at low temperature and pressure (ITER-CDA design). Schematically the geometry is shown in Fig. 1.

Problems of fatigue/fracture interaction have been investigated. Within the first part of the Contract linear elastic fracture mechanics (LEFM) was used. Within the second part two different approaches of elastic plastic fracture mechanics (EPFM) have been applied together with several inelastic material models.

Fatigue crack growth has been investigated parametrically:

- at different critical locations
- and for starter cracks of different size and shape.

Upper and lower bounds on the life predicted have been found by the application of different fracture mechanical approaches and different material models. Depending on some assumptions (to be made in the models) life assessment by EPFM may be more conservative than by LEFM. The lifetime predicted varies by a factor of two. However, the location identified as most critical with respect to fatigue is different. From the EPFM approach location C (at the heated surface) is identified as life limiting, whereas from the LEFM approach cracks located in the cooling tube (either at A or B) have the shortest fatigue life. Fig. 2 summarises the lifetime

Life assessment under various approaches

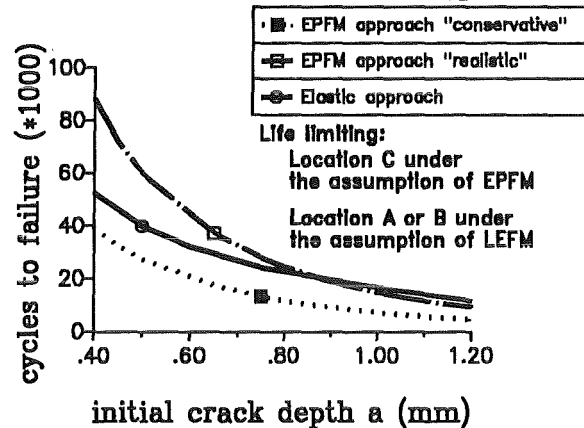


Fig. 2: Final failure off FW under different approaches

predicted under the assumption of various starter cracks and for different approaches.

Staff:

E. Diegele

G. Schweinfurther

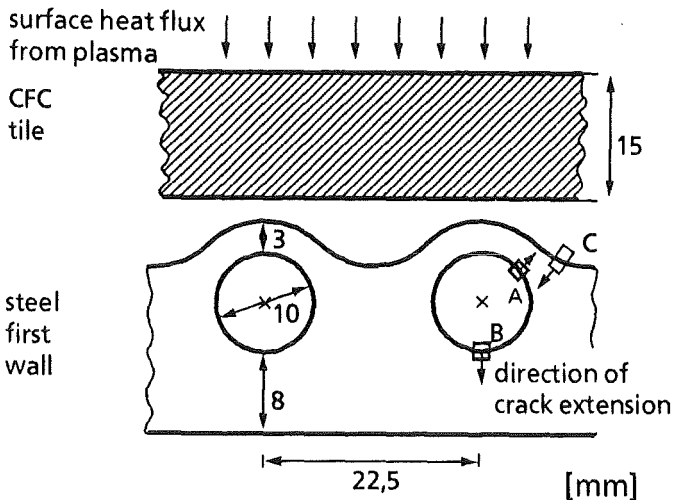


Fig. 1: Sketch of FW geometry

Impact of ITER Liquid Metal Blanket Design Options on Safety Level and Licensing in Germany

Inside the ITER-EDA different coolant media and structural materials are under discussion for first wall, blanket, divertor and vacuum vessel. There is a preference at present for liquid lithium as breeder material and coolant medium for the first wall and blanket, with vanadium alloys as structural material. Inside the EC Fusion Programme, however, liquid lithium has been excluded so far as coolant and breeder material due to its potential chemical reaction hazards. To qualify from the EC point of view the ITER-EDA options presently under discussion, five design options for blanket/first wall cooling concepts have been assessed in a NET study (Table 1).

Table 1: Blanket/first wall design options assessed in this study

Option	Component	Coolant	Breeder	Type
I	Blanket/FW Divertor Vacuum Vessel	Li NaK NaK	Li	self-cooled
II	Blanket/FW Divertor Vacuum Vessel	He He H ₂ O	Li	tube in pool
III	Blanket/FW Divertor Vacuum Vessel	He He He	Li	tube in pool
IV	Blanket/FW Divertor Vacuum Vessel	He He H ₂ O	LiPb	tube in pool
V	Blanket/FW Divertor Vacuum Vessel	H ₂ O H ₂ O H ₂ O	LiPb	tube in pool

The study covers the following topics with respect to the five blanket options: (1) Literature survey on chemical reaction processes of the liquid metals involved, (2) layout of the liquid metal blanket options with an assessment of the coolant and breeder inventories, (3) assessment and discussion of the main radioactive inventories, (4) review of the confinement strategy and concepts with view to necessary modifications, and (5) definition of safety and design issues and discussion of their relevance to the five options, leading to a ranking.

The literature survey focused on the chemical reactions of the liquid metals included in the five blanket options assessed, i.e., lithium, Pb-17Li and NaK. As possible reactants the most common environmental media were considered, namely air, nitrogen, carbon-dioxide, water and concrete. Several basic design rules can be derived. (a) Lithium-water reactions must be avoided by not allowing lithium and water carrying components in the same compartment. (b) Concrete must be

protected by leak-tight steel liners against potential lithium pools, catch pans are insufficient. (c) Nitrogen must be excluded for inertization in rooms containing lithium components. (d) For components and rooms carrying Pb-17Li or NaK no extra safety measures beyond common practice in liquid metal technology are deemed necessary.

The layout of the main circuitry led to the following results: The total breeder inventory for the helium cooled lithium blankets (options II and III) is on the order of $2.6 \cdot 10^5$ kg. For the self-cooled blanket it is doubled. The total breeder inventory for options IV and V (Pb-17Li) amounts to $5.7 \cdot 10^6$ kg. The total helium mass in options II - IV is $\approx 1.4 \cdot 10^4$ kg, most of which (90 %) is in the loop and components. In option V we have $\approx 6.6 \cdot 10^5$ kg of water in the circuitry. The main pipes of the helium loops in option II - IV are ≈ 1.1 m in diameter when assuming 8 parallel systems. An extreme design challenge will be the helium feeders, where 5 inlet and 5 outlet pipes of ≈ 0.4 m diameter per 1/24 sector are needed.

The assessment of the radioactive inventories implies large uncertainties. For the options with lithium as breeder the tritium recovery process becomes a key feature in reaching the ITER target value of < 200 g of tritium in the whole lithium circuitry. For Pb-17Li permeation constraints and extraction techniques strongly determine the inventory, which is expected to be about 20 g. Tritium extraction from helium to sufficiently low levels (≈ 10 g) is not seen as a critical issue. Maintaining low levels in the water cooling system of option V seems to be feasible but implies safety concerns.

The triple-barrier confinement concept employed by NET is regarded as appropriate for the five liquid metal blanket options, as long as the primary circuitry is entirely enclosed within the 2nd barrier. A first layout of the primary (breeder and coolant) and secondary circuitry showed that the required space is mainly dictated by the piping rather than by the size of the components. For the primary circuits compartments on the order of 5000 - 13000 m³ are needed for one quarter of the machine, not including depressurization volumes. Compared to the volume allotted for the steam generator compartments in NET (with lower fusion power), this is a factor of 2 - 5 larger.

A three level ranking scheme has been adopted to the five blanket options, based primarily on engineering judgement and to some extent on the quantitative results obtained in this study. The ranking is done with respect to (a) safety relevant design aspects including technical feasibility, and (b) safety concerns relevant to licensing. Two classes of issues have been identified, i.e. 11 design issues (like vanadium alloy qualification, tritium inventory in breeder, high coolant pressure, MHD pressure drop, first wall cooling effectiveness, etc.), and 12 safety issues (like potential breeder-H₂O reactions, potential lithium reactions with environmental media, tritium extraction from breeder, Be-water reaction, etc.). Within each class a ranking level A or B or C was then

assigned to each of the issues relative to the ranking criteria defined in Table 2.

Literature:

- [1] K. Kleefeldt, F. Bourbon, W. Kramer, K. Schramm, M. Steinbrück, Unpublished Report of KfK

Staff:

F. Bourbon
 K. Kleefeldt
 W. Kramer
 K. Schramm
 M. Steinbrück

Table 2: Ranking levels and criteria		
Ranking Level	Ranking Criteria for	
	Design Level	Safety Level
A	Option seems to be feasible with respect to the issue within ITER time schedule, or issue is not applicable.	Option does not raise major safety concerns beyond current NET safety measures, or issue is not applicable.
B	Option seems to be feasible within ITER schedule but requires substantial R&D effort or entails design complexity or threatens availability and reliability goal.	Option raises severe safety concerns but defense-in-depth concept can mitigate consequences to guarantee the safety rules.
C	Option is judged to be technically not feasible within ITER time schedule with proof of reliability.	Option raises severe safety concerns leaving risk, at present uncertainties, to fail the safety rules.

The ranking procedure shows, that each option has at least one issue (design or safety) ranked "C" (critical) and, hence, no one would be viable for ITER according to this ranking scheme. Yet, there are differences. Options I and II are penalized by four "C" each and are by far the less favorable solutions. Option III and IV received two "C", both of them with the vanadium alloy qualification issue as the dominating one. If this problem could be solved, e.g. by choosing steel instead of vanadium, both options were attractive, especially option IV, where the Be-water reaction issue could be bypassed by eliminating water from the vacuum vessel. Option V has one critical issue only, the Be-water reaction hazard, and has otherwise the highest number of issues ranked "A". However, unless it can be shown that the Be-water reaction problem in combination with the high water pressure in the blanket can be coped with, we would rank option V after IV.

In conclusion, the five options have been ranked from the feasibility and safety level point of view in the following order: IV, V, III, I, II. The modified option IV with steel instead of vanadium and NaK or He instead of water in the vacuum vessel seems to be a viable option.

Appendix I: Allocation of Tasks

Task No.	Title	KfK Departments
----------	-------	-----------------

Plasma Facing Components

PSM 3	Low Cycle Fatigue of 316L and Welds	IMF II
PSM 8	High Emissivity Coatings on 316L	IRS
PPM 1	Development and Characterization of Graphites and CFCs	IMF I
PPM 3	Off-Normal High Heat Loads	INR
PPM 4	Ceramics for Heating and Current Drive Systems	IMF I
PPM 6	Erosion, H-Retention, Gas Interaction	INR, IRCH
PDT 1	First Wall Mock-up and Tests	IATF, IMF II
PDT 2	Divertor Mock-up and Tests	IRS

Superconducting Magnets

MCOI	Model Coil	ITP
MCON	Full-Size 40 kA Conductor	ITP
MTOS	TOSKA Upgrade for Model Coil Testing	ITP, HIT, HPE
MBAC	High Field Operation of NbTi at 1.8 K	ITP, HIT, HPE

Vacuum and Fuel Cycle

TPV 1	Mechanical Vacuum Components	HIT
TPV 2	Optimization of Cryogenic Vacuum Pumping of Plasma Exhaust	HIT
TEP 2	Permeation und Catalytic Cracking: Alternative Options	IRCH

Nuclear Engineering / Basic Blanket

NDB 2	Neutronics Data Base - Benchmark Experiments	TU Dresden
-------	----------------------------------------------	------------

Remote Handling / Maintenance

RHB 1	RH Common Subsystems	IAI
RHT 1	Articulated Boom Transporter	HIT, IAI, HVT
RST 2	Cutting and Welding Tools	HIT

Safety and Environment

SEA 3	Analysis of Reference Accident Sequences	IRS
SEP 1	Radioactive Inventories and Source Terms	IRCH
SEP 2	Environmental Impact of Tritium and Activation Products	INR

Long Term Program for Materials Development

LAM 2.1	Low-Activation Fusion Materials Development	IMF I
LAM 3.2	Development of Low Activation Martensitic Steel	IMF I, IMF II
MANET 1.1	Characterization and Optimization of MANET-II-Steel	IMF I, IMF II
MANET 2.3	Diffusion Welding	IMF III
MANET 3.2	Pre- and Post-Irradiation Fatigue Properties	IMF II
MANET 3.4	Pre- and Post-Irradiation Fracture Toughness	IMF II, HVT/HZ
MAT 5	Ion-Beam Irradiation Fatigue and Creep Fatigue Tests	IMF I

Test Blanket Development

BS - Solid Breeder Test Blankets

BS DE-D 1	Solid Breeder Test Blanket Design	IMF III, INR, IRS
BS BE-D 1	Beryllium	INR
BS BR-D 1/D 2	Preparation and Characterization of Ceramic Breeder Materials	IMF III
BS BR-D 3	Irradiation Testing and Post Irradiation Examination	IMF III, HVT/HZ
BS BR-D 4	Tritium Release	INR, HVT/HZ
BS BR-D 5	Irradiation Testing and Post-Irradiation Examination	IMF I
BS BR-D 8	Thermochemistry of the Reaction of Lithium Orthosilicate with Hydrogen	IRCH
BS NN-D 1	Helium Blanket Test Loop	IMF III, INR
BS NN-D 2	Irradiation Experiments and Non Nuclear Tests	IMF III, INR
BS NN-D 3	Irradiation Experiments and Non Nuclear Testing	IRCH

BL - Liquid Metal Test Blankets

BL DE-D 1	Liquid Metal Test Blanket Design	IMF III, INR, IATF, IRS
BL PC-D 2	Active and Inactive Impurities and Clean-up of Molten Pb-17Li	HIT
BL EI-D 1	Electrical Insulation and Coatings	IMF I, IMF III, IATF, IRS
BL MH-D 1	Liquid Metal MHD	IATF
BL SA-D 1	Reliability Assessment	IRS, IMF II
BL SA-D 2	Safety Analysis of Self-cooled LM Breeder Blankets	IRS

Development of ECRH Power Sources

ITP, IMF III

Tritium Supply and Management

HVT

Appendix II: Table of NET Contracts

Theme	Contract No.	Working Period
Extended Jacket Material Characterization of the Model Coil	ERB 5000 CT 920044 NET	10/92 - 9/93
Crack Growth in the NET First Wall	ERB 5000 CT 9100 72 NET	11/91 - 10/92
Impact of ITER Liquid Metal Blanket Design Options on Safety Level and Licensing in Germany	ERB 5000 CT 930028 NET	6/93 - 8/93

Appendix III: KfK Departments Contributing to the Fusion Project

KfK Department	KfK Institut/Abteilung	Director	Ext.
Institute for Materials Research	Institut für Material- und Festkörperforschung (IMF)	I. Prof. Dr.K.-H. Zum Gahr	3897
		II. Prof. Dr. D. Munz	4815
		III. Dr. J. Haußelt	2518
Institute for Neutron Physics and Reactor Engineering	Institut für Neutronenphysik und Reaktortechnik (INR)	Prof. Dr. G. Keßler	2440
Institute for Applied Thermo- and Fluiddynamic	Institut für Angewandte Thermo- und Fluiddynamik (IATF)	Prof. Dr. U. Müller	3450
Institute for Radiochemistry	Institut für Radiochemie (IRCH)	Prof. Dr. H.J. Ache	3200
Institute for Reactor Safety	Institut für Reaktor-sicherheit (IRS)	Prof. Dr. D. Cacuci	2550
Central Engineering Department	Hauptabteilung Ingenieur-technik (HIT)	Dr. H. Rininsland	3000
Institute for Technical Physics	Institut für Technische Physik (ITP)	Prof. Dr. P. Komarek	3500
Central Experimental Engineering Department - Hot Cells - Tritium Laboratory Karlsruhe	Hauptabteilung Versuchstechnik (HVT) - Heiße Zellen (HVT-HZ) - Tritiumlabor Karlsruhe (TLK)	Dr. Schubert	3114
		DI. Enderlein	3650
		DP. Jourdan	2514
Remote Handling Laboratory	Handhabungstechnik-Labor (HT)	Dr. Scholl	2942
Central Safety Department	Hauptabteilung Sicherheit (HS)	DP. W. Koelzer	2660
Institute for Applied Informatics	Institut für Angewandte Informatik (IAI)	Prof. Dr. H. Trauboth	5700
Institute for Nuclear and Atomic Physics of the Technical University Dresden		Prof. Dr. K. Seidel	035101/8982

Appendix IV: Fusion Project Management Staff

Head of the Research Unit	Dr. J. E. Vetter	ext. 5460
Secretariate:	Fr. I. Sickinger	ext. 5461
	Fr. I. Pleli	ext. 5466
	Fr. V. Lallemand	ext. 5466
Project Budgets, Administration, Documentation	BW G. Kast	ext. 5462
Studies, ITER / NET Contacts	Dr. J.E. Vetter	ext. 5460
Blanket Development and Test Facilities	DI H. Sebening	ext. 5464
Superconducting Magnets, Development of Gyrotrons and Transmission Components	DI H. Knuth	ext. 5468
Tritium Technology Structural Materials	Dr. H.D. Röhrig	ext. 5463
Safety and Environmental Impact, Remote Handling	DI A. Fiege	ext. 5465

Address: Kernforschungszentrum Karlsruhe GmbH
Nuclear Fusion Project Management

Post Office Box 3640, D-76021 Karlsruhe / Germany

Telephone No: 07247-82- Extensions

Telefax No: 07247 - 82 - 5467

Telex No: 17 724 716